Numerical models and experimental simulation of irradiation hardening and damage effects on the fracture toughness of 316L stainless steel

A thesis submitted to The University of Manchester for the degree of PhD

in the Faculty of Engineering and Physical Sciences

2012

Giuseppe Cornacchia

School of Materials

Table of Contents

final word count: 52954

List of Abbreviations and Definitions

LWR : Light Water Reactor

PWR : Pressurized Water Reactor

fcc : face centered cubic

dpa : displacement per atom

NRT : Norgett–Robinson–Torrens model for displacement dose rates

FEA : finite element analysis

GTN : Gurson–Tvergaard–Needleman model for porous plasticity

CT : compact tension specimen

DCT : disk compact tension specimen

HRR : Hutchinson-Rice-Rosengren crack tip fields

CMOD : crack mouth opening displacement

LLD : load-line displacement

J_c : fracture toughness for unstable crack growth

J_{Ic} : fracture toughness for stable crack growth

K_{Jc} : stress intensity factor from fracture toughness value for unstable crack growth

vvf: void volume fraction

“as received” : the state of the material as dispatched by the vendor;

“undamaged” : the state of the material after that one solution annealing at 1050 °C for 30 minutes followed by water quenching is executed on the “as received”;

“damaged” : the state of the material after that the experiments intended to put damage into its matrix are executed on the “undamaged”.

List of Figures

Abstract

In nuclear environments, irradiation hardening and damage have a detrimental effect on materials performance. Among others, fracture toughness of austenitic stainless steels decreases under neutron irradiation. Helium arising from transmutation reactions is one source of embrittlement leading to that decrement and it is here assumed as a case study, austenitic steel 316L being the material under investigation. The experimental reproduction of irradiation hardening effect on yield stress is attempted here by pre-strain under tensile loading at room temperature. The experimental production of porosity is attempted by inducing ductile damage, creep damage or a combination of them. Damage at the microstructural level is analyzed by metallography, fractography, X-ray tomography and quantified by image processing.

After calibrating the elastic, the plastic and the porous plastic constitutive equations by the means of tensile tests on smooth and notched specimens, results from damaging experiments are validated by finite element analysis using the Gurson-Tvergaard-Needleman model. The numerical models obtained represent different levels of damage into the material, as induced by the experiments.

Material presenting different levels of damage is then machined for fracture toughness evaluation in the shape of sharp-notched round bars. Fracture toughness initiation is inferred from the load vs. displacement plots applying an opportune fracture criterion. In order to test the suitability of the Gurson-Tvergaard-Needleman model, the load vs. displacement results are validated by retrofitting opportune constitutive laws for each "damaged" state. Retrofitting is discussed in relation to the type of damage produced.

Results show that the reproduction of the macroscopic effect of irradiation hardening on yield stress may be attempted for 316L by a pre-strain tensile loading at room temperature for levels up to 1.5 dpa or slightly more. These interrupted tensile tests did not give evidence of void volume fraction production. Creep tests at 650 °C showed sensitization at the grain boundaries but not porosity into the matrix. Creep tests at 1000 °C created 1.2% to 1.8% void volume fraction from grain boundary sliding. Finally, one 7% pre-strained specimen was subjected to creep test at 900 °C and stopped at 5% creep strain, without evidence of porosity into the matrix.

Fracture toughness tests on the "damaged" states obtained before showed a decrement of fracture toughness initiation when compared with "undamaged" 316L. Specimens with 30% and 40% eng. strain presented a sensible decrement and exhibited a brittle-like behaviour. The differences in porosity size and physical processes involved suggest not stating that a correlation exists with the helium embrittlement effect on the same property. The Gurson-Tvergaard-Needleman model worked for the "undamaged" material. It proved to be not suited for the brittle-like 30% and 40% eng. strain "damaged" materials because it did not capture the experimental progression of damage.

In the end, fracture toughness numerical predictions were made using different values of initial void volume fraction. It was argued that, starting from a threshold value, the brittle-like 30% and 40% eng. strain "damaged" materials revert to a ductile behaviour.

Declaration of Copyright

No portion of the work referred to in the thesis has been submitted in support of an application for another degree or qualification of this or any other university or other institute of learning.

Acknowledgments

Many thanks to my supervisors, first Prof. Andrew Sherry and then Dr. João Quinta da Fonseca, for their constant encouragement, the exchanges and the insight provided during three years. Many thanks to the fellow researchers based at Materials Performance Centre for their advice, in particular Dr. Fabio Scenini, and to the lab technicians working at the School of Materials, Mr. Stuart Morse among them.

In the end, I am grateful to my sponsors for their generous allowance: the "Keeping the Nuclear Option Open" consortium, Nexia Solutions and the Materials Performance Centre itself. I hope my efforts were worth the investment.

Author's background

Giuseppe Cornacchia, 1973, received his Laurea in "Ingegneria Nucleare" (five years course in nuclear engineering plus final dissertation) from the University of Pisa, Italy.

Chartered engineer in Italy since 2004, he worked three years as an independent consultant in the southern city of Foggia. He modelled and implemented software for the evacuation of urban networks, starting from his academic dissertation findings. He also completed an economic and structural project of one small, cheap, three blades wind turbine for the Italian market, but it was dropped at the prototyping stage.

In 2006, Giuseppe relocated to England in order to pursue a career in the nuclear field abroad. He attended an MSc in "Physics and Technology of Nuclear Reactors" at The University of Birmingham, graduating with Merit. After a summer project at the Materials Performance Centre, The University of Manchester, he was offered and gladly accepted a PhD scholarship there. This thesis represents the final act.

1. Introduction

About 440 nuclear power plants are in use today. The share in world electricity is about 16% and constant since the mid 1980s. Some new plants are in construction and several others are being commissioned, mainly from emerging countries. This renewed interest is partly due to the need to alleviate the man-produced carbon emission in the atmosphere, led to a "renaissance" being declared in the mainstream media in the early 2000s, after two decades of decline following the accidents of Three Mile Island and Chernobyl. Other factors playing a role were the cost-effectiveness of nuclear, compared with other available large-scale sources, and the geopolitical matter of security of supply in spite of the inner volatility of oil and gas prices. On the other side, a vast ongoing debate centres on public acceptance and the final storage of highly radioactive waste, two of the criticalities still in need of being fully solved. The very recent accident in Japan has added new uncertainty to the prospects of the nuclear industry in the early 21st century.

The most widespread class is water moderated and the Light Water Reactors (LWRs) make the biggest number at 360 out of total 440. In particular, Pressurized Water Reactors (PWRs) are about 270 and constitute the most consistent experience in the civil use of nuclear energy. Pressurized Water Reactors are also used for marine propulsion in the number of about 220. Together with 250 research reactors in the world (not all PWRs), they complete the nuclear allowance for peaceful usage.

Almost all of the nuclear power plants were built in the second half of the 20th century. They are rapidly going to be shut down, having been 40 years their planned operational life. However, considering the high cost of replacement and the uncertainties of the geopolitical scenario, many countries are extending the working life of their plants up to 60 years, provided that a strict safety and functionality test of the most critical components is passed. In that sense, this doctoral project mainly finds its niche in the investigation of some structural components in the pressurized water reactors, for which it is now required a detailed investigation, more than in the design phase, in order to support life extension and improve the design for the plants to come.

1.1 Project overview

Materials used in nuclear reactors are subject to irradiation damage from neutrons during reactor operation, which leads to the formation of atomic scale defects and transmutation products, including helium and hydrogen within them. An important performance issue relates to the embrittling effects of such gases generated through irradiation and, particularly, their diffusion and condensation to form voids on internal boundaries. Void swelling has a detrimental effect on the mechanical and fracture properties of core materials after extended periods of operation and fracture toughness decreases.

Austenitic stainless steel 316L is the material of interest in this project. Its main application in nuclear power plants involves core internals in Light Water Reactors and some structural components in the fusion reactors to come. In that working environment, fracture toughness sharply decreases to a saturation value with increasing dose, this saturated value being three to four times lower than the value exhibited by unirradiated material. Ductility also decreases and yield stress increases. These effects are the principal area of concern for the performance of austenitic stainless steels and will be addressed in this project by using both numerical models and experimental simulations.

1.2 Project aims

Uniaxial tensile and creep loading will be used to introduce damage into the given material. The attempt is to reproduce the said detrimental effects of neutron irradiation and helium bubbles on fracture toughness. These effects are going to be described in the literature review. In particular, plasticity will be used to reproduce the irradiation hardening effect on yield stress and tentatively correlated in terms of dpa. Creep testing at low and high temperature will be employed for producing porosity. These methods are uncommon in the practice and their suitability in this line of work will be questioned from a physical, mechanical and numerical point of view.

Metallographic and tomographic evidence from the "damaged" material will be evaluated in order to quantify the porosity introduced. That would act as initial void volume fraction in the specimens machined for fracture toughness testing.

Fracture toughness tests will follow, making use of standard and non-standard specimens machined from the said "damaged" material. Among non-standard specimens, a sharp-notched round bar will be employed and discussed.

Finite element analysis will be extensively used to introduce the fracture toughness estimation procedures, validate the experimental results and make predictions. For the "undamaged" and for each "damaged" state obtained, a coherent set of constitutive parameters for their elastic, elastic-plastic and porous-plastic behaviour will be proposed. Finite element analysis will also be used to predict fracture toughness against different values of initial void volume fraction for "undamaged" and "damaged" material.

The Gurson-Tvergaard-Needleman model, as implemented in Abaqus, will describe the damage progression. Its suitability will be questioned on a case-by-case basis. Its parameters and their relation with the damage produced will also be investigated.

1.3 Structure of this thesis

First, a detailed literature review will be conducted with regard to:

- austenitic stainless steels fundamentals and their usage in the nuclear industry;

- plasticity, ductile damage and creep damage as the mechanisms used in this project for creating yield stress increment and porosity leading to fracture toughness decrement;

- irradiation and helium embrittlement effects on fracture toughness into austenitic stainless steels, so that a benchmark is given;

- a comparison between work hardening and irradiation hardening, and the effect of irradiation on creep;

- fracture mechanics and crack behaviour in the continuum framework, as employed in this project;

- computational and experimental fracture mechanics, for presenting how fracture toughness is modelled numerically and the standards used for testing experimentally.

The goal is to identify the research territory, establish and occupy one niche of interest.

After the literature review, the numerical and the experimental procedures followed in this project will be presented. They are logically divided into four tasks: 1) identifying the given material; 2) introducing damage into the given material; 3) estimating the fracture toughness of the "damaged" material obtained and make numerical predictions for different values of initial void volume fractions; 4) comparing fracture toughness of the "damaged" material to irradiated material's one.

The first and preliminary task is the identification of the "as received" material that will lead to the definition of the "undamaged" state. One hardness test and some metallographic examination will give a hint of the yield stress state. A standard solution annealing procedure will be executed to get the "undamaged" state. An estimation of the grain size will follow: lower the grain size, higher the yield stress level because of the higher number of obstacles to the propagation of dislocation lines. After that, tensile tests at room temperature for both "as received" and "undamaged" states will be done on smooth and notched round bar specimens. Smooth tensile tests will serve to calibrate the elastic and the plastic constitutive laws of the numerical model for the "undamaged" state. Notched tensile test results will be used to calibrate the porous plastic part, relying upon the emphasis on the softening effect they show opposed to hardening coming from smooth tensile tests. At that point, the "undamaged" state of the given 316L austenitic steel will be defined both experimentally and, numerically, in terms of the Gurson-Tvergaard-Needleman model.

The second task is to introduce damage into the "undamaged" 316L and eventually quantify it in terms of void volume fraction. Experimental procedures will be set up to raise the yield stress and get porosity (from decohesion of inclusion particles) by using interrupted uniaxial tensile tests at room temperature. Creep tests at low and high

temperatures will be employed to introduce porosity. One combination of pre-strain and creep will also be attempted. The quantification of damage will be done by the means of image processing on the metallographic and X-ray tomographic evidence gained from these experiments. One set of differently "damaged" materials will be produced and fracture toughness specimens machined from them.

The third task is the evaluation of fracture toughness initiation of the "damaged" material. Preliminarily, some standard specimens used in fracture toughness testing will be analyzed numerically, in order to familiarize with their behaviour. Then, one direct comparison between same size Compact Tension (CT) and Disk Compact Tension (DCT) specimens will be attempted; the Disk Compact Tension is of particular interest in the nuclear industry, because of its symmetry and because it fits well the irradiation rigs. One small DCT specimen is here taken as benchmark for the fracture toughness decrement effect under neutron irradiation. Given the shape and the size of the material employed in this project, that is to say round bars, two different fracture toughness tests will be performed on the "undamaged" material and the differently "damaged" materials produced. One test will use the standard small DCT specimen, while the other one will use the non-standard sharp-notched round bar. Results will be validated by using finite element analysis. Fracture toughness initiation will also be computed numerically against a grid of different values of initial void volume fraction, as they could be obtained from future experiments in this line of work.

The fourth, final task is the comparison of the results obtained with the fracture toughness decrement induced by neutron irradiation and helium embrittlement, as found in the literature, in order to state whether a correlation may exist. Attention will be given to the suitability of the Gurson model on a case-by-case basis and to its parameters. The focus will then be extended to the broader literature, so that this doctoral work is put into the proper context of the activity ongoing at international level in this field.

In the end, following a discussion of the results obtained and the lessons learnt, a further protocol of experiments and numerical computations will be suggested.

2. Literature review

The three main areas from which this doctoral project finds its niche are here discussed.

First comes a short introduction to steels: what they are, where they come from, how they are classified, how they are used in the nuclear industry; then austenitic stainless steels are described with regard to their microstructural appearance and their general properties. This project is based on the investigation and modelling of a 316L grade, very similar to the ones used for internal structural components in nuclear power plants. The same material is also currently investigated for applications in the fusion cycle and in some of the so-called Generation IV plants.

Second comes a presentation of microstructural damage mechanisms. The concepts of deformation, ductile damage, creep damage and the effects of radiation damage and helium embrittlement in nuclear environments are introduced in succession.

Finally, fracture toughness is presented as the macroscopic property of interest in this project: cracks may go unnoticed during the operational life in nuclear power plants so putting at risk both the business and the safety of the personnel. A short summary of experimental and computational fracture mechanics at linear elastic, elastic-plastic and porous plastic levels is provided. It makes the basis for the numerical modelling and the experimental simulation of helium embrittlement effects on the fracture toughness of the said 316L austenitic steel. A conventional, cheap way to model, reproduce and simulate that detrimental effect is the main goal for this doctoral project.

2.1 Stainless Steels

Pure iron exists in two crystal forms at atmospheric pressure. One body centered cubic (bcc) (α-iron ferrite) remains stable from low temperatures up to 910 °C, when it transforms to a face centered cubic (fcc) form (γ-iron austenite). This remains stable until 1390 °C, when it reverts to the bcc form (now δ-iron) up to the melting point of 1536 °C

[1]. Pure iron is quite difficult to obtain and is very weak. The addition of a small concentration of carbon (0.1 - 0.2 wt %) as interstitial solute atoms has a great strengthening effect and it is sufficient to form a steel. The iron - iron carbide diagram, Fig. 2.1, provides the foundation to start investigating phases in the binary Fe – Fe_3C system.

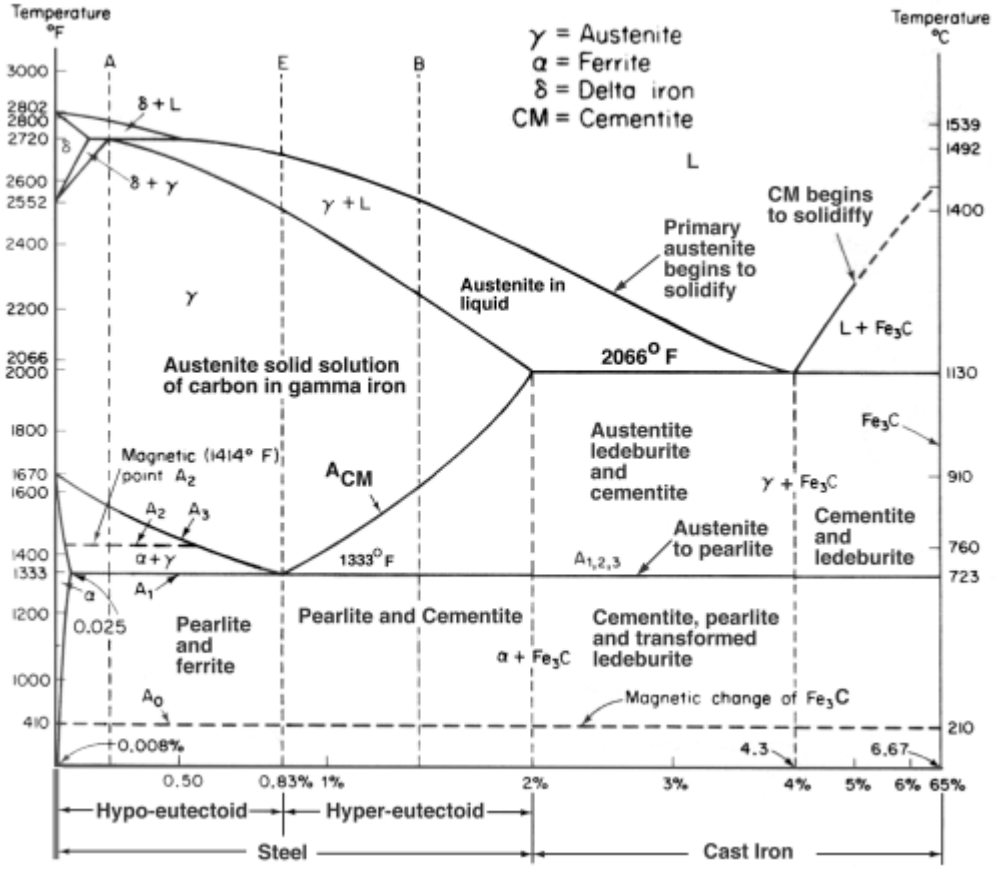

Fig. 2.1. The iron - iron carbide diagram [2].

Nitrogen is the other common alloy element derived from production and acting at interstitial level. Metallic alloying elements have much larger atoms and enter the iron lattices into substitutional solid solution.

Alloying elements can influence the iron-carbon equilibrium by expanding the γ-field (Ni, Mn, Co, inert metals, C, N, Cu, zinc, gold), that is to say encouraging the formation

of austenite over wider compositional limit [3], or contracting it (Si, Al, Be, phosphorus, boron and strong carbide forming elements such as titanium, vanadium, molybdenum and chromium).
Nevertheless when 18 wt% chromium is added to a low carbon steel containing 8 wt% nickel, the austenite is retained at room temperature and corrosion resistance is greatly improved both at room and elevated temperatures [3]. This leads to the group of austenitic stainless steels based on 18Cr 8Ni wt%. With both lower and high Cr contents, more nickel is needed to retain γ at room temperature [3].

2.1.1 History

Stainless steels were invented, developed and produced by the end of 19th century in the USA, Japan, Germany and the United Kingdom as a cheaper and stronger evolution of cast and forged iron, soon becoming the dominant materials in the industry and research [4]. Their relation to the economy of the main developed countries was upward until the 1970s, when new materials (such as silicon, plastics, aluminum) came to prominence. Steels are widely used today and the latest research focuses on developing new grades in order to improve the macroscopic properties for applications in the globalized industry. Its phases, mathematical modelling, the investigation of microstructure and its effect on macroscopic properties are the main subjects of investigation [5], with the United Kingdom enjoying a leading role [6].

2.1.2 Classification

Several standards organizations have developed a classification of alloys and steels by their composition and physical properties. It is worth citing here the unified numbering

system UNS from which the AISI-SAE steel grades in Fig. 2.2 and the relevant British Standard BS EN 10020:2000 [7] come. Similar standards exist in Germany, Italy, Japan.

Carbon Steel	10XX	Plain carbon steel , Mn 1.00% max
	11XX	Resulphurised free cutting
	12XX	Resulphurised - Rephosphorised free cutting
	15XX	Plain carbon steel, Mn 1.00-1.65%
Manganese Steel	13XX	Mn 1.75%
Nickel Steel	23XX	Ni 3.50%
	25XX	Ni. 5.00%
Nickel Chromium Steel	31XX	Ni 1.25%, Cr 0.65-0.80%
	32XX	Ni 1.75%, Cr 1.07%
	33XX	Ni 3.50%, Cr 1.50-1.57%
	34XX	Ni 3.00%, Cr 0.77%
Molybdenum Steel	40XX	Mo 0.20-0.25%
	44XX	Mo 0.40-0.52%
Chromium Molybdenum Steel	41XX	Cr 0.50-0.95%, Mo 0.12-0.30%
Nickel Chromium Molybdenum Steel	43XX	Ni 1.82%, Cr 0.50-0.80%, Mo 0.25%
	47XX	Ni 1.82%, Cr 0.50-0.80%, Mo 0.25%
Nickel Molybdenum Steel	46XX	Ni 1.05%, Cr 0.45%, Mo 0.20-0.35%
	48XX	Ni 0.85-1.82%, Mo 0.20-0.25%
Chromium Steel	50XX	Ni 3.50%, Mo 0.25%
	51XX	Cr 0.27-0.65%
	50XXX	Cr 0.80-1.05%
	51XXX	Cr 0.50% C 1.00% min
	52XXX	Cr 1.02%, C 1.00% minCr 1.45%, C 1.00%
Chromium Vanadium Steel	61XX	Cr 0.60-0.95%, V 0.10-0.15%
Tungsten Chromium Steel	72XX	W 1.75%, Cr 0.75%
Nickel Chromium Molybdenum Steel	81XX	Ni 0.30%, Cr 0.40%, Mo 0.12%
	86XX	Ni 0.55%, Cr 0.50%, Mo 0.20%
	87XX	Ni 0.55%, Cr 0.50%, Mo 0.25%
	88XX	Ni 0.55% Cr 0.50% Mo 0.35%
Silicon Manganese Steel	92XX	Si 1.40-2.00%, Mn 0.65-0.85% Cr 0.65%
Nickel Chromium Molybdenum Steel	93XX	Ni 3.25%, Cr 1.20%, Mo 0.12%
	94XX	Ni 0.45%, Cr 0.40%, Mo 0.12%
	97XX	Ni 0.55%, Cr 0.20%, Mo 0.20%
	98XX	Ni 1.00%, Cr 0.80%, Mo 0.25%

Fig. 2.2. AISI carbon and alloy steels grade [8].

The AISI range also includes stainless steels, which are three-digit numbers starting with 2, 3, 4 and 5 [8]. AISI tool steels and high-speed steels are defined as one letter followed by 1 or 2 digits [8].

2.1.3 Use in the nuclear industry

The first decade of the 21st century saw many governments from developed countries focussing on energy and on the ways to procure it in a safe, cheap and reliable manner. Geopolitical dynamics and high volatility in the commodities markets have been forcing the need of a strategic approach to this problem at the highest level. Nuclear energy still plays an active role with 436 active plants and more than 20 recently ordered, for a contribution of about 15% to the general output of electricity [9]. A "renaissance" is being declared [10-11] after twenty years of decline following a number of major accidents (notably Windscale, Brown Ferry, Three Mile Island, Chernobyl in the second half of the 20th century), but the very recent accident in Japan has added new uncertainty. The United Kingdom is very active and committed both at governmental and industrial / academic level [12-13]. In this context, materials research & development is considered a fundamental activity for extending the operational life of existing plants and choose suitable advanced / innovative processes to be used by the next Generation of plants coming. This doctoral project is funded by the Keeping the Nuclear Option Open consortium, part of the Research Council UK Energy Programme, a four-year initiative set up to address the challenges related to increasing the safety, reliability and sustainability of nuclear power. It represented the single largest commitment to fission reactor research in the United Kingdom for more than thirty years [14].

Pressurized Water Reactor (PWR) is a mature technology born in the United States and makes the basis for developing the advanced fleet being licensed these years, known as Generation III, which is the current state of art and commerce in the nuclear field. The main concern at materials level is about the reactor pressure vessel, made of ferritic – tempered bainitic steel and subject to radiation damage leading to hardening and embrittlement. In fact, bcc metals exhibit a ductile-to-brittle transition temperature (DBTT) because they have a temperature dependent yield stress, in particular at low temperatures, and a crack propagation stress that almost does not depend on temperature. The mode of failure changes from ductile fracture at high temperatures ("upper shelf") to brittle fracture at low temperatures ("lower shelf"). Radiation embrittlement is manifested

in an increase of DBTT together with a decrease in the upper shelf energy fracture, which leads to a decrease in fracture toughness [15]. Nevertheless, many modern plants have the potential for life extension to 60 years, following regulatory safety assessment of that embrittlement level.

It is also being appreciated that several of the internal components, made of austenitic stainless steel, receive high neutron doses and thus radiation induced mechanical properties degradation (mainly swelling and embrittlement). This is now becoming a key issue for standard PWR designs [15]. Other detrimental phenomena are under industrial and academic investigation, namely stress corrosion cracking, irradiation assisted stress corrosion cracking and fatigue [16-17]. One example of analysis protocol for internals is represented in Fig. 2.3 and it is mandatory for all plants under the NEI 03-08 in the USA.

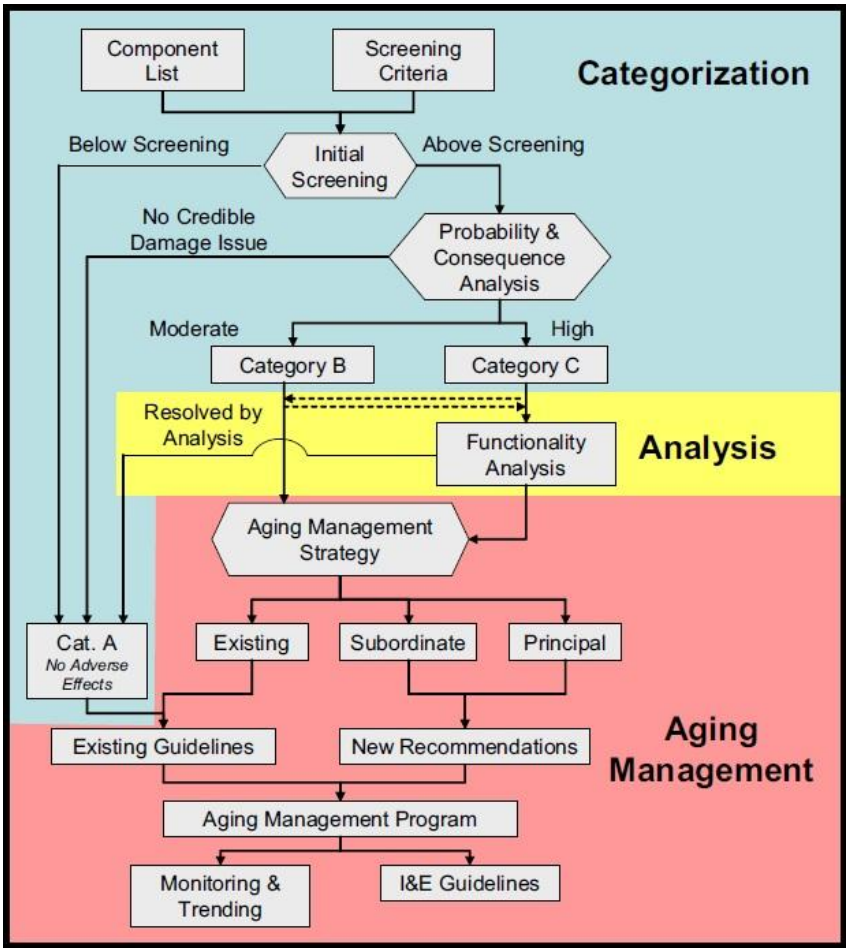

Fig. 2.3. Aging Management Protocol for reactor internals [16].

The protocol is a document (procedure, instruction, specification) that describes a plant's programme to ensure the long-term integrity and safe operation of PWR internals. It requires identifying the damage mechanisms of concern, to define the metrics used to characterize a damage mechanism, to focus on the observable effects / consequences on functionality, to circumscribe the location of degradation, to estimate the likelihood and timing of future damage. That is done by inspection, monitoring or trending techniques. Industry trend curves for strength and ductility are embedded in computer codes for the lower core plate, the baffle-former-barrel, the core shroud, obtained from in field experience. It is possible to extrapolate to remaining components based on fluence and temperature. Fracture toughness estimation is required for components with active cracking mechanisms. Susceptibility to thermal embrittlement is also accounted for. Probability and consequence analyses are conducted in terms of risk, which is calculated multiplying the probability of an event by its consequence. The risk contribution of individual independent events is then added to obtain a total risk estimate. In the end, this estimate is compared against given risk acceptance criteria.

The investigation carried on in the last 30 years on the internals did not answer all the questions. It has to be remarked that their design methodology was based solely on unirradiated material properties and that a combined effort of rethinking and in depth analysis is still very recent. For that reason, on the research side the analysis is now conducted by using so called multiscale modelling of radiation damage. The current leading programme at European level is called PERFORM 60, part of the Seventh Framework Programme of EURATOM for Nuclear Training and Research Activities [18]. Its aim is to unify experiences and procedures used in the European area in order to derive one single predicting tool for plants to come.

Austenitic stainless steels are also being reviewed as structural candidates for the Generation IV Supercritical Water Cooled Reactor [19-20] and for the fusion reactors [21-22]. These research projects are funded at international level in the Western world and are open to the leading Asian countries. There is a wide interest in this class of materials. It contributes to justify the investment into this line of work.

2.1.4 Austenitic Stainless Steels

In the 3xx family (AISI) there is one general-purpose alloy (18-20 % Cr, 8–10 % Ni, referred to as 304 and being the low carbon alternative to the general parent 302); the others derive from it, with compositions calibrated for special purposes as for Fig. 2.4:

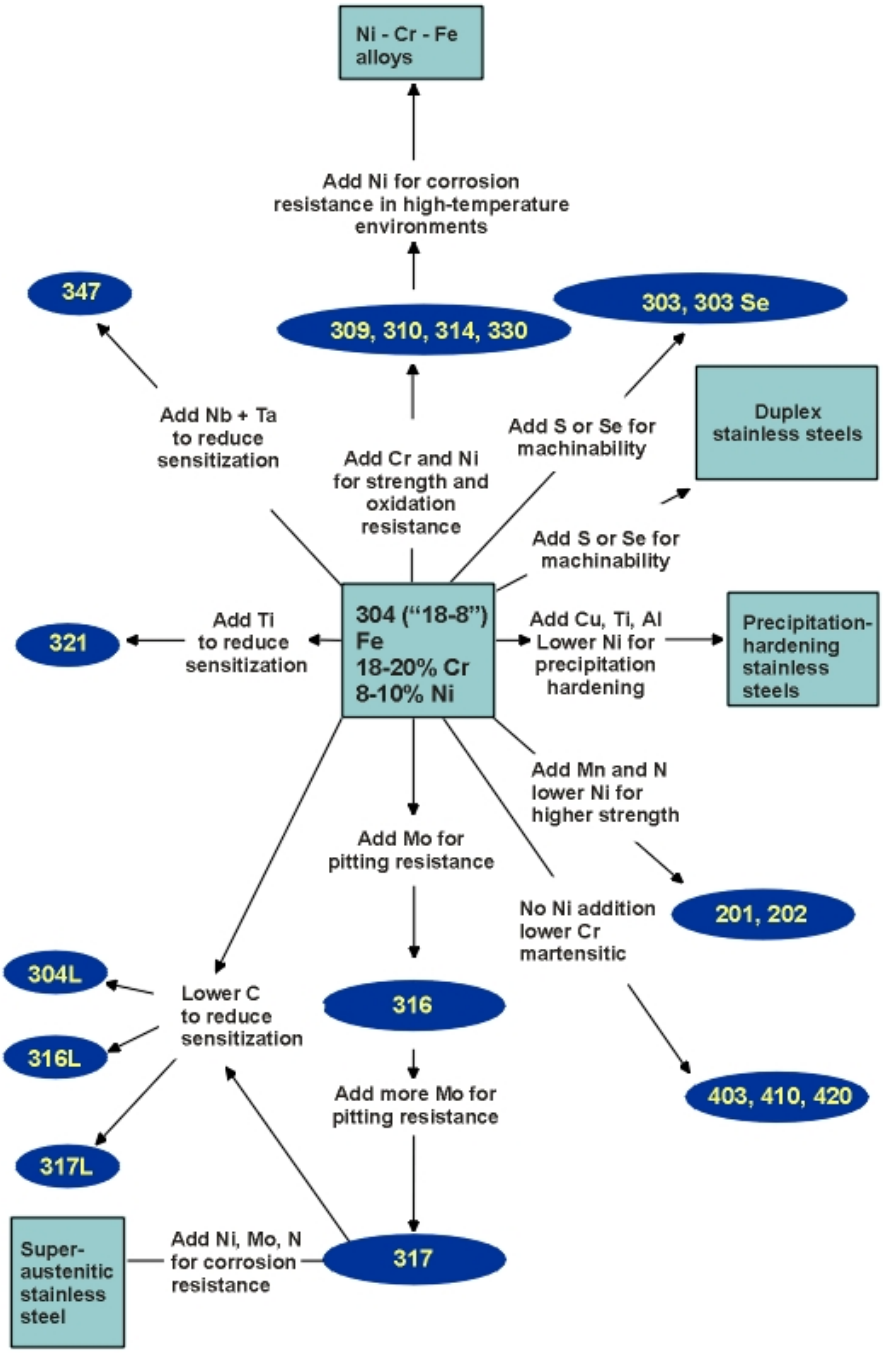

Fig. 2.4. Austenitic stainless steel family [23].

Austenitic steels have a face-centered cubic (fcc) lattice, as shown in Fig. 2.5, where the arrow represents the Burgers vector in this dislocation glide system. The shortest lattice vector is from one corner of the cube to the nearest face centre.

As deformation usually operates on a plane where there is close atomic packing, slip (the process by which plastic deformation is produced by a dislocation motion) occurs on $\{1\bar{1}1\}$ planes in <110> directions. Slip occurs between planes containing the smallest Burgers vector because a splitting into smaller Burgers vectors is always energetically favourable. Dislocations with large Burgers vectors, in fact, would immediately split into two or more.

In fcc metals, there are twelve slip systems in total, as the {111} planes have four different orientations.

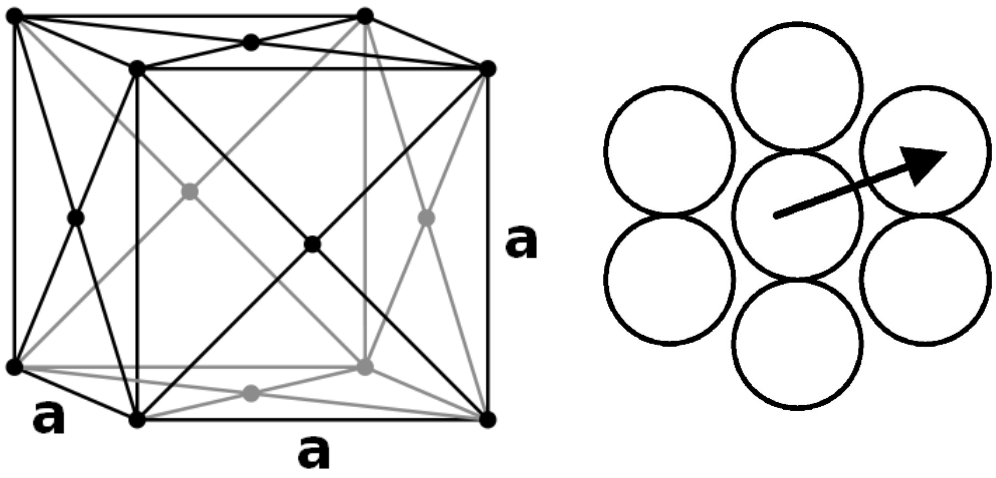

Fig. 2.5. Unit cell of an fcc material and lattice configuration of the close packed slip plane in an fcc material.

An edge dislocation in a 2D close-packed plane can be described as an extra 'half-row' of atoms in the structure. Dislocations are responsible for the plastic deformation within metals [24]. Their slip direction is described in terms of Burgers vector. Dislocations

allow slip to be localized so that the stress required for plastic deformation is greatly reduced when compared to the sliding of planes over one another. Inhibiting their motion can therefore increase the strength.

Within fcc metals, close-packed atom layers are stacked in ordered ABCABCABC sequences as shown in Fig. 2.6: the third plane is placed above the "holes" not covered by the second plane. However, the sequence can occasionally contain errors or stacking faults, often produced by the dissociation of a unit dislocation into two imperfect dislocations. This occurs to minimize the overall defect energy. Stacking layers can, for example, change to ABCACABCA, and therefore create a stacking fault.

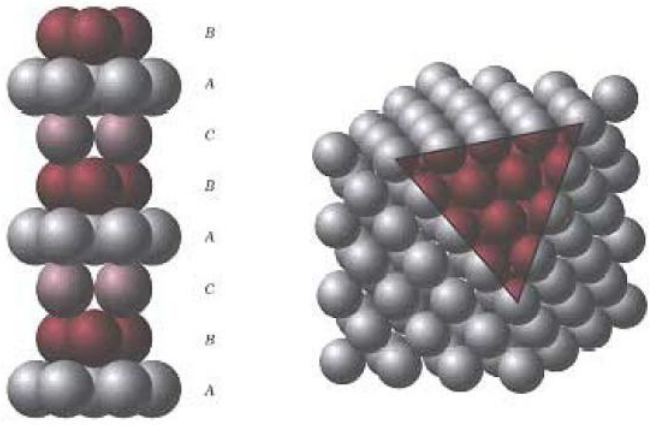

Fig. 2.6. Stacking sequence ABCABCABC [25].

2.2 Damage

Deformation in continuous solids is characterized by a distance change between two neighbouring points [26]. In engineering design and in modelling of materials it is usually implied that deformation is small compared to the solid size. Constitutive equations link the amount of deformation to the external stresses imposed on the representative volume of the solid. The source of these stresses can be mechanical, thermal, irradiative and

environmental. In nuclear power plants, a combination of these is applied and the response of the material is not always straightforward. Analysis at the local level instead of the global level may become necessary.

Damage is defined as the occurrence of irreversible microstructural alteration in the solid. It worsens the macroscopic structural properties of the component so threatening its functionality and its expected performance. In order to understand the processes involved in this project, the fundamentals of ductile, creep and irradiative damage on austenitic stainless steels are presented.

2.2.1 Ductile damage

Stress vs. strain curves from uniaxial tensile tests at room temperature for ductile metals are similar to the one in Fig. 2.7. Stress (external force over the area it is applied to) and strain (elongation over initial length) are defined as follows:

$$\sigma = F / A \tag{2.1}$$

$$\varepsilon = (l - l_o) / l_o \tag{2.2}$$

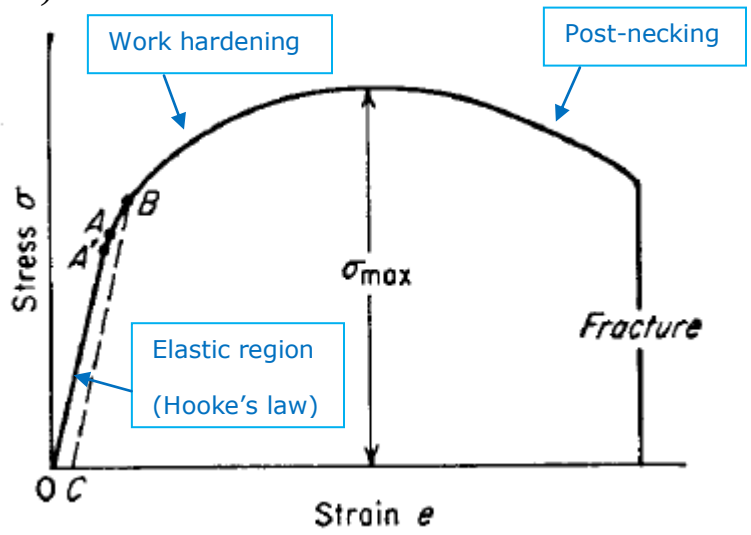

Fig. 2.7. Eng. stress / eng. strain curve for ductile steels [27].

Plastic deformation in metals induces changes in the microstructure. Each region of the lower interatomic or interface (between hard dispersed precipitates and the matrix) cohesion is the preferred place for ductile fracture initiation. One other initiating mechanism is the cracking of the same inclusion particles. Under the triaxial stress state, before the crack front, the microvoids enlarge and join, forming dimples. So discrete voids or cracks nucleate and grow within the material and then coalesce to form macrocracks, leading to material failure. Coalescence occurs when a critical value of void volume fraction (or of equivalent plastic strain) is reached in the matrix, under the effect of a loading condition expressed in the form of stress triaxiality and strain rate. These degrading defects are known as ductile damage [28].

The stress triaxiality ratio is noted as:

$$\frac{\sigma_m}{\sigma_{eq}} = \frac{\frac{1}{3}(\sigma_{xx} + \sigma_{yy} + \sigma_{zz})}{\frac{1}{\sqrt{2}}[(\sigma_{xx} - \sigma_{yy})^2 + (\sigma_{yy} - \sigma_{zz})^2 + (\sigma_{zz} - \sigma_{xx})^2]^{1/2}} \tag{2.3}$$

where σ_{eq} is the von Mises effective stress and σ_m the hydrostatic mean stress. The nine components of the second order stress tensor completely define the state of stress at a point in body.

The stress tensor can be written as follows:

$$\sigma_{ij} = \begin{bmatrix} \sigma_{xx} & \tau_{xy} & \tau_{xz} \\ \tau_{yx} & \sigma_{yy} & \tau_{yz} \\ \tau_{zx} & \tau_{zy} & \sigma_{zz} \end{bmatrix}, \tag{2.4}$$

where σ_{xx}, σ_{yy} ,σ_{zz} are normal stresses and τ_{xy}, τ_{xz}, τ_{yz}, τ_{yx}, τ_{zx}, τ_{zy} are shear stresses.

Higher triaxiality accelerates the creation of voids by augmenting the deviatoric part of the tensor:

$$s_{ij} = \sigma_{ij} - \frac{\sigma_{xx} + \sigma_{yy} + \sigma_{zz}}{3}\delta_{ij} \tag{2.5}$$

Voids grow in the transverse direction. Direct impinging with little internal necking of the internal ligament happens. When triaxiality is low, little lateral growth happens.

The ductile damage process is visible at the macroscale as a plastic flow and can be intensified by an additional successive loss of cohesion on the interfaces. The damage process is represented in Fig. 2.8 and its three stages are briefly discussed.

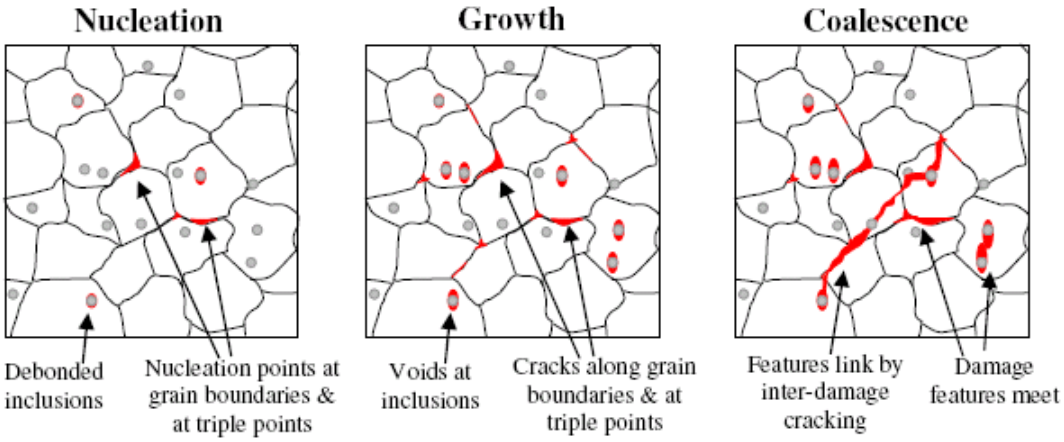

Fig. 2.8. The ductile damage process.

Nucleation: In metallic materials, cavity initiation sites are usually associated with second phase particles or non-metallic inclusions [29]. They may derive from alloying processes or as impurities from solidification: for example, gas pores –trapped gas in the die cavity- or shrinkage pores –from lack of liquid metal feeding the volume changes during solidification. Other sources may be precipitates from high temperature exposure, that is to say solids formed during chemical reactions, and ternary oxide inclusions. As a general rule, nucleation results from the inhomogeneity in plastic deformation between the matrix and the inclusions, usually modelled as elliptical shapes with a direction. Dislocation theory (for crystalline materials) or pure continuum mechanics have been proposed to approach this problem.

Dislocations pile up at the discontinuities until some sort of plastic relaxation happens. If the matrix is ductile and the particles are brittle, then the particles are unable to

accommodate the plastic deformation and void formation starts. If the chemical bonds are weak at the interface, simple debonding can happen. Nucleated voids may be uniformly spread through the microstructure or preferentially located along the grain boundaries.

Continuum mechanics assumes that the substance of the body is distributed throughout and that it completely fills the space it occupies. A continuum is a body that can be continually sub-divided into infinitesimal small elements with properties being those of the bulk material; a material may be assumed as a continuum when the distance between the real physical particles is very small compared to the dimension of the problem. Continuum mechanics deals with physical quantities of solids and fluids that are independent of any particular coordinate system in which they are observed, that is to say intrinsic properties (for example density, as opposed to mass). These physical quantities are then represented by tensors, which are mathematical objects that do not depend on the choice of a coordinate system.

According to Goods and Brown [30], the applicability of one approach or the other is mainly a function of particle size: the critical radius of particles above which continuum mechanics can apply is of the order of 1 μm, depending on the work-hardening rate of the material (work hardening rate increases with decreasing the particles size) [29]. This happens because real materials are packed in a certain manner leaving voids between them; work hardening rate affects the continuum assumption of homogeneity of properties for all the infinitesimal small elements and invalidates it. Two criteria must be satisfied for the formation of cavity. One energy criterion: the elastic energy released from the particle by interfacial separation is at least equal to the surface energy created; and one stress criterion, in the sense that a critical stress σ_d must be achieved at the interface or inside the particle. Several models have been proposed to approach the local stress-strain field as a function of the far field applied to the material.

Beremin [31] proposed one model accounting for inhomogeneities and inclusions:

$$\sigma_d = \sum_1 + k(\sigma_{eq} - \sigma_y) \tag{2.6}$$

where $\sum_1$ is the maximum principal stress, k (dimensionless) and σ_d are temperature-independent material parameters that are function of the particle shape, while σ_y is the yield strength of the material and σ_{eq} is the equivalent von Mises stress. This model works for particles size larger than ~ 0.1 μm to 1 μm. Below this size, a dislocation-based theory must be used [32].

It has to be noted that nucleation does not occur simultaneously during plastic deformation, that is to say the fraction of cavities is an increasing function of plastic strain. In addition, cavities are not homogeneously distributed and a statistical approach can be used in order to model ductile fracture, where the material is presented as a grid and every cell is assigned a random parameter [33]. The loss of macroscopic strain hardening capacity, as it happens in the case of simultaneous nucleation of voids, has been investigated by Hutchinson and Tvergaard [34].

Growth: The growth of voids is strongly dependent on stress and strain states. In relation to micromechanical analysis, it can be distinguished an uncoupled approach based upon the von Mises criterion as a flow criterion, and coupled approach (the alloy is considered a porous medium and the influence of voids on plastic flow cannot be avoided) based upon the Gurson model [35] and its modification by Tvergaard–Needleman [36], known as GTN model. Gurson developed a void growth model in which the von Mises flow potential is modified by introducing the volume fraction of voids, *f*, as a damage parameter. This model was extended to account for effects of void nucleation and coalescence. The development of the plastic deformation around the void leads to its enlargement.

Coalescence: Cavity coalescence is still very poorly understood and it requires a large research effort. Geometrical parameters (void size, shape, spacing, orientation), material properties (strain rate sensitivity, work hardening rate) and stress state (stress triaxiality) influence this event.

Geometrical criteria from McClintock [37] and Brown and Edbury [38] are based upon the impinging of voids and void length equal to the intervoid spacing respectively. A

critical strain to failure is used to express these conditions and the stress state is not taken into account.

The porous plasticity model from Gurson-Tvergaard-Needleman is based upon the void volume fraction modification of the yield surface. Coalescence occurs at a critical value of void volume fraction. It is the sudden transition from the void growth stage to a localized mode of plastic deformation in the ligament between voids either normal to the main loading direction (coalescence by internal necking) or in shear (in void sheet coalescence mechanism, the stable void growth is suddenly terminated while the voids are still quite apart) [39]. In the former, cavity growth occurs continuously until the voids impinge together; in the latter, cavity growth initiated from large second phase particles is bypassed by the formation of shear bands between growing cavities, where smaller cavities are initiated from strengthening precipitates. These are shown in Fig. 2.9.

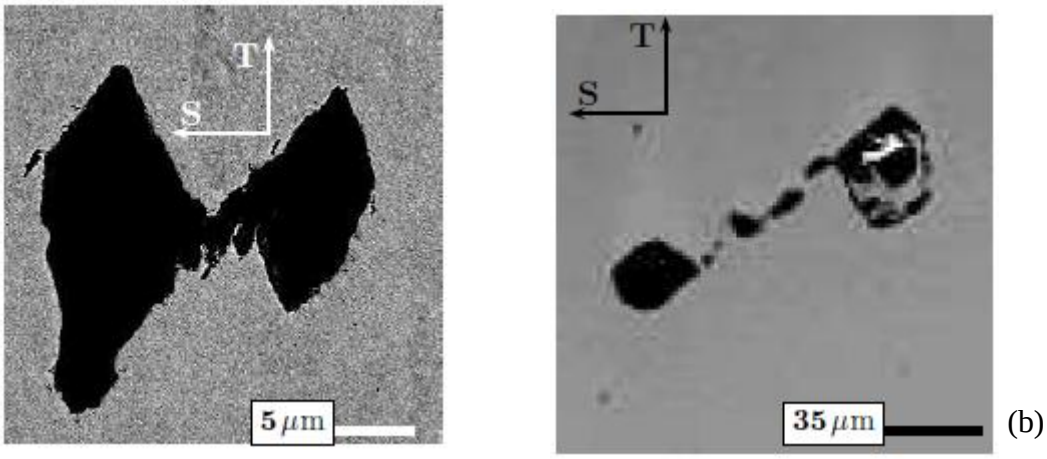

Fig. 2.9. Modes of void coalescence. (a) Necking of intervoid ligament or coalescence in a layer. (b) Coalescence in a micro-shear band. [39]

Plastic flow localization and shear band formation are discussed in [40-41].

Debonding is the disconnection between particles and matrix, while fracture in particles happens at transgranular or intergranular level of the particles themselves.

One analytical model by Thomason [42], valid for non-hardening materials, gives a plastic limit load for failure in terms of a critical mean stress for internal necking multiplied by the current area fraction of intervoid matrix.

Coalescence in ductile fracture also depends on the strain rate. Tonks [43] proposed a void cluster model based on void coalescence of existing voids. At low loading strain rates, the biggest cluster has time to grow much more rapidly than smaller clusters to break the sample. At high loading strain rates, large clusters cannot grow any faster than smaller clusters so the sample breaks when enough clusters grow independently to form a fracture surface by random accumulation. The mechanism of coalescence in ductile fracture is analyzed by the means of atomistic simulations. Among others, Rudd [44] studied the critical inter-void ligament distance at which the onset of void coalescence occurs in ductile materials. In addition, recent developments in tomography allow researchers to capture void coalescence experimentally. Weck [45], for example, analyzed the behaviour of an embedded array of holes in comparison with the prediction of several models. He showed the strong effect of macroscopic necking on the coalescence path. He also showed that increased material strength and nucleation of secondary voids result in greatly reduced coalescence strains. Other studies involve coalescence of void sheet subjected to shear stress [46].

.

The key concepts that form the basis of almost all classical theories of plasticity are:

- The decomposition of strain into elastic and plastic parts;

- Yield criteria: they predict whether the solid will respond elastically or plastically (Tresca, von Mises); the GTN model accounts for porosity and further modifies the yield surface;

- Strain hardening rules, which control the shape of the stress-strain curve in the plastic regime (isotropic hardening, kinematic or cyclic hardening);

- The plastic flow rule, which determines the relationship between stress and plastic strain under multi-axial loading;

- The elastic unloading criterion, which models the irreversible behaviour.

Plastic flow is used to calculate the plastic strain induced by loading beyond yield. Starting from the magnitude of the plastic strain increment, the use of a yield criterion leads to the definition of a so called “consistency condition” (the stress during flow

remains on the elastic domain boundary) under uniaxial loading. Then it is possible to specify the ratios of the plastic strain components by the means of a function of stress and strain history.

As an example, the plastic flow potential Φ of the GTN model, at the yield point, takes the form:

$$\Phi = \frac{\sigma_{eq}^2}{\sigma_f^2} + 2q_1 f^* \cosh\left(\frac{3q_2\sigma_m}{2\sigma_f}\right) - 1 - q_3 f^{*2} = 0 \qquad (2.7)$$

where σ_{eq} is the equivalent stress, σ_f is the flow stress, σ_m is the hydrostatic stress and q_1, q_2, q_3 are adjustable parameters. The internal variable f^* accounts for the rapid loss of stiffness due to void coalescence beyond some critical volume fraction f_c and is defined as

$$\begin{aligned} f^* &= f && \text{for} && f \le f_c \\ f^* &= f_c + K(f - f_c) && \text{for} && f > f_c \end{aligned} \qquad (2.8)$$

where K is a function of f_c and of the void volume fraction at failure f_f.

Research in the field of ductile damage and fracture criteria is nowadays focussed on the improvement of both coupled (incorporating damage accumulation into the constitutive equations) and uncoupled (neglecting the effects of damage on the yield stress of materials) approaches. An up-to-date and comprehensive analysis from an experimental and a computational point of view is given in [47]. It is widely debated there the predominance of one single mechanism of failure on the others while using standard specimen geometries and loading conditions. There is a discreet set of fracture criteria used to predict ductile failure in plastic deformation processes. They are based on different fracture mechanisms. A broad understanding of the conditions at which one criterion or one other is used is still an open field for experimental research.

2.2.2 Creep damage

Creep is the continuous plastic deformation of a material that is subjected to a constant stress below its yield stress when the material is at a high homologous temperature ($T > 1/3\ T_m$, being T_m = 1400–1420 °C the melting temperature for the austenitic steel used in this project). The micromechanisms controlling creep deformation involve not only dislocation glide (or slip), but also dislocation climb and, at low stresses, diffusion controlled mass transport along the grain boundaries [48].

The obstacle blocking the slip of a dislocation on its glide plane causes additional dislocations generated by a nearby source to pile up behind it [49], as in Fig. 2.10.

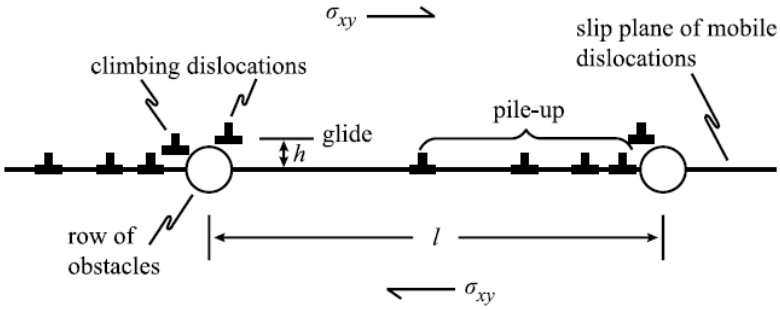

Fig. 2.10. Schematic of climb and glide creep with pile-up of dislocations [49].

Dislocation lines moving through the solid cause a material to deform plastically under an applied shear stress. They can only move in certain directions by diffusion (thermally activated climbs). In addition, dislocation joggings may impede the motion at low temperatures, so producing a strain hardening effect. At high temperatures, they may become mobile and climb in a direction perpendicular to the normal stress applied. Climb is a diffusional process and depends strongly on the solid atoms ability to diffuse to or away from the dislocation. Dislocation sources may interact, in the sense that they are pinned and strain harden the material. A strain energy is associated with lines, jogging and sources interaction and, at high temperatures, the kinetics is favourable so that the defect is removed releasing the strain energy. The dislocation density is reduced. This process is called recovery and its main mechanisms are annihilation of dislocations with opposite sign, polygonization of the lattice and coarsening (loss of boundary area) [50].

Creep can be ideally thought as a three stages process: primary stage, secondary or steady stage and tertiary stage, as shown in Fig. 2.11.

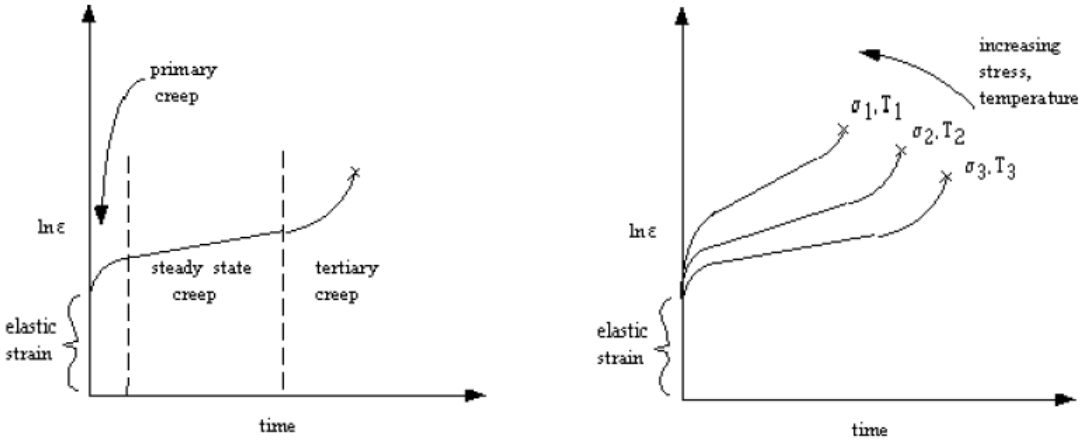

Fig. 2.11. Creep stages (a) and their relation with stress, temperature (b) [51].

The mechanism in the primary region is the climb of dislocations that are not pinned in the matrix. It is usually less than one percent of the sum of the elastic, steady state and strongly depends on the history of the material. The creep strain rate is reducing because of work hardening, until equilibrium is reached.

In the secondary or steady state creep, the strain rate is constant, that is the rate of strain hardening by dislocations is balanced by the rate of recovery. The prevalent mechanism between $T_m = 0.3$ and $T_m = 0.7$ is dislocation climb, that is the climb of dislocation jogs and the strain rate can be calculated as follows:

$$\dot{\varepsilon} = A \cdot \sigma^n \cdot e^{-\frac{H}{kT}} \tag{2.9}$$

with H being the activation energy for diffusion, A a constant, k the Boltzmann constant, n the stress exponent and σ the stress.

Climb over second phase particles leads to an increase of dislocation line length [52].

When higher temperatures are applied above 0.7 of the melting temperature, a different mechanism becomes dominant. In this region, the creep is analogous to viscous flow and the mechanism is diffusion of atoms from one place to another.

In the tertiary region, the high strains will start to cause necking in the material just as in the uniaxial tensile test. This necking will cause an increase in the local stress of the component, which further accelerates the strain. Eventually the material will pull apart in a ductile fracture around defects in the solid. These defects could be precipitates at high temperatures or grain boundaries at lower temperatures.

It has been suggested that creep fracture occurs by wedge type cracking at grain boundary triple points, most easily at high stresses (lower temperatures) and larger grain sizes; their nucleation has also been addressed to grain boundary sliding. Another mode of failure has been associated with round-type cavities. With the 316L austenitic steel in the 500 - 800 °C range (or a bit larger window, literature does not fully agree about the span), nucleation, growth and coalescence of grain boundary cavities leads to the formation of intergranular cracks. The two modes are related and described in [51, 53]. Fig. 2.12 reports the expected creep mechanisms at a fixed temperature and varying the stress level.

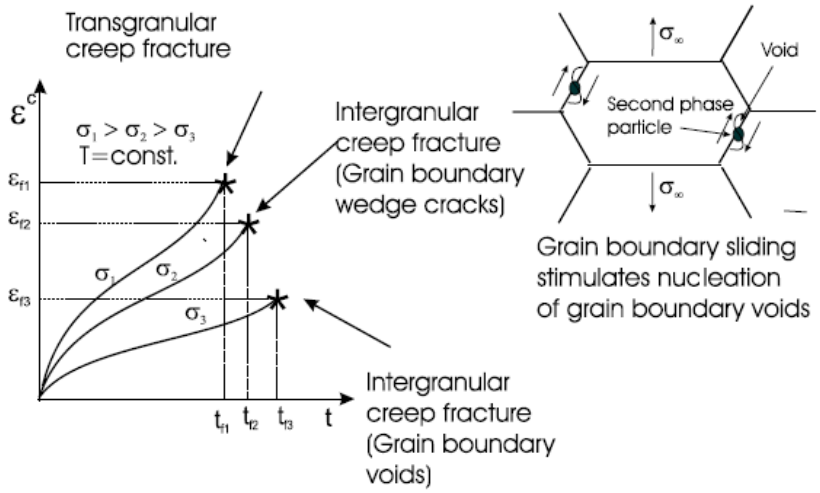

Fig. 2.12. Schematic of creep fracture mechanisms.

Fig. 2.13 shows round-type cavities and the wedge mechanism.

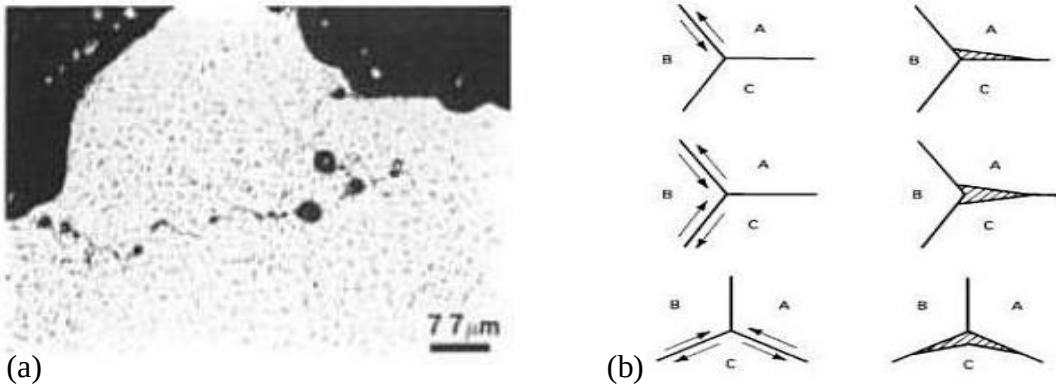

Fig. 2.13. Round type cracks (a) and wedge type mechanism (b) for 316 ss under creep [54].

A fracture mechanism map for 316 stainless steel is presented in Fig. 2.14. It shows the predominant deformation mechanisms at different temperatures and stresses for a rupture time of 10,000 hours. Recent literature has put much effort into the analysis, construction and simulation [55-57] for several alloys. This answers the need for specific performance at finely narrowed values of temperature and stress. These are sometimes located where competing processes overlap, so that classical theories fail to account properly for the experimental evidence.

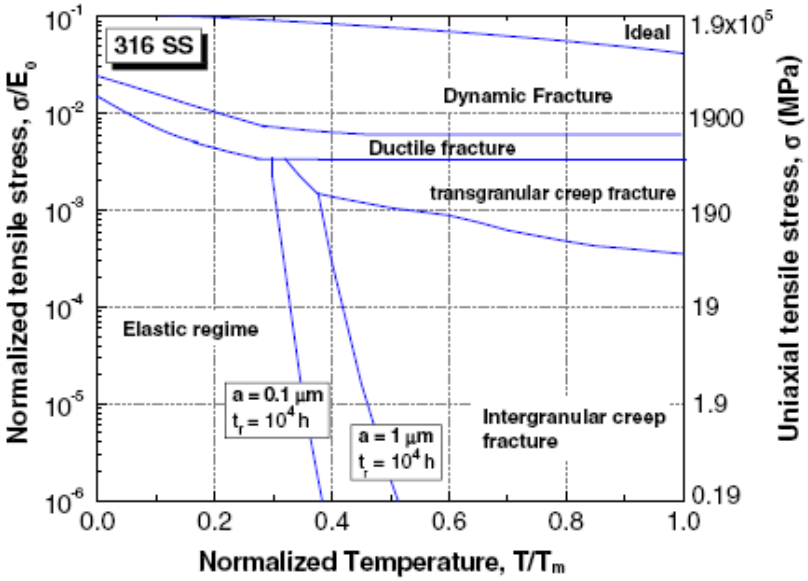

Fig. 2.14. Deformation mechanism map for stainless steel 316 [56].

One extensive collection of results from exposure in high temperature plants was prepared by the European Creep Collaborative Committee, an independent group of plant

manufacturers, in the 1990s and released publicly in 2005 [58]. It collated creep rupture data for a number of high temperature steels, including 316, 316L, 316 Ti, 316 LN, 316 L(N), 316 LNB and rupture times greater than 10,000 hours. For the aim of this project, however, such a timescale appears too large to be considered. What happens to 316 stainless steel during shorter tests (below 1000 hours) at higher temperatures is described by the ASM Handbook n.12 [54]. It is observed that the creep rate increases with load and temperature -while decreasing for greater grain size- and that the area of fracture reduces with increasing temperature as graphically shown in Fig. 2.15.

Fig. 2.15. Macrographs for 316ss specimens tested at 760 °C, 815 °C, 870 °C, 925 °C, 980 °C [54].

Slightly different times to rupture are observed for 316, 316L and the nuclear grade 316 L(N) in creep tests below 1000 hours when the same stress is applied [59-61]. Different temperatures are going to be tried in this project and the planned time to rupture would not exceed the 1000 hours.

The deformation map at 0.7 *Tm*, Fig. 2.16, accounts for mechanisms such as diffusional flow (at very low level stresses) and grain boundary sliding that are going to be used in this work. In fact, both may produce voids that can be of interest for this project. The grain size of the material going to be tested will be controlled by a standard solution annealing (1050 °C for 30 minutes followed by water quenching) of the "as received" 316L ss. The idealized mechanism of diffusional flow for a cuboidal grain is presented in Fig. 2.17. The faces act as the sources and sinks for vacancies [62]. It is suggested in the literature that the grain structure deforms via diffusional creep if the grain size is in the range of a few µm. Nevertheless, it has to be pointed out that diffusional flow is not fully understood in stainless steels yet.

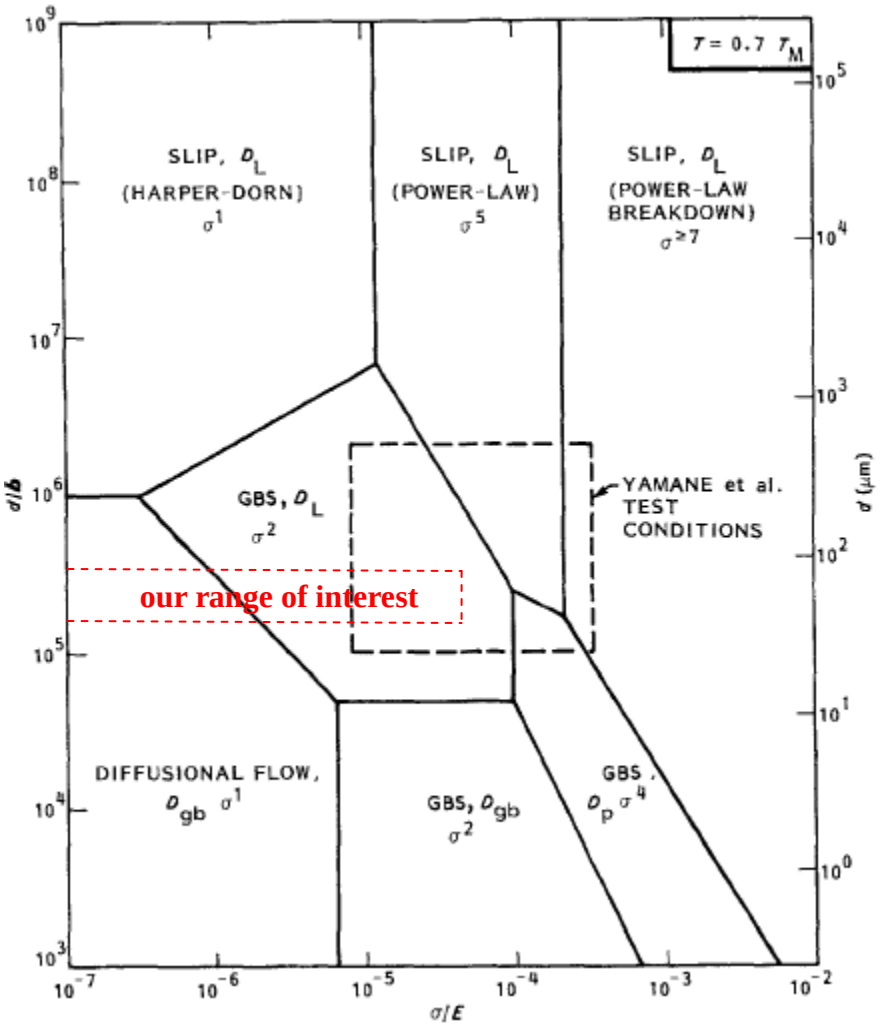

Fig. 2.16. Deformation mechanism map for close-packed metals at $T = 0.7\ T_m$ [63].

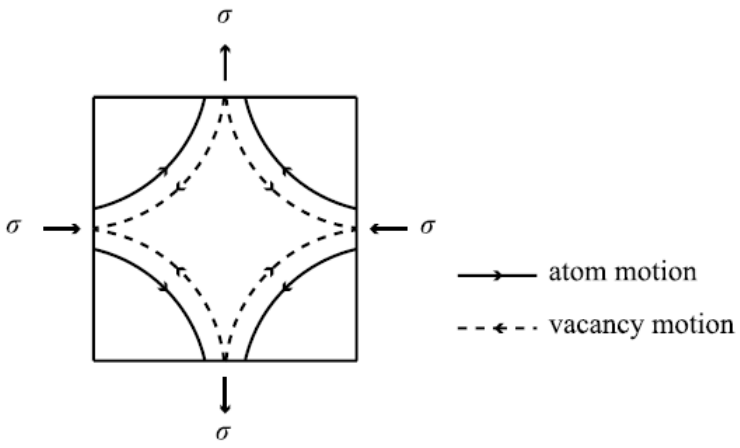

Under the applied stress, vacancies will follow the paths described by the dashed lines and atoms will move in the opposite direction (solid lines). Note that the vacancy flow is from the faces acted on by the tensile stress to those acted on by the compressive stress [62].

Fig. 2.17. Idealization of diffusional vacancy and atom flow between grain faces [62].

As for the degradation that happens at the grain boundary level when exposed to a temperature into a certain range (500–800 °C are the usual values reported for 316L, the minimum being 400 °C and the maximum 900 °C), it is called sensitization or carbide precipitation. The grain boundary acts as an anode and the main area of the grain as a cathode. This results in the flow of energy from the small anode area to the large cathode area, which causes rapid attack penetrating deeply into the metal [64]. The chromium along grain boundaries tends to combine with carbon to form chromium carbides. The effect is a depletion of chromium and the lowering of corrosion resistance in the areas adjacent to the grain boundary [63]. For carbon contents < 0.030%, such as in 316L, no significant chromium depletion occurs. Nevertheless, sensitization can still occur under prolonged heating in the critical temperature range [65].

At microscopic level, the sequence of precipitation and resolution or dissolution of the various phases is summarized in Table 2.1 for 550 °C and 600 °C. They strongly depend on the time of exposure. The $M_{23}C_6$ (M = Cr, Fe, Mo, Ni) carbide is normally the first phase to form in austenitic stainless steels.

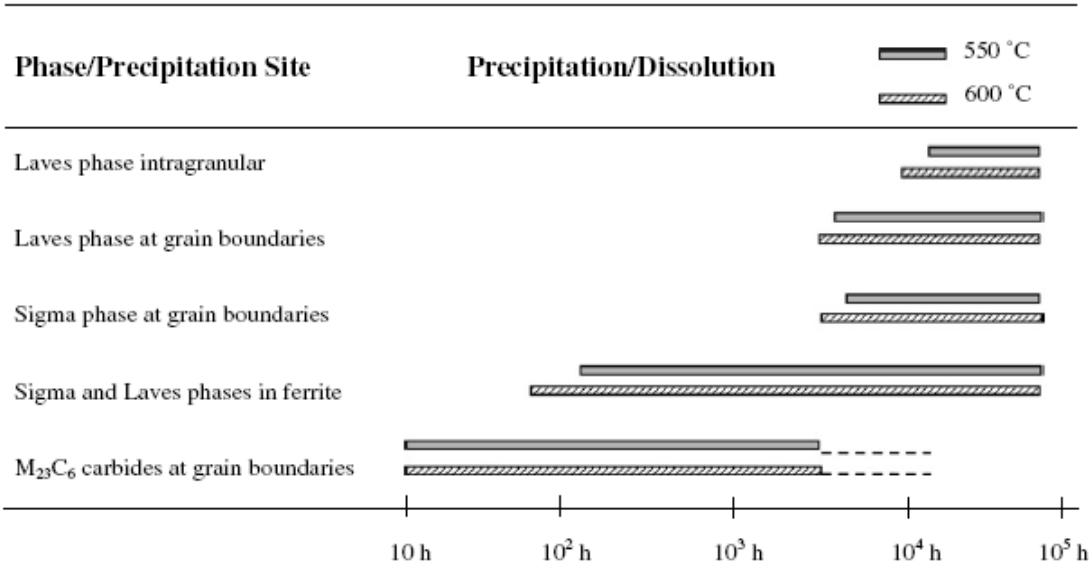

Table 2.1. Phase reactions during ageing of AISI 316L(N) at 550 °C and 600 °C [66].

2.2.3 Radiation damage models and effects

During the operational life in nuclear power plants, high-energy neutron radiation can lead to degradation processes in the materials of critical components in or near the cores of thermal and fast reactors [15], where they are exposed to fluxes with energies ranging from several MeV down to ~ 0.025 eV. This degradation alters the macroscopic properties of the components and poses a threat to the safety of both the business and the personnel, even if design against catastrophic accidents and a strict quality assurance are used to minimize the risk.

Neutron radiation damage in metals and alloys is produced by two principal mechanisms, namely: direct displacement of atoms and creation of impurity atoms. This Section is going to introduce them together with the range of neutron irradiation of interest in this project.

The radiation damage event is actually composed of several distinct processes [67]; their order of occurrence is the following and summarized in Fig. 2.18:

- an energetic incident particle interacts with a lattice atom; neutrons interact by elastic scattering and lose kinetic energy until they are slowed to thermal energy;
- kinetic energy is transferred to the lattice atom leading to a primary knock-on atom (PKA);
- the atom is displaced from its lattice site;
- the displaced atom passes through the lattice and leads to the creation of additional knock-on atoms, provided it has sufficient kinetic energy;
- a displacement cascade is produced ;
- the primary knock-on atom comes to rest and terminates as an interstitial.

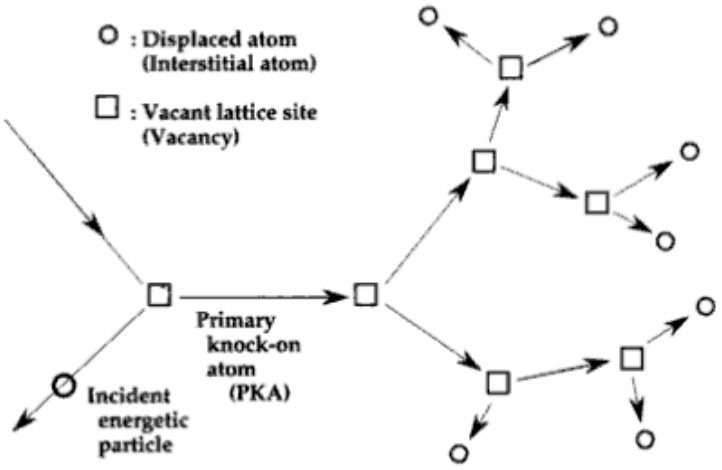

Fig. 2.18. Schematic illustration of the collision cascade.

An energy transfer of ~ 25 eV is required to displace an atom and energy above ~ 1 keV is required to produce a cascade. A single typical fast neutron-atom collision creates a PKA of typically tens of keV and so leads to several collision cascades at the end of the PKA track, with dimensions of 10 nm or less.

A large fraction of the point defect population annihilates by mutual recombination, while a small proportion escape the cascade as freely migrating defects [67].

In alloyed steels, the ultimate defect configuration affecting materials behaviour under irradiation will depend on, in addition to neutron and PKA energies, parameters such as irradiation temperature, pre-existing point and defect line populations, point defect-dislocation and point defect – solute interactions [67]. Raising temperature means that atom bonds become longer and atoms vibrate, raising their kinetic energy: so it would be easier to knock them out their position. Pre-existing defect populations behave as sinks or obstacles to the mobility of new defects.

From PKA chains, physical effects are originated such as swelling, growth, phase change, segregation and transmutation. They mainly lead to mechanical effects such as hardening, embrittlement and fracture toughness variation.

Neutrons are also absorbed in nuclear reactions resulting in changes in atomic nuclei and the creation of new elements such as impurity atoms. This is termed "transmutation". Both thermal and high-energy neutrons can be involved. Metallurgically, the most important are the (n, α) and (n, p) reactions, which generate helium and hydrogen respectively [15], where n is a neutron, α an alpha particle or $^{4}_{2}He^{2+}$ and p a proton or hydrogen nucleus. The complete notation for the reactions would be of the form: A(b,c)D, which is equivalent to A + b gives c + D, where A is the target nucleus, b the incident particle, c the ejected particle and D the recoil nucleus.

Helium transmutation involves nickel, boron and iron as follows:

- thermal neutrons and nickel are involved in the two-step reaction:

$$^{58}Ni(n,\gamma)^{59}Ni \rightarrow {}^{59}Ni(n,\alpha)^{56}Fe\,; \tag{2.10}$$

- thermal neutrons and boron are involved in the reaction:

$$^{10}B(n,\alpha)^{7}Li \tag{2.11}$$

- fast neutrons (> 6 MeV) are involved in the threshold type (n, α) reactions principally with nickel, but significant contributions from other major alloying elements.

Other reactions are also possible in fusion reactor environments.

Atomic displacements rather than neutron dose are linked to irradiation changes, so the damage is most meaningfully characterised in terms of the average number of times that an individual atom is displaced from its lattice site [15]. This leads to a damage/exposure unit termed 'displacement per atom' (dpa) which is generally accepted as a correlation parameter for mechanical property and microstructural changes in reactor materials irradiated in different neutron spectra. It is based on the Norgett–Robinson-Torrens model [68] and incorporated into the international standard ASTM E521-96 [69].

According to the model, the efficiency of defect production in irradiated materials is defined as follows:

$$\eta = \frac{N_D}{N_{NRT}} \tag{2.12}$$

where the number of stable displacements at the end of the collision cascade is N_D and the number of defects calculated by the NRT model is N_{NRT}.

The number of defects (Frenkel pair) predicted by the NRT formula is equal to

$$N_{NRT} = \frac{0.8}{2E_d} T_{dam} \tag{2.13}$$

where E_d is the effective threshold displacement energy (derived from electron irradiation experiments and widely available in literature) and T_{dam} is the energy transferred to lattice atoms reduced by the losses for electronic stopping of atoms in displacement cascade.

Neutron damage in reactor structural materials can be evaluated by the testing or examination of samples machined from spent or failed components, or by using standard or miniature test pieces placed in rigs and irradiated in or close to the cores of materials test reactors. An alternative procedure is to irradiate samples with high-energy ion beams in accelerators or cyclotrons, with the aim of simulating neutron radiation damage processes; these results need however a benchmark against reactor data and associated correlation procedures.

A range of microstructural and mechanical property changes occurs in reactor materials because of the damage processes. These include radiation hardening and embrittlement, high temperature helium embrittlement and irradiation creep, cavity and gas bubble formation, radiation enhanced diffusion and solute segregation effects [70].

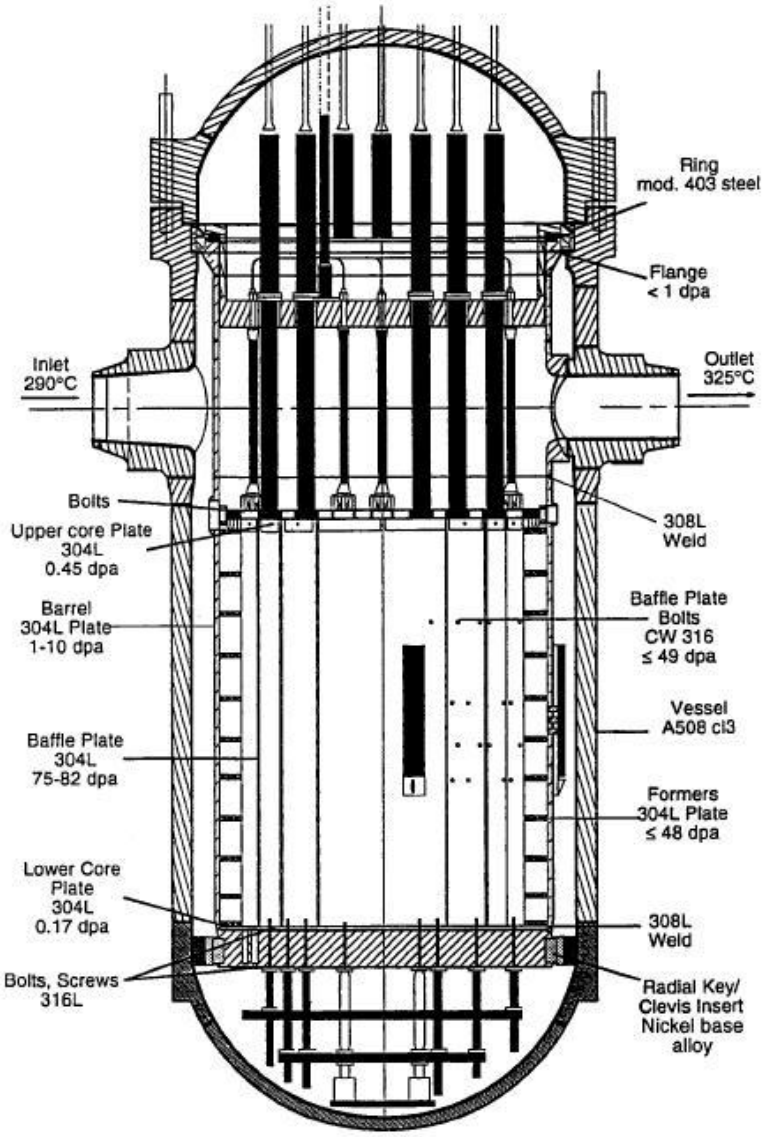

Fig. 2.19. PWR internals with indication of grade used and dose expected [15].

The real life references in this project originate from helium embrittlement data in austenitic stainless steels (in particular 316L and nuclear grades), those usually adopted in Pressurized Water Reactors [71] core internals, as for Fig. 2.19, and proposed for some fusion reactor components as first wall, blanket, vacuum vessel, cooling pipelines [72].

Despite the multiplicity of functions of the PWR internals, they are designed and fabricated solely on unirradiated material properties, but radiation induced

(< 1 dpa to > 80 dpa at the end of the operational life) mechanical properties degradation is now becoming a key issue for some existing reactors [15]. That is the reason justifying the line of research insisting in the experimental simulation of helium embrittlement effect and this doctoral project.

The internal structures in the core subdivide into three groupings as follows:

- above core structure;
- lower core support;
- separation ring.

The lower core components of support (core barrel, baffle plate, formers, lower core support) are the most critical due to the high irradiation dose experimented during service and because they support and maintain in position the core subassemblies.

A principal area of concern is irradiation embrittlement as manifested by increases in yield stress, decrease in ductility and loss of fracture toughness [15]. There are two aspects to consider. First is the relation between strength and toughness. Second is the need to keep the stresses in the elastic range (so that no permanent deformation occurs).

Several papers [73–79] report the yield stress variation with dpa and temperature for the 316 stainless steel. Data are collected from direct neutron irradiation or ion-simulated neutron irradiation (the nearest and most widely used way to simulate the effects of neutron irradiation in the lab). In particular, for 316L it is observed the behaviour shown in Fig. 2.20 for irradiation followed by test at room temperature. Early increase in the yield strength is explained with the interaction of dislocations with irradiation-produced defects. Failure strain in 7.5 dpa is marginally lower than in 1.5 dpa [79].

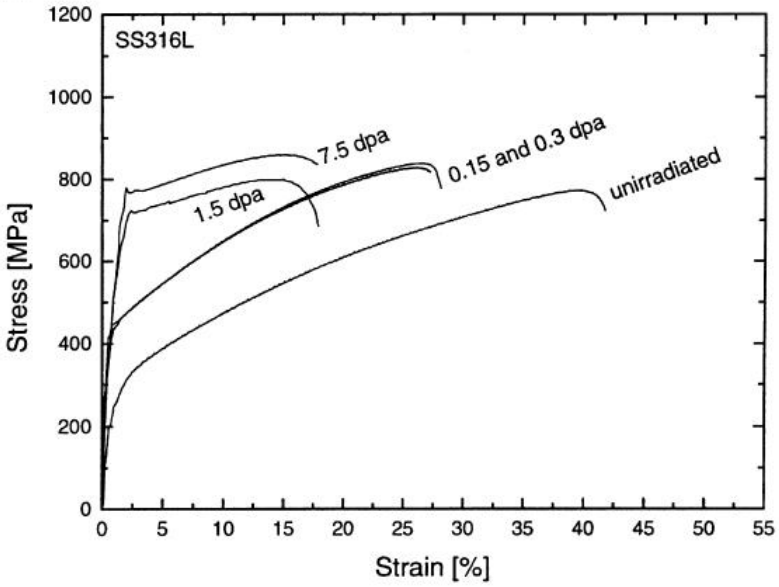

Fig. 2.20. Variation of yield stress with dpa for 316L stainless steel [79].

This plot suggests that it could be possible to relate a certain level of tensile pre-strain in the unirradiated material to a certain level of dpa in the irradiated one in terms of yield stress. This sort of relation comes from an extension of recent results of Byun [80].

While cold work leads to a homogeneous deformation, irradiated materials (to doses beyond a certain dose level) are unable to deform plastically in a homogeneous manner [81]. In fact, they exhibit yield drop, negative work hardening and plastic instability. Plastic instability is the reason of unsuitability for their use in service in a radiation environment [81].

There is saturation in the yield strength value after a certain level of dpa, as shown in Fig. 2.21. In addition, yield strength depends on temperature as well as on dose level as shown in Fig. 2.22, where the maximum is reached at about 330 °C without regard of the dose level. The irradiated yield strength is independent of temperature up to about 200°C and then increases to a maximum near 300-330°C. This maximum in hardening correlates with maxima in the number density of faulted Frank loops and small cavities [74]. The decrease after that temperature is explained with the onset of significant vacancy mobility [82].

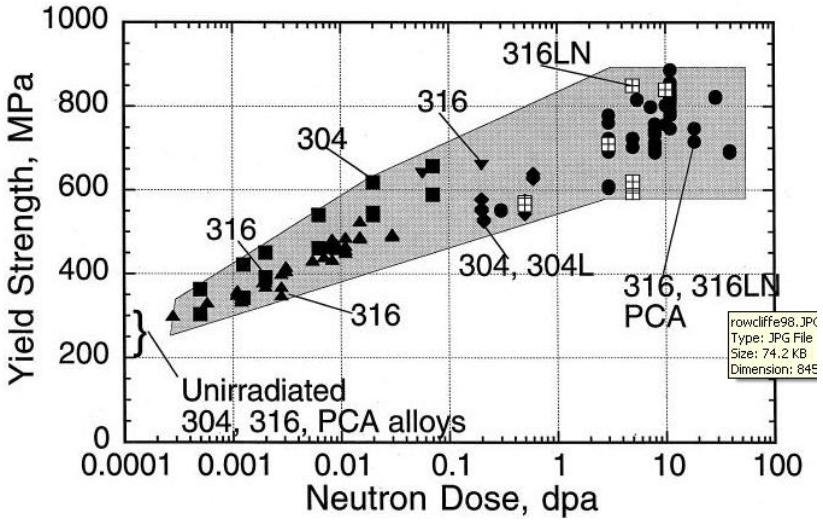

Fig. 2.21. Yield strength as a function of neutron dose [74].

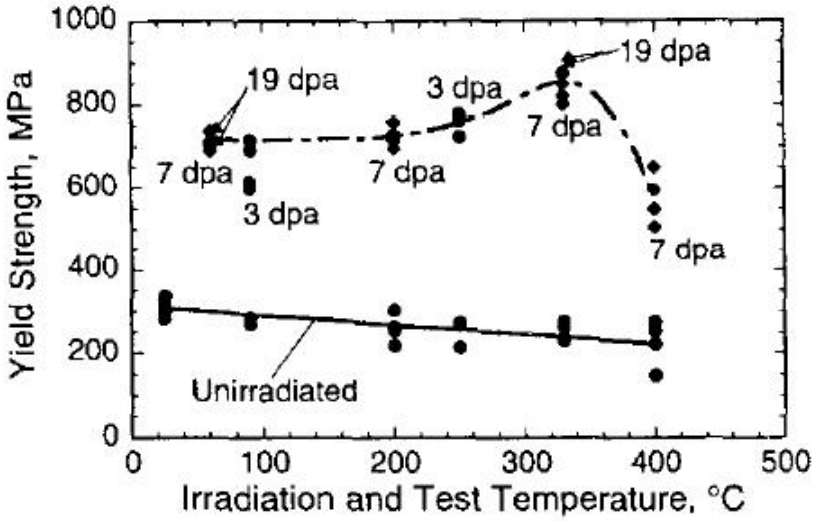

Fig. 2.22. Yield strength as a function of temperature for different dpa levels [75].

A compilation of data about the effects of radiation on the fracture toughness of a range of 300-series austenitic stainless steels can be found in [83-85]. The relevant results for this project are shown in Fig. 2.23 in the form of fracture toughness of 316L vs. dpa. There is considerable scatter, but trends show a sharp reduction in toughness after only a few dpa followed by saturation at a lower bound elastoplastic toughness [15].

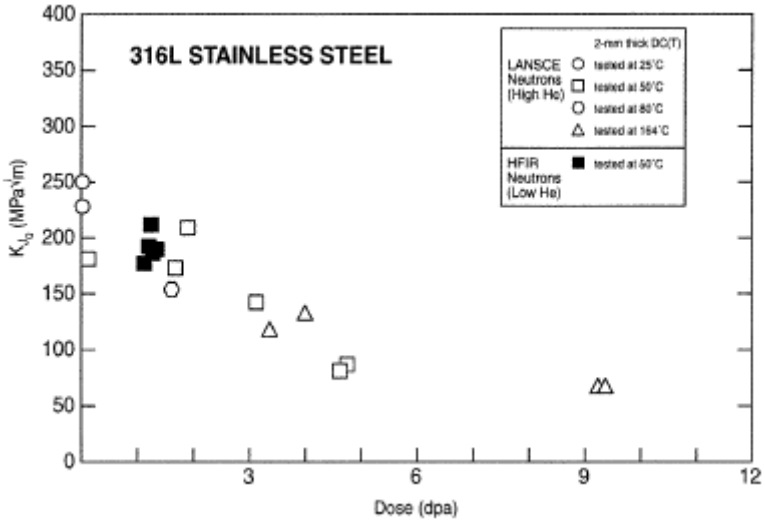

Fig. 2.23. Dose dependence of fracture toughness for 316L [85].

In general, the metallographic investigations accompanying the fracture toughness measurements have shown that ductile microvoid coalescence remains the fracture mode after irradiation, which is consistent with the relatively high (40–70 MPa $m^{0.5}$) saturation toughness levels recorded [15]. Other investigations show some change in the fracture type to a "channel fracture" mode [86] and this could be accompanied by further lowering of fracture toughness [15]. Channel fracture is essentially a low ductility mode of fracture characterized by crystallographic facets (cleavage) and arises from highly localized dislocation slip processes which accompany shearing and ultimate removal of radiation induced (and other) obstacles; the result is the formation of submicron wide channels followed by ultimate planar separation at fracture [15].

2.2.4 Helium embrittlement effects

Embrittlement consists of loss of ductility and toughness with little change in mechanical properties such as strength or hardness [87]. It can be caused by internal or external factors: a decrease or increase in temperature, a change in the internal structure of the material, an introduction into a corrosive environment, or the presence of surface notches.

Helium is introduced via (n, α)-reactions in fusion / fission reactor environments or via direct injections. In a thermal flux spectrum, the main source of helium in steel is the reaction [15]:

$$B^{10} + n \rightarrow Li^{7} + He^{4} \tag{2.14}$$

where n is a neutron.

Small quantities of boron in stainless steel give substantial quantities of helium, due to the high cross section or probability that a certain nuclear reaction will take place, defined as an effective size of the nucleus for that reaction in the form of:

$$\sigma = \frac{R}{I} \tag{2.15}$$

where R is the number of reactions per unit time per nucleus and I is the number of incident particles per unit time per unit area. The usual unity is the barn, equal to $10^{-28}\ m^{2}$.

Boron in steel is often associated with grain boundary carbides [15], so helium becomes available where it can do the most damage. Boron is burned out in the early life of the reactor.

Nickel can also transmute to He through the following two-step reaction:

$$Ni^{58} + n \rightarrow Ni^{59} + \gamma \tag{2.16}$$

$$Ni^{59} + n \rightarrow Fe^{56} + He^{4} \tag{2.17}$$

This reaction occurs throughout the lifetime of the reactor.

Fast neutron flux induces (n, α) reactions in all components of the metal to give helium; nickel and iron are the most important helium producers; nitrogen and boron also contribute as impurity elements.

Helium precipitation will lead to changes in the structure of the material, inter-granular embrittlement, a roughening of the surface of the material, and affect the magnitude of the swelling of the material. These effects are due to several reasons: the diffusion and the clustering of atomic defects and their transport to interfaces and grain boundaries; the formation of matrix and interface cavities under irradiation and stress induced vacancy super-saturation; nucleation and growth of gas bubbles and dislocation loops; and irradiation and stress induced evolution of the dislocation structure. These processes are interrelated [88].

The nature of helium embrittlement is still under discussion and many theories have been postulated. One comprehensive work of Fabritsiev [89] reports them [90-100]. General modelling of the growth of helium bubbles is not a problem by the means of the widely accepted rate theory [87]. It is difficult to model the supercritical micro-discontinuity formation because theories do not take account of the dynamic processes occurring in the material during in high temperature deformation [89]. According to Gifkins [101], pores in materials containing helium forming at grain boundaries, stabilise at much lower stresses than in materials without helium because of precipitation of helium at pore nuclei [89]. Via tensile tests, it can be seen that the growth of pores, and inter-granular failure in specimens containing helium start at much lower stresses and strains than in specimens that don't contain helium [89].

Helium has to travel to the grain boundaries and this leads into the mechanism of helium embrittlement. There is a strong dependence between the bubble nucleation growth and the flow of helium to the grain boundaries [82, 102]. The helium diffusion is strongly influenced by microstructure defects such as vacancies and impurities, or extended microstructure defects like dislocations, solid precipitates or helium bubbles formed on them. These defects are known as traps. Under creep conditions, the already formed

helium bubbles make the most effective traps. The nucleation of these bubbles is the main cause of helium embrittlement. How this nucleation occurs, and its particular effects, depends on whether it occurs under low temperatures or high temperatures [103-104]. More details about the models are given in Appendix A.

The effects of helium on 3xx austenitic stainless steels -in addition to the effects of displacement damage- are well known. Helium (from transmutation) will generally increase the strength, decrease the ductility, reduce the creep and stress rupture properties, decrease the fatigue life and weldability, and promote swelling; in addition, displacement damage (production of vacancies and interstitials) would also increase the strength and decrease the ductility [82]. The approximate temperature ranges for these damage categories are illustrated in Fig. 2.24. Even if their temperature range may overlap, they are usually considered separate. It is suggested that synergistic effects may be of significant importance to component performance in intense spallation neutron sources [82]. Fig. 2.25 links helium concentration to dose level in a direct manner.

Fig. 2.26 reports experimental data about fracture toughness for different batches of 316 stainless steel at different helium concentration. This will be a benchmark to correlate with the experimental simulation of the same detrimental effect attempted in this project.

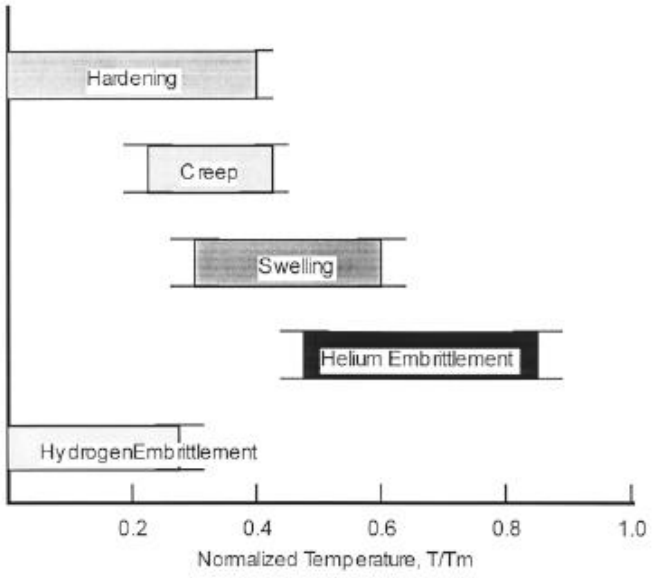

Fig. 2.24. Temperature ranges for the various types of radiation damage typical of radiated metals and alloys [82].

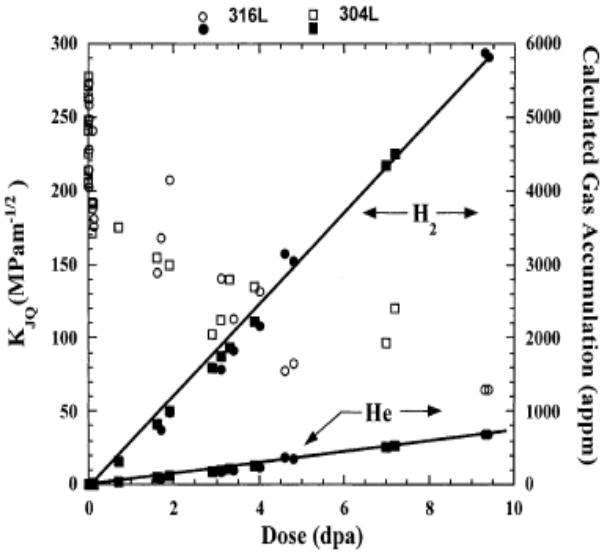

Fig. 2.25. Transmutation gas concentration for irradiated specimen [15].

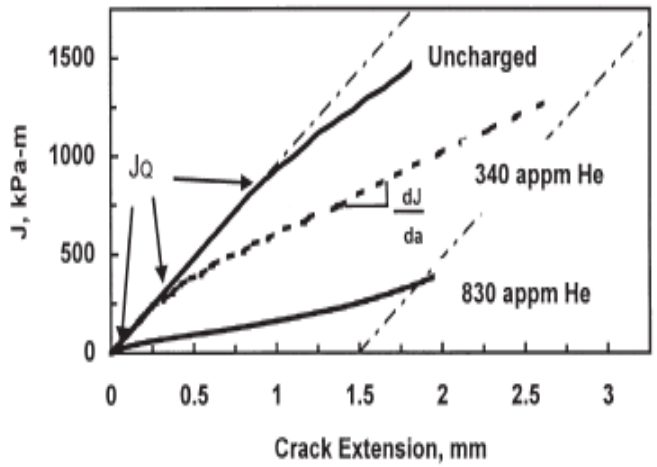

Fig. 2.26. Fracture toughness reduction with increasing helium concentration in austenitic stainless steels tested at room temperature [82].

The usual size distribution of helium bubbles is in the order of very few nanometres. Their behaviour under stress at different temperatures is described in [105].

As for modelling, a multiscale approach passes information about the controlling physical mechanisms over relevant lengths and timescales [106]. The length scale domain [107] for this project is μm to mm and involves continuum mechanics (constitutive properties), fracture mechanics (material failure) and finite elements (macroscopic systems).

2.2.5 Comparison and contrast of damaging mechanisms

A dislocation is a line that forms a boundary between a region of the crystal that has slipped and one that has not. The existence of dislocations provide for much reduced shear stress in crystals [108]. When an external force of sufficient magnitude is applied to a crystal at room temperature, the dislocations move and produce slip. At higher temperatures, dislocations may also climb by the means of thermally-activated diffusion. Climb is the motion of a dislocation out of the slip plane onto a parallel plane directly above or below the slip plane.

Cold working involves the increase of dislocation density in the metal from the activation of sources (for example, Frank-Read sources) or from nucleation (homogeneous or heterogeneous from defects present in the crystal, for example grain boundaries steps and ledges, this being the usual way [109]). Dislocations start to move on their slip planes along preferential directions and, when not on parallel planes, interact among them and increase the resistance to further motion. The motion of dislocations may also be impeded by grain boundaries, because of the different crystallographic orientation that cuts off the slip plane. Other obstacles, such as solid-solution particles, impurity atoms, etc., contribute to strengthen the material by forcing dislocations to bow [110]. Cutting of impurity particles can also happen. Microscopic strain localization may also happen in the form of twinning and channelling, in dependence of material and testing conditions [111].

Irradiation enhances the concentration of defects and creates new species, notably: isolated vacancies and interstitials, clusters, precipitates, stacking fault tetrahedra, dislocation loops and lines, voids and bubbles [112]. The actual number of defects that survive the displacement cascade and their spatial distribution in the solid will determine their effect on the irradiated microstructure [113]. Dislocations then interact with the radiation-produced defects. The stress required to move a dislocation on its glide plane increases and the resistance to motion is enhanced by these obstacles [114]. The net effect is an increase in yield strength up to a saturation value that depends on dpa [115].

Byun [116] proposed one room temperature deformation map for 316 ss as a true stress vs. dose space, Fig. 2.27. It shows the expected mechanisms and that the possible stress range for plastic deformation decreases as dose increases.

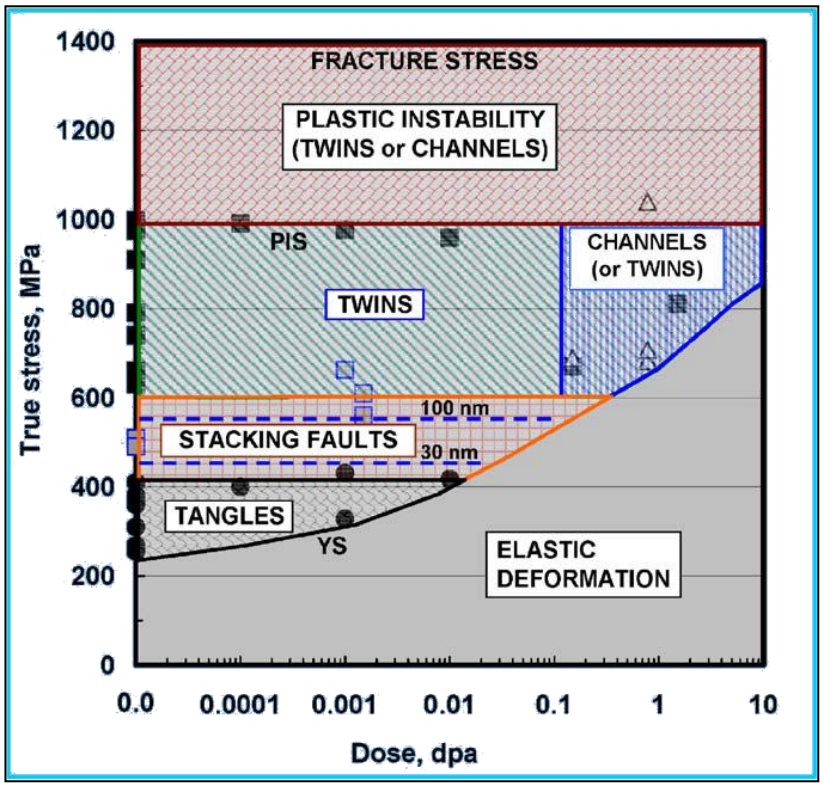

Fig. 2.27. A deformation mode map for 316 and 316LN stainless steels in the true stress–dose space [116].

More recently, the same author proposed one comprehensive work about the analysis of tensile deformation and failure of austenitic stainless steels in dependence of irradiation doses [117] and temperature [118]. He suggested that the strain hardening behaviour in 316 stainless steel family is independent of irradiation [80]. This means that dislocation-dislocation interaction occurring in the post-yielding region is not changed by irradiation. By extension, we can say that the effect of irradiation hardening is similar to strain hardening. Post yielding behaviour on the fracture process is still under study.

Irradiation enhances thermal creep at high temperatures and induces creep at low temperatures due to increased defects (vacancies) and diffusion-rates. In addition, at high temperatures and under a constant load, there is almost a complete loss of creep strength due to severe embrittlement arising from irradiation [119]. A detailed description of the effects of irradiation on creep is given in [120].

The effects of irradiation on creep for 316 stainless steels were described by Zinkle [111], who proposed deformation mechanism maps for undamaged and 1 dpa damaged material with 50 µm grain size. The boundary between elastic behaviour and the various plastic deformation fields was drawn for an arbitrary plastic strain rate of $10^{-8}\,s^{-1}$, as in Fig. 2.28 and Fig. 2.29. One extension of the dislocation creep zone can be noticed in Fig. 2.29. The very slow plastic strain rate case $10^{-10}\,s^{-1}$ was calculated as in Fig. 2.30. A great relevance of irradiation creep and diffusional creep can be noticed in this case. Zinkle also gave equations to determine the elastic-plastic boundary for other strain rates.

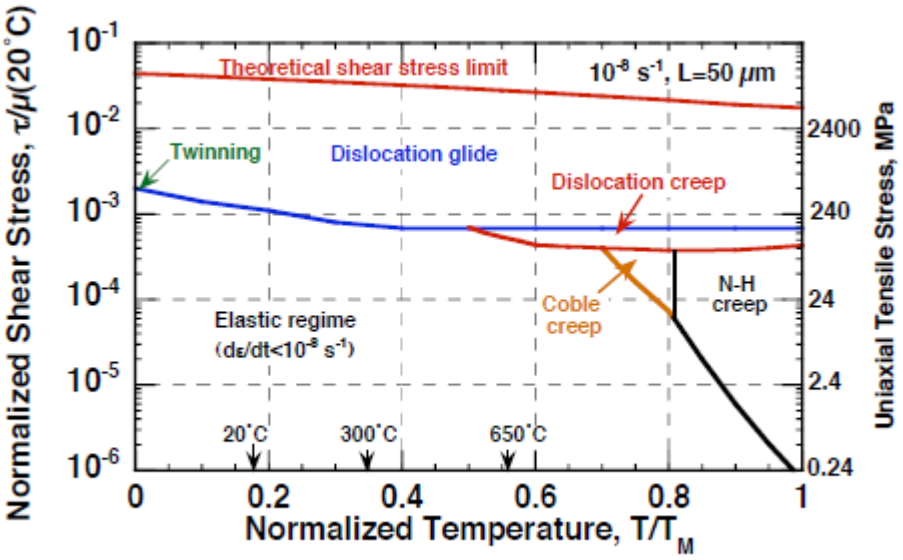

Fig. 2.28. Deformation map for 316 austenitic stainless steel at a plastic strain rate of $10^{-8}\,s^{-1}$ [111].

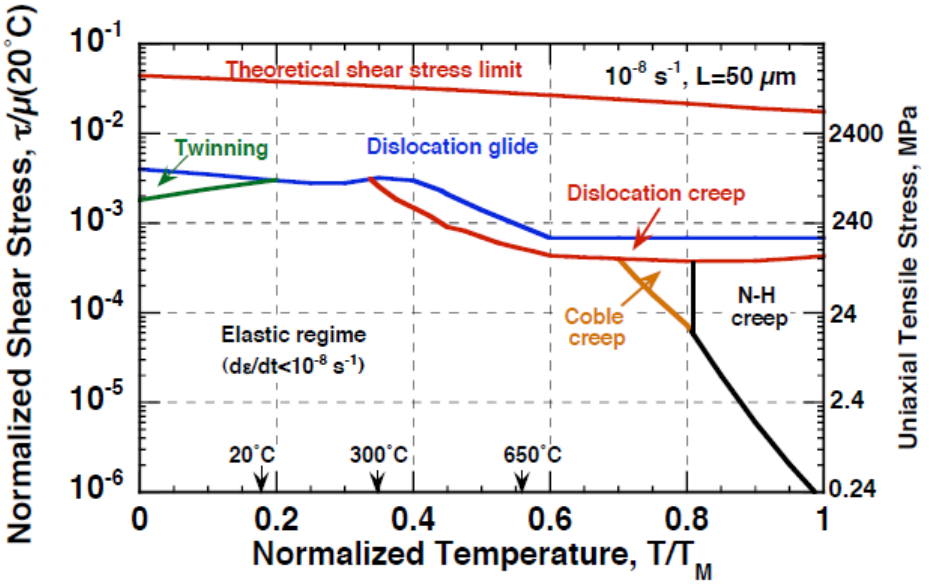

Fig. 2.29. Deformation map for 316 austenitic stainless steel irradiated to 1 dpa at 10^{-6} dpa/s for a plastic strain rate of $10^{-8}s^{-1}$ [111].

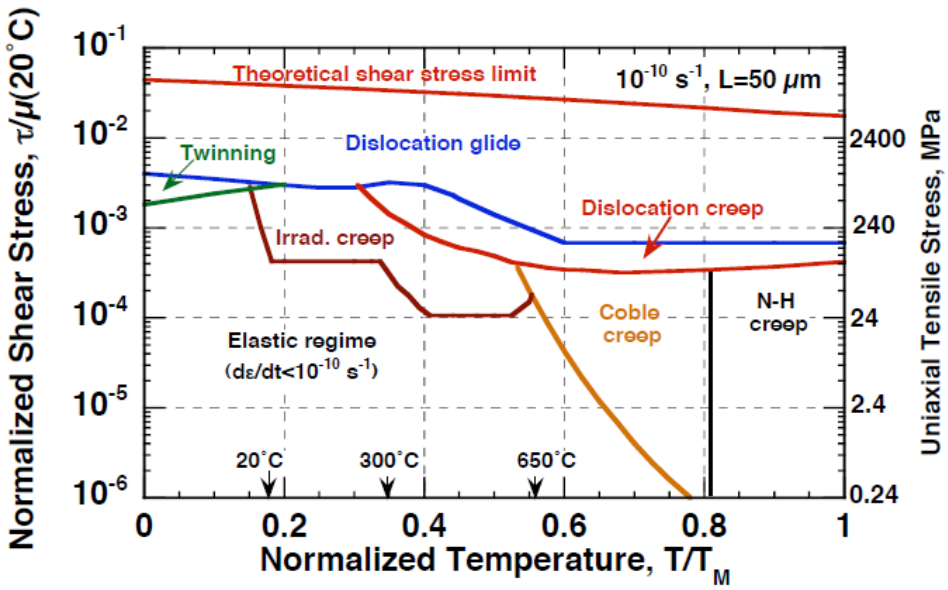

Fig. 2.30. Deformation map for 316 austenitic stainless steel irradiated to 1 dpa for a plastic strain rate of $10^{-10}s^{-1}$[111].

It has to be remarked that, in this project, creep was used in order to produce voids and not as a damaging mechanism itself.

2.3 Fracture toughness and crack behaviour

Fracture mechanics can be approached from a number of points of view, including energy to cause failure, stress analysis, micromechanisms of fracture, applications of fracture, computational methods, material behaviour and experimental testing [121]. This section will discuss the research in the field, both in general and applied to the austenitic stainless steel tested in this project. A short introduction to fracture toughness will be followed by the description of elastic, elastic-plastic and porous plastic constitutive models. Then computational and experimental fracture procedures will be presented in relation to the simulative approach attempted in this project.

2.3.1 Fracture toughness

Fracture toughness is a non-intrinsic material parameter related to the amount of energy needed to propagate a pre-existing flaw. Flaws can appear as cracks, voids, metallurgical inclusions, weld defects, design discontinuities, or their combinations. In the last twenty years, micromechanical approaches and numerical methods have shown the fracture toughness dependence on specimen's size (for brittle fracture) and geometry (for ductile fracture, being the cavity growth largely sensitive to triaxiality stress ratio).

2.3.2 Fracture mechanics

Fracture mechanics deals with the study of cracks, crack-like defects and the mechanical behaviour of the affected bodies. It is based on flaw size and features, loading condition, component geometry and toughness property in order to assess the resistance of a flawed component to fracture. Linear elastic fracture mechanics is used for brittle materials or in absence / negligibility (small scale yielding) of plastic effects at the tip of the crack, while elastic-plastic fracture mechanics is used for ductile materials or where non-negligible

plasticity arises. Porous plasticity models are implemented in order to simulate the nucleation–growth–coalescence sequence observed in ductile fracture.

2.3.2.1 Linear Elastic Fracture Mechanics

The foundational work for linear elastic fracture mechanics is from Griffith [122]. He then defined a critical stress for failure. In Fig. 2.31, a sheet with initial crack length a, loaded with tensile stress σ, is depicted. Near the crack tip, the stress is elevated above the average stress of σ. Due to this high stress the material near the crack tip will undergo large strains and will eventually fail, allowing the crack to propagate ahead [123].

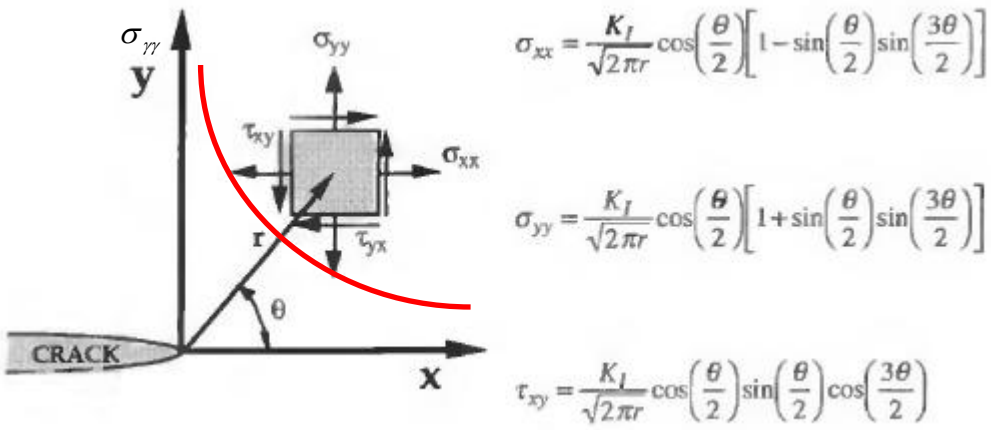

Fig. 2.31. Stresses near the tip of a crack in an elastic material [124].

If the material were to behave linearly elastically right up to the point of fracture then the stress ahead of the crack would be

$$\sigma_{yy} = \frac{K_I}{\sqrt{2\pi.r}} \tag{2.18}$$

where *r* is the distance from the crack tip and K_I, called stress intensity factor, is related to the applied stress. That definition is due to Irwin in the late 1940s.

Stress-intensity factors K_I, K_{II}, K_{III} in accordance with the crack loading mode, Fig. 2.32, being mode I the worst case [125], are used to determine the fracture toughness of most materials relying upon the linear elastic fracture theory. In particular K_I solely drives crack tip deformation and fracture under the so called "small scale yielding" assumption, that is when the size of the zone near the crack tip in which plastic deformation occurs is small relative to *a*, so that the stress outside of this yielding zone will be well approximated by equation (2.19) [126].

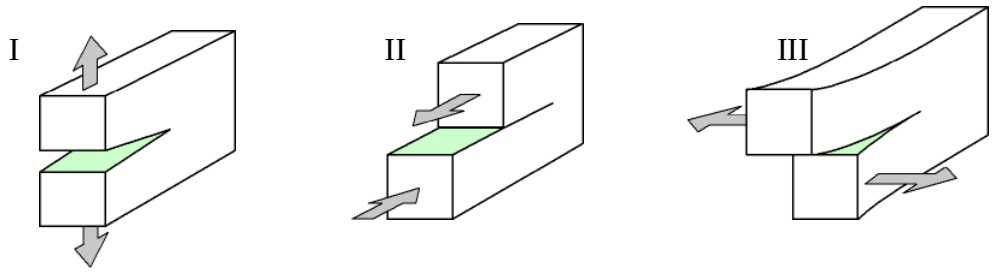

Fig. 2.32. Mode I, mode II, mode III of crack tip deformation.

The mode I stress intensity factor can be represented by the following general equation:

$$K_I = \sigma\sqrt{\pi.a}\beta \tag{2.19}$$

K_I is the stress intensity factor in MPa $\sqrt{m}$

σ is the applied stress in MPa

a is the crack length in meters

β is a dimensionless factor that depends on the crack length and the geometry of the specimen

K_I represents the only driving force for fracture in small scale yielding conditions. If K_{IC} is a measure of the material resistance, known as fracture toughness, failure occurs when

$$K_I \geq K_{IC} \tag{2.20}$$

that is to say, fracture must occur at critical stress intensity.

K_{IC} is commonly reported in reference books and other sources together with other mechanical properties of a material, for a standard geometry. The main reference is the British Standard 7448 [127]. Stress intensity factors have in fact to be evaluated for the particular boundary conditions and new references are continuously appearing thanks to advancements in both computer hardware and methods of analysis.

Fracture toughness K_{IC} is dependent on material thickness as illustrated in Fig. 2.33:

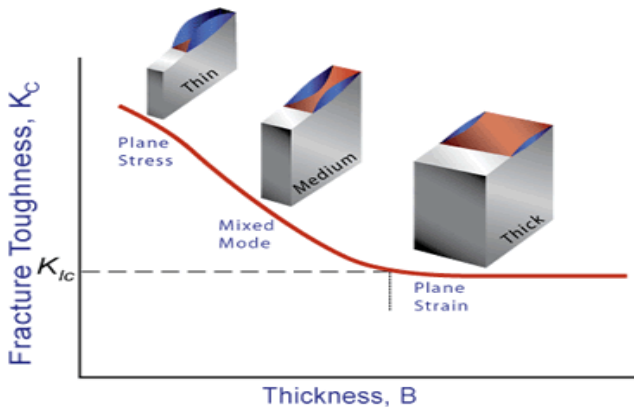

Fig.2.33. Stress intensity factor for mode I related to thickness [128].

This results because, in ductile materials, the stress states adjacent to the flaw change with the specimen thickness until the thickness exceeds some critical dimension. That is, the crack grows preferentially in the region of high triaxiality [128]. Crack growth on the outer regions of the specimen lags behind, and occurs at 45° angle to the applied load; the resulting fracture surface exhibits a flat region in the centre and 45° shear lips on the edges.

Loading a material with a crack in tension leads to developing plastic strains as the yield stress is exceeded in the zone near the crack tip. Material within the crack tip stress field, which is close to a free surface, can deform laterally because no stresses can exist normal to the free surface. The state of stress is considered biaxial and a ductile material fractures with a 45^o shear lip forming at each free surface. This is called “plane-stress" and it occurs in relatively thin bodies where the stress through the thickness cannot vary appreciably due to the thin section.

On the contrary, material away from the free surfaces of a relatively thick component is constrained by the surrounding material and not free to deform laterally. The stress state under these conditions tends to be triaxial and there is zero strain perpendicular to both the stress axis and the direction of crack propagation when a material is loaded in tension. This condition is called “plane-strain”.

2.3.2.2 Elastic-Plastic Fracture Mechanics

Irwin [129] and Orowan followed Griffith in the late 1940s and tried to apply his theory to ductile materials such as steels. In particular, they added a contribution from plastic deformation, in terms of plastic work, to the surface energy of Griffith, so defining the fracture energy and modifying his critical stress for fracture.

When the loading force does a work (that is when it gives a displacement) and the area of the crack varies, the elastic energy of the body varies as follows [130]:

$$dU = Pd\Delta - GdA \tag{2.21}$$

where U is the elastic energy, P is the force, Δ is the displacement, G is the energy release rate and A is the area of the crack.

The fracture energy Γ is the small fraction of the work done by the loading force, which goes to inelastic processes such as breaking atomic bonds and plastic deformation, that is:

$$Pd\Delta = dU + \Gamma dA \tag{2.22}$$

This definition of the fracture energy is independent of microscopic processes, be they bond breaking or plasticity.

If the strain energy release rate, *G*, is the reduction of the elastic energy associated with the crack increasing per unit area (it is also called crack driving force), a fracture criterion based on the energy approach is depicted as:

$$G \geq \Gamma \tag{2.23}$$

where *G* is the available energy release rate, or the energy dissipated per unit area of new fracture surface [131], and Γ is the energy per unit area required to propagate a crack. Representative values of Γ, obtained experimentally, are: glass: 10 J/m^2, ceramics: 50 J/m^2, polymers: 1000 J/m^2, aluminum: 10000 J/m^2, steel: 100000 J/m^2 [130].

Irwin found that in small-scale yielding, plane strain condition, the energy release rate *G* is linked to K_I by:

$$G = \frac{K_I^{\,2}}{E} * \begin{cases} 1 & \text{plane stress} \\ (1-\upsilon^2) & \text{plane strain} \end{cases} \tag{2.24}$$

E is the Young modulus of the material, υ the Poisson ratio. This is not so when small scale yielding is violated, which is the case for tearing fracture of ductile materials.

The energy release rate is generally computed, these days, by the finite element method.

Rice [132] demonstrated that in the elastic plastic case, this energy variation could be described by a path independent line integral called *J*. In general, the stress intensity factors K_I, K_{II}, and K_{III} are related to the energy release rate [133].

For homogeneous, isotropic materials, it is:

$$J = \frac{1}{\overline{E}}(K_I^2 + K_{II}^2) + \frac{1}{2\mu}K_{III}^2 \tag{2.25}$$

Where $\overline{E} = E$ for plane stress and $\overline{E} = E/(1-\nu^2)$ for plane strain, axisymmetry, and three dimensions. E is the Young's modulus of the material, μ is the shear modulus and υ is the Poisson ratio. Young's modulus and Poisson ratio are the only two independent constants needed to describe the elastic property for an isotropic, homogeneous solid.

As the stress state ahead of a crack tip is three-dimensional, the shape of the plastic zone is not necessarily a circle, but needs to be determined using an appropriate yield criterion; either the Tresca criterion or the von Mises criterion is applied. The equations indicate significant differences in the sizes and shape of the mode I plastic zones for plane-stress and plane-strain conditions [134]. The latter condition suppresses yielding, resulting in a smaller plastic zone for a given stress intensity factor, as in Fig. 2.34.

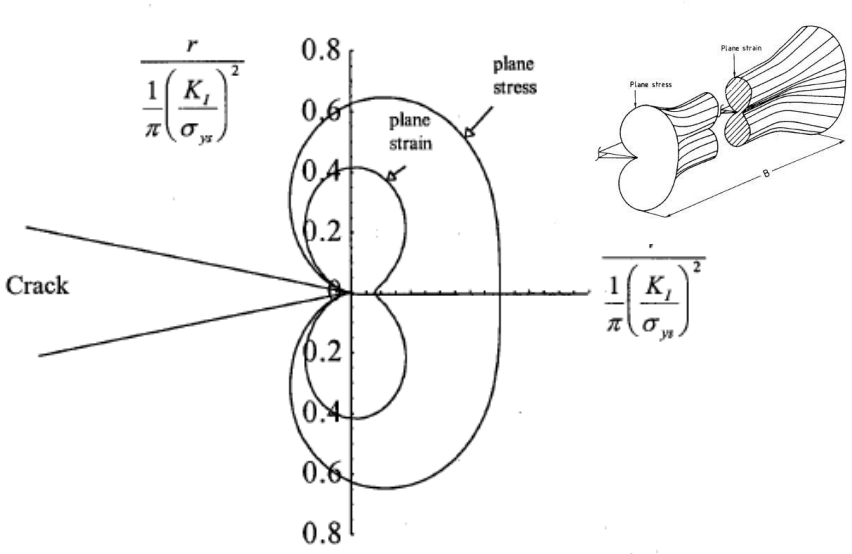

Fig. 2.34. Plane stress and plane strain zones over the thickness [134].

It is important to point out that although the plastic zone at the middle of the plate is smaller than that near the surface, the high triaxial stress that exists at the middle of the plate (this is sometimes called plastic constraint) causes crack growth to occur there first,

under both static and fatigue conditions. A minimum thickness *B* of the specimen is required when determining the plane-strain fracture toughness. Slip-planes around a mode I crack for plane stress and plane strain are shown in Fig. 2.35.

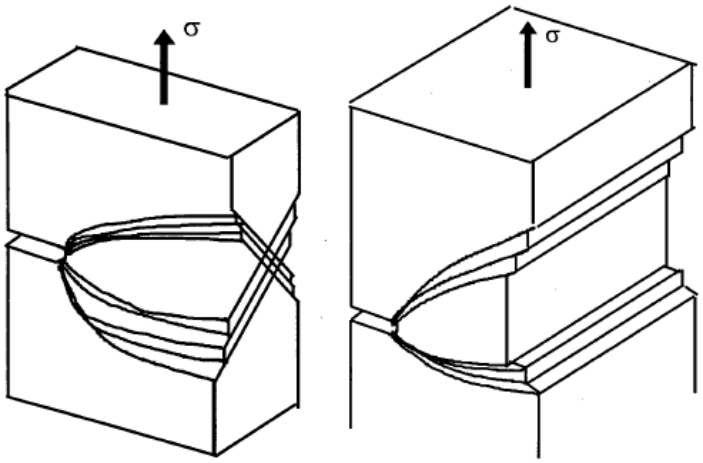

Fig. 2.35. Slip-planes around a mode I crack for plane stress and plane strain.

Details about that thickness will be given in Section 2.3.3, which accounts for experimental fracture mechanics and introduce the standards for good practice. It is here noted that under plane-strain conditions the fracture toughness will not depend on specimen thickness and therefore, constitutes a fundamental material property [135].

A more general theory of crack growth must consider two aspects. First, the local conditions for initial crack growth which include the nucleation, growth, and coalescence of voids or decohesion at a crack tip. Second, a global energy balance criterion (considering when the energy available for crack growth is sufficient to overcome the resistance of the material) for further crack growth and unstable fracture. This can be done by using a ductile damage model and a set of rules for a systematic crack growth along one direction. Section 2.3.2.3 will introduce one of the models used for porous plasticity, which has the characteristic of modifying (weakening) the yield criterion.

When the plastic energy at the crack tip is not negligible, and it is not possible to determine valid K_{IC} values, other fracture mechanics parameters, such as crack tip opening displacement (CTOD) and the *J* integral can be used. The data produced by these tests is dependent on the thickness of the specimen and will not be a true material

property. However, plane-strain conditions do not exist in all structural configurations and using K_{IC} values in the design of relatively thin areas may result in excess conservatism. In cases where the actual stress state is plane-stress or, more generally, some intermediate -or transitional- stress state, it is appropriate to use *J*-integral data, which account for slow, stable fracture (ductile tearing) rather than rapid (brittle) fracture. In particular, the quantity J_{IC} defines the point at which large-scale plastic yielding during propagation takes place under mode one loading.

The *J*-integral is defined in terms of the energy release rate associated with crack advance and is based on a model developed by Rice [132]. It can be related to the stress intensity factor if the material response is linear. Initial stresses are often not included in the *J*-contour integral formulation.

From a numerical point of view: for a virtual crack advance $\lambda(s)$ in the plane of a three-dimensional fracture, the energy release rate is given in [136] and the contour path is depicted in Fig. 2.36:

$$\bar{J} = \int_A \lambda(s)\mathbf{n}\cdot\mathbf{H}\cdot\mathbf{q}d\mathbf{A}, \tag{2.26}$$

where d**A** is a surface element along a vanishing small tubular surface enclosing the crack tip or crack line, **n** is the outward normal to d**A**, and **q** is the local direction of virtual crack extension. **H** is given by

$$\mathbf{H} = (W\mathbf{I} - \boldsymbol{\sigma}\cdot\frac{\partial\mathbf{u}}{\partial\mathbf{x}}) \tag{2.27}$$

For elastic material behaviour *W* is the elastic strain energy density. For elastic-plastic or elasto-viscoplastic material behaviour, *W* is defined as the elastic strain energy density plus the plastic dissipation, thus representing the strain energy in an "equivalent elastic material." Therefore, the *J*-integral calculated is suitable only for monotonic loading of elastic-plastic materials.

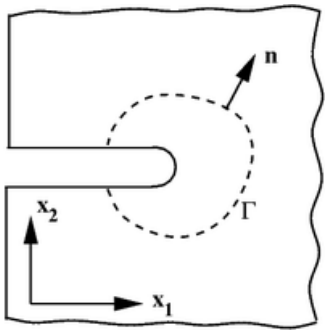

Fig. 2.36. Arbitrary contour around the tip of a crack.

If the *J*-integral is to be used to characterize the intensity of stress–strain field in the elastic–plastic condition, the validity of *J*-integral must be analyzed when the specimen is loaded to the crack initiation. If the Hutchinson [137] and Rice and Rosengren [138] (HRR) field approximately exists near the crack tip, the condition is called *J*-dominant. So, the *J*-integral can be considered effective as a fracture parameter. The HRR field is valid for small strain theory and does not take into account crack tip blunting [139].

Under plane strain and small scale yielding conditions, for *J* dominance the uncracked ligament of the specimen must be greater than 25 times the CTOD or $\approx 25 \times J / \sigma_0$ [140]. The variation in stress ahead of the crack is depicted in Fig. 2.37:

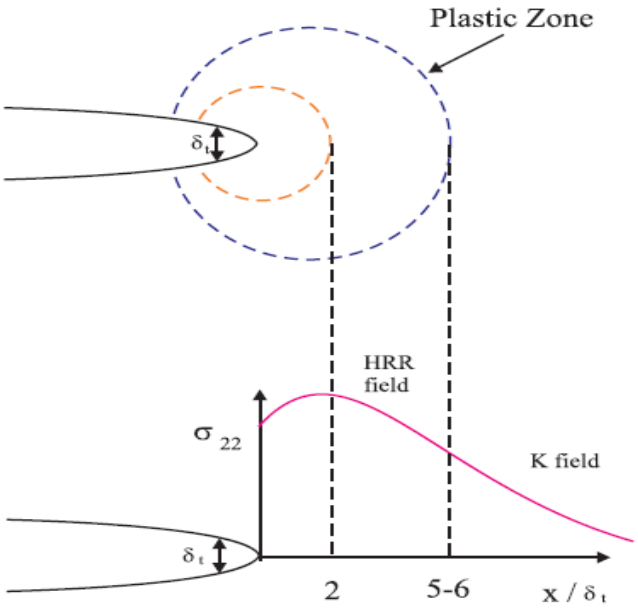

Fig. 2.37. Variation in stress ahead of the crack [140].

Assuming pure power-law material response as:

$$\frac{\varepsilon}{\varepsilon_0} = \alpha\left(\frac{\sigma}{\sigma_0}\right)^n \tag{2.28}$$

where: α = material constant = 1, n = strain hardening exponent

σ_0 = reference yield strength, ε_0 = reference yield strain,

the crack tip fields (HRR field) can be derived as [137-138]:

$$\sigma_{ij} = \sigma_0\left[\frac{J}{\alpha\sigma_0\varepsilon_0 I_n r}\right]^{\frac{1}{n+1}} \tilde{\sigma}_{ij}(\theta, n) \tag{2.29}$$

where r is the distance from the crack tip, n is the strain hardening exponent, θ is the angle in the polar coordinates and the functions $I_n, \tilde{\sigma}_{ij}(\theta, n)$ are tabulated by Shih [141] for the relevant specimens at the positions (r, θ).

2.3.2.3 Porous Plastic Fracture Mechanics

The different stages of ductile fracture (nucleation, growth and coalescence) can be modelled by the means of one or more parameters characterizing the state of internal damage in the material. A coupled (incorporating damage accumulation into the constitutive equations) or an uncoupled (neglecting the effects of damage on the yield stress of materials) approach can be used. The very recent study from Li [47] shows that the Gurson-Tvergaard-Needleman (GTN) model [35-36] is comparatively more reliable in predicting the sequence of the fracture for tensile tests at high triaxiality, the kind of experiment at the heart of this doctoral project. It has to be noted that, at lower triaxialities, ductile fracture may happen in the form of shear fracture due to shear band localization, for which the role of the nucleation, growth and coalescence process becomes weaker. Xue [142] modified the GTN model to account for that in the late 2000s, but it will be here used in its common form.

In particular, the model is focussed on the void growth stage. It represents a simplified version of the voided material as a hollow sphere or a matrix, which is assumed to be rigid, isotropic and perfectly plastic with a yield limit, obeying a standard von Mises yield criterion and flow rule. As deformation increases, voids gradually grow and the stress field among them is modified, leading to the nucleation of new voids, which finally coalesce. The analysis consists of two steps:

- to find a family of velocity fields compatible with the boundary conditions;
- to minimize the plastic dissipation within the proposed family.

The main result is an estimate of the yield function for the porous metal, which can be used to derive the plastic flow direction [143].

The flow potential Φ of the resulting GTN model, at the yield point, is expressed as:

$$\Phi = \frac{\sigma_{eq}^2}{\sigma_f^2} + 2q_1 f^* \cosh\left(\frac{3q_2\sigma_m}{2\sigma_f}\right) - 1 - q_3 f^{*2} = 0 \qquad (2.30)$$

$$\sigma_{eq} = \sqrt{\frac{(\sigma_1-\sigma_2)^2 + (\sigma_2-\sigma_3)^2 + (\sigma_1-\sigma_3)^2}{2}} \qquad \text{von Mises equivalent stress} \qquad (2.31)$$

$$\sigma_m = \frac{\sigma_1+\sigma_2+\sigma_3}{3} \qquad \text{hydrostatic stress} \qquad (2.32)$$

$\sigma_1, \sigma_2, \sigma_3$ are the principal stresses (the left eigenvalues of the stress tensor); σ_f is the flow stress; q_1, q_2, q_3 are adjustable parameters for the effect of void shape changes, of large strain-hardening exponent and of void interaction.

The internal variable f^* accounts for the rapid loss of stiffness due to void coalescence beyond some critical volume fraction f_c and is defined as:

$$f^* = f \qquad \text{for} \qquad f \le f_c \qquad (2.33)$$

$$f^* = f_c + K(f - f_c) \qquad \text{for} \qquad f > f_c$$

where K is a function of f_c and of the void volume fraction at failure f_f.

The shape of the yield surface for different values of f is given in Fig. 2.38.

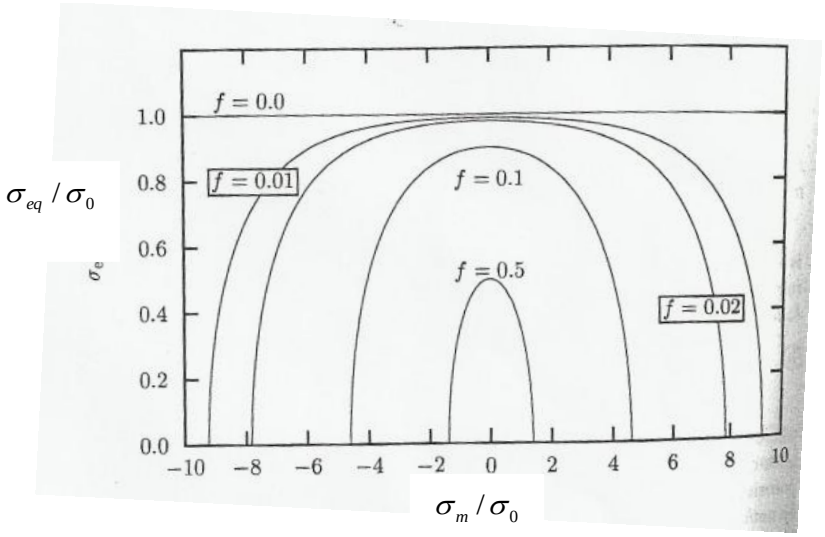

Fig. 2.38. Shape of the yield surface in the $\sigma_m - \sigma_{eq}$ plane.

In order to apply the Gurson model to a particular alloy, the elastic-plastic material behaviour can be determined from conventional tensile tests; a second set of parameters is related to the nucleation and growth of the voids during the loading process until final coalescence and failure. Numerical and experimental procedures must be combined.

The parameters q_1, q_2, q_3, f_0 (initial void volume fraction, based on experimental observations), f_c (critical void volume fraction), f_f (void volume fraction at final failure), ε_n (mean nucleation strain), s_n (standard deviation of void nucleating particles), f_n (void volume fraction of particles available for void nucleation) must be specified. Numerical studies have demonstrated strong dependence of f_c on f_0 and on the shape of the part [129].

The initial porosity value f_0 and the volume fraction of void-nucleating particles f_n can be determined by microscopical examination of the undamaged material; ε_n and s_n should be found in literature. Coalescence void volume fraction f_c and failure void volume fraction f_f can be estimated by numerical fitting of finite element analysis to

tensile tests on circumferentially notched axisymmetric specimens, respectively when the necking happens and when the failure diameter reduction is registered.

The values of the fitted parameters depend on the mesh size [144] and one approach is to average over the critical length of the material microstructure [145]. Mesh dependence could be removed by making use of non-local models [146], but it was not done here.

Therefore, the damage model ideally accounts for the three main phases of ductile evolution: nucleation, growth and coalescence. In terms of porosity, it can be said that:

$$df = df_N + df_G + df_C \tag{2.34}$$

The microvoid volume-fraction increment due to nucleation is expressed by the normal distribution of Chu and Needleman [147]:

$$df_N = \left(\frac{f_N}{S_N \sqrt{2\pi}} \right) \exp\left\{ -\frac{(\bar{\varepsilon}^p - \varepsilon_N)^2}{2S_N^2} \right\} d\bar{\varepsilon}^p \tag{2.35}$$

This normal distribution of the nucleation strain has a mean value ε_N, a standard deviation S_N and f_N the volume fraction of voids which could nucleate (only in tension) if sufficiently high strains are reached. With this distribution, 68% of voids nucleates between the effective plastic strain values $\bar{\varepsilon}^p = \varepsilon_N + S_N$ and $\bar{\varepsilon}^p = \varepsilon_N - S_N$.

The nucleation function is shown in Fig. 2.39 and the softening action in Fig. 2.40.

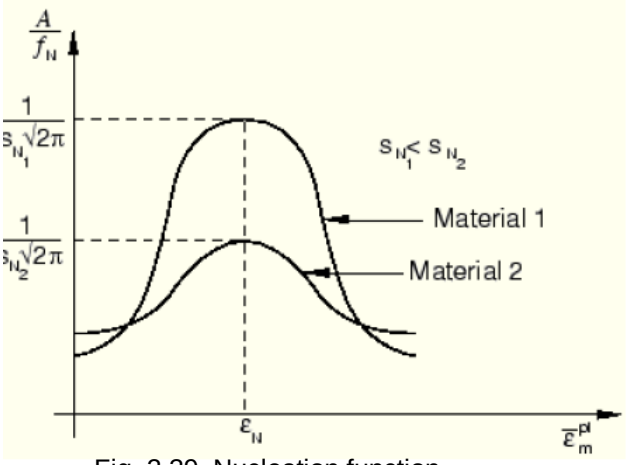

Fig. 2.39. Nucleation function.

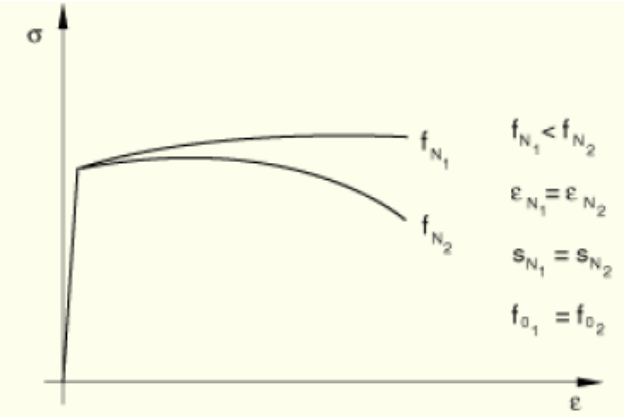

Fig. 2.40. Softening as a function of f_N.

The growth of the existing voids is based on the apparent change of volume and the conservation of mass, being expressed as:

$$df_G = (1-f)(d\varepsilon_{11}^p + d\varepsilon_{22}^p + d\varepsilon_{33}^p) \tag{2.36}$$

The modification of the yield condition to account for coalescence is introduced through the function $f^*(f)$ specified by Tvergaard and Needleman [36] as

$$\begin{aligned} f^* &= f, && f < f_C \\ f^* &= f_C + \delta(f - f_C) && f \geq f_C \end{aligned} \tag{2.37}$$

with the accelerator ratio

$$\delta = \frac{f_u^* - f_c}{f_f - f_c} \tag{2.38}$$

and $f_u^* = \dfrac{1}{q_1}$ is the ultimate value of f^* at ductile rupture, f_C a critical value of the void volume fraction when the coalescence of microvoids occurs and the stress-carrying capability of the material sharply drops and finally, f_f the void volume fraction for which the stress-capability totally vanishes leading to final failure.

As for coalescence, it is important to remark that, when modelled, it is actually a competition between viscoplastic hardening and damage softening, as shown in Fig. 2.41:

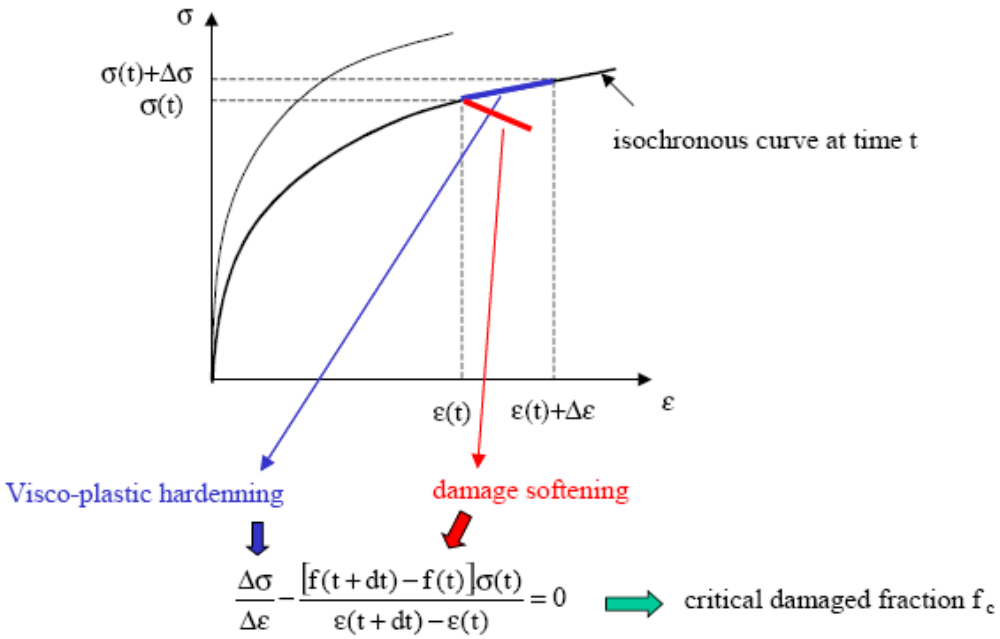

Fig. 2.41. Viscoplastic hardening and damage softening competition in coalescence [57].

The softening rate will be enhanced by increasing the stress triaxiality ratio and the equivalent stress. The viscoplastic hardening curve gradient will decrease under increasing equivalent stress. Two competing coalescence mechanisms are suggested by Thomason [42] for low triaxiality cases and Gurson-Tvergaard-Needleman [35-36] for high triaxiality cases. Notches increase stress triaxiality ratio and enhance softening.

The ductile criterion assumes that the equivalent plastic strain at the onset of damage, $\bar{\varepsilon}^{pl}{}_{D}$, is a function of stress triaxiality and the equivalent plastic strain rate, where triaxiality is defined as the ratio between the hydrostatic stress and the equivalent von Mises stress. Numerically speaking, the criterion for damage initiation is met when the state variable associated with damage, which increases monotonically with plastic deformation, reaches a critical value. At each increment during the analysis, the increase in that state variable is computed.

2.3.3 Experimental fracture mechanics

A fracture toughness test measures the resistance of a material to crack extension. A single toughness value is usually sufficient to describe a test that fails by cleavage; crack growth by microvoid coalescence, however, usually yields a rising *R* curve and one can quantify ductile fracture resistance either by the initiation value or by the entire *R* curve. The *R* curve characterizes the resistance to fracture of materials during slow, stable crack extension and results from the growth of the plastic zone ahead of the crack as it extends from a fatigue precrack or sharp notch [148]. It provides a record of the toughness development as a crack is driven stably under increasing applied stress intensity factor *K* [148]. For a given material, *K*-*R* curves are dependent upon specimen thickness, temperature, and strain rate. The amount of valid *K*-*R* data generated in the test depends on the specimen type, size, method of loading, and, to a lesser extent, testing machine characteristics [148].

The cracks in test specimens must be introduced by fatigue in order to have sharp cracks before loading, but in this project, it was not possible to perform the task.

Five types of specimens are permitted in ASTM standards that characterize fracture initiation and crack growth, namely: compact specimen (Fig. 2.42), single-edge-notched bend geometry, arc-shaped specimen, disk compact specimen (Fig. 2.42) and middle tension panel. Each configuration has three important characteristic dimensions: the crack length *a*, the thickness *B* and the width *W*. In most cases $W = 2B$ and $a / W = 0.5$.

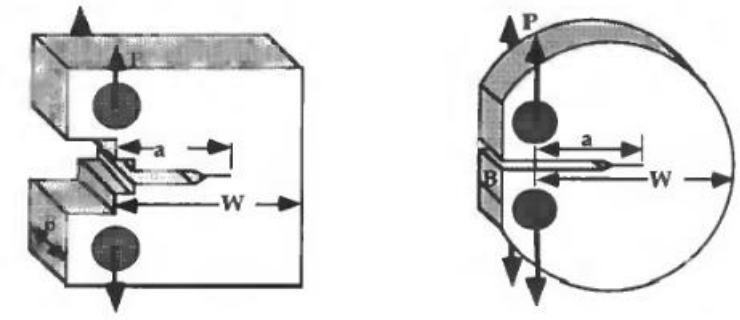

Fig. 2.42. Compact specimen and disk compact specimen [149].

The sensitivity to orientation is particularly pronounced because a microstructure with a preferred orientation may contain planes of weakness, where crack propagation is relatively easy [150]. The unloading compliance technique allows the crack growth to be inferred by partially unloading at various points during the test in order to measure the elastic compliance, which can be related to the crack length.

In certain cases, grooves are machined into the sides of a fracture toughness specimen with the aim of maintaining a straight crack front during a resistance curve test. A specimen without side grooves is subject to crack tunnelling and shear lip formation because the material near the outer surfaces is in a state of low-stress triaxiality. Side grooves remove the low triaxiality zone.

When a material behaves in a linear elastic manner prior to failure, such that the plastic zone is small compared to the specimen dimensions, a critical value of the Mode I stress-intensity factor K_{IC} (the plane strain fracture toughness) may be an appropriate fracture parameter for the material. Historically, ASTM E 399 [151] and British Standard 5447 [152] are good practice references. The specimen size requirements in ASTM E 399 are very stringent to ensure that the specimen fractures under nominally linear elastic conditions. A validity check is needed to determine the appropriate specimen dimensions. The size requirements for a valid K_{IC} are as follows:

$$B, a \geq 2.5\left(\frac{K_{IC}}{\sigma_{YS}}\right)^2, \qquad 0.45 \leq a/W \leq 0.55 \tag{2.39}$$

In order to determine the required specimen dimensions, the user must make a rough estimate of the anticipated K_{IC} for the material. Such an estimate can come from data for similar materials or from a table of recommended thicknesses for various strength levels contained into the ASTM standard itself.

The K_{IC} test is of limited value to structural metals because of the dimensions needed to get a valid result. Once a result is declared invalid, ASTM E 399 offers no recourse for deriving useful information from the test.

A more recent standard, the ASTM E 1820 [153], provides an alternative test methodology that permits valid fracture toughness estimates from supposedly invalid *K* tests. ASTM E 1820 combines *K*, *J* and CTOD parameters in a single standard. If a test specimen exhibits too much plasticity to compute a valid K_{IC}, the fracture toughness of the material can be characterized by *J* or CTOD. British Standard 7448: Part I [127] is its British equivalent.

The basic procedure of ASTM E 1820 aims to measure toughness near the onset of ductile crack extension J_{IC} by the means of a *J* resistance curve. The crack growth is not monitored so a multiple-specimen procedure is required. In such cases a series of nominally identical specimens are loaded to various levels and then unloaded. Different amounts of crack growth occur in the various specimens; the crack growth in each sample is marked after the test by heat tinting or fatigue cracking. Each specimen is then broken and the crack extension measured.

In addition to measuring crack growth, a *J* value must be computed for each specimen in order to generate the *R* curve. It is convenient to divide *J* into elastic and plastic components:

$$J = J_{el} + J_{pl} \tag{2.40}$$

The elastic *J* is computed from the elastic stress intensity:

$$J_{el} = \frac{K^2(1-\nu^2)}{E} \tag{2.41}$$

where *K* is inferred from the load and the crack size through

$$K_I = \frac{P}{B\sqrt{W}} f(a/W) \tag{2.42}$$

with $f(a/W)$ the compliance relationship tabled for each standard specimen in [154].

The basic procedure in ASTM E 1820 [153] includes a simplified method for computing J_{pl} from the plastic area under the load-displacement curve:

$$J_{pl} = \frac{\eta A_{pl}}{B b_0} \tag{2.43}$$

where η is a dimensionless constant:

$$\eta = 2 + 0.522\, b_o / W \tag{2.44}$$

for compact specimens, A_{pl} is the plastic area under the load-displacement curve and b_o is the initial ligament length.

These equations do not correct J for crack growth but they are based on the initial crack length. This is of little consequence when measuring J_{IC} because the purpose of the R curve in this instance is to extrapolate back to a J value where Δa is small and a crack growth is not necessary. That J is computed as J_Q -that is a provisional J_{IC}- from the R curve as in Fig. 2.43:

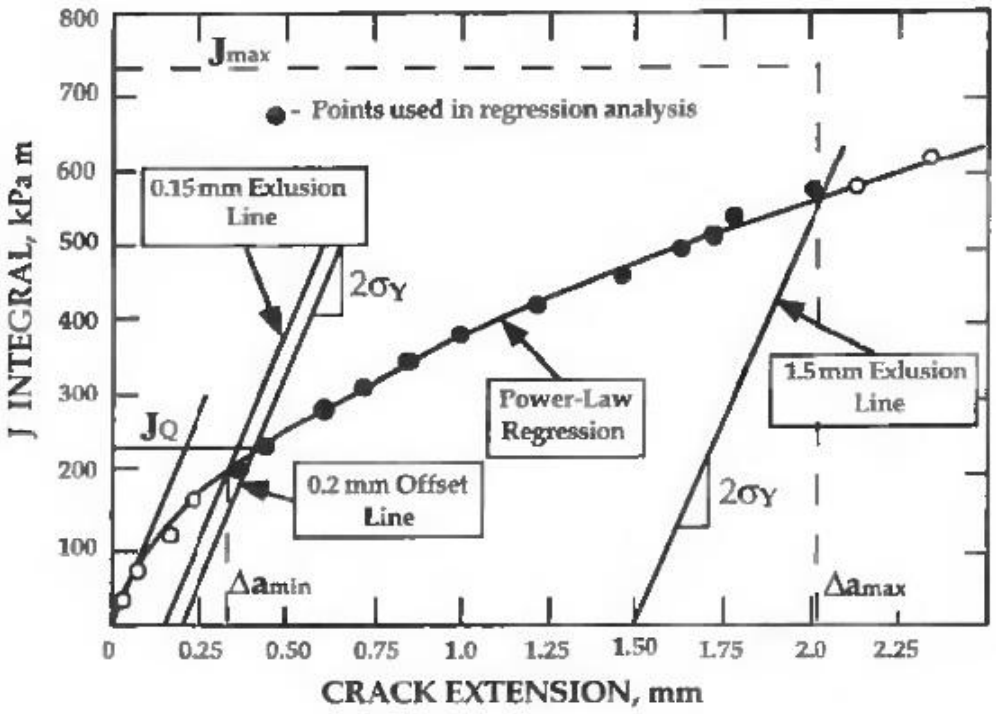

Fig. 2.43. Determination of J_Q from a complete J curve [155].

Exclusion lines are drawn at crack extension values of 0.15 and 1.5 mm. These lines have a slope of $M\,\sigma_y$, where σ_y is the flow stress defined as the average of the yield and tensile strengths. The slope of the exclusion lines is intended to represent the component of

crack extension that is due to crack blunting, as opposed to ductile tearing. The blunting line characterizes the apparent crack advance that occurs due to a geometric blunting during the early part of the *J* curve development before the sharp tearing cracks begins [156].

The value of *M* can be determined experimentally or a default value of 2 can be used, but for austenitic stainless steels, this definition has been improved by Landes himself [156], giving the following equation for 316 stainless steel blunting line:

$$J = 3.85\sigma_u \Delta a_B \tag{2.45}$$

where σ_u is the ultimate tensile strength and Δa_B is the blunting crack advance.

A horizontal exclusion line is defined at a maximum value of *J*:

$$J_{\max} = \frac{b_0 \sigma_Y}{15} \tag{2.46}$$

All data that fall within the exclusion limits are fitted to a power-law expression:

$$J = C_1 (\Delta a)^{C_2} \tag{2.47}$$

The J_Q is defined as the intersection between the previous equation and a 0.2 mm offset line. If all other validity criteria are met, $J_Q = J_{IC}$ as long as the following size requirements are satisfied:

$$B, b_0 \geq \frac{25 J_Q}{\sigma_Y} \tag{2.48}$$

which are much more lenient than the K_{IC} requirements from ASTM E 399.

In the resistance curve procedure, instead, *J* is computed incrementally with updated values of crack length and ligament length. The *J* curve can be obtained from a single specimen by using the unloading compliance method, that is by partially unloading the specimen and measuring the compliance; as the crack grows, the specimen becomes more

compliant (less stiff). Compliance is the displacement in the load curve that results from deformation and action of the load train linkages of the frame.

The ASTM standard requires relatively deep cracks ($0.50 < a / W < 0.70$) because the unloading compliance technique is less sensitive for $a / W < 0.5$.

One other option for monitoring crack growth during a *J* test is the normalization method [156-159], which entails inferring the crack growth from the load-displacement curve. A specimen with a growing crack growth shows a maximum load plateau followed by a decrease in load. The load-displacement would continue to rise in the absence of crack growth.

For computing *J* for a growing crack, the ASTM procedure utilizes the deformation theory definition of *J*, which corresponds to the rate of energy dissipation by the growing crack (i.e. the energy release rate).

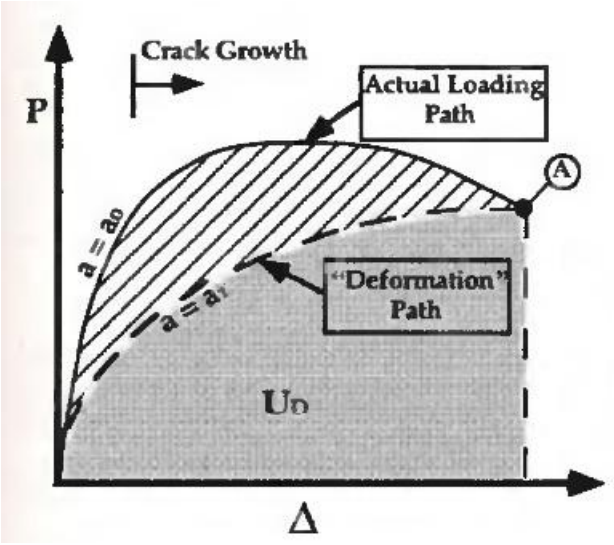

Fig. 2.44. Schematic load-displacement curve with a crack that grows from a_0 to a_1 [160].

From Fig. 2.44, the deformation *J* is related to the area under the load-displacement curve for a stationary crack, rather than the area under the actual load-displacement curve, where the crack length varies.

$$J_D = \frac{K_I^{\,2}}{E^I} + \frac{\eta_P U_{D(p)}}{Bb} \tag{2.49}$$

Since the crack length changes continuously during *J* curve test, the *J* integral must be calculated incrementally. For a given measuring point *i*, where $1 < i < n$, the elastic and plastic components of *J* can be estimated from the following expressions

$$J_{el(i)} = \frac{K_{(i)}^{\ 2}(1-\nu^2)}{E} \tag{2.50}$$

$$J_{pl(i)} = \left[J_{pl(i-1)} + \left(\frac{\eta_{i-1}}{B_N b_{i-1}}\right) \frac{(P_i + P_{i-1})(\Delta_{i(pl)} - \Delta_{i-1(pl)})}{2} \right] \mathrm{X} \left[1 - \gamma_{i-1} \frac{a_i - a_{i-1}}{b_{i-1}} \right] \tag{2.51}$$

where $\Delta_{i(pl)}$ is the plastic load-line displacement, $\gamma_i = 1 + 0.76\,(b_i / W)$ for compact specimens, $\eta = 2 + 0.522\,(b_i / W)$ and *K* as defined before.

ASTM E 1820 [153] has the following limit on *J* and crack extension relative to specimen size:

$$B, b_0 \geq \frac{20 J_{\max}}{\sigma_Y}, \qquad \Delta a_{\max} \leq 0.25 b_0 \tag{2.52}$$

ASTM E 1820 also provides a procedure for CTOD. In particular, when applying the basic test method to a ductile material, the value of CTOD is considered at the maximum load plateau. In accordance with the relevant failure scenarios as in Fig. 2.45, three types of CTOD result can be obtained and they are mutually exclusive, i.e. they cannot occur in the same test.

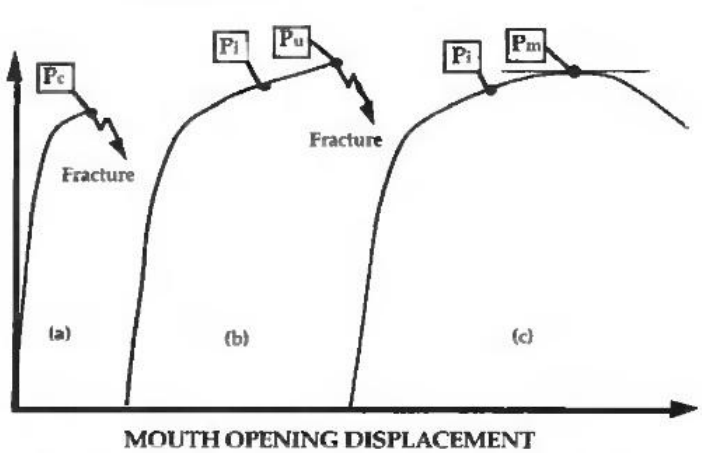

Fig. 2.45. CMOD test scenarios [161].

It has to be noted that there is usually no detectable change in the load-displacement curve at the onset of the ductile crack extension. The onset has to be detected directly by fractographic observation after unloading (for example in a multispecimen approach, unloading at successive load levels and measuring crack growth) or indirectly by the use of a failure criterion in finite element analysis. The only deviation is the reduced rate of increase in load as the crack grows. The maximum load plateau occurs when the rate of strain hardening is exactly balanced by the rate of decrease in cross section. However, the initiation of crack growth cannot be detected from the load-displacement curve because the loss of cross section is gradual. Thus, δ_{IC} must be determined from an *R* curve.

In nuclear practice, it is often needed to choose the shape, the size and the orientation of the specimens starting from the available damaged material. In dependence of the macroscopic property being investigated, the use of standard or non-standard tests will be considered. Another limiting reason is the size of the laboratory equipment chosen to simulate neutron irradiation. The benchmark [85] here adopted for neutron irradiation damage on fracture toughness, for example, used a small disk compact tension specimen, 12.54 mm diameter and 2-4 mm thickness, which was used for fitting the irradiation rig at Los Alamos Neutron Scattering Center in order to simulate high-energy neutron damage. That specimen had been proposed in the early 1990s for fusion development, for example by Elliott [162], and is now accepted into the Standard ASTM E1820 [153]. Nevertheless, there is not a detailed comparative literature with the more widespread Compact Tension specimen, such as the work from Nevalainen and Dodds [163]. Some comparison will be attempted in the introductory stage of this doctoral project.

In the recent years, other and subsize specimens have been used for fracture toughness evaluation. These specimens are often not standardized but are able to provide valuable results. One recent article from Wallin [164] reports that a considerable relaxation of the standard requirements is possible without affecting the reliability of the test result. In general, it is suggested that it could not be selected a single fracture toughness test method that would be useful for all materials or even for a single material over the full range of possible strength levels [165]; so different test methods have to be assessed in order to determine their possible correlation with plane-strain fracture toughness K_{IC}

measurements. It has to be remembered that J_{IC} is a more adequate measurement in austenitic steels to account for their plastic deformation at the crack tip. The existing correlations between K_{IC} and J_{IC} could allow a first attempt at K_{IC}, remembering that a plastic term still needs to be computed in an opportune manner (even from simple load vs. load-line displacement plots) and added.

Slow bend fatigue precracked Charpy test [166], Charpy round bar impact test [167], Chevron notched round bar specimens [168] are widely used. Nevertheless, apart from inherent theoretical issues, they are ruled out of this project because the minimum size for a good test is not achievable here.

Notched round bar specimens are one other class that is sometimes considered in the literature for fracture toughness purposes, mainly for materials exhibiting brittle fracture. The effectiveness for ductile fracture is still debated, depending upon the shape of the notch (that is to say the triaxiality) and the plastic deformation at the notch tip. Some results from Nath [169], Shabara [170] and Scibetta [171] constitute a good reference for the aim of this doctoral project. Nath suggested that as the notch angle decreases, K_{IC} increases towards the plane strain condition. Shabara studied and correlated the effect of different notch angles of non-precracked specimens on the plane-strain fracture toughness of metallic materials. Scibetta, in his doctoral research, analyzed in detail the cracked round bar specimens (notched round bars with a fatigue pre-cracking) for Linear Elastic Fracture Mechanics, Elastic Plastic Fracture Mechanics, cleavage and ductile fracture mode. The lack of a well developed and validated analysis method to evaluate experimental data and the absence of guidelines regarding the minimum specimen dimensions that are required to obtain meaningful fracture toughness data still remain and further stimulate the interest in this matter.

Scibetta [172] continued in this line of work with a direct reference to reactor pressure vessels, which are ferritic. He proposed the definition of a path independent *J*- integral in axisymmetric configuration from the load versus displacement record:

$$J = \frac{K^2(1-\nu^2)}{E} + \eta \frac{U_{pl}}{\pi b^2} \tag{2.53}$$

so introducing an incremental evaluation of the *J*-integral for a growing crack based on the deformation theory with a varying η factor:

$$\eta = 1 \qquad \text{for a / R > 0.7}$$

$$\eta = \frac{-1.497 + 1.55676\frac{R}{b} - 0.01869\left(\frac{R}{b}\right)^3}{-1.497 + 3.11352\frac{R}{b} - 0.6539(\frac{R}{b})^2 - (\frac{R}{b})^2 + 0.03738(\frac{R}{b})^3} \qquad \text{for a / R > 0.7} \tag{2.54}$$

His starting point was that in axisymmetric configuration the J-integral is different from the one in 2D plane stress or plane strain and that an additional surface term, given by η, should be taken into account.

As for ductile crack initiation, Scibetta suggested that cracks initiate due to a combined effect of stress triaxiality and strain ahead of the crack tip. His analysis showed that the lower stress triaxiality of cracked round bars compared to compact tension specimens was compensated for by higher strain. Nevertheless, he concluded –from experiments and theory- that the cracked round bar specimen is not fully adequate to derive tearing resistance curves as the amount of ductile crack growth is limited. This is inherent to the geometry and leads to early ductile crack growth instability, in particular for material with low toughness. It has to be noted that he experimentally used a multi specimen technique and that the analysis of his data was done by using the *J*-integral without updating the crack length, that is to say a normalization method.

One recent, similar study from Trattnig [173] was focussed on austenitic stainless steels and considered several specimens with respect to their stress triaxiality ratio at fracture. Cracked round bars and compact tension specimens, among others, were used. He determined a fracture line for the examined austenitic steel deformed in a stress triaxiality regime between 0.6 and 2.7, as in Fig. 2.46. He also found that the plastic equivalent strain at fracture decreases exponentially with increasing stress triaxiality ratio at fracture.

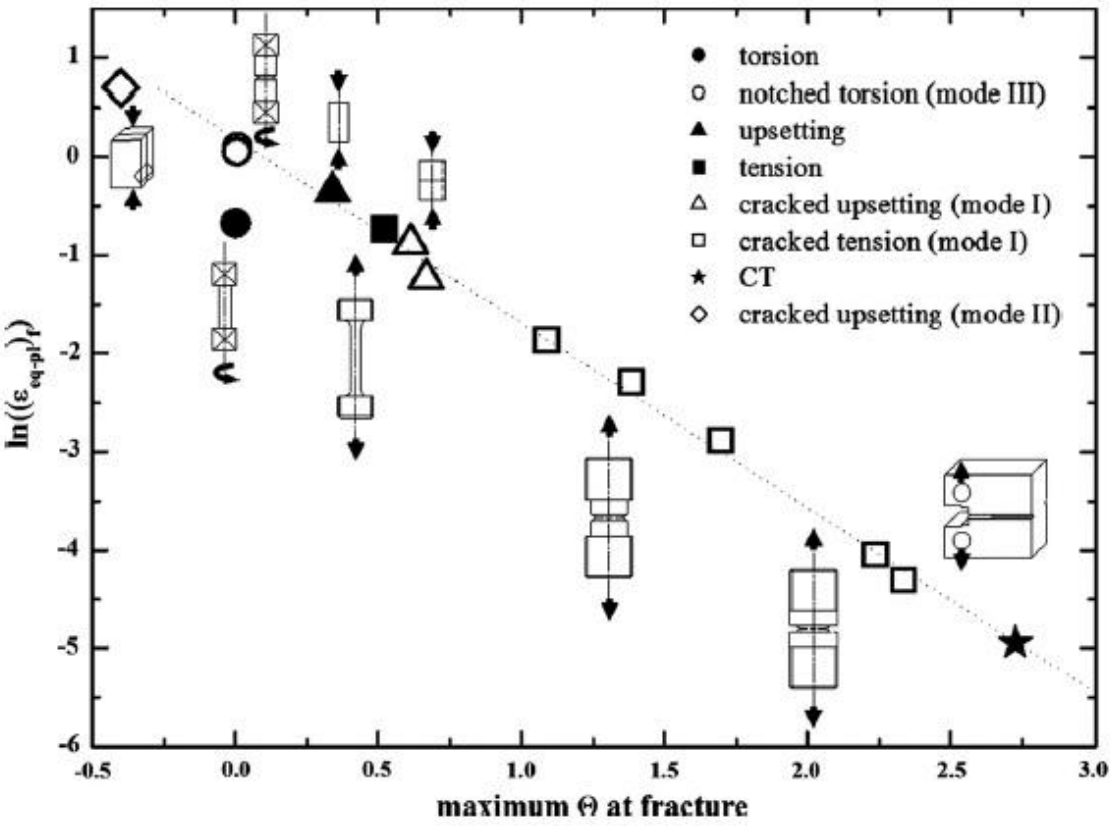

Fig. 2.46. Fracture line for austenitic stainless steels [173].

In addition to shape, differently sized specimens tend to be evaluated with interest. In particular, from Alexander [174] in the early 1990s to Lucon [175] and Lucas [176] in the 2000s, subsize specimens have been investigated for fusion materials development. One of the reasons is that they can fit the irradiation rigs used to simulate the effects of the fusion reactors environment damage. Scibetta [177] similarly did this for ferritic steels.

From a more conventional origin, instead, the recent small punch specimen for fracture toughness purposes is described in [178-180]. It can be used for ductile materials and, fundamentally, its critical plastic energy may be used to predict the fracture toughness by finite element analysis. Once the plastic strain energy reaches the critical value, the crack may propagate rapidly in an uncontrolled fashion. The small punch test is quite attractive because it makes use of a very small quantity of material: 10 mm diameter, 1 mm thickness disks are enough today to conduct reliable tests. However, it was not possible to make use of it in this project.

2.3.4 Computational fracture mechanics

In the very recent literature, some leading researchers in the field of computational ductile fracture offer a review of the latest analytical and numerical developments. The goal is to provide tools that allow designers to increase the efficiency of structures while keeping or increasing safety. The 2010 works from Li [47], Besson [181], Benzerga [39] cover extensively the matter and in particular the "top-down" or "local" approach, in which a detailed and physically based description of damage phenomena is used to represent the rupture process zone. Damage and rupture can then be represented on a surface (cohesive zone model) or in the volume (continuum damage mechanics, where average values on the macroscopic scale are obtained). Both methods can be implemented in the finite element method and experiments are used to provide calibration of fracture at the smallest scale of relevance.

The finite element method, as it is implemented, is generally based on the following procedure [182]:

1) Divide the body into small parts, called elements;
2) interpolate the test function by its nodal values;
3) enforce the weak statement for arbitrary nodal values of the test function, leading to a set of algebraic equations;
4) interpolate the displacement field by its nodal values;
5) use the stress-strain relations to express the stress in terms of the nodal displacements;
6) determine the nodal displacement by solving the linear algebraic equations.

When the body is divided into very small finite (not infinitesimal) elements, the nodal displacements approach the displacement field. Elements can be two-dimensional or three-dimensional.

The basis of the finite element method is the so-called "weak statement". Let us first introduce the divergence theorem for calculus as:

$$\int \frac{\partial f}{\partial x_i} dV = \int f n_i dA \tag{2.55}$$

being $f(x_1, x_2, x_3)$ a function defined in a volume in the space (x_1, x_2, x_3) and n_i the unit vector normal to the surface enclosing the volume.

Let us say that $b(x_1, x_2, x_3)$ is the distributed external force per unit volume and t_i the traction vector or force per area on the plane vector. Considering a body that occupies a volume in the space, the equilibrium equations are:

$$\frac{\partial \sigma_{ij}}{\partial x_j} + b_i = 0 \tag{2.56}$$

$$\sigma_{ij} n_j = t_i \tag{2.57}$$

where (2.56) holds at every point in the volume and (2.57) holds at every point on the surface. They are equivalent to:

$$\int \left(\frac{\partial \sigma_{ij}}{\partial x_j} + b_i \right) \omega_i dV + \int (t_i - \sigma_{ij} n_j) \omega_i dA = 0 \tag{2.58}$$

holding for an arbitrary function ω_i called the test function.

In the end, using the divergence theorem with (2.44) it results:

$$\int \sigma_{ij} \frac{\partial \omega_i}{\partial x_j} dV = \int b_i \omega_i dV + \int t_i \omega_i dA \tag{2.59}$$

The equations (2.55) to (2.59) represent a first, short basis for finite element analysis.

Coming back to fracture toughness computation, the historically foundational work by Rice [132], based on *J*-integral, can only deal with pre-existing cracks and cannot be applied to model crack initiation and propagation from a notch. In addition, it strongly depends on specimen geometry and it cannot be applied to complex geometries such as welds [181]. A two parameter approach, namely the *J*-*Q* by O'Dowd [183], and other methods using the crack-tip opening displacement or the crack-tip opening angle suffer

from the same limitations. In addition, they are generally linked to the small scale yielding assumption mostly used for linear elastic fracture and to large scale yielding from non-linear fracture mechanics, so being not adapted to the study of ductile fracture under large-scale deformations.

By contrast, the local approach introduced by Pineau [184] considers the crack tip situation: micromechanical models and stress – strain fields ahead of the crack are employed. The following principles are followed: precise evaluation of local material loading; failure criterion; characteristic length, usually associated with the mean spacing among inclusions; experimental characterization / testing followed by modelling, calibration and then simulation. Micromechanical models are based on the already discussed nucleation, growth and coalescence of voids by using the principles of plasticity theory. The boundary value problem consisting of one or a few voids surrounded by a non-linearly deforming material subject to a general state of applied strain is then solved. These models are more complex to develop than the historical global approach but physically more representative. Voids are generally modelled as ellipsoidal (but shape and direction can vary) and a representative cell unit is employed.

Void growth makes use of the Gurson model; void nucleation is generally strain controlled and based on the work of Chu and Needleman [147]. For coalescence, one acceleration of porosity rate as given by Tvergaard and Needleman [36] or one localized plastic flow as given by Thomason [42] are employed. It has still to be noted that such coalescence methods do not address fracture toughness and tearing resistance, for which dissipation must be accounted. Practitioners generally make use of a critical value for failure (void volume fraction, fracture strain, maximum principal stress) based on experimental evidence from the given material.

For the aim of this project, the GTN model was comparatively the best possible. Its implementation is fully incorporated in the ABAQUS package available. Details of that implementation will be provided in the Chapter 4, but some practical comments from the manual and from literature are reported here. First: for small scale yielding, the boundary model is representative and non-linear geometries are not computed. Nevertheless, this project will not use small scale yielding because it is not suited for ductile materials.

Second: symmetry in the models plays an important role. Forces tend to be smaller (and crack advances larger) in the case of full meshes for a given crack mouth opening displacement (CMOD) because one element only is broken at each time instead of two. Third: in the Gurson model, generally $q_1 = 1.25$ and $q_2 = 1.0$ are kept unchanged for different materials, but recent studies show that they are somewhat dependent on plastic hardening. In particular, the parameter q_2 increases the effect of triaxiality on the yield locus [185-187]. As for Chu-Needleman parameters, void nucleation is typically considered secondary since it is extremely sensitive to the microstructure (particles distribution, size, shape, clustering) and stress state. For simplicity, void nucleation models are used to characterize nucleation independent of microstructure [188-190]. The values used for steel are $\varepsilon_n = 0.3$, $s_n = 0.1$, $f_n = 0.04$ [191]. Simulations of early irradiation must account for void nucleation and growth processes, since annihilation, aggregation, and cluster ripening take place concurrently [192-193]. For that reason, a lower value of ε_n is expected, compared with "undamaged" material.

Some criticism about the Gurson-Tvergaard-Needleman parameters, their calibration and their actual physical meaning is made by Bonora [194]. He states that while a great attention has been given to the parameters from a theoretical point of view, much less has been paid to the experimental aspects. First, according to the model the presence of plasticity does not affect the set of constitutive equations for the porous material. Second, the implied mechanism of coalescence is the internal necking of the ligament between the growing cavities instead of the often-observed localized shear across the ligament, especially in high-triaxiality conditions where microvoids remain spherical during the growth phase. Third, the secondary nucleation generally modelled by the means of the Chu-Needleman distribution is material dependent. Fourth, it is not easy to understand which specific void growth (among the matrix of cells –or elements in the finite element analysis- making the simulated material) triggers the macroscopic loss of stiffness measured at a bigger scale. Fifth, porosity is assumed to be exponential for all kinds of metal, while according to Bonora it is not. Sixth, the mutual dependence among the parameters leads to non-unique choices of the set to be accepted. Seventh, four node elements should be preferred while using axisymmetric models and this project did that.

Eight, large displacements should be allowed and this was used in this project for the experimental fit described before. One other problem may be given at high levels of damage by experimentally observed strain localization, which counters the hypothesis of the Gurson model itself. Even if Bonora seems to discourage the use of the GTN model – and in fact he proposes one alternative in the form of a continuum damage model – he stills acknowledges that an opportune combination between numerical and experimental techniques may lead to the definition of at least one acceptable set of parameters.

One further thing to note is about the numerical implementation of a fracture criterion in the form of critical void volume fraction. Among the parameters just described, it is important to point out that different void volume fractions come from four-node elements and eight-node elements when subjected to the same displacement, as in Fig. 2.47. Literature reports that a difference between four-noded and eight-noded elements exists after crack initiation: as long as initiation has not been reached, results obtained with linear (four-noded) and quadratic (eight-noded) elements are similar if the mesh refinement is sufficient [195]. Bonora forcefully states that eight-node elements, in an axisymmetric formulation, can result in a convergence problem, due to the difficulty in balancing the residual forces at the midside nodes, under extensive plastic flow; four-node elements perform quite well and should be preferred [194]. The best strategy here is to try to compare both elements.

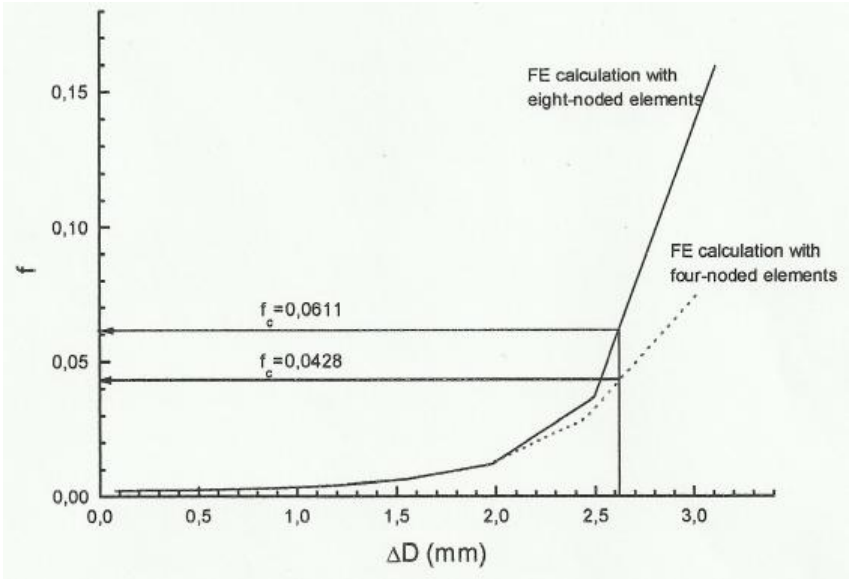

Fig. 2.47. Void volume fraction with four-noded and eight-noded elements [191].

This project will make use of one opportune implementation fitted on the experimental evidence up to initiation point. It can be anticipated that a four-noded axisymmetric element CAX4R will be adopted.

The relevant outputs from the package are going to be: equivalent plastic strain, void volume fraction, void volume fraction due to void growth and void volume fraction due to void nucleation. These will be used for defining the fracture criterion relative to the differently "damaged" materials obtained from experiments. If needed, the fracture toughness estimation can be performed by ABAQUS itself, building the *J–R* curve for ductile materials while the crack advances. However, it can also be inferred in an indirect manner starting from the crack mouth opening displacement (CMOD) or from the load line displacement (LLD) of the model, usually one from the compact tension family. CMOD and LLD would then be related to provisional values of CTOD and J_{IC} respectively [196-197]. For all these numerical cases, linear front advance is going to be used, that is to say no tunnelling effect is permitted.

Summary of the literature review with aims and objectives

Austenitic stainless steels have been presented in relation to their origin and use in the nuclear industry. A 316L grade is the material of interest in this project. Its behaviour under ductile damage, creep damage and irradiation damage has been introduced. A comparison of damage mechanisms has been made.

Fracture toughness is the material property under investigation. The detrimental effects of irradiation on that property have been described. These effects will be tentatively reproduced in this project by the means of experiments inducing strain hardening and generating porosity (by ductile damage or creep damage) into the solution annealed material. Standard and non-standard experimental techniques for fracture toughness evaluation have been presented and will be used.

Finite element analysis will play a decisive role in describing the constitutive laws, validating the experimental results and making predictions about the fracture toughness initiation of the "undamaged" and the "damaged" materials obtained experimentally. The suitability of the Gurson-Tvergaard-Needleman to describe the progression of damage will be discussed on a case-by-case basis.

3. Experimental methods

This chapter introduces the experimental methods used to investigate the mechanical properties and behaviour of the given austenitic stainless steel, induce damage and evaluate its fracture toughness.

3.1 Material

Material was a 316L stainless steel in the form of a 14 mm diameter bar and 28 mm diameter bar. In order to estimate the yield stress state of the "as received" material, hardness measurements were made on one metallographic sample cut from the 14 mm diameter bar along the longitudinal direction and prepared. Empirical relationships enabling the estimation of yield strength from hardness measurements are described by Was [198]. The tests were performed using a Wilson Tukon 2100 machine. The reference used was the standard BS EN ISO 6507 [199]. Three random measurements were executed on one specimen. A force of 0.5 kgf was chosen for the diamond indenter, that being a standard value for stainless steels. Edge effects were not considered.

3.1.1 Heat treatment

A solution annealing treatment was planned on the "as received" material to get control of the actual internal stress state. The pieces were cut from a 14 mm diameter round bar. It was needed to understand the distribution of heat in a cylindrical furnace, in order to establish the maximum dimension of the pieces to have homogeneous treatment.

Solution annealing at 1050 °C in Argon environment (inert gas, in order to preserve the external surfaces against oxidation) for 30 minutes followed by rapid quenching in water was performed for each of them, leading to "undamaged" state.

Larger pieces were cut from the 28 mm diameter bar with the aim of inducing damage and machining specimens for fracture toughness evaluation. Their solution annealing was outsourced to Bodycote Testing Ltd.

3.1.2 Metallography

Metallography [200-201] consists in the preparation of a metal surface for analysis by grinding, polishing, and etching in order to reveal the microstructural constituents. Grinding was done using rotating discs covered with silicon carbide paper and water. Grades of paper 240, 400, 800, 1200 (grains of silicon carbide per square inch) were used; before moving next grade, the samples were washed in water; then the scratches from the previous grade were oriented normal to the rotation direction; after the final grinding operation at 1200 paper, the samples were washed in water followed by alcohol and dried. The polisher consisted of rotating discs covered with soft cloth impregnated with diamond particles (6, 1 and ¼ micron size) and oil lubricant. Etching is used with a double aim: to remove chemically the highly deformed thin layer left by grinding and polishing; and to relieve chemically the stresses on the surface, allowing different crystal orientations, grain boundaries, precipitates, phases and defects to be distinguished in reflected light microscopy. Oxalic acid in 10% solution [202] was used for about 50 seconds at 6 V voltage.

After preparation, the sample could be analyzed by the means of optical or electron microscopy. The optical microscope was an Olympus with five different magnification lenses and one camera mounted on top to record pictures. Optical microscopy principles are introduced and described in detail by Davidson and Abramovitz [203].

Grain size had also to be determined. The standard followed was BS EN ISO 643:2003 [204]. One “as received” and one “undamaged” specimen were prepared for metallography and etched in 10% oxalic acid in order to reveal the grain features.

3.1.3 Mechanical testing

In order to apply a local damage model, it was necessary to measure the "undamaged" material yield and flow behaviour [205]. A series of tensile tests at room temperature were undertaken. The specimens were extended at a fixed displacement rate and the extension, as the applied force or load increases, was continuously measured.

The reference standard used was BS EN 10002 -1, "Metallic materials – tensile testing" [206]. The bar diameter was > 4 mm and the Annex D was considered. Fig. 3.1 reports the dimensions of the specimens machined from "as received" and "undamaged" material.

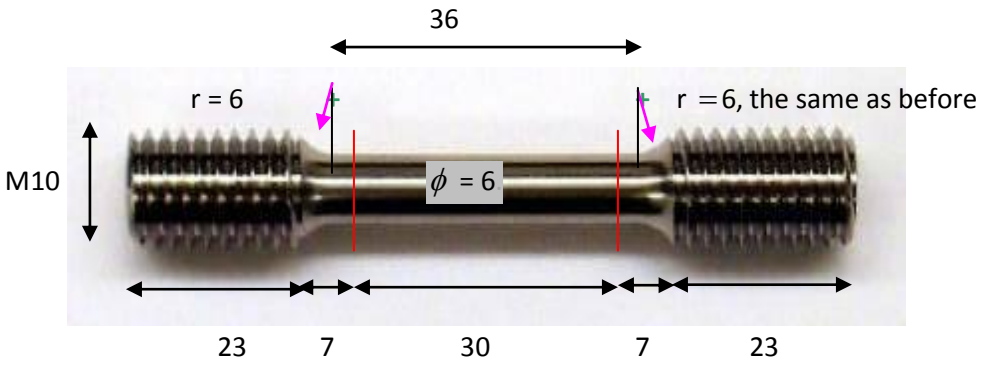

Fig. 3.1. Smooth bar tensile specimen.

Starting from the effective diameter, chosen to be equal to 6 mm, the maximum load to be applied by the testing machine could be estimated. If the ultimate tensile strength of the material is 1000 N/mm², and the effective area is:

$$A = \pi\left(\frac{d}{2}\right)^2 = 28.274 \text{ mm}^2, \tag{3.1}$$

the maximum load to be applied is UTS * A = 28,274 N = about 30 kN

This value had to be matched with the resisting threaded area. The reference standard BS EN 10002 suggested to adopt a grip threaded length > 1.5 nominal diameter (15 mm in our case, for M10). A grip-threaded length of 23 mm, 1.5 times that value, was adopted.

The testing machine was the MTS Alliance RT 100 (up to 100 kN load capacity). The axial extensometer was the MTS 634.12 model. Its gauge length was fixed at 10 mm. The crosshead displacement rate was fixed at 0.3 mm/min.

In order to use in Abaqus, the true stress – true strain (true plastic strain) values, needed to account for section reduction after necking, were given by the following relations:

$$\varepsilon_{true} = \ln(1+\varepsilon_{eng}) \tag{3.2}$$

$$\sigma_{true} = \sigma_{eng}(1+\varepsilon_{eng}) \tag{3.3}$$

$$\varepsilon_{true}^{pl} = \ln(1+\varepsilon_{eng}) - \frac{\sigma_{true}}{E} \tag{3.4}$$

In addition, three different configurations of axisymmetric notched specimens were used to obtain the parameters of the Gurson-Tvergaard-Needleman model. Higher triaxiality accelerated the creation of voids by augmenting the deviatoric part of the tensor, as for example said by Benzerga [39]. This manner it was possible to exploit directly the softening mechanism in the material. They were designed to have notched radii of 1.5, 3 and 6 mm ($NT_{2.5}$, NT_5, NT_{10}) in accordance with the Fig. 3.2. Three specimens for each notched radius were used. This multispecimen approach wanted to counteract the non-uniqueness of the set of parameters that can be obtained from fitting, as argued by Bonora [194]. Single-notched and double-notched specimens were designed to attempt fractographic analysis of the broken zone and metallographic analysis near the failure zone. Double-notched specimens in Fig. 3.3 also underwent tensile test, in order to break one of the notched zone and have a metallographic observation of the fracture initiation at the other one.

The tests were performed at MTS Alliance RT 100 machine under displacement control (crosshead displacement rate equal to 0.5 mm/min). The load applied and the minimum cross-sectional diameter reduction were continuously recorded by the means of a radial extensometer in order to obtain the load - diameter reduction curves.

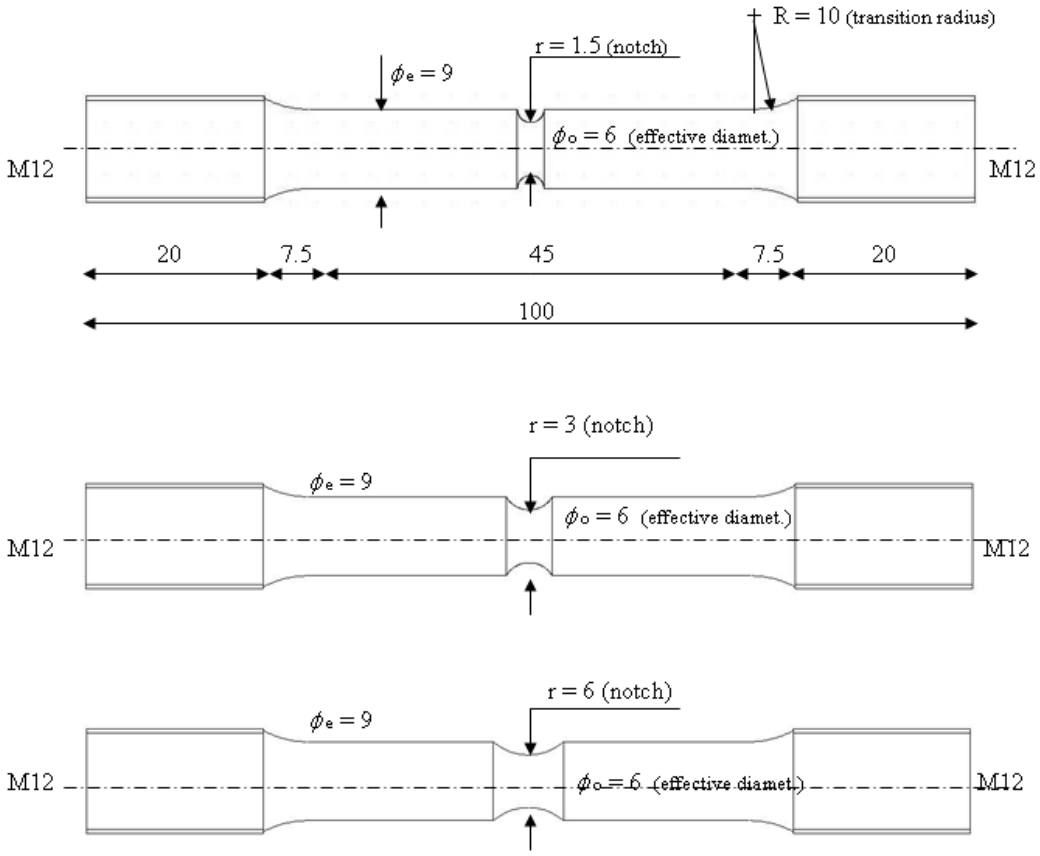

Fig. 3.2. Single notched tensile specimens.

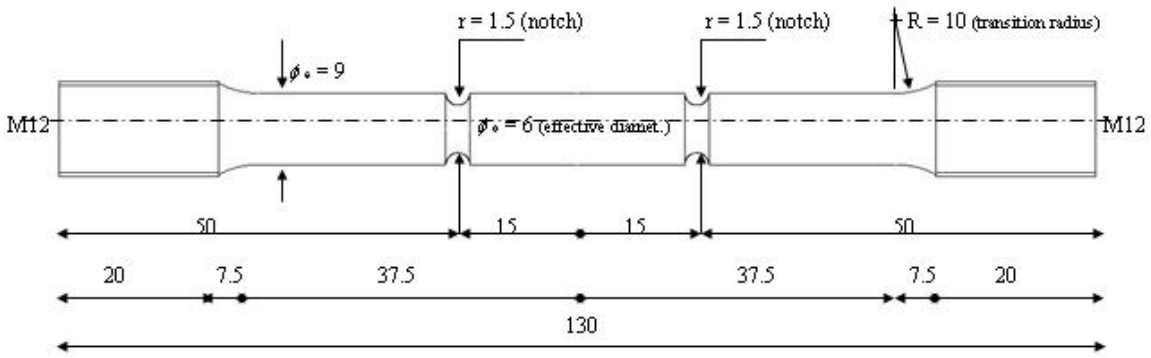

Fig. 3.3. Double notched tensile specimen.

3.1.4 Fractography

Fractography studies the fracture surfaces of materials and aims to determine the cause of failure. The existence of several crack growth mechanisms leads to different features on the surface, which can help to identify the failure mode. A historical perspective and some background for metals are given by Parrington [207].

Fractography can be done by electron microscopy using the fractured specimen as it is or after electropolishing. At the basic investigation level, it was expected to get the features of ductile fracture, which are cup and cone shape and dimples. Two electron microscopes were used during this project: one Amray 1810 and one Zeiss Evo 50. An introduction and details about scanning electron microscopy can be found in [208].

Prior to examination, specimens were sectioned as in Fig. 3.4, 2 cm below the fracture surface, using a cutting wheel machine. A Struer 356 CA [209] abrasive wheel at 3000 rpm, suited for stainless steels, was employed with cooling water in order to minimize mechanical damage, thermal damage and debris. The specimens were then cleaned ultrasonically in acetone and dried. Procedures for the preparation and preservation of fracture surfaces are reported in the ASM Handbook, Vol. 12 [210].

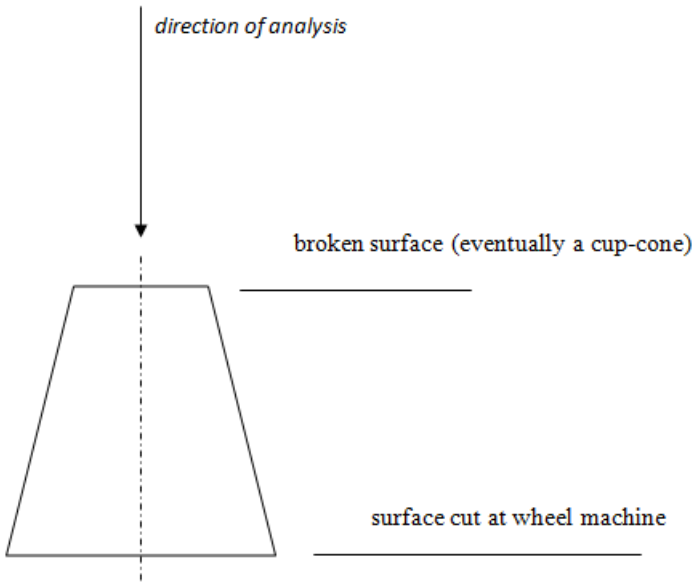

Fig. 3.4. Specimen for fractography.

3.2 Introducing damage into the material

Plastic strain and creep damage were used to induce damage experimentally into the given austenitic stainless steel, with the tentative aim of reproducing the detrimental effects of neutron irradiation and helium bubbles on fracture toughness. The numerical constitutive models (elastic part, plastic flow, Gurson-Tvergaard-Needleman model parameters and initial void volume fraction) of the "undamaged" and "damaged" 316L material were then validated on experimental results by finite element analysis.

The logical approach that was implemented is summarised in Table 3.1, as follows:

as received 316L	void into the matrix	void at grain boundaries
Solution annealed		
Plastic strain	Interrupted uniaxial tensile test at room temperature	
Plastic strain + solution annealing + Plastic strain	Interrupted uniaxial tensile test at room temperature + solution annealing + interrupted uniaxial tensile test at room temperature	
Creep damage	Creep test at 650 °C	Sensitization
Creep damage + anneal	Creep test at 1000 °C	Grain boundary sliding, diffusional flow?

Table 3.1. Logical sequence of the damaging processes

The contribution of void nucleation can be separated from the effect of growth on total void volume fraction. This was experimentally attempted by using notched tensile tests and plotting the void volume fraction after failure against distance from the fractured

surface. Different levels of triaxiality were tested in order to investigate void volume production with distance from the fracture surface, as graphically shown in Fig. 3.5:

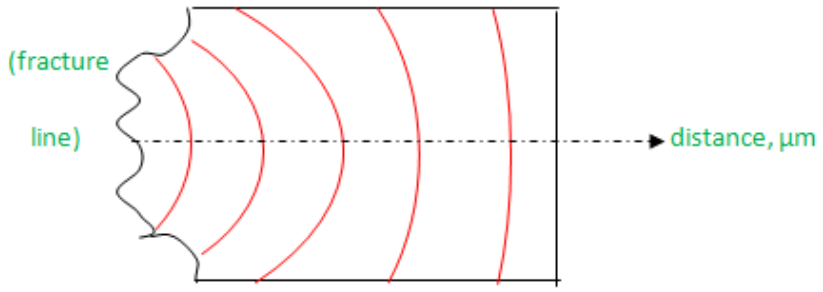

Fig. 3.5. Prospective field of void volume fraction.

3.2.1 Uniaxial tensile testing at room temperature

One analytical approach to estimate the critical stress – interfacial decohesion strength of spherical carbide particles in steels is discussed in [211-212]. The surface stress distribution under straining conditions for 316L containing local heterogeneities has been numerically determined in [213]. It is there reported that plastic strain values as low as 3.8% and 6% are enough to lead to crack and crack propagation through MnS inclusions, while cracks in the metallic matrix remain substantially unchanged.

Starting from that and for the aims of this project, tests were planned in accordance with the following procedure:

- 30% engineering strain;
- 30% engineering strain + 10% engineering strain;
- 30% engineering strain + solution annealing + 10% engineering strain.

Annealing was performed in order to preserve the eventual voids induced created from decohesion while relieving the internal stress state generated.

Each test was performed using one smooth bar specimen, as depicted in Fig. 3.6. At the end of the procedure, three differently "damaged" specimens were obtained.

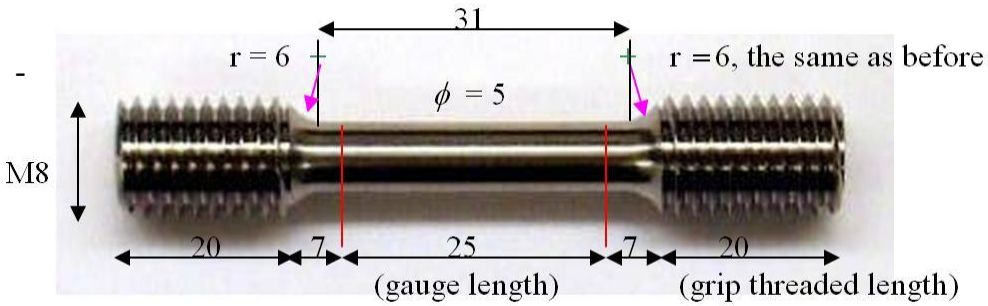

Fig. 3.6. Specimen for interrupted tensile test.

In order to get "damaged" material from which machining fracture toughness specimens, the entire procedure was repeated using one set of larger specimens, as in Fig. 3.7, machined from a 28 mm diameter bar:

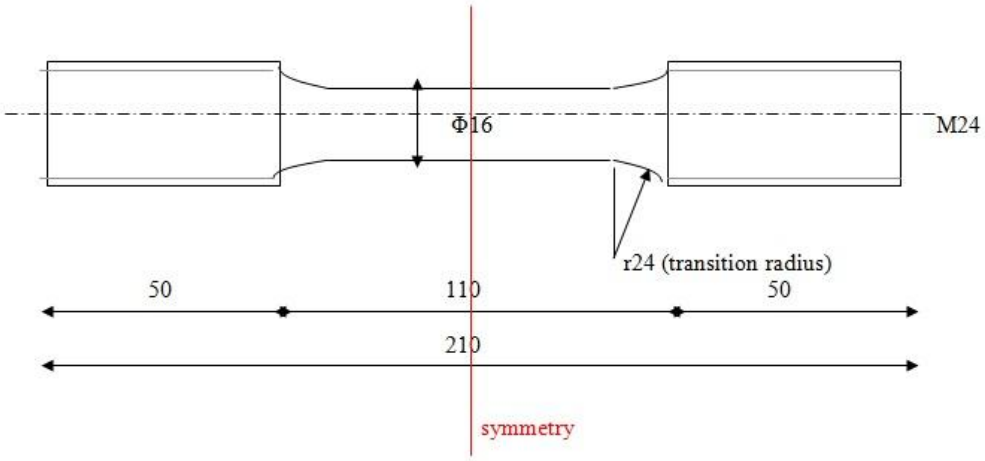

Fig. 3.7. Large interrupted tensile test specimen.

3.2.2 Creep testing

From the deformation mechanism map in Fig. 2.14, it was chosen to attempt creep at 650 °C and induce transgranular or intergranular creep fracture. The yield stress value at 650 °C was interpolated from literature data. It was planned to have failure after about 1000 hours and explore the suitability of that timescale for producing voids into the matrix. The actual level of stress to apply was then interpolated from one other set of literature data in terms of stress vs. time to rupture.

Two Mayes 20, Denison Mayers Group, creep-testing machines were set up. Their furnaces were equipped with a Three Zone Temperature Controller TRI-Z40ZV Eurotherm. Three thermocouples were applied to work in the gauge length zone: one internal to the machine and controlling the temperature itself; one fixed to the gauge length of the specimen and connected to a digital reader out of the furnace; the third was a fully external thermocouple connected to a manual temperature reader. The load was applied by the means of loading bars screw coupled to a universal joint (also taking care of the axiality), so that a lever ratio 10:1 was guaranteed. The specimen had the shape and the size depicted in Fig. 3.8:

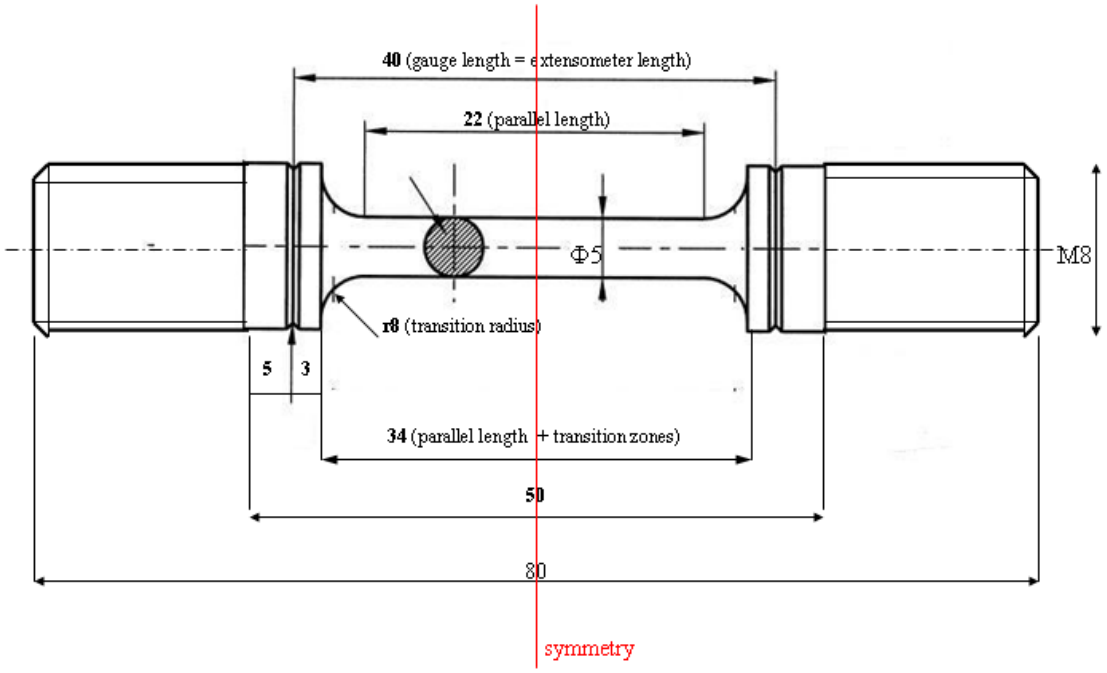

Fig. 3.8. Specimen for creep.

Two creep studies at 650 °C, one lasting about 1500 hours and the other lasting 70–150 hours. The level of stress was interpolated from literature data. The tests were not able to produce the expected results in terms of porosity. On the other hand, different levels of sensitization were produced, but sensitization was not considered fruitful for the aim of this project. It was then decided to raise the creep temperature. From the deformation mechanism map in Fig. 2.16, T = 1000 °C was considered for producing damage from grain boundary sliding or diffusional flow, without sensitization. The stress was planned to be in the range of 2-3 MPa and time to failure was expected not to exceed 1000 hours. Oxidation played a role during the test and the stress was reduced to less than 0.5 MPa in the very early stage. The creep procedure at 1000 °C was repeated using one larger specimen, from which "damaged" material for successive fracture toughness evaluation was obtained. Physical constraints on the creep machine apparatus limited the scalability (with respect to Fig. 3.8) of the larger specimen to the following dimensions: 330 mm total length, 200 mm extensometer length, 170 mm parallel length, 18 mm diameter, M 1" BSF thread.

3.2.3 Combination of pre-strain and creep

In the end, a combination of pre-strain hardening at room temperature and creep at 900 °C was attempted to superimpose voids created from decohesion to creep voids. The 900 °C temperature for creep was chosen in order to avoid oxidation. The mechanical limits of the available testing machines were the main constraint for this experiment. The same larger specimen for creep at 1000 °C was used. Opportune grips were designed and machined in order to connect the large specimen to the uniaxial tensile test machine for the pre-strain procedure. It was only possible to perform 7% eng. strain at room temperature. In fact, due to the dimensions of the specimen, a load equal to 110-120 kN was necessary to reach the level and it was deemed to be not safe to allow more than that. From the perspective of this project, this prestrain was deemed to be barely useful to produce decohesion into the matrix. Stress was initially 13 MPa and slowly raised during the test up to 17 MPa.

3.3 Quantitative measurement of the damage produced

Damage can be measured by using indirect or direct ways [214]. Among indirect ways: density, Young's Modulus and acoustic methods. Direct measurement can be done by surface microscopy and X-ray tomography. The images obtained can be processed and analyzed manually or by software. The length scale of interest for the damage produced and measured in this project was µm.

3.3.1 Image processing from notched tensile test of "as received" and "undamaged" material

A grid of 100 µm x 100 µm quadrants was applied to metallographic images, as in Fig. 3.9, up to 1 mm distance from the fracture line.

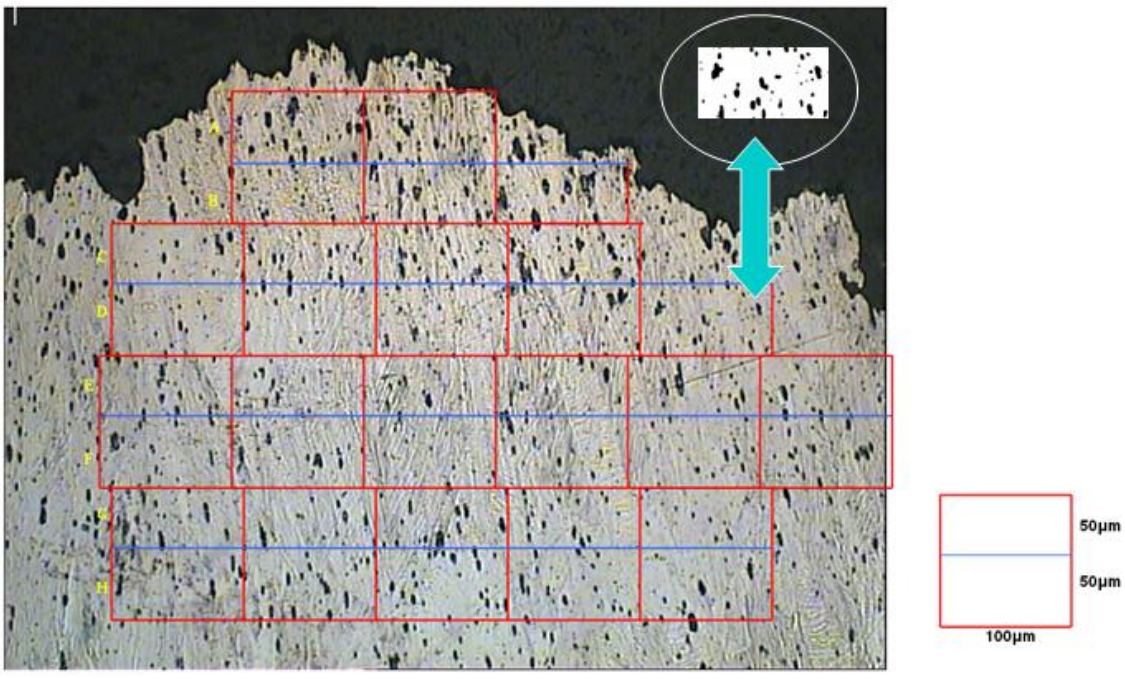

Fig. 3.9. Grid for computing voids from notched tensile tests.

For each quadrant, void volume fraction was computed improving the image contrast and then applying black and white binarization with the help of the Image J software. Several quadrants for each fixed distance from the fracture line were considered. Voids volume

fraction was computed statistically and plotted against distance from the fracture line. It has to be noted that the etching procedure chemically removed a layer of surface from the material, but its influence on the model was not addressed. Non-planarity of the fracture surface was accounted for by not considering the two quadrants at the top of Fig. 3.9.

3.3.2 Image processing from creep at 1000 °C "damaged" material

One small specimen used for inducing damage at 1000 °C was subjected to tomographic analysis after having found evidence of voids. Tomography principles and limitations, sample preparation, data collection and analysis are extensively described in [215].

The upper half of the specimen, Fig. 3.10, starting from its ruptured surface, was used for X-ray Microtomography at the Henry Moseley lab, The University of Manchester, as it was obtained from creep test, after grinding the outer zone to fit the Xradia microXCT window [216]. The 10× objective lens, 2.6 mm field of view with ~1.6 µm pixel size, was used.

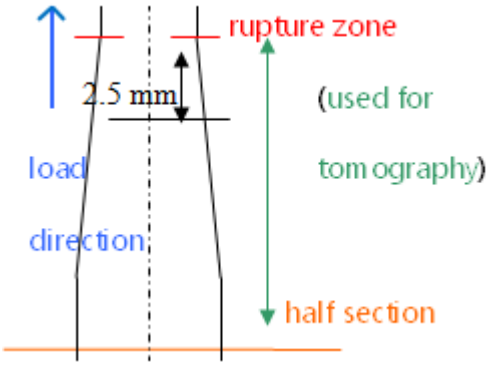

The part was about 11 mm long; the upper zone was tested, for a total length of about 2.5 mm. It was assumed that below that point, porosity was homogenous or still slowly decreasing.

Fig. 3.10. Part of the specimen used for tomography.

In order to optimize the acquisition setting, energy of 140 keV was required, so that about 1000 counts in the bulk of the part were registered. The number of slices taken was a little short of 1700, that requiring about 25-26 hours processing. The total cumulative dimension of the images was 17 GB and accepted like that.

After the scan, reconstruction was performed by using XTRM 7.0.2311 program and the related algorithm. In the end, 1668 transverse slices were generated as a cumulative 3D image of the 2.5 mm zone. Six slices were selected at representative distance from the fracture line and processed in the same way described for quadrants in Section 3.2.4.1.

One set of 1668 slices was obtained from one small specimen presenting voids from grain boundary sliding after creep at 1000 °C. They were numbered as in Fig. 3.11:

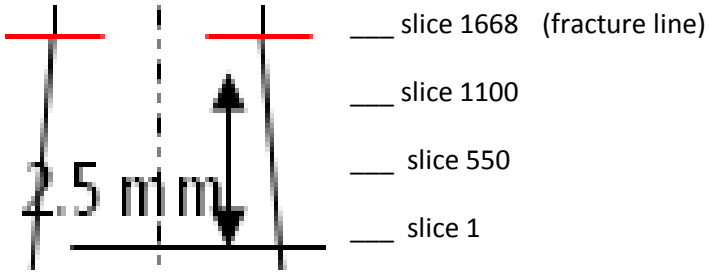

Fig. 3.11. Slices enumeration from tomography.

Slices from 1100 to 1668 were excluded from analysis because of they included the actual necking zone, which can be approximated to a notch in the line suggested by Bridgman [217]. Representative area from slices in the necked zone was not consistent with the area taken from slices outside the necked zone, so making comparison difficult. In addition, it was important to assess the mechanical production of creep voids outside that zone. The computation then started at about 0.8 mm from the fracture line.

1100 slices remained as the useful part of the scan, for a total of about 12 GB (one image being 10.9 MB). It was not possible to process together all the images by the Avizo Fire 6.1 package skeleton option, because of memory constraint. It was therefore chosen to process one pack of slices at a time, in order to limit the weight on the system; one pack was made of 22 slices and the memory size requested to the workstation so limited to 256 MB. This also prevented the acquisition of a 3D porosity skeleton.

Six packs were considered for a global analysis of the useful part of the scan: slices n. 10 to n. 32; slices n. 229 to n. 251; slices n. 446 to n. 468; slices n. 663 to n. 685; slices n. 880 to n. 902; slices n. 1078 to n. 1100. One representative slice from each pack is presented in Fig. 3.12:

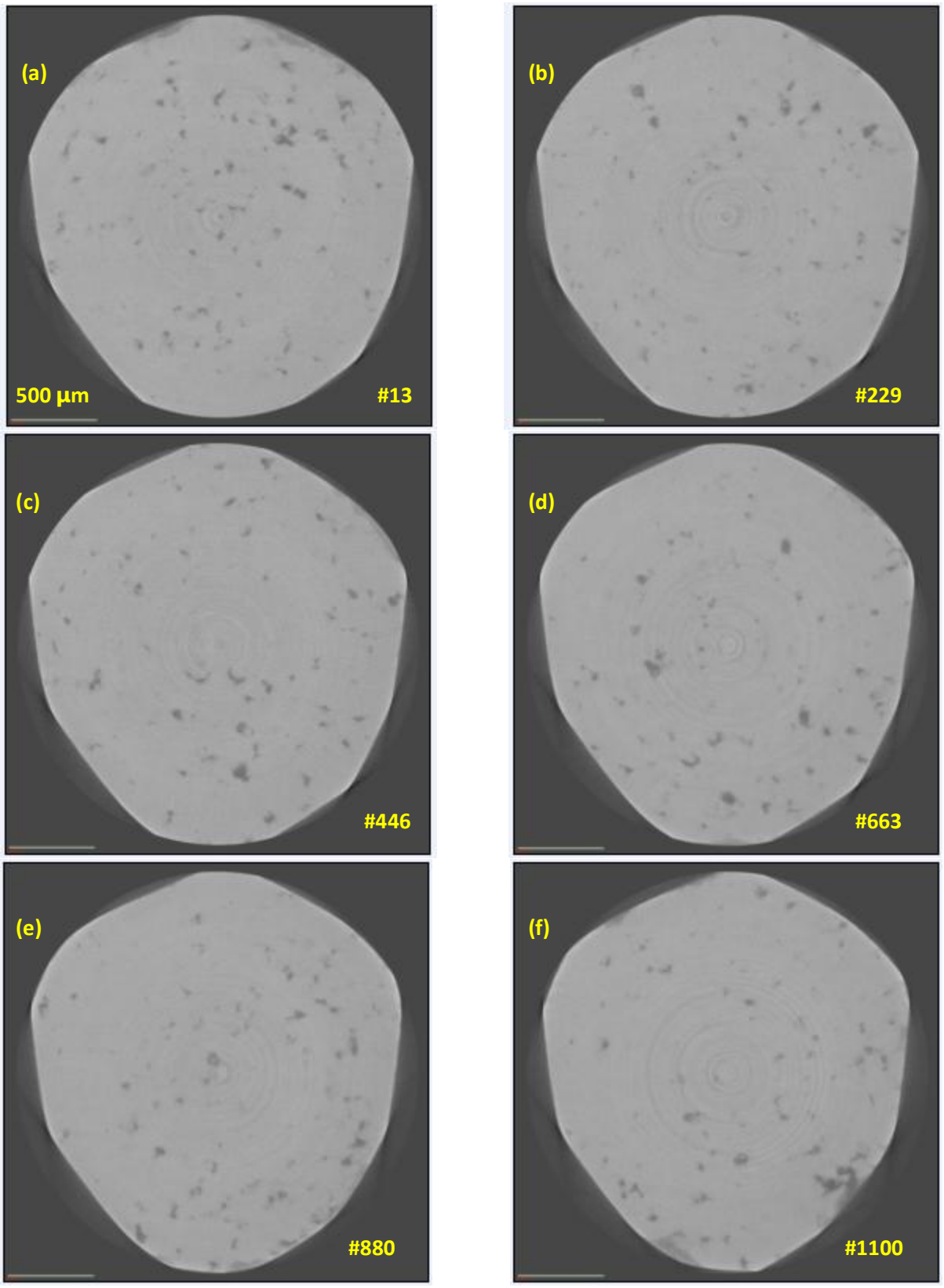

Fig. 3.12(a)-(f). Representative slices from tomography.

In order to infer void volume fraction in the transverse direction, it was necessary to process the images using Avizo Fire or by manual processing with the Image J package. It was found that the results are almost coincident and that the margin of error due to human sensitivity in filtering – binarizing operations with Image J can be reduced with practice.

Both the Avizo Fire and the Image J ways of processing images required a preliminary cropping, as in Fig. 3.13. It cut out the part of the area and made the contrast between voids and the bulk of the matrix uniform enough. The crop was selected as symmetrical as possible with respect to the "damaged" surface.

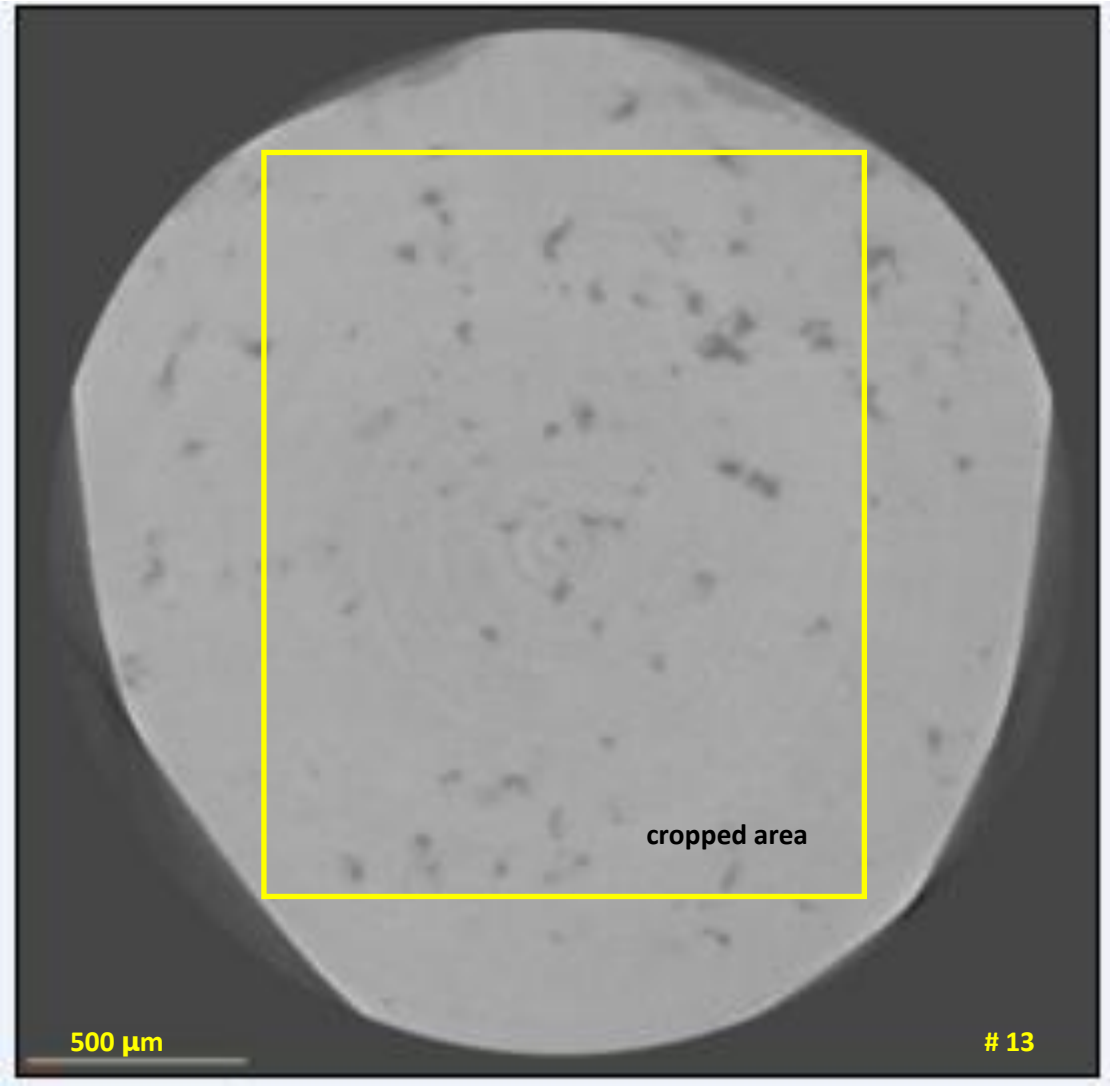

Fig. 3.13. Cropped area from one of the slices.

The resulting images used to compute voids, with improved contrast, are in Fig. 3.14.

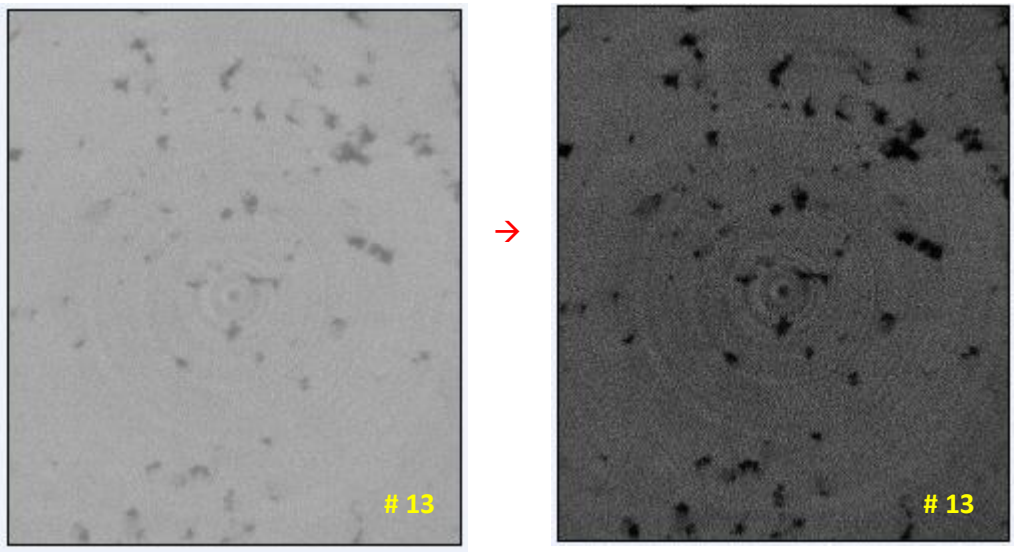

Fig. 3.14. Improving contrast on the cropped area of one slice.

At this point, binarization followed. It could be done automatically using Avizo Fire (by using MedianFilter3D option followed by binarization) or manually with Image J (operator sensitivity). The results are the following for the cropped image # 13, Fig. 3.15. This procedure was repeated for the other relevant slices shown in Fig. 3.12.

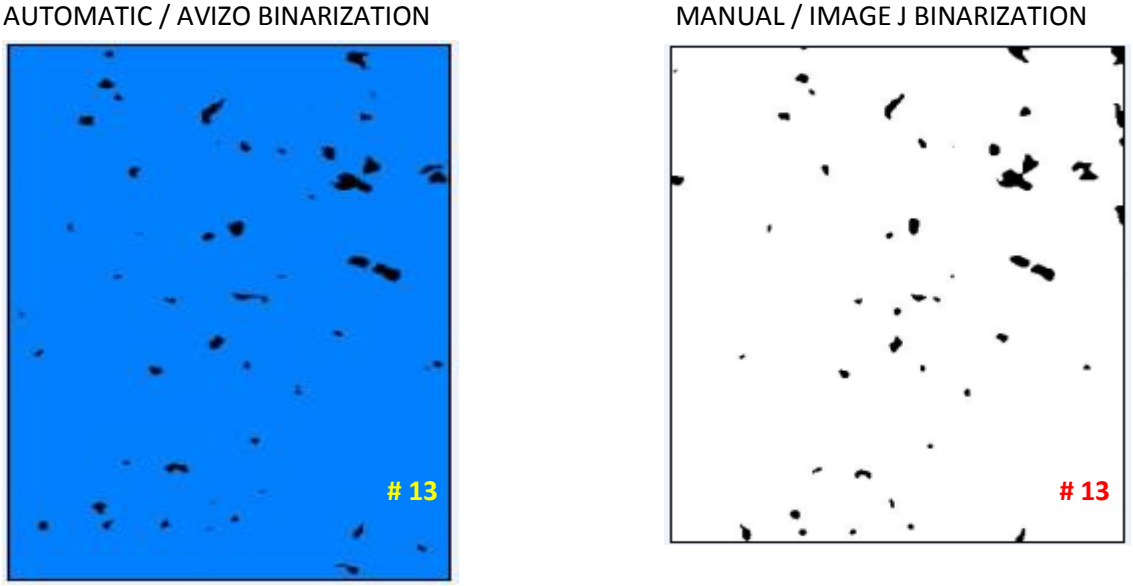

Fig. 3.15. Automatic and manual binarization on one slice.

3.4 Fracture toughness testing

Depending upon the size of the material obtained from ductile and creep damaging tests, fracture toughness evaluation was performed experimentally by using small Disk Compact specimens or sharp-notched round bar specimens. These were the easiest to test in the given conditions at the universal machine MTS Alliance RT 100 or one of its lower maximum load counterparts available. It was not possible to use unloading compliance, which is not suited to these machines and not implemented in an automatic manner. One manual programming of the loading-unloading sequence appeared to be not satisfactory. Because of that, only fracture toughness initiation (crack initiation) was attempted, starting from load vs. displacement plots.

A dimple size technique [218] and tentative tearing resistance curves by using a normalization method [156-159] were also taken into consideration. Results were qualitative. They are presented in Appendices B and C respectively, for future work.

Fracture toughness specimens for quantitative results were obtained from the following "undamaged" and "damaged" materials:

a) undamaged 316L stainless steel;
b) 30% eng strain at room temperature;
c) 30% eng strain + sol. ann. + 10% eng strain, tested at room temperature;
d) 30% eng strain + 10% eng strain, tested at room temperature;
e) Creep at 1000 °C;
f) Combination of 7% pre-strain at room temperature followed by creep at 900 °C.

Starting from the dimension and the shape of the available "damaged" material, two different specimens were achieved for fracture toughness experimental evaluation:

1) a circumferentially notched specimen, with a sharp notch angle;
2) a disk compact tension specimen, where available.

The specimens are depicted in Figs. 3.16 and 3.17, with detail of the testing procedures.

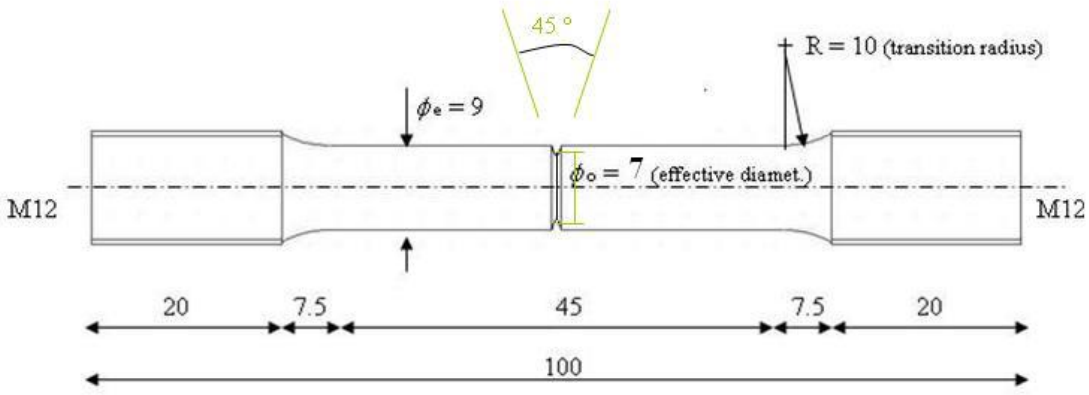

Fig. 3.16. Sharp-notched tensile specimen for fracture toughness purposes.

One longitudinal extensometer with length equal to 10 mm was located at the notch zone in order to register the displacement without suffering compliance. Crosshead displacement rate was limited to 0.4 mm/min for all the sharp-notched specimens.

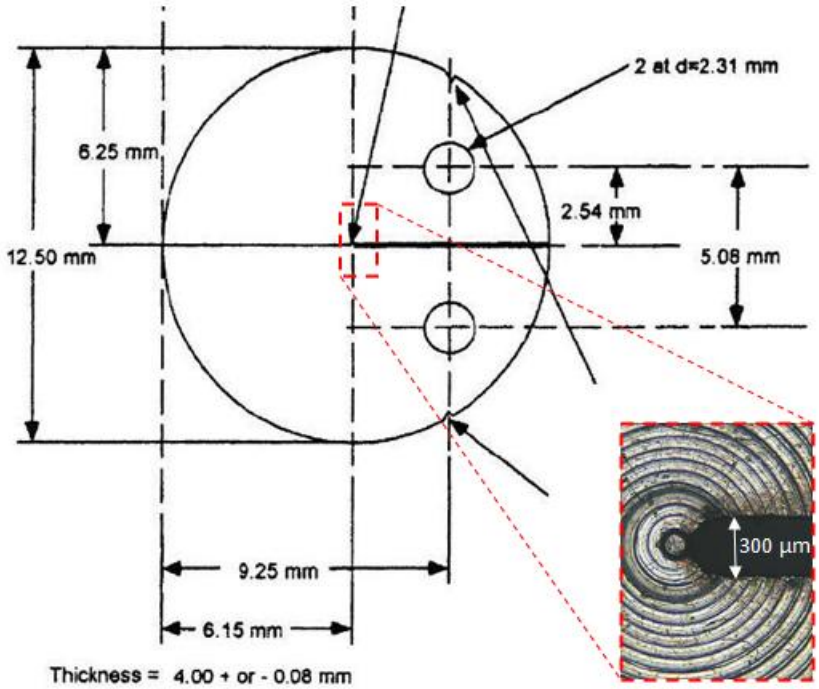

Fig. 3.17. Disk compact specimen with detail of the actual notch.

One axial extensometer was connected to the pin-clevis system machined to execute the test, so that it could register the line displacement. Its initial measuring length was 20 mm. Crosshead displacement rate was kept to 0.2 mm/min for all the disk specimens.

The sensitivity to fracture surface orientation with respect to the rolling direction, Fig. 3.18, is particularly pronounced in fracture toughness measurements, because a microstructure with a preferred orientation may contain planes of weakness, where crack propagation is relatively easy [219]. The ASTM standards require that the orientation must be reported along with the measured toughness [219].

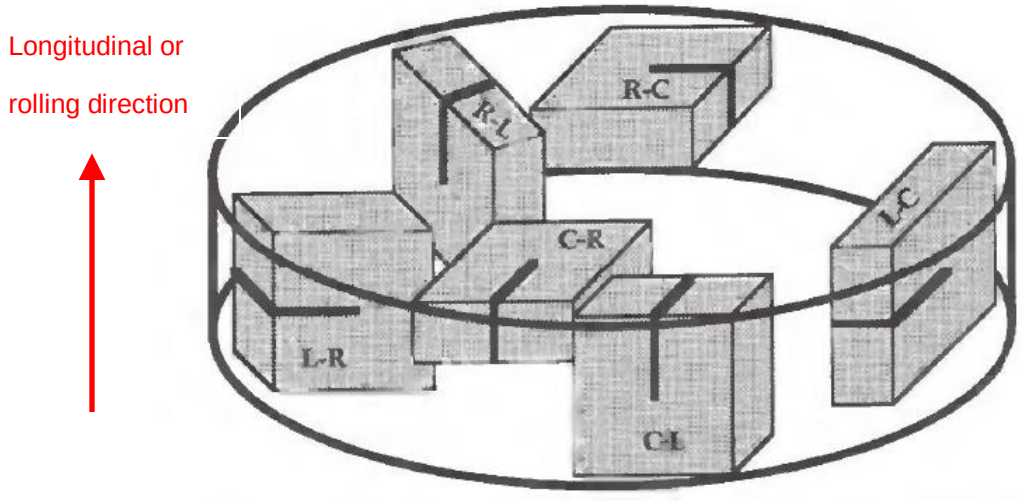

Fig. 3.18. ASTM notation for specimens extracted from disks and hollow cylinders [219].

As for this project, the raw material for the sharp-notched bar specimen, depicted in Fig. 3.19, was cut from the parallel length of the larger specimen in Fig. 3.7 and from the one scaled up from Fig. 3.8 for creep at 1000 °C, after they were used to induce damage into the 316L. Machining followed in order to get the proper dimensions and the L-R notch.

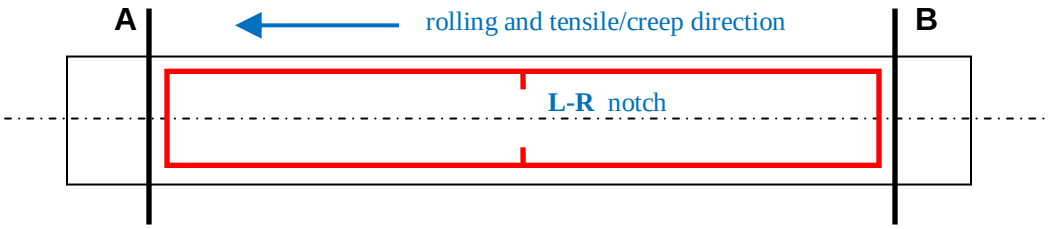

Fig. 3.19. Raw material for sharp-notched specimen from the “damaged” bigger specimen.

The raw material for the small disk compact specimen in Fig. 3.20, where available, was cut from the gauge length zone of the larger specimens. The notch was machined in the radial direction with respect to the circumferential face.

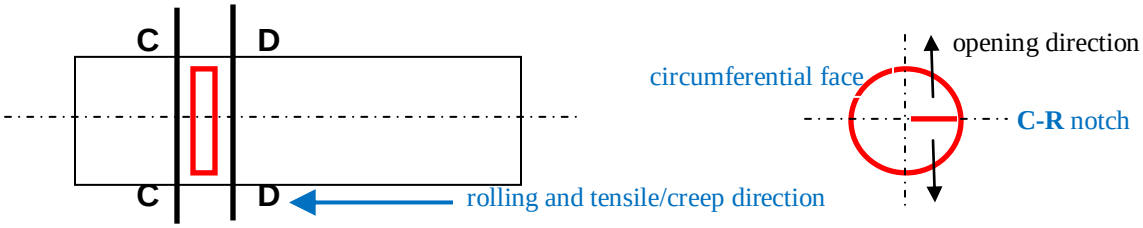

Fig. 3.20. Raw material for disk compact specimen from the "damaged" bigger specimen.

The fracture surface from the sharp-notched specimen and the disk compact specimen was differently orientated. Difference in fracture toughness values, if any, would be stated from experimental findings. One recent and comprehensive review of irradiation effects on LWR core internals [220] reports a strong orientation effect on fracture toughness of austenitic stainless steels. In particular, fracture toughness in the transverse orientation is significantly lower than that in the longitudinal orientation. This is attributed to the presence of long, narrow particles oriented in the rolling direction, which results in a long and narrow quasi-cleavage structure parallel to the crack advance, thereby accelerating the crack advance [220].

Small Disk Compact specimens were not fatigue pre-cracked because it was not possible to perform that in the lab. In addition, multispecimen unloading compliance was not executed because only one or two specimens were machined from each "damaged" material. Load vs. displacement plots were obtained. The axial extensometer, 20 mm gauge length, was located on the pin-clevis system designed for allowing the connection to the testing machine. At this goal, a D2 tool steel was used and machined as in Fig. 3.21.

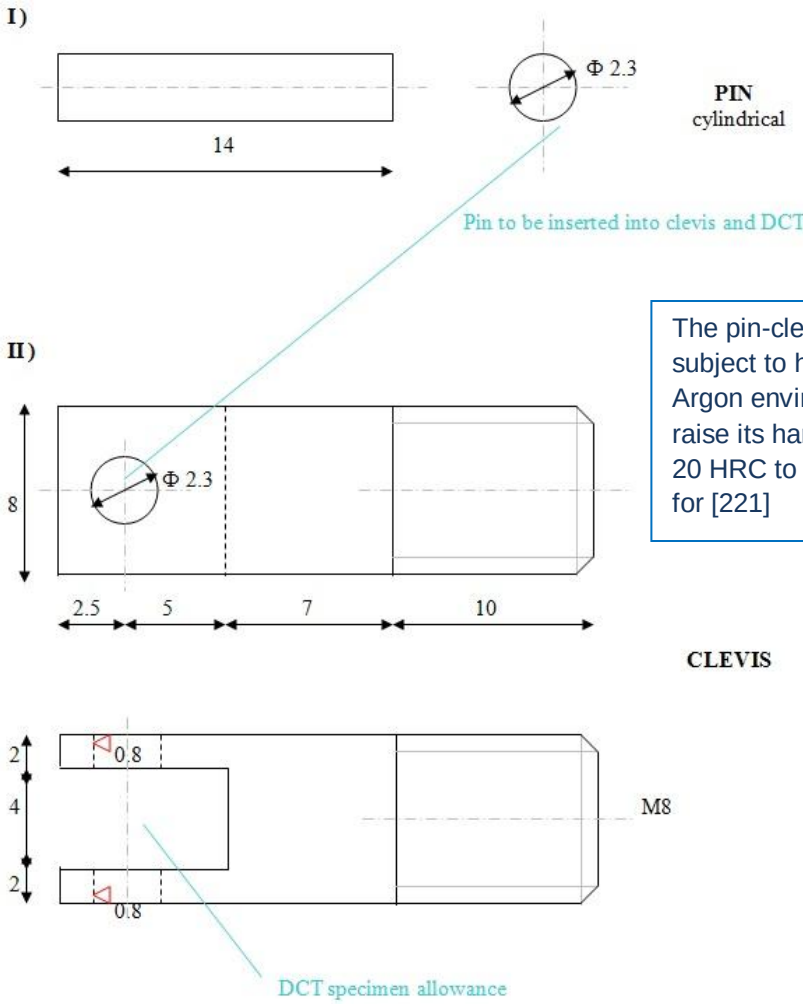

The pin-clevis system was subject to heat treatment in Argon environment in order to raise its hardness from about 20 HRC to about 60 HRC, as for [221]

Fig. 3.21. Pin-clevis system for testing disk compact specimen.

Back to the fracture toughness technique adopted, it has to be said that the load vs. displacement data do not show precisely where fracture happens. Because of that, a numerical fracture criterion must be applied in order to estimate the point of crack initiation. Such criterion depends on the material: if brittle, some uniaxial maximum stress can be considered; if ductile, critical equivalent plastic strain or void volume fraction must be applied. Fracture criteria for this project were proposed and combined with experimental results from sharp-notched round bar tensile tests in order to estimate the crack initiation point. For ductile materials such as the 316L here considered, it is generally wrong to imply the crack initiation process starting at the maximum load level in the load vs. displacement plot. In fact, it has been found experimentally that fracture starts a bit before that [222].

4. Numerical Methods

Finite element analysis derives the solution of problems like stress analysis, fracture mechanics, fluid mechanics and electro-magnetism by splitting the region of interest into small units known as elements. Within each element, the governing equations are applied by numerical approximation. Boundary and loading conditions are applied, and the behaviour of the entire structure is solved at discrete points known as nodes. ABAQUS is one of the most widely used packages in the industry and research. CAE Student versions 6.6.1 and 6.9.2 were used. The analyses were conducted in a static mode, in that reproducing the experimental procedures, by using the Standard version of the package.

4.1 Gurson model calibration on the "undamaged" state

The numerical calibration of the the elastic, elastic-plastic and porous-plastic constitutive equations for the "undamaged" state was done starting from smooth tensile and notched tensile tests. Four numerical axisymmetric models were used for calibration. They reproduced the shape and the size of the specimens used in the experimental studies. The first session used a smooth bar as in Fig. 4.1(a). The second session used the three differently notched tensile specimens shown in Fig. 4.1(b). Notch detail is in Fig. 4.2.

Calculations were made on the full specimens and axisymmetry was employed. The mesh element was the four-noded CAX4R. The effects of mesh refinement on results were analyzed for notched specimens but they were not critical at this stage because there was no characteristic length to take account of. It is reported in the literature that for axysimmetric bars a sharp drop of the load occurs when a localization band appears at the center of the specimen [223]. After the onset of the load drop, the result is mesh size dependent and the load drop is faster with the smallest mesh size [223]. Load was applied at the top of the specimen in the form of displacement, as worked out from the experimental results. The lower section of the model was fully constrained. The incremental steps of computation (in scale from 0 to 1) were automatic, the minimum

being 10^{-9} and the maximum 0.01. The initial step was 10^{-6}. Computations did not give any warning or error. Table 4.1 reports details of the number of nodes and elements employed. Meshing techniques are also declared.

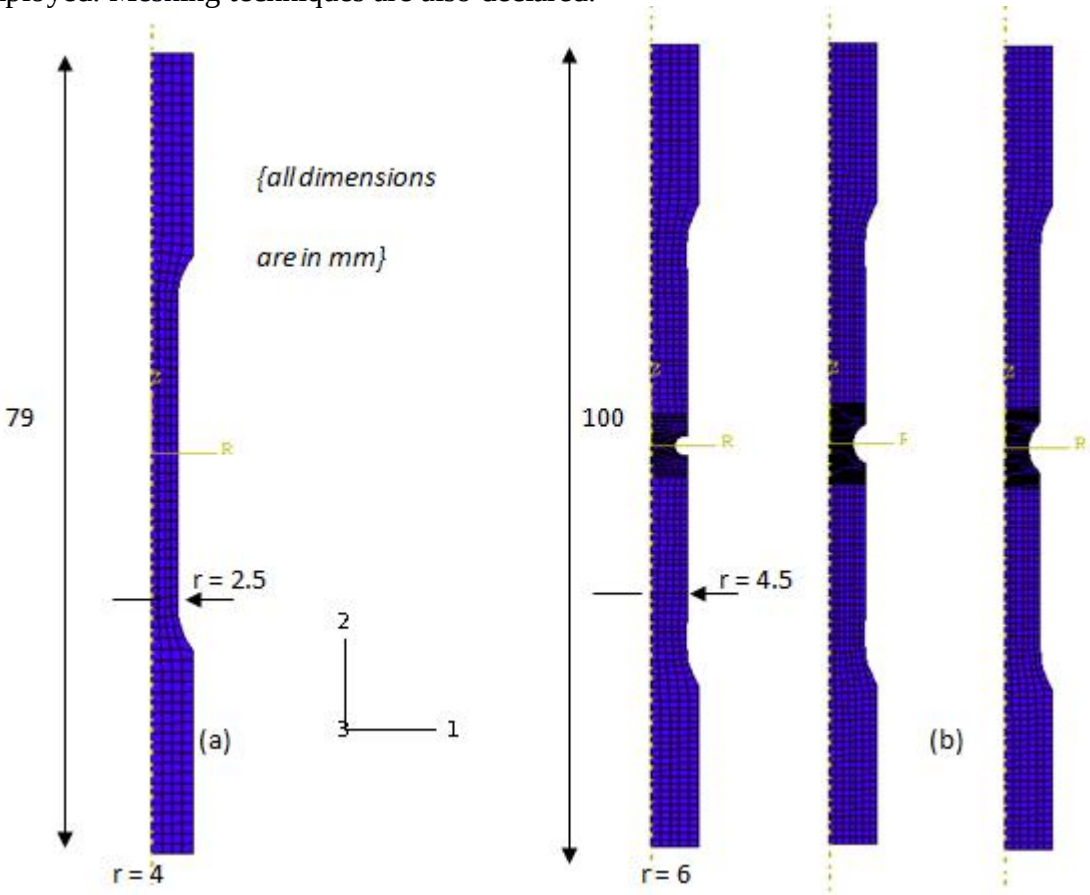

Fig. 4.1. Smooth bar model (a) and the set of three notched tensile models (b).

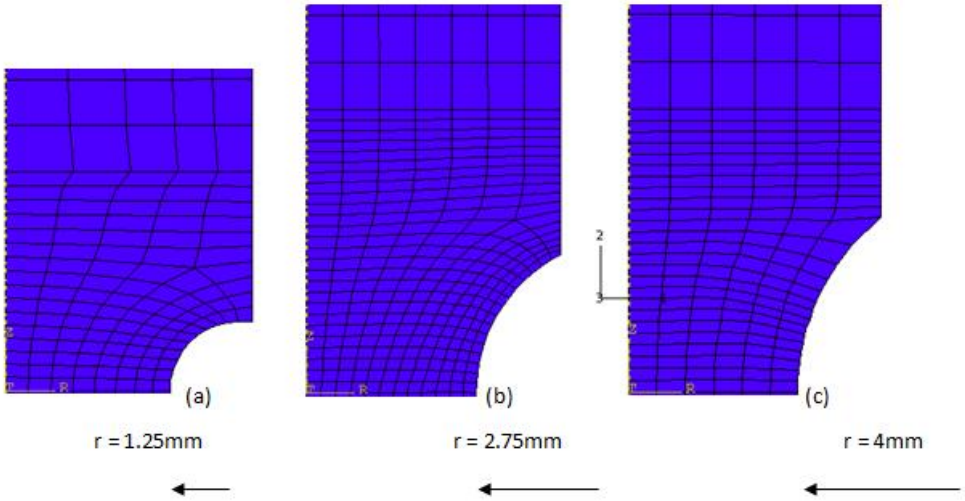

Fig. 4.2. Detail of the three different notches used.

MODEL	NODES	ELEMENTS	TECHNIQUES
smooth bar	410	324 CAX4R	free meshing + minimize transition
NT small	952	778 CAX4R	Same
NT medium	1486	1294 CAX4R	Same
NT large	1126	948 CAX4R	Same

Table 4.1. Finite element models specification for calibrating

4.2 Irradiation hardening effect on formation of constitutive hardening equation

Irradiation hardening effects on yield stress were tentatively reproduced by the means of strain hardening at room temperature. Fig. 2.20, which reports the stress vs. strain curves for unirradiated and neutron irradiated 316L, as obtained for example by Bailat [79].

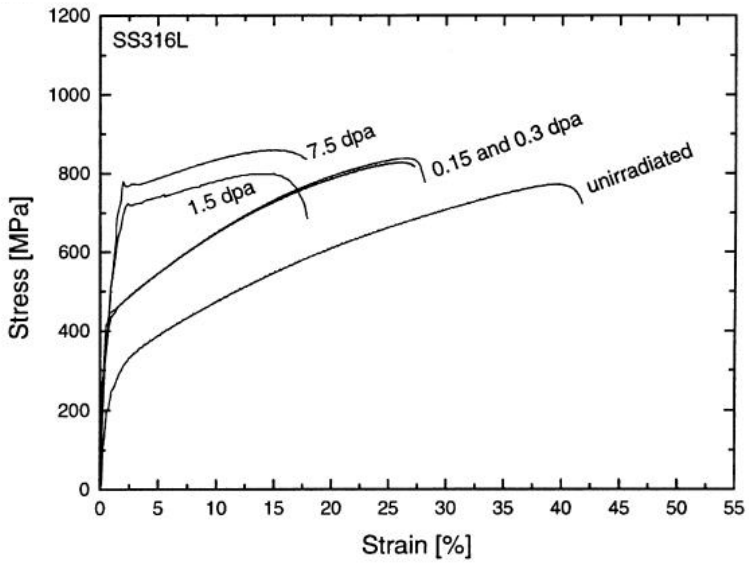

Fig. 2.20. Variation of yield stress with dpa for 316L stainless steel [79].

Several researchers aimed to compare irradiation hardening with strain hardening. In particular, Byun T.S., active since the late 1990s, states that radiation-induced defects and deformation- produced dislocations result in similar net effects on post-yield strain-hardening behaviour [80]. For an fcc configuration such as austenitic stainless steels, similar strain-hardening behaviour is produced by channel (or twinning) deformation in irradiated materials and by the uniform deformation in unirradiated materials. Yield stress increases with dose up to plastic instability at about 30 dpa value. Consequently, the irradiated plastic flow may be put in relation to the unirradiated plastic flow by shifting the curve in the positive direction by opportune strains, as in Fig. 4.3.

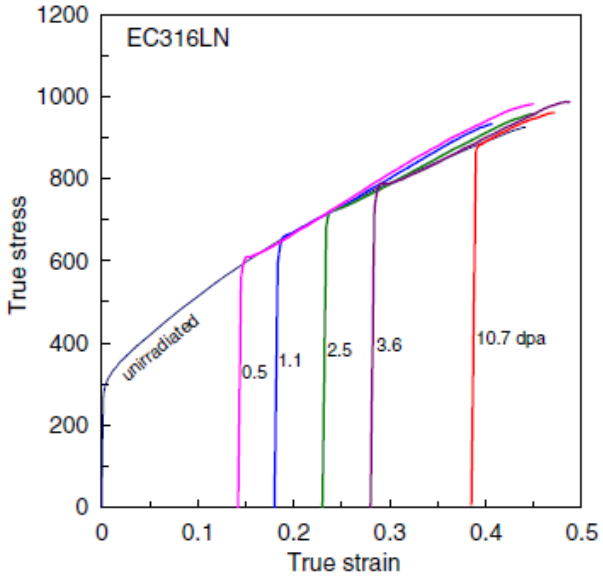

Fig. 4.3. True stress – true strain curves for EC316LN ss [80].

As for this project, the true stress - true strain plot obtained from interrupted tensile tests of the large specimen in Fig. 3.7 was superimposed to the one in Fig. 2.20. A rough estimation of the dpa associable with 10%, 30% and 40% engineering strain followed, as an extension to the yield strength value of the results from Byun.

4.3 Preliminary analysis of candidate specimens for fracture toughness evaluation

Given some standard candidate specimens, finite element analysis was used at the early stage of this doctoral prohect to predict parametrically, against the benchmark [163], the J integral for elastic-plastic materials by the means of contour integrals [132]. The normalized stress on the crack plane and the crack tip field (HRR field) were also attempted. Normalized load – displacement responses were computed for Compact Tension (CT) and small Disk Compact Tension (DCT) specimens, when a parametric power-law material response is assumed. The following consistent units were used: Force (N), length (mm), time (s), stress (N/mm^2 = MPa), strain (dimensionless, mm/mm). Materials were assumed to be isotropic. The following constants were adopted: elastic modulus E = 210000 MPa, Poisson's ratio $\nu = 0.3$, generally valid for metallic materials. Materials were considered to be elastic-plastic; the hardening curve followed a power law for a true stress – true plastic strain relation, as originally suggested by Ramberg and Osgood [224]:

$$\frac{\varepsilon}{\varepsilon_0} = \frac{\sigma}{\sigma_0} \qquad \varepsilon \le \varepsilon_0 ; \qquad \frac{\varepsilon}{\varepsilon_0} = \left(\frac{\sigma}{\sigma_0} \right)^n \qquad \varepsilon > \varepsilon_0 \tag{4.1}$$

where ε_0 and σ_0 define limits for the initial portion of the response.

Computations were attempted for a strongly hardening material (n = 5, characteristic of civil and marine structural steels), for a moderately hardening material (n = 10, characteristic of many pressure vessel and pipeline steels) and for a very low hardening material (n = 20), as in Fig. 4.4:

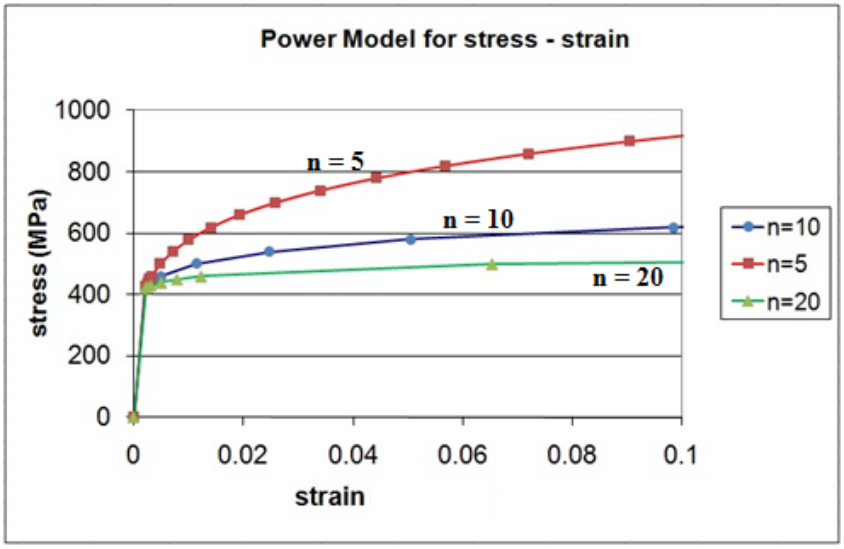

Fig. 4.4. Power model for stress - strain curves.

Starting from the eng. stress / nominal strain results generally provided by a standard tensile test, it can be written:

$$\varepsilon_{true} = \ln(1+\varepsilon_{eng}), \quad \sigma_{true} = \sigma_{eng}(1+\varepsilon_{eng}), \quad \varepsilon_{true}^{pl} = \ln(1+\varepsilon_{eng}) - \frac{\sigma_{true}}{E} \qquad (4.2a, b, c)$$

in order to pass to true stress – true plastic strain values needed for the software. It gave $\varepsilon_{true}^{pl} = 0$, when $\sigma_{eng} = 420$ MPa ($\equiv \sigma_0$ = yield stress of the material simulated). Therefore, $E/\sigma_0 = 500$.

Single Edge Notched Bend ($a/W = 0.1$ and $a/W = 0.5$) and Compact Tension ($a/W = 0.6$) specimens were modelled from [163], together with the experimental Disk Compact Tension specimen [85] (here with aspect ratio $a/W = 0.335$ because not fatigue precracked) as a contribution to the aim of this project. The relevant Standard for experiments is ASTM E 1820 [153].

Meshing was refined in the crack tip zone in accordance with the benchmark [163] and in order to have the smallest elements coherent with the scale of the process to investigate. The specification (aspect ratio, finite elements) of the 3D models is provided in Table 4.2. Later in this project and when performing the original parte of this research, more

attention was given to the characteristic length values for the notch zone, as suggested in recent literature [225].

geometry	a/W	W/B	nodes	Elements	Elem. type	Smallest dist at crack tip
SENB	0.1	1	37230	34486	C3D8R and C3D6	84.55 μm ; bias 2, 20 elements ahead of the crack tip
	0.1	2	21654	19546		
	0.1	4	13888	12216		
	0.5	1	24274	22410		169.11 μm ; bias 2 , elements 20 ahead of the crack tip
	0.5	2	15269	13722		
	0.5	4	10476	9138		
CT	0.6	1	7676	6200	C3D8R and C3D6	253.10 μm ; bias 2, 20 elements ahead of the crack tip
	0.6	2	6587	5220		
	0.6	4	6253	4926		
DCT	0.335	1	19192	17604	C3D8R and C3D6	41.80 μm ; bias 2, 20 elements ahead of the crack tip
	0.335	2	8834	7818		
	0.335	4	6925	6082		

Table 4.2. Finite element models specification for benchmarking.

Bias is defined as the ratio of the size of the coarsest element to the size of the finest element along an edge. All models were subjected to sweep meshing technique: once a mesh is created on one side of the region, ABAQUS copies the nodes of that mesh, one element layer at a time, until the final side is reached. The nodes are copied along an edge

that is called "sweep path". One semicircular cell for the crack-tip zone (meant to have a biased and denser mesh) and one cell for the rest of the model were used in order to minimize the transition between the partitions. One quarter of the specimen was modelled each time, relying on symmetry of two planes.

The models were subjected to a stress by the means of a surface load or of the direct displacement of critical nodes in the mesh. The load conditions were then normalized to the actual *Javg* and to the deformation level (or remaining ligament length). Non-linear geometry conditions were allowed for the elastic-plastic computation in order to consider large strain analysis. The simulation was performed at the "static" level, that is to say the rate of loading did not introduce dynamic effects. The time unit was divided in an automatic manner and each step did not involve more than 0.05 of it; where necessary, a minimum step of 0.01 was requested.

The crack was modelled as a one-dimensional sharp crack (called crack tip) and its plane of advancement (called crack front) was along the midsection plane of the specimen in order to allow symmetry. Half specimen models were then used. It has to be noted that this assumption is generally not observed in the experimental reality. Details of the models are shown in the following Figs. 4.5 – 4.11 and Tables 4.3 – 4.5.

4.3.1 SENB specimen

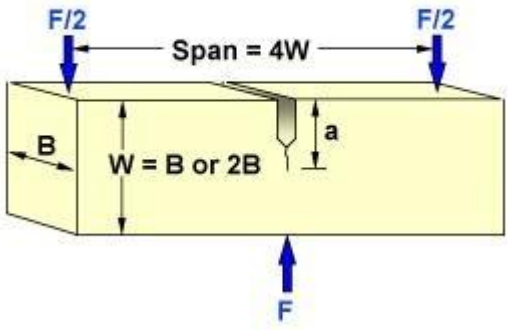

Fig. 4.5. SENB specimen.

F is the external load (N)

B is the thickness (mm)

W is the width (mm)

a is the nominal crack length (mm)

W – a is the ligament (mm)

a / W and W / B are called aspect ratios

Several aspect ratios are examined to account for different geometries, in particular:

	W / B (W= 50 mm)		
a / W			
0.1	1	2	4
0.5	1	2	4

Table 4.3. SENB geometries

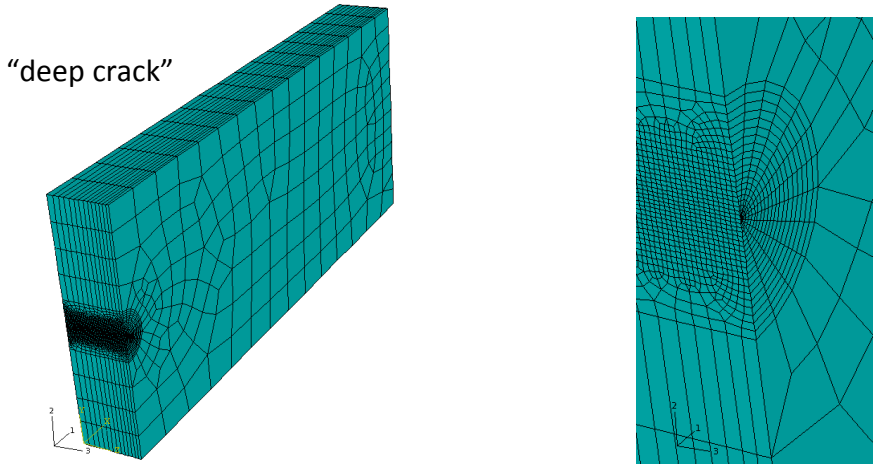

Fig. 4.6. One quarter model of SENB, a/W=0.5, W/B=2, with detail of the crack tip zone.

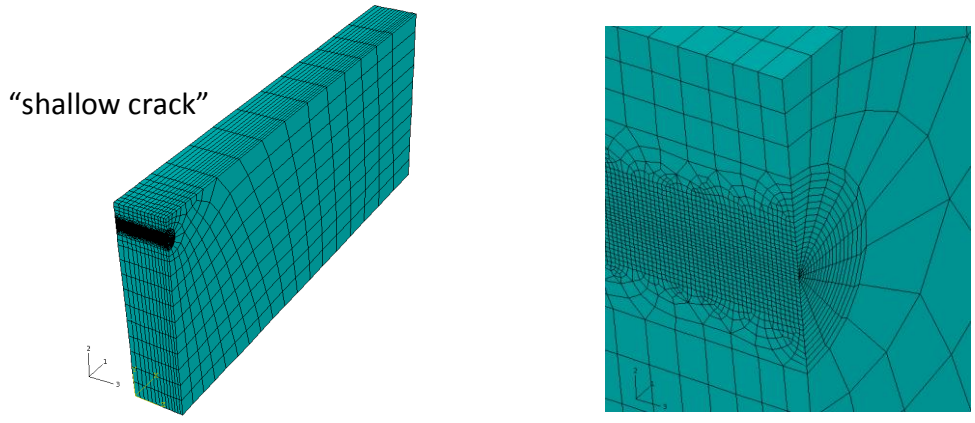

Fig. 4.7. One quarter model of SENB, a/W=0.1, W/B=2, with detail of the crack tip zone.

4.3.2 CT specimen

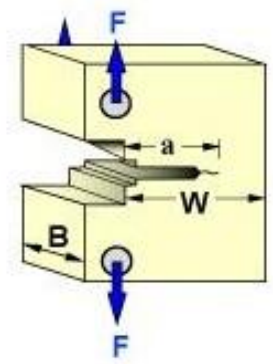

Fig. 4.8. CT specimen.

F is the external load (N)

B is the thickness (mm)

W is the width (mm)

a is the nominal crack length (mm)

W – a is the ligament (mm)

a / W and W / B are called aspect ratios

As done for SENB, several aspect ratios were examined to account for different geometries and plastic zones ahead of the crack tip:

	W / B (B = 12.5, 25, 50 mm)		
a / W			
0.6	1	2	4

Table 4.4. CT geometries

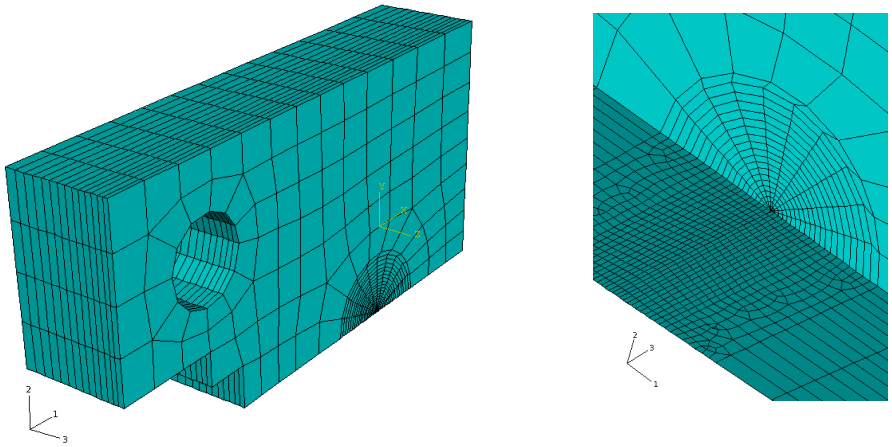

Fig. 4.9. One quarter model of CT, a/W=0.6, W/B=2, with detail of the crack tip zone.

4.3.3 DCT specimen

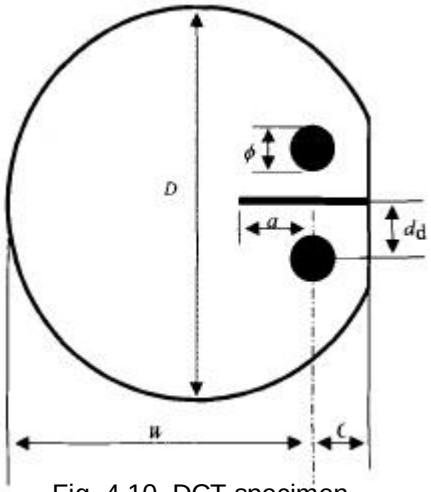

Fig. 4.10. DCT specimen.

The DCT specimen was modelled in accordance with the experimental paper of Snead [85], without fatigue pre-cracking.

The line load-displacement was monitored and the load applied as a pressure on surface.

The same as for SENB and CT, several aspect ratios were examined to account for different geometries and plastic zones ahead of the crack tip:

	W / B (W = 9.25 mm)		
a / W			
0.335	1	2	4

Table 4.5 – DCT geometries.

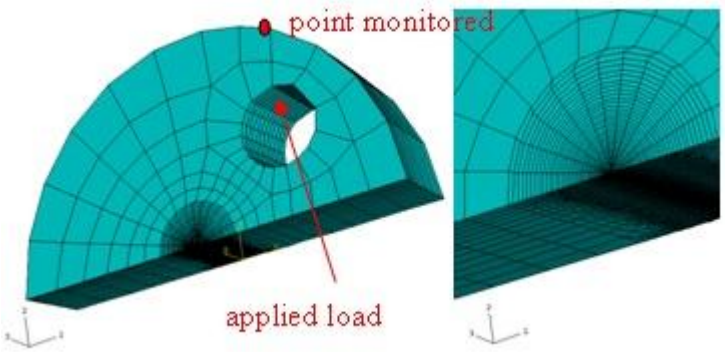

Fig. 4.11. One quarter models of DCT, a/W=0.335, W/B=2, with detail of the crack tip zone.

4.4 Fracture toughness modelling

Load vs. displacement plots from sharp-notched round bar tensile tests were validated numerically by fitting the experimental data up to the fracture initiation point. Fitting after that point would have required implementing one automatic fracture criterion into a looping procedure in order to remove elements. That was not relevant for the aim of this project. Non-linear effects of large deformations and displacements were considered. The Gurson-Tvergaard-Needleman model was used to describe the progression of damage for each "damaged" material obtained.

4.4.1 Sharp-notched round bar specimen

The sharp notch makes the full model not desirable because of the sensible difference between the relative dimensions of the specimen and the crack front. The half-specimen symmetry was exploited in the model. Its specification is shown in Table 4.6:

MODEL	NODES	ELEMENTS	TECHNIQUES
notched bar 45° (half a bar model)	983	920 CAX4R	structured meshing + minimize transition; free meshing + minimize transition at crack front

Table 4.6. Finite element model specification for sharp-notched specimen.

The half bar was actually used for validating results and inferring fracture toughness initiation. Half bar model employed axisymmetry plus symmetry to the crack front plane, as in Fig. 4.12.

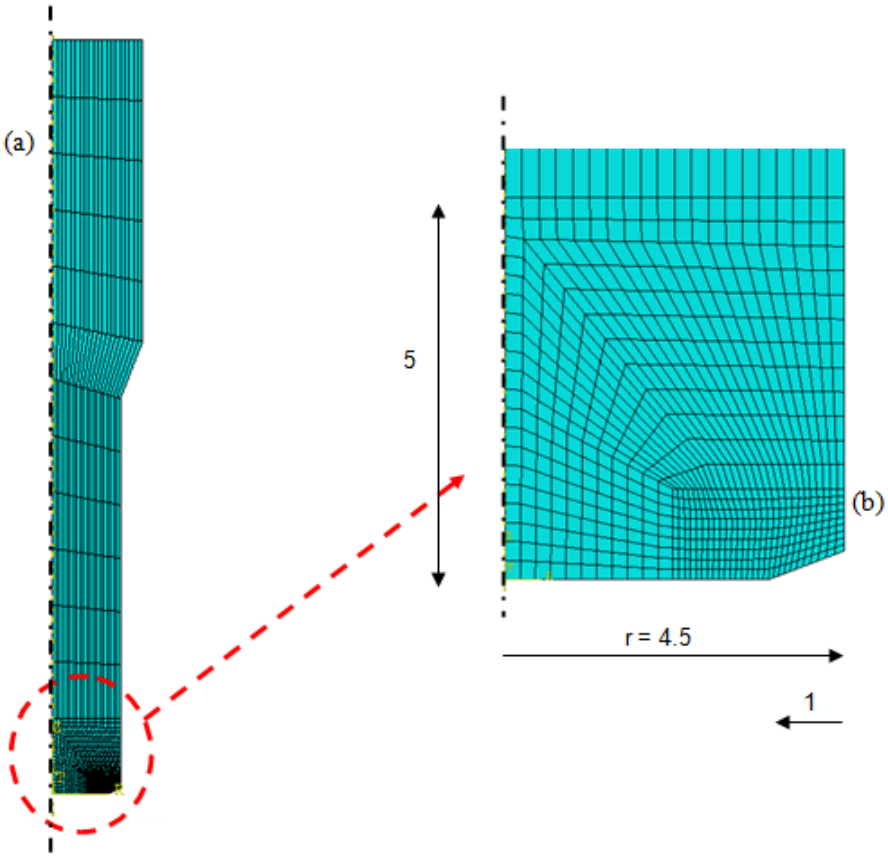

Fig. 4.12. Half notched bar 45° (a) and half gauge zone detail (b).

The crack front was made of regular elements each spaced 70 µm. It accounted for the characteristic length [226] of the microstructure, so that the localization of fields was not spuriously set by spatial discretization. Stress and strain gradients are very high at the crack tip; for a given applied displacement, the deformation computed for Gauss points (the internal locations where the element solves for strain and stress) close to the crack tip will be larger for fine meshes leading to early initiation [227]. This means that mesh size affects initiation of fracture. It also affects propagation: more mechanical work is dissipated by increasing the element height. In order to avoid both problems, mesh size at the crack front is calibrated upon a characteristic length associated with mean inclusions spacing in the material. This depends upon the internal stress state of the material. In the case of "undamaged" 316L, the distance between two inclusions may be in the order of 50–100-200 µm [223], which was assumed to be the class size of the elements to be modelled at crack front for propagation. Practitioners retrofit that on the experimental plots and choose the best fitting value.

More in depth, several researchers analyzed the influence of mesh density, notch size and notch depth on finite element solutions for axisymmetric problems involving strain localization and failure. Borvik [228] studied the uniaxial tensile behaviour of one unirradiated structural steel. He employed shallow notched specimens with different notch radius and mesh density. He suggested that elongation to failure is significantly increased when the mesh is too coarse in the gauge zone, while the peak force is unaffected by mesh density. This may conflict with similar findings related to characteristic length, as presented for example in [229]. Borvik's practical solution was to calibrate his model on experimental findings while keeping mesh density as refined as possible against computational efficiency. More accurately for the aim of this project, Wu [230] took into account sharp and semi-circular notches, both shallow and deep, for a 316L annealed steel before and after irradiation. He made use of the Gurson model for simulating damage progression and one of his specimens is very similar to the one depicted in Fig. 4.12, which was used in this project. The size of the mesh element in the gauge zone was equal to the grain size, in the same range used for this project. Other researchers [231] tried to develop non-local models for damage in order to avoid dealing with mesh size and characteristic length. That way, it could be possible to simulate large strain gradients, which is not possible by using local damage models.

4.4.2 Small DCT specimen

The Disk Compact Tension specimen, Fig. 4.13, was the same used in [85] apart of fatigue pre-cracking. It could be a 3D or 2D model and only one half was considered for symmetry reasons. This was employed for fracture toughness computation of both "undamaged" and "damaged" materials. The region ahead of the crack tip presented a regular array of elements of size equal to 80 μm. Load was applied as a displacement at the reference point of the rigid pin. Computations did not give any warning or error.

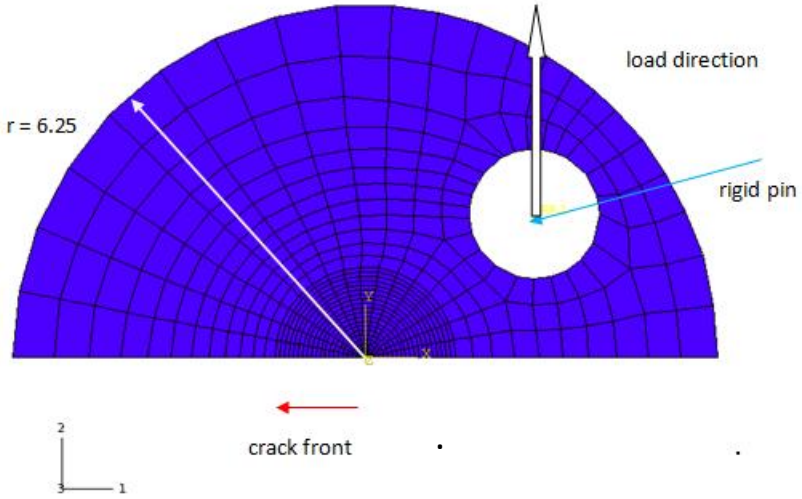

Fig. 4.13. Model from disk compact tension specimen.

The elements and size making the models are described in the following Table 4.7:

MODEL	NODES	ELEMENTS	TECHNIQUES
DCT	245 + 341 crack zone + rigid pin hole	203 CPE4R + 320 CPE4R crack zone + rigid pin hole	Free and sweep meshing + minimize transition for crack zone

Table 4.7. finite elements model specification for disk specimen

It has to be remarked that the *J*-integral varies along thickness of Compact Tension specimens [163], so 2D models (which imply constant *J* along all the thickness) may not be suited to this project. Nevertheless, it was showed that the maximum value of *J* for the Disk Compact Tension specimen employed here was always located at the midsection. As a consequence, fracture initiation happened at midsection and the use of 2D models could be justified for computational simplicity. In addition, the thickness of the DCT specimens tested from "damaged" material was going to be a factor for stating plane strain, plane stress or intermediate condition. The first was preferred because it leads to a fracture toughness initiation value K_{IC} that is assumed to be a material property in the Standards. Nevertheless, only one thickness, taken from the experimental work of Snead [85] here acting as a benchmark, was adopted. It was then discussed against the experimental findings (generally not plane strain) for every "damaged" state employed.

4.5 Correlation with helium effect on fracture toughness

It was important to establish if the fracture toughness decrement obtained by using conventional techniques might be correlatable to the decrement due to irradiation hardening and helium embrittlement, as reported in the literature by Snead [85] and Little [15]. One problem was the reproducibility of the macroscopic effect, one other was the opportunity to state that a correlation exists, given the differences in the mechanisms of the processes involved. In the practice, it was required to identify and formulate a coherent decreasing trend, if possible.

It was also required to investigate the suitability of the Gurson-Tvergaard-Needleman model for simulating the damage progression. One question concerned the mechanical process involved into its cell model (spherical void growing without changing its shape), very effective for high triaxiality specimens made of ductile material but probably not so effective for irradiated / hardened materials behaving in a brittle-like manner. It was also considered that helium bubbles tend to manifest their detrimental effect migrating to grain boundaries and coalescing there, a process not intercepted by the GTN model.

That said, the comparison was performed in a very simple manner. One benchmark from Snead [85] was superimposed to the results obtained in this project. A short discussion followed about the relevance to the practice in the nuclear field.

5. Experimental results

5.1 Material

The material for this project was 316L in the form of round bars, 14 mm and 28 mm diameter. One sample was sent to Bodycote Testing Ltd for evaluation of the chemical composition, getting the following result in Table 5.1:

C	Si	Mn	P	Cr	Mo	Ni	Cu	S	N	Co
0.018	0.35	1.39	0.029	16.80	2.10	10.40	0.31	0.026	0.064	0.110

Table 5.1. Measured composition of the “as received” material

Hardness measurements were made on one metallographic sample. The material was 245-297HV0.5, with single values of 245 (average diagonal length = 61.55 μm), 261 (av = 59.58 μm) and 297 (av = 55.81 μm). The Vickers Number (HV) was determined by the ratio of the force applied to the diamond and the surface area of the resulting indentation. The nomogram from the BS EN ISO 6507 gave the same result. Empirical relationships enabling the estimation of yield strength from hardness measurements, described by Was [198], were not considered at this stage. Literature, for example Tsubota [232], reports that the values obtained may be linked to the effect of some cold working, say about 20%, probably due to cold drawing of the bar.

5.1.1 Microstructure

The main features to be analyzed from metallography were grain size, twins (both mechanical and annealing) and inclusions. Figs. 5.1 and 5.2 show the XY plane and the XZ plane (longitudinal direction).

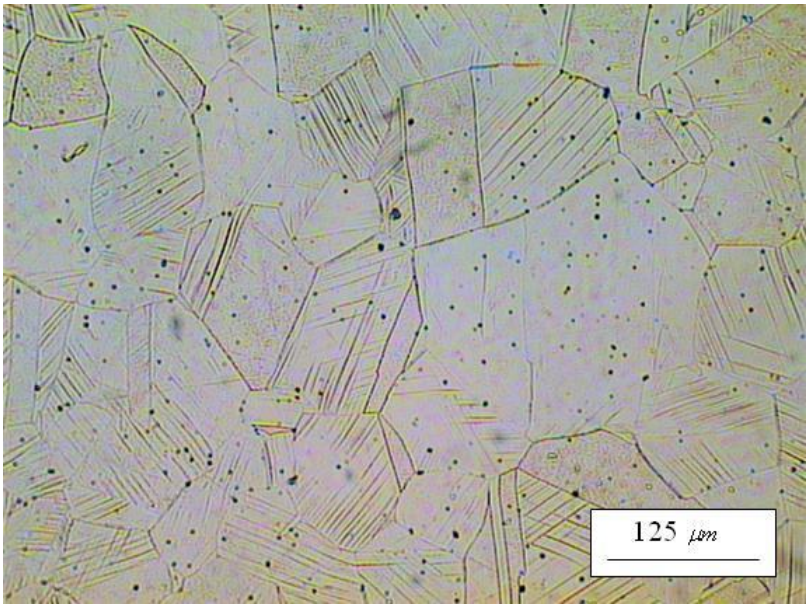

Fig. 5.1. Microstructure of the “as received” material, XY section.

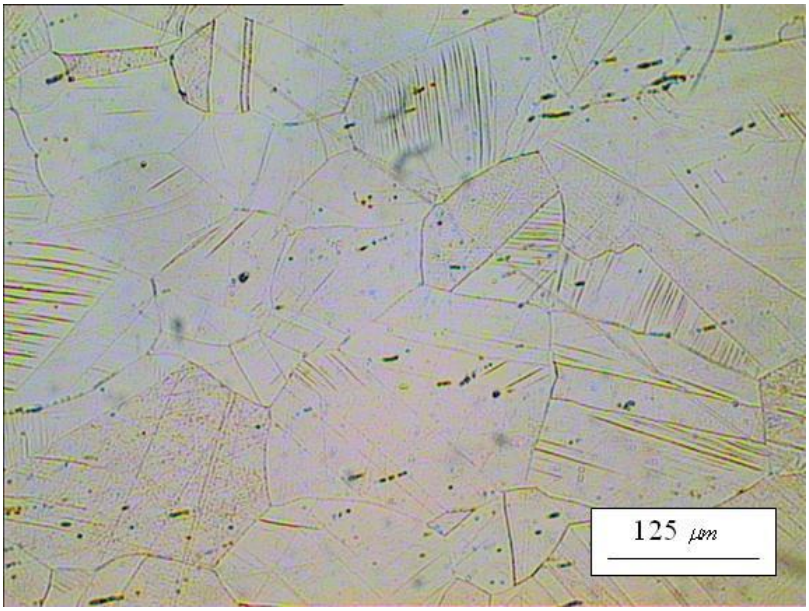

Fig. 5.2. Microstructure of the “as received” material, XZ section (longitudinal direction).

Parallel lines inside some of the grains in Fig. 5.1 and Fig. 5.2 support evidence of intense slip. These figures also show the presence of twins. They can be mechanical (arising from sheared crystal planes, introduced by deformation process) or annealing (developing after recrystallization due to atomic readjustment reactions).

Dark spots in Fig. 5.1 could be zero dimensional end-grain I pits, while the black strings in Fig. 5.2 should be their correspondent lines (1D feature) along the Z direction, as in Fig. 5.3. These are one effect of the etching procedure: oxalic acid highlights the grain boundaries, but also ferrite stringers in the material.

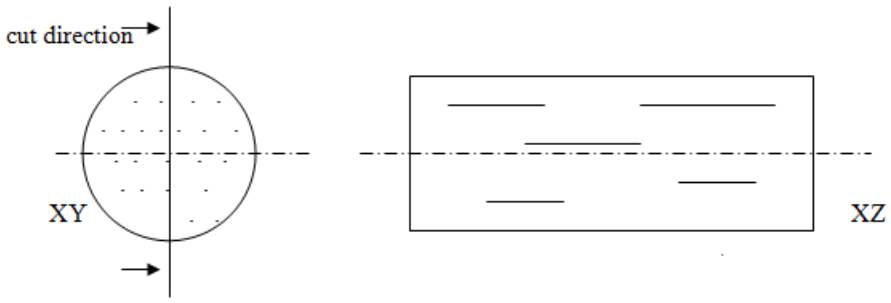

Fig. 5.3. Dark spots and strings in the different directions of the as received material.

Grain size is linked to deformability: higher the number of grains in a given volume, higher the number of obstacles to dislocations in the plastic deformation process. Grain size measurements, as number of grains per unit length and number of grain boundaries per unit length, were attempted in accordance with the proper Standard [201] on both "as received" and the "undamaged" material. For the "as received" material, solution annealed at 1050 °C for 4 hours according to the vendor, a grain size 83 μm ± 9 μm was found. The relevant Standard [204] suggests for cold worked AISI 316L a grain size of 100 μm or less. For the "undamaged" (solution annealed at 1050 °C for 30 minutes followed by water quenching) material, grain size was found to be in the class 65-70 μm. The difference was explained in terms of different solution annealing times.

5.1.2 Mechanical testing

One solution annealing treatment was then performed on the "as received" material for 30 min at 1050 °C followed by rapid quenching in water and leading to "undamaged" state. It was followed by metallography on both "as received" and "undamaged" states. The material was then tested for tensile properties. The relevant values are the tensile

strength and the yield strength on the strength side, the percent elongation and the reduction of area on the ductility side. Plots are shown in Figs. 5.4 – 5.5.

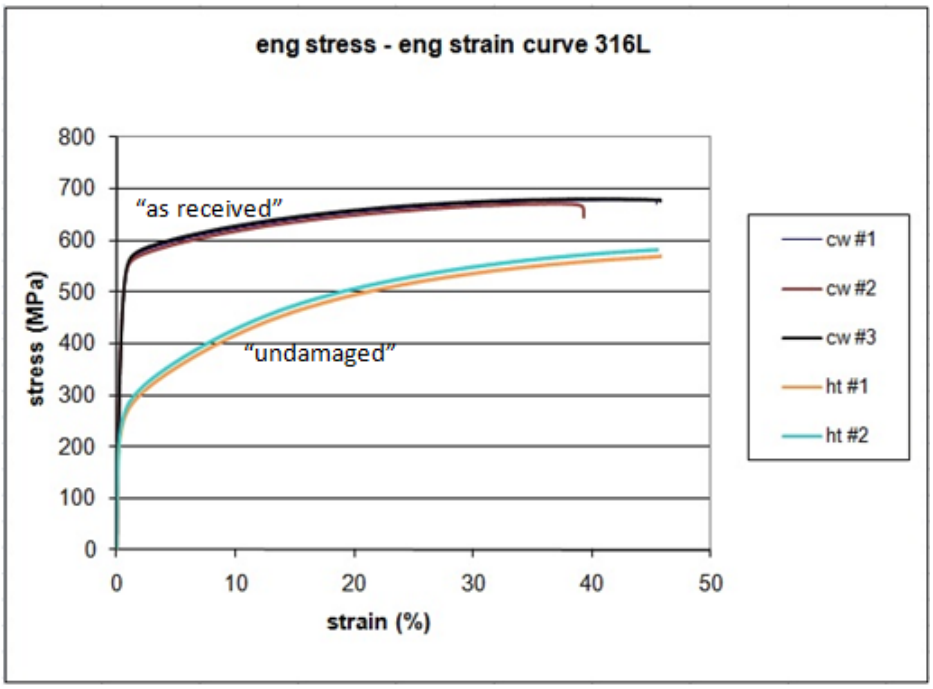

Fig. 5.4. Stress vs. strain plot for "as received" and "undamaged" 316L.

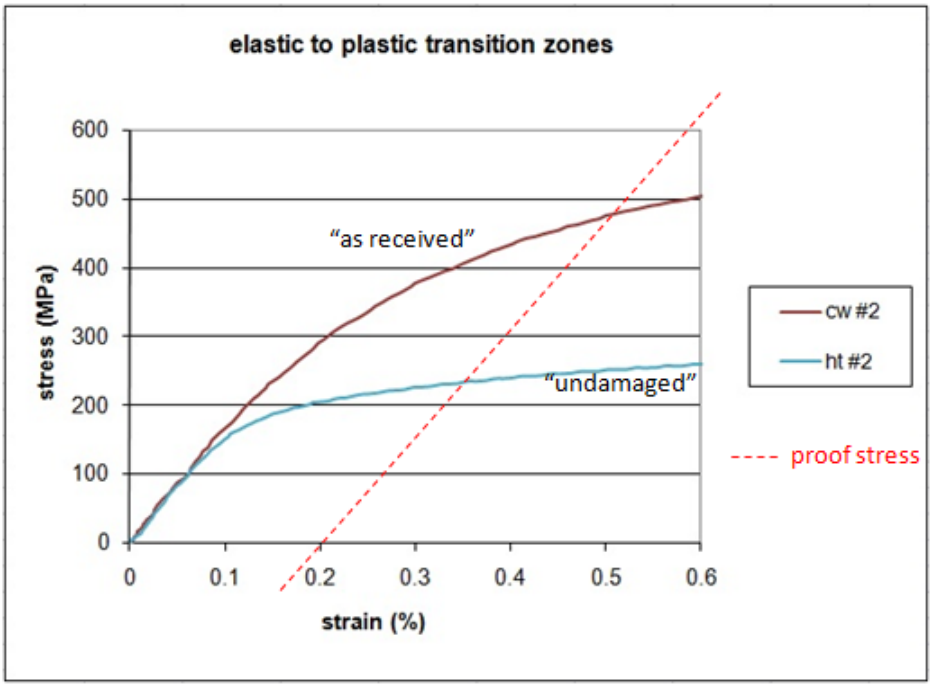

Fig. 5.5. Elastic to plastic transition zones for "as received" and "undamaged" 316L.

Tensile strength was about 680 MPa for the "as received" and slightly below 600 MPa for the "undamaged". Proof stress was 475 MPa and 230 MPa respectively. Elongation should be formally registered from 2-inch diameter specimens. Just considering the ones used here, 6 mm diameter, it was about 65% for the "as received" and about 85% for the "undamaged", as measured in relation to the initial parallel length. Area reduction was 25% for the "as received" material and about 40% at the necking zone. Area reduction is a better indicator of ductility because it is measured at the minimum diameter of the neck. Elongation, on the contrary, is not uniform over the gauge length and is greater at the neck.

Load vs. diameter reduction curves from tensile test of notched specimens, used to get parameters for the Gurson model into ABAQUS, are shown in Figs. 5.6 and 5.7:

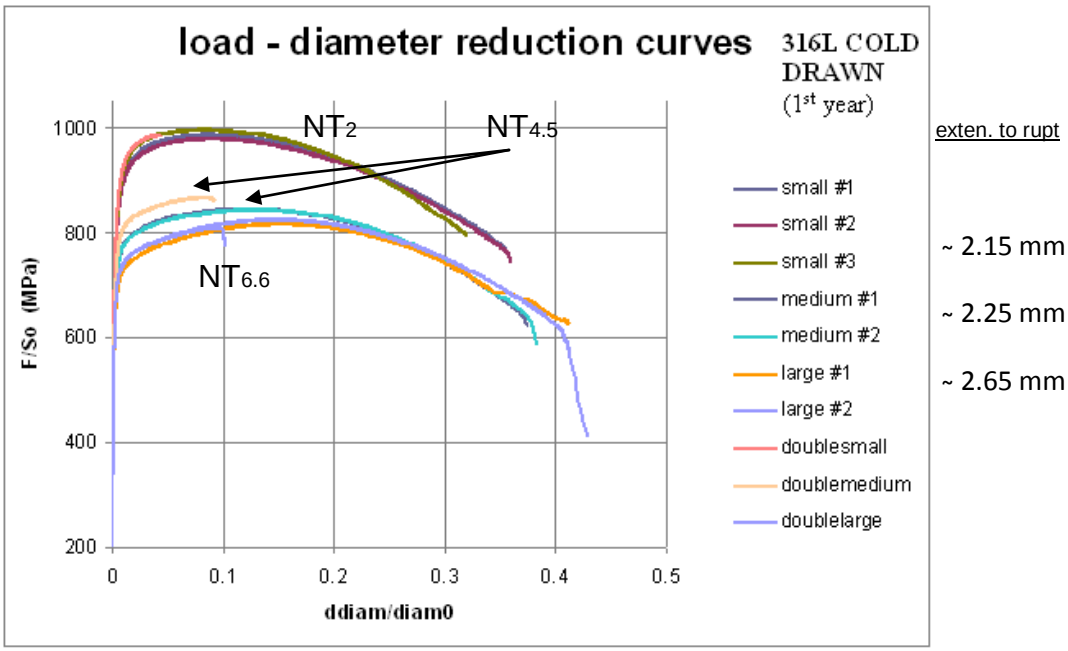

Fig. 5.6. Load vs. diameter reduction curves for "as received" material.

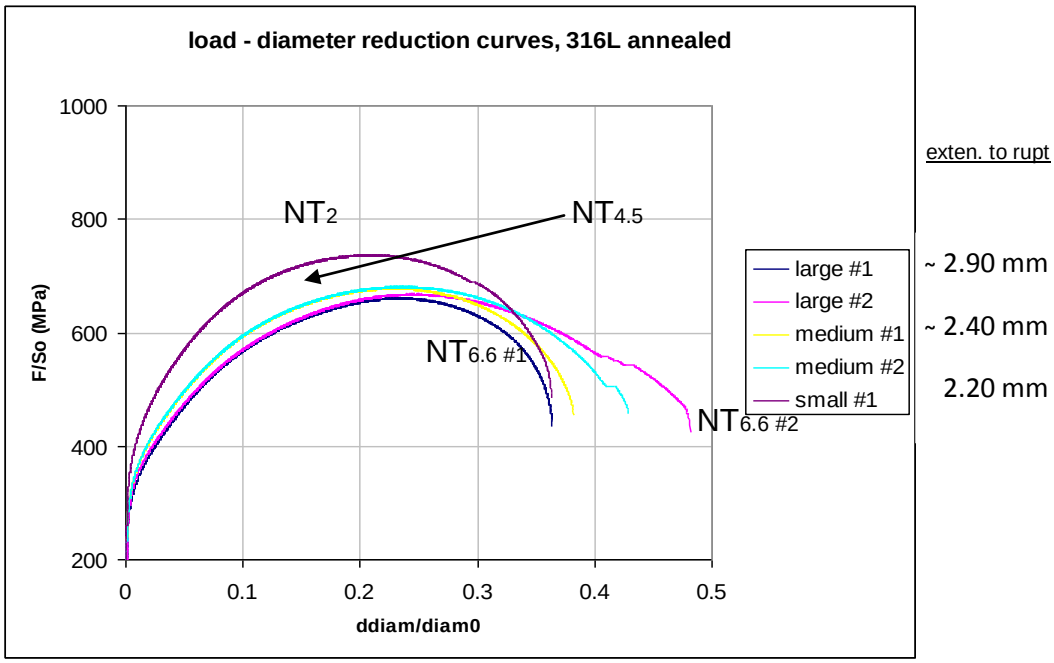

Fig. 5.7. Load vs. diameter reduction curves for "undamaged" material.

It has to be noted that the "medium" ($NT_{4.583}$) and the "large" ($NT_{6.6}$) specimens did not exhibit a greatly different behaviour, especially in the solution annealed condition.

5.1.3 Fractography of notched tensile surfaces

The relevant features of the fractured specimens are presented in the following Figs. 5.8 - 5.11. The most important features in Fig. 5.8 are the grown voids typical of ductile fracture. They are highly directional, in accordance with the tensile loading direction. Three coalesced couples of voids have been labelled C1, C2, C3.

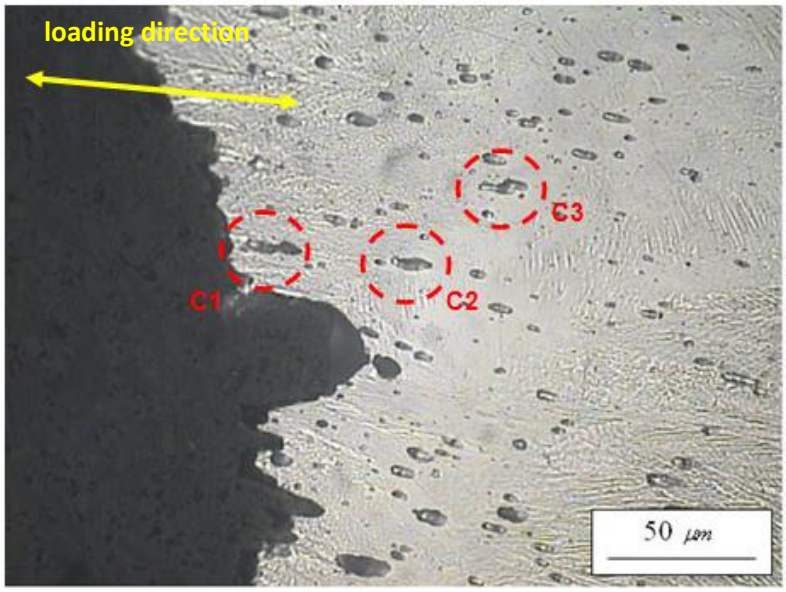

Fig. 5.8. Microvoids detail from “as received” material, NT “large” specimen.

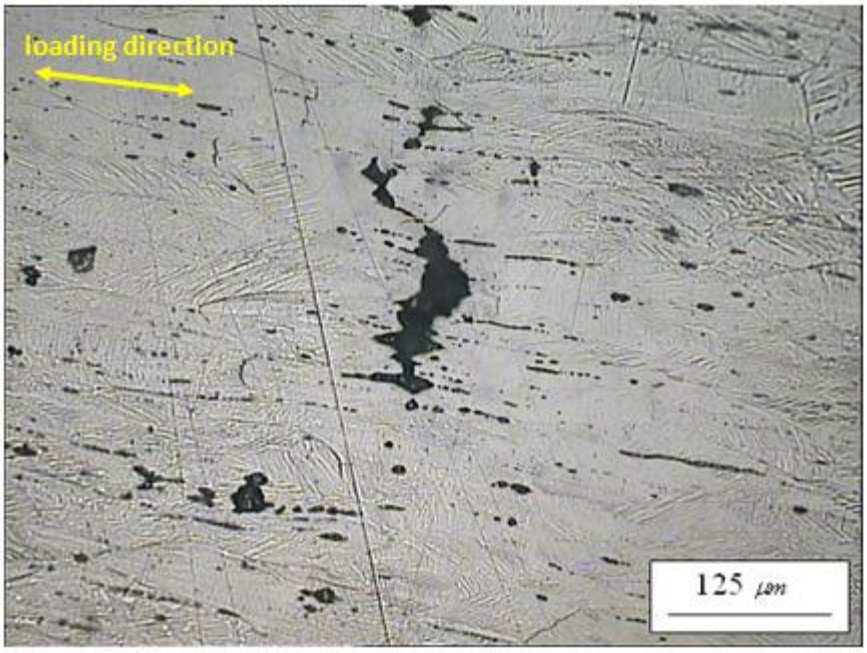

Fig. 5.9. Voids detail from “as received” material, NT “small” specimen.

Fig. 5.9, from one specimen with a "small" notch, shows a large coalesced feature. Fig. 5.10 shows the cup and cone feature, typical of ductile fracture. They can also be seen three long shear lines, labelled A1, A2, A3; their origin could be due to the sudden release of potential energy immediately following the fracture process, leading to shear along preferential directions. Fig. 5.11 shows dimples. Inclusions can also be seen and one coalesced zone.

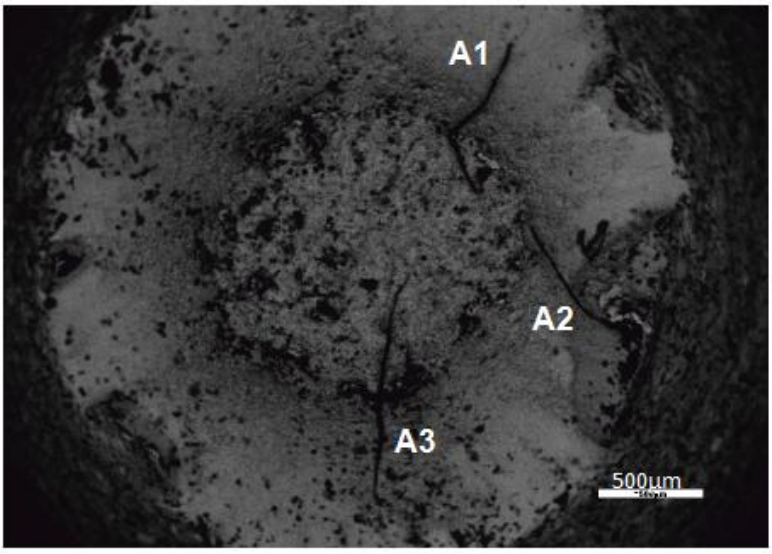

Fig. 5.10. Fracture surface from "as received" material after tensile test.

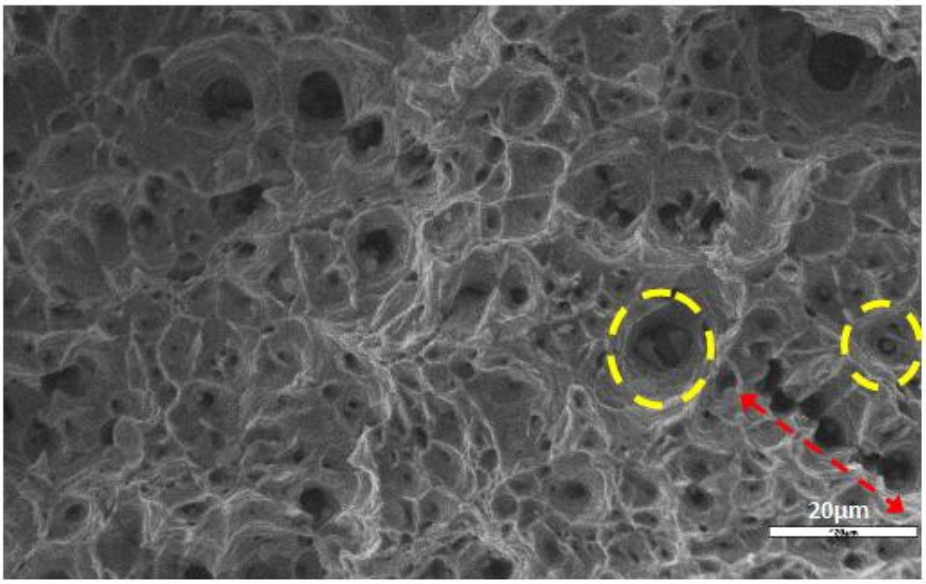

Fig. 5.11. Ductile fracture features after tensile test, NT "large" specimen.

5.2 Introducing damage into the material

5.2.1 Interrupted uniaxial tensile testing

"Undamaged" 316L was tested in accordance with the procedure described in Section 3.2. The engineering stress vs. engineering strain plots are shown in Fig. 5.12.

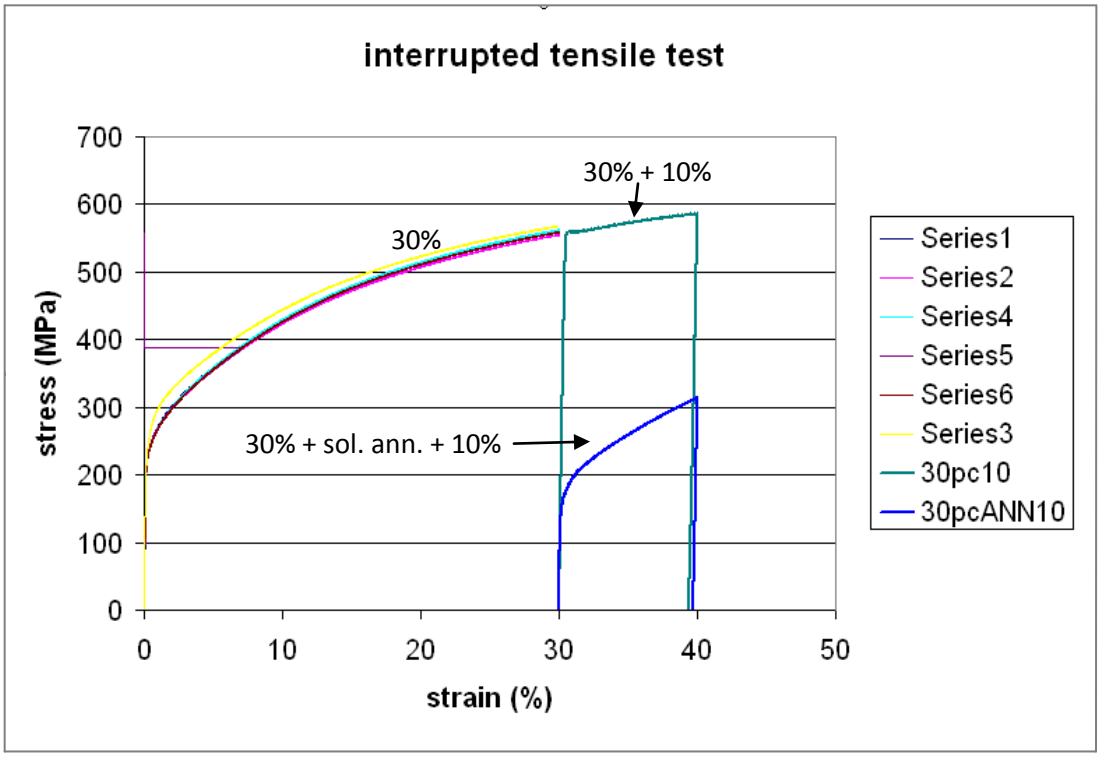

Fig. 5.12. Interrupted tensile test on "undamaged" 316L.

It can be seen the unloading – reloading behaviour associated with the 30 % + sol. ann. 10% and 30% + 10% specimens. The true plastic strain values corresponding to 30% engineering strain and 30% + 10% engineering strain are, namely, 25.89% and 33.28%.

Datsko [233] suggested that when re-testing specimens after unloading, they reach the same ultimate strength of the original specimen, fracture at the same final load level and exhibit a deformation that is equal to the one of the original specimen minus the deformation subtracted by reporting to zero (that is considering the re-tested specimen as virgin). Yield stress increases in accordance with the increment of cold work.

5.2.1.1 Metallography of interrupted uniaxial tensile test specimens

Evidence of inclusion particles still in the original location is given in Fig. 5.13 for 30% + sol. anneal. + 10% eng. strain. Particles are marked as A, B, C. It was not possible to perform an X-ray spectroscopy and confirm their nature. Nucleation by decohesion of inclusion particles from the matrix was suggested. It appeared very complicated to analyze numerically the onset, the growth and the relative dimensions of the voids. At this aim, it would have been necessary to locate some inclusions in the "undamaged" material and then follow their decohesion, for example performing one microtensile test of some small dogbone specimens inside one scanning electron microscope chamber. That was out of reach and deemed to be not decisive for this project. On the contrary, no noticeable evidence of voids was found in 40% eng. strain specimens, as shown in Fig. 5.14. In retrospect, this could raise a doubt about the origin of the inclusions in Fig. 5.13, maybe linked to the etching procedure

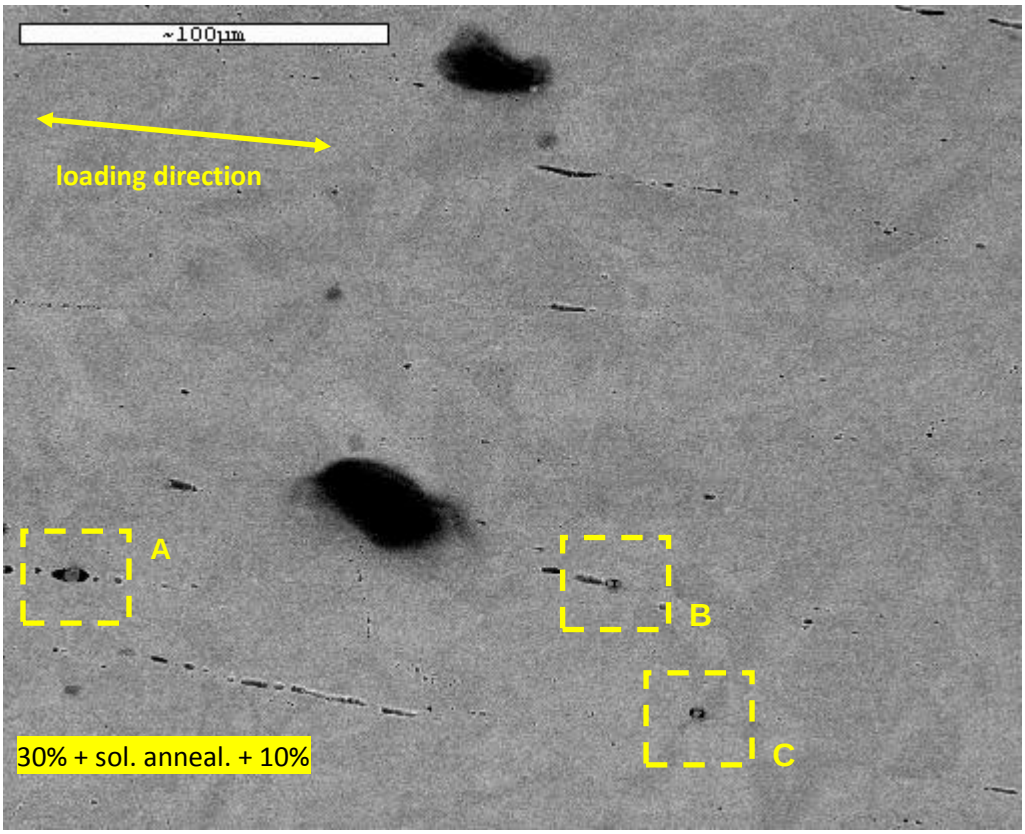

Fig. 5.13. 30% + sol. anneal. + 10% engineering strain metallography, detail.

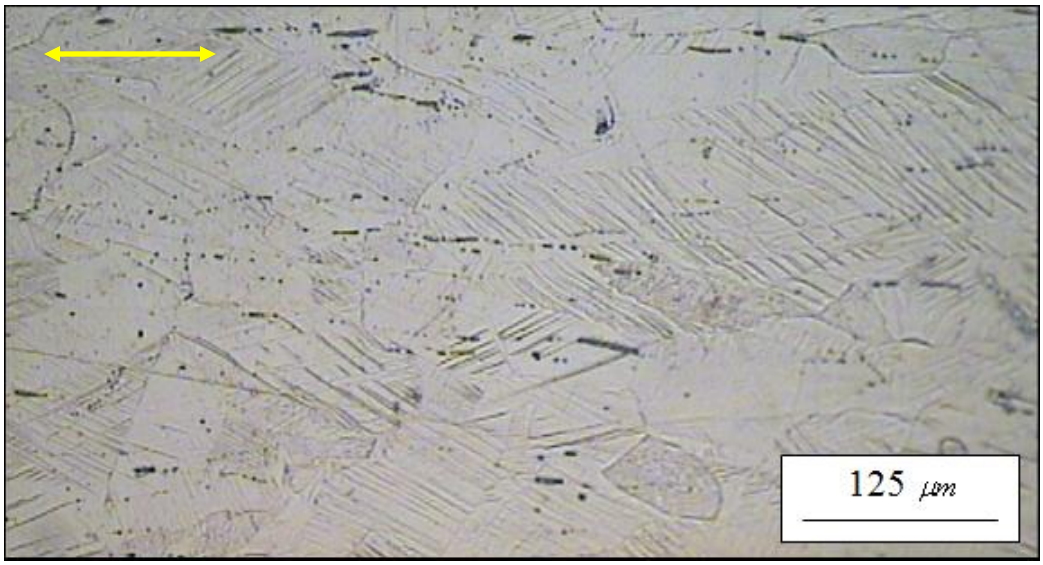

Fig. 5.14. 30% + 10% eng. strain metallography

5.2.2 Creep testing at 650 °C

T = 650 °C was selected to induce transgranular or intergranular creep in the material, as for the deformation mechanism map in Fig. 2.14. In order to choose the appropriate level of stress, the variation of the yield stress in 316L with temperature was worked out from literature data. Results are summarised in Fig. 5.15:

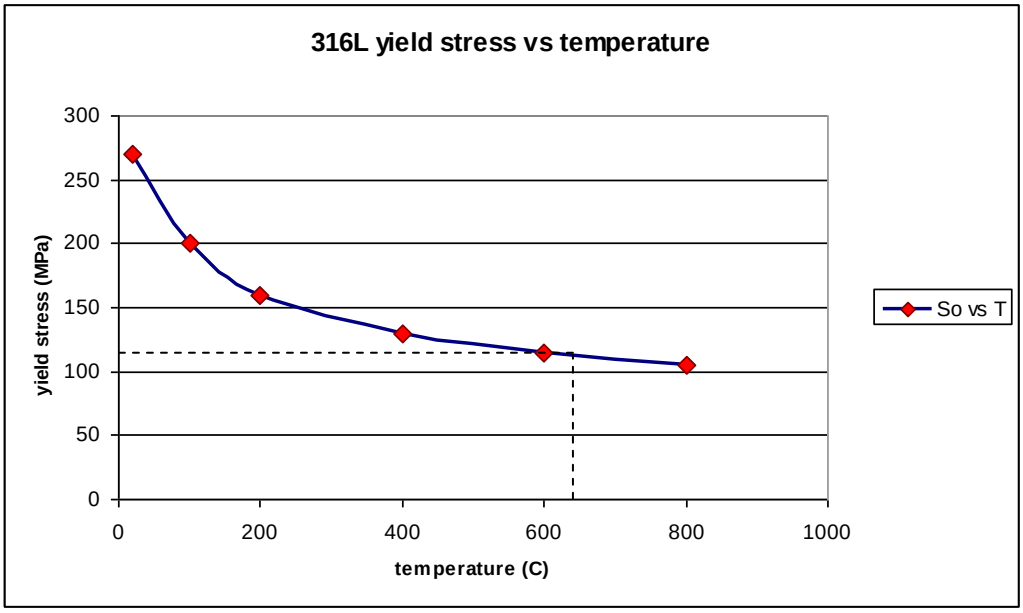

Fig. 5.15. Yield stress variation of 316L with temperature.

The yield stress at T = 650 °C appeared to be about 115 MPa.

One constraint during this project was time. It was deemed to be important that each study would not last more than about 1000 hours. It was also deemed to be interesting to explore the suitability of that timescale for the production of voids, paying attention to the deformation mechanism map. Literature had to be investigated again for stress vs. time to rupture at 650 °C. Data mining [58-61] and interpolation led to the plot in Fig. 5.16.

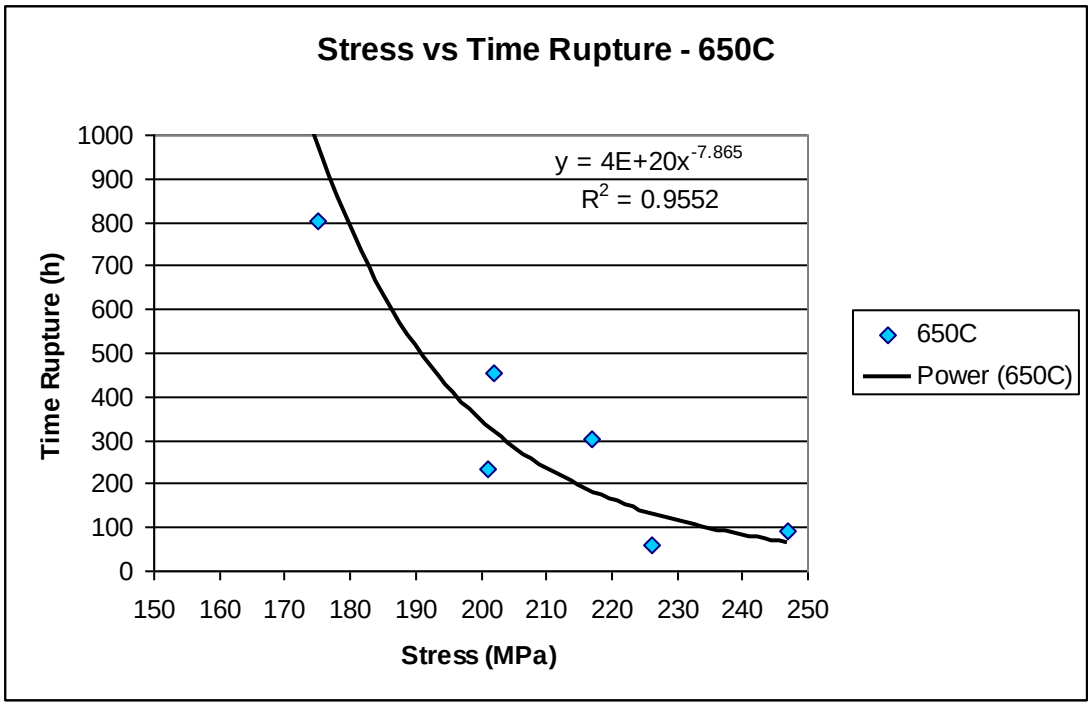

Fig. 5.16. Creep time rupture vs. stress for 316L at 650 °C.

It can be seen that 175 MPa was the stress expected to cause rupture in 1000 hours. At that stage, it was deemed to not be important to improve the estimation but start with the experiment. That level of stress was well above the yield stress established in Fig. 5.15 and, as that, invalidated the definition of creep. The athermal component of the stress was then expected to contribute to the creep deformation in the form of plastic deformation [234]. On the other hand, the deformation mechanism map in Fig. 2.14 still indicated intergranluar creep fracture mechanism.

Two studies of two tests each were performed at 650 °C. The stress imposed was well above the yield stress at that temperature in both cases, being 148 MPa and 180 MPa respectively.

The first study took about 1500 hours and aimed at calibration. The second study lasted 70-150 hours and was used for comparison purpose. Results are presented in the form of elongation (%) vs. time (hr) in Fig. 5.17:

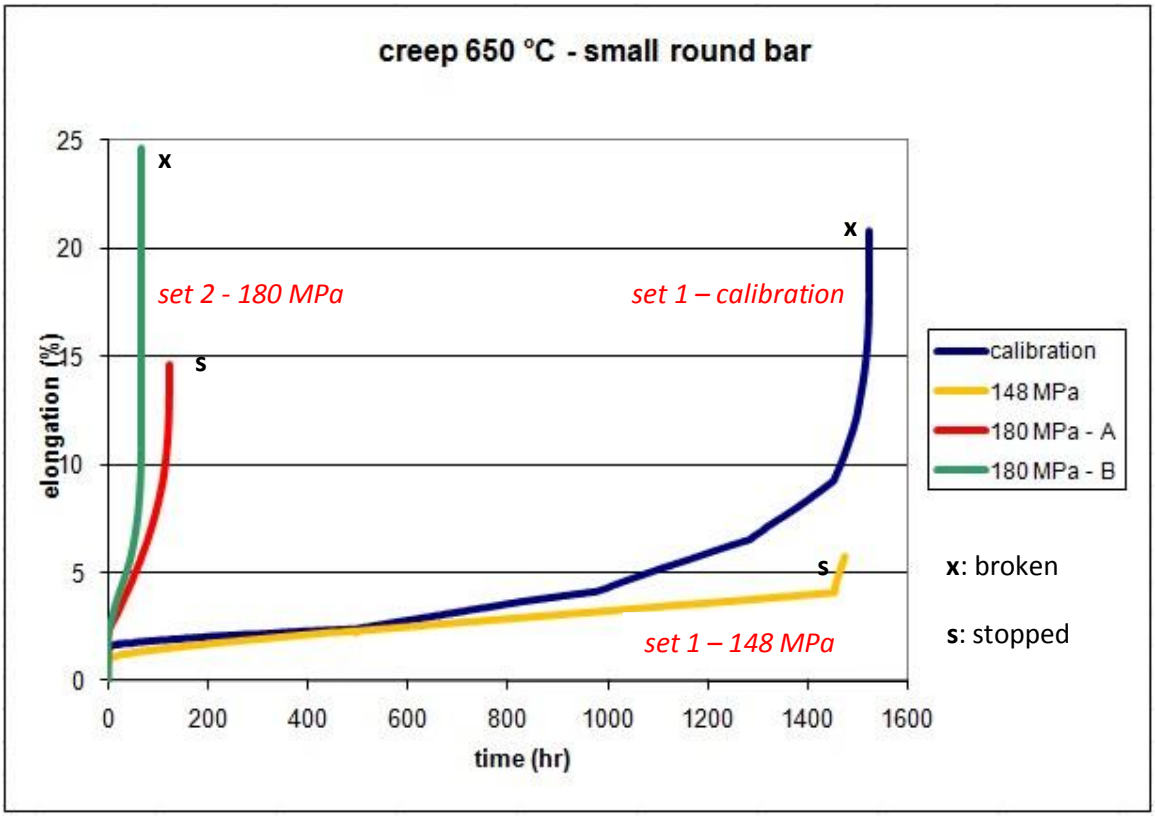

Fig. 5.17. Creep at 650 °C, elongation (%) vs. time (hr).

From the set 1 – calibration plot, the transition from secondary to tertiary stage of creep can be noticed. The stress acting on that specimen was raised in a constant manner. The other test from set 1 was kept at constant 148 MPa stress level and stopped soon after the calibration specimen failure.

The set 2 tests were both made at 180 MPa stress level. One went to failure after about 70 hours, the other was stopped after 150 hours at the onset of the tertiary stage.

5.2.2.1 Metallography of creep test specimens at 650 °C

Metallography along the midsection of the 70 hours broken specimen gave evidence of elongated grains, together with partial sensitization. Fig. 5.18(a)–(b) show these features as observed in the microscope. No evidence of useful damage into the matrix was found.

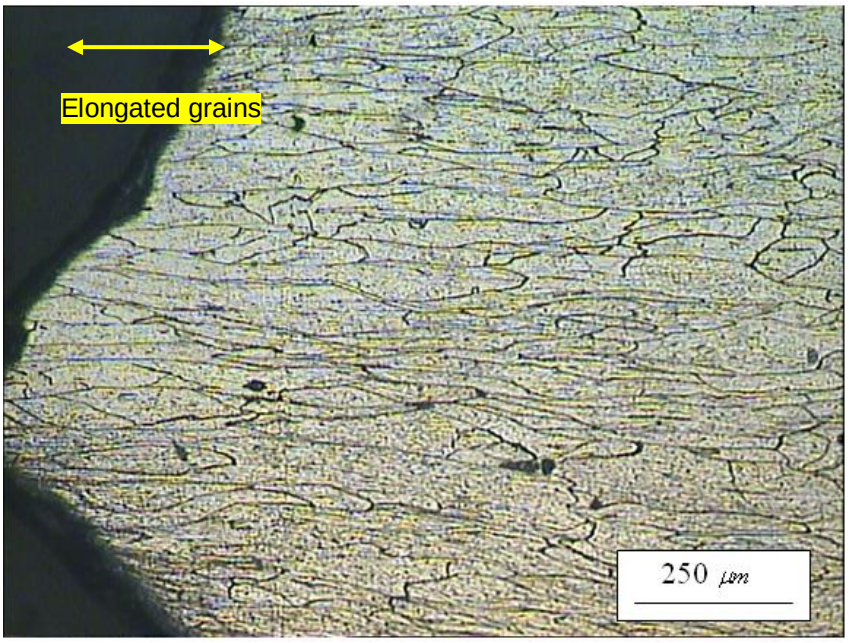

(a)

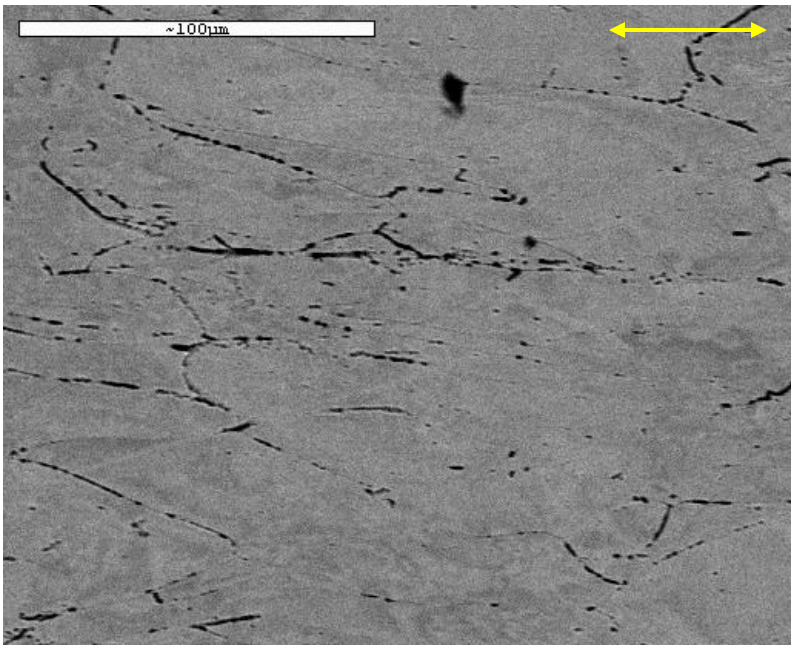

(b)

Fig. 5.18. Elongated grains (a) and partial sensitization (b) in the 70 hr broken specimen.

Metallography in Fig. 5.19, taken along the elongated zone of the 150 hr specimen, shows sensitization and no evidence of useful damage into the matrix.

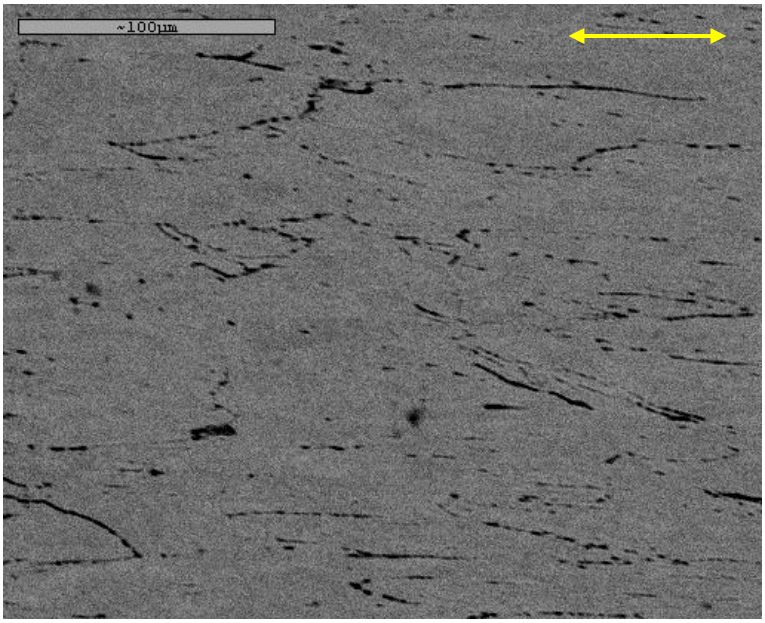

Fig. 5.19. Partial sensitization in the 150 hr specimen.

The specimen tested at 148 MPa stress and stopped at 4% strain after 1500 hours presented evidence of fully developed sensitization at the grain boundaries, Fig. 5.20(a), together with aging effect in the matrix, probably from deposition, in Fig. 5.20(b).

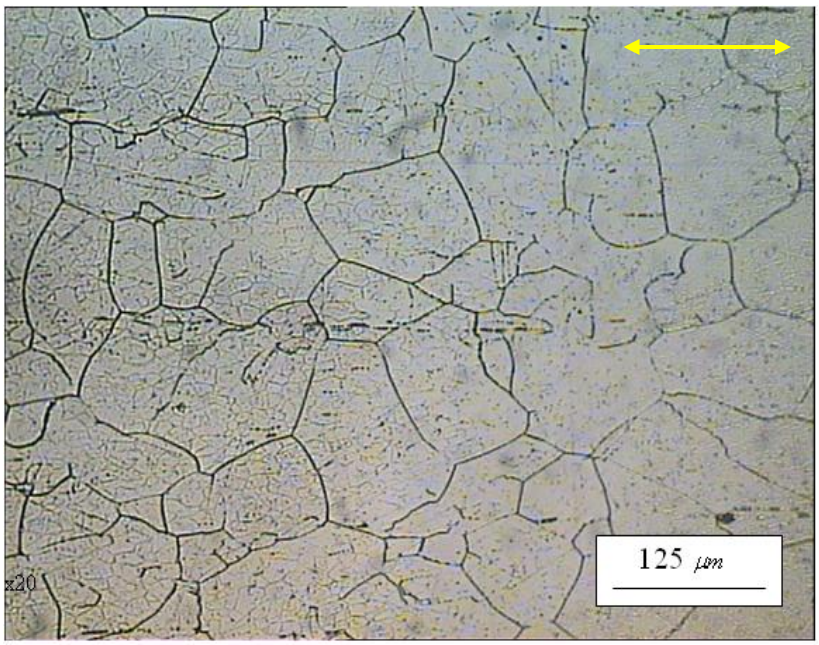

(a)

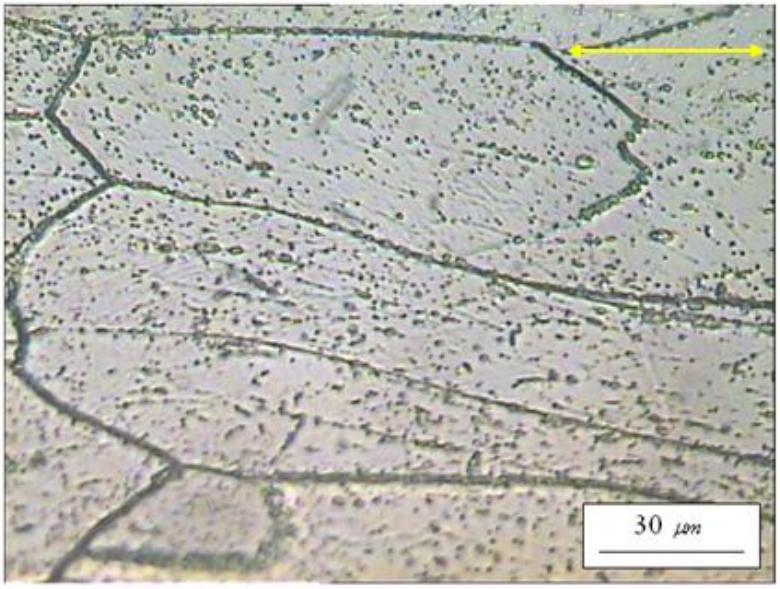

(b)

Fig. 5.20. Full sensitization (a) and aging effect in the matrix (b) of the 1500 hr broken specimen.

Fractography from the two sets of specimens (70–150 hours and 1500 hours creep time) was performed by scanning electron microscopy. The specimen tested at 180 MPa and broken after 70 hours exhibited a cup-cone fracture surface, characteristic of ductile fracture, together with dimples.

It is reported in the literature [235-237] that sensitization leads to some fracture toughness decrease. That way was not followed in this work because a different approach in the modelling of damage was needed, along the path suggested for example in [238-239]. In these works, intergranular stress corrosion cracking is approached by using a three-dimensional polycrystalline model that takes into consideration grain size, shape, crystal orientation and grain boundary structure. The cracks are assumed to grow along the grain boundaries and cohesive elements are used between the grains. It could have been an interesting way in terms of correlation with the mechanism of helium embrittlement. In facts, one recent comparative study from Morgan [240] states: "It appears that carbides in the microstructure affect the fracture mode in a similar manner as the decay helium bubbles but on a different scale". In retrospect, even without the comfort of numerical validation, performing fracture toughness experiments on the differently sensitized material at 650 °C would have added something to this project.

5.2.3 Creep testing at 1000 °C

Two specimens were used, one subjected to stress 0.24 MPa and the other to stress 0.40 MPa. The elongation (%) vs. time (hr) plot follows in Fig. 5.21.

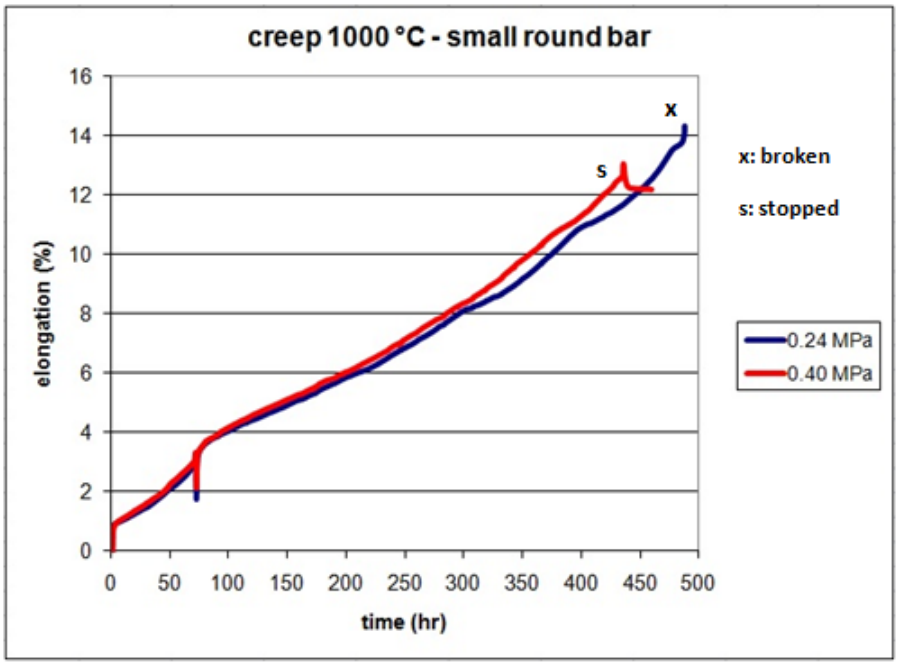

Fig. 5.21. Creep at 1000 °C, elongation (%) vs. time (hr).

Failure happened in the specimen at the upper edge of the parallel length. The original diameter was 4 mm; after creep, the measured diameter was about 3 mm. The zone subject to necking went in a regular progression to 2 mm before failure.

The specimen showed signs of oxidation due to the air atmosphere. It is thought that this is likely to have reduced the time to failure by contributing to reduce the area of the specimen during the experiment.

One study describing the oxidation effects on a similar stainless steel was found from Guillamet [241]. For the aim of this project, however, oxidation was not relevant because voids from grain boundary sliding were eventually produced.

5.2.3.1 Metallography of creep test specimens at 1000 °C

Both specimens tested at 1000 °C exhibited some voids from grain boundary sliding as follows from microscope evidence in Figs. 5.22 – 5.23. Quantification of that porosity was performed by tomographic analysis.

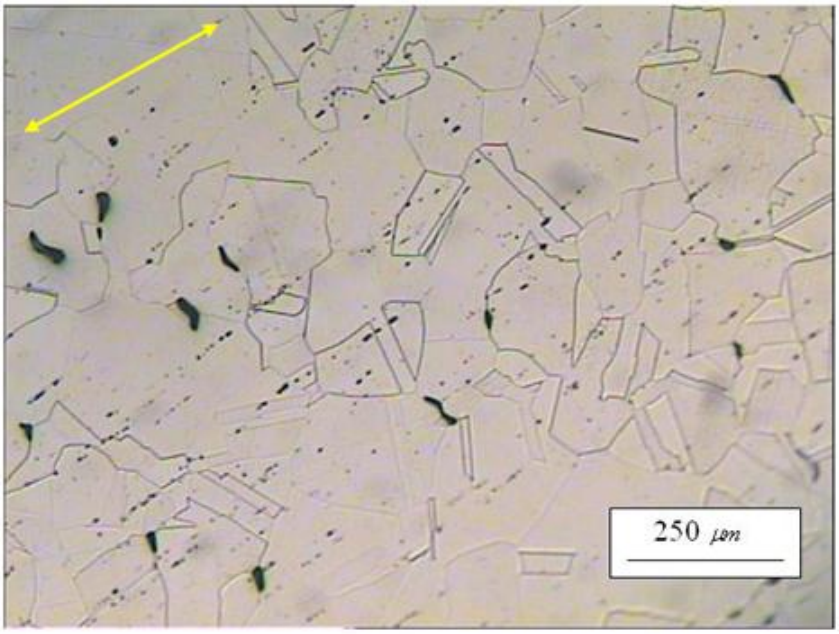

Fig. 5.22. Grain boundary sliding voids from spec #1, creep 1000 °C.

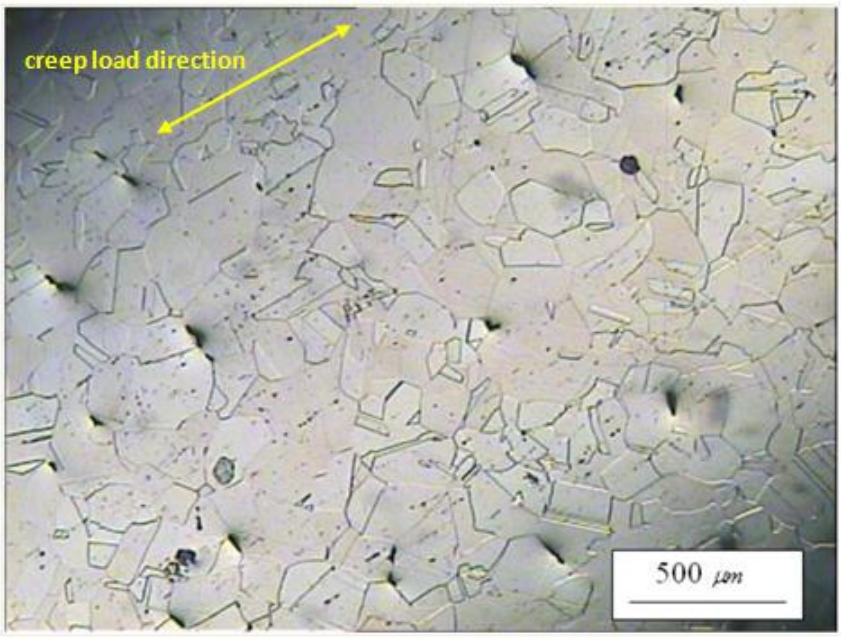

Fig. 5.23. Grain boundary sliding voids from spec #2, creep 1000 °C.

5.2.4 Creep testing at 1000 °C using larger specimens

Having got voids from small specimens at 1000 °C, it was necessary to repeat the experiment using larger specimens, so that "damaged" material for fracture toughness evaluation could be obtained. It was also considered useful for confirming the presence of voids (that is to say to make sure it was not dependent on the size of the specimen) and for weighing the effect of air oxidation. The elongation vs. time plot is shown in Fig. 5.24:

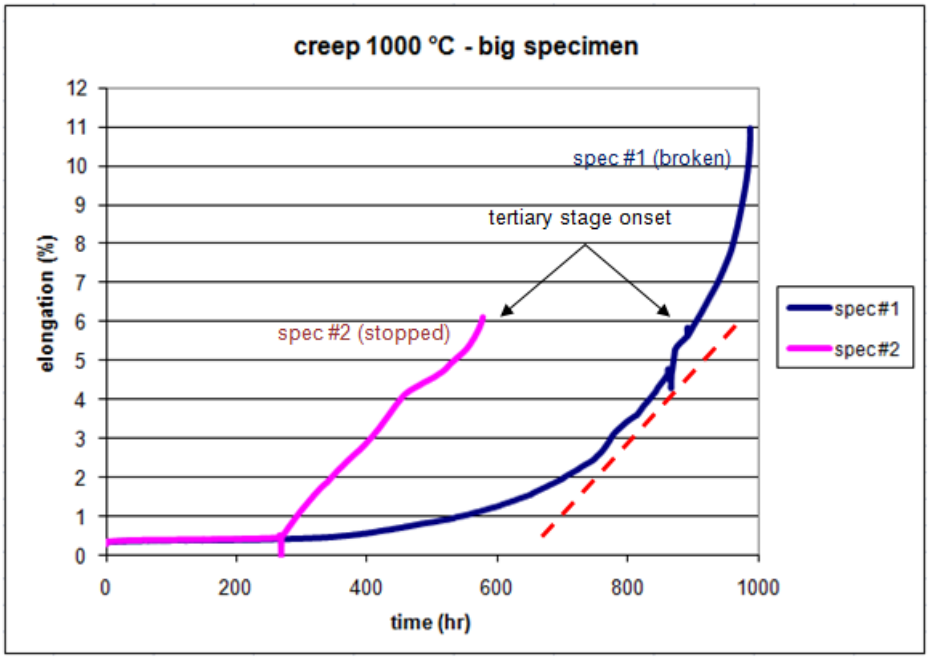

Fig. 5.24. Creep at 1000 °C, elongation (%) vs. time (hr), larger specimens.

The stress imposed upon specimen #1 was raised in succession from 1.5 MPa to 6.5 MPa, while it was kept constant upon specimen #2 at 1.5 MPa for about 250 hours and then raised directly to 6.5 MPa. While specimen #1 was broken at 11% elongation, specimen #2 was stopped after 580 hours creep at 6% elongation. The air oxidation layer was evident but considered not decisive, because it was small compared with the active area of the larger specimen. The layer had a thickness slightly lower than 1 mm. Grain boundary sliding voids were observed again.

5.2.4.1 Metallography of larger creep test specimens at 1000 °C

Figs. 5.25 - 5.26 show the grain boundary sliding voids that were generated.

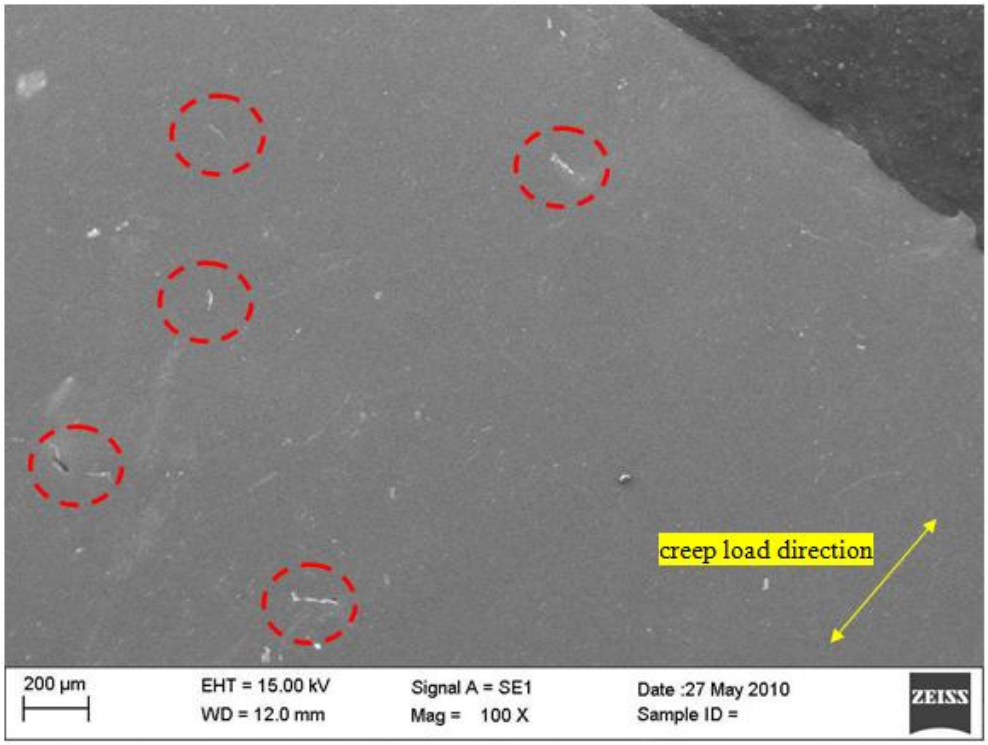

Fig. 5.25. Creep at 1000 °C, big specimen #2.

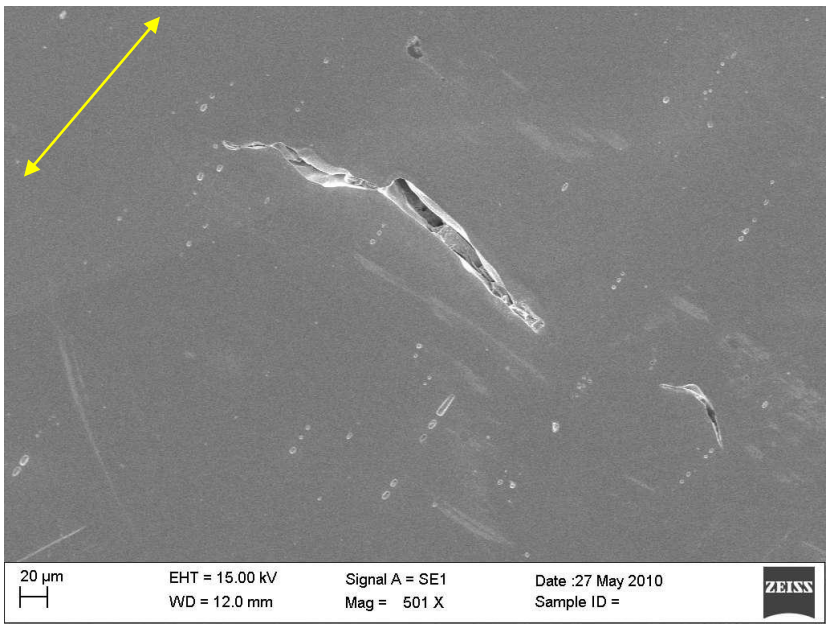

Fig. 5.26. Creep at 1000 °C, big specimen #2, detail of voids.

One other effect to be mentioned from creep at 1000 °C is some grain growth, activated by boundary energy reduction [242]. Even if this process was not analyzed in detail (for example computing the equivalent plastic strain along the relevant surface of the axisymmetric specimen), one consequence to expect was some lowering of fracture toughness initiation due to the reduction of the yield stress.

5.2.5 Combination of pre-strain and creep

One combination of 7% pre-strain at room temperature and creep test at 900 °C was executed on one big specimen. Stopped at 6% creep elongation after 680 hours because of a mechanical limit reached at the testing machine, it gave no voids into the matrix. It was expected some decohesion from the initial pre-strain, but it did not happen. The creep procedure simply annealed out prior work. It can be seen in Fig. 5.27 that the specimen was still into its secondary creep stage at the moment the test was stopped.

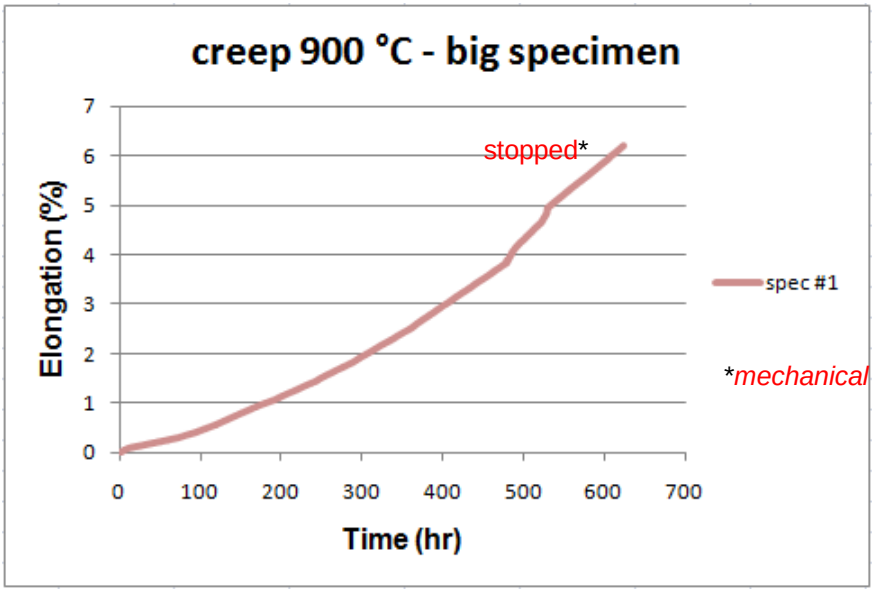

Fig. 5.27. Creep at 900 °C, elongation (%) vs. time (hr), 7% pre-strained specimen.

Material from this test was machined for fracture toughness evaluation for comparison purposes, suspecting a modification of yield stress from possible grain growth.

5.3 Quantitative measurement of the damage produced

Porosity induced by notched tensile tests at room temperature of "as received" and "undamaged" material and by creep at 1000 °C was computed from post-test metallographic and tomographic evidence. Details are given and discussed.

5.3.1 "As received" and "undamaged" material

According to literature, the value for critical void volume fraction at the fracture line used in the numerical computation for austenitic stainless steels is 15% [197]. That value has been here recalculated experimentally to be 8% - 9%. Two different notch sizes, $NT_{6.6}$ and $NT_{2.083}$, were accounted for. Results were are presented in the following Figs. 5.28 – 5.31:

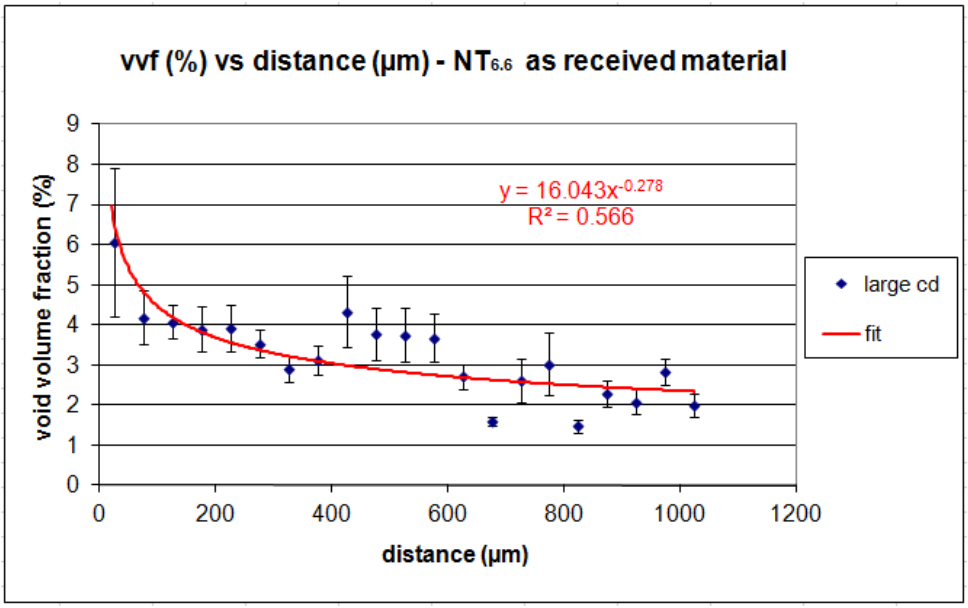

Fig. 5.28. Void volume fraction for "as received" material, large notch.

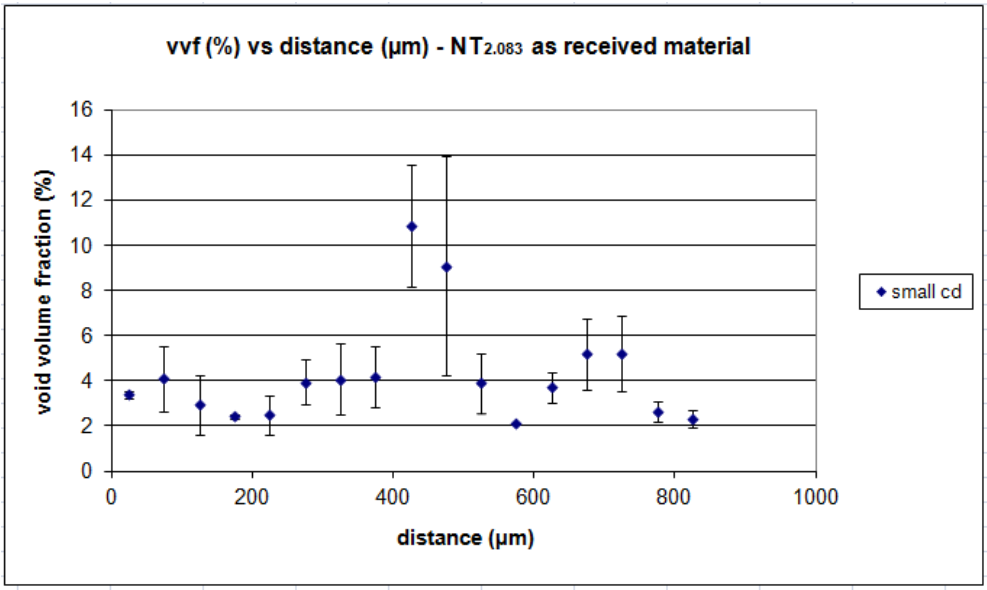

Fig. 5.29. Void volume fraction for “as received” material, small notch.

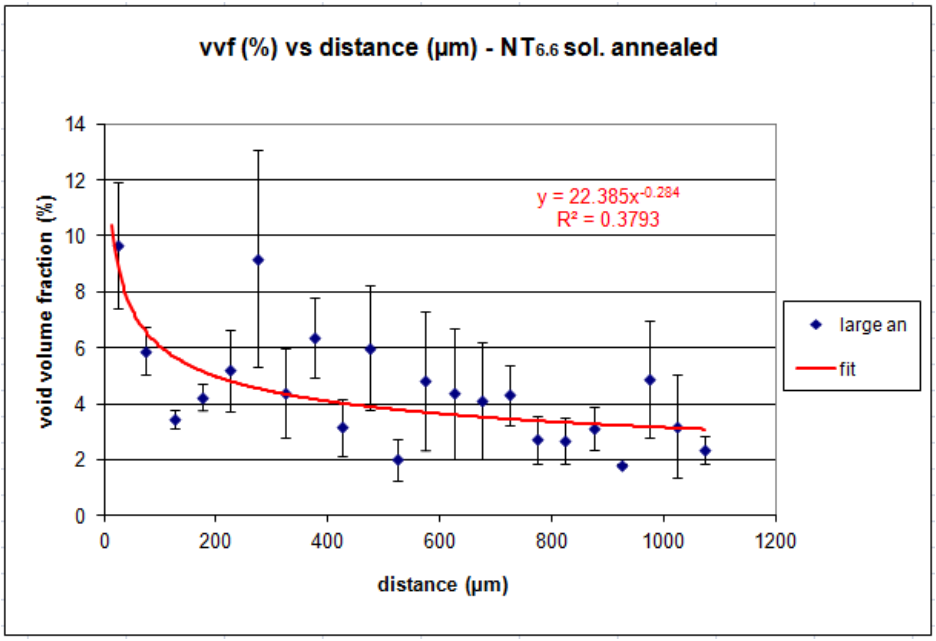

Fig. 5.30. Void volume fraction for “undamaged” material, large notch.

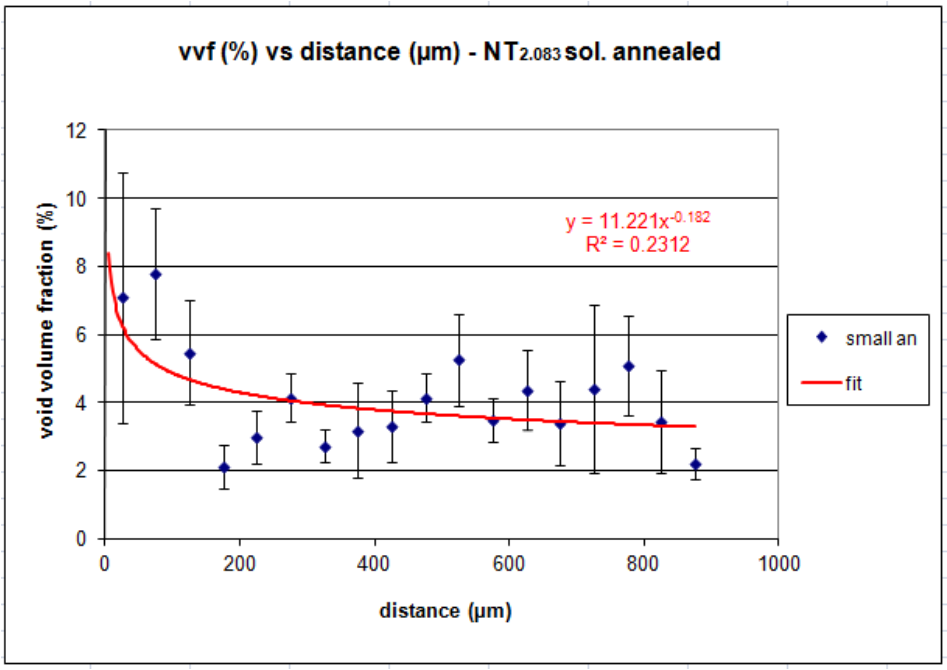

Fig. 5.31. Void volume fraction for "undamaged" material, small notch.

The behaviour appears to be quite irregular, due to the presence of semi-coalesced voids randomly distributed along the distances considered. Fracture had happened at a value about 8 - 9 % void volume fraction for the "undamaged" material and something lower for the "as received" material (which was supposed to be 20% cold worked).

As for the former case, quantification of damage led to the identification of the ductile fracture criterion for the aim of this project, which made use of similar notched tensile specimens for fracture toughness evaluation. In fact, considering the nearest values to the fracture line from the "undamaged" material in the Figs. 5.30 - 5.31, it could be said that the median critical void volume fraction for the two cases reported was:

$$vvf_{crit} = (0.098 + 0.072) / 2 \pm (0.011 + 0.033) = 0.085 \pm 0.044 \quad (5.1)$$

This value will be numerically fitted as $vvf_{crit} = 0.09$ by employing large strains and using the same class of specimens, that is a similar constraint, with the four-noded elements CAX4R. That will be used as a ductile fracture criterion for this project.

5.3.2 Creep at 1000 °C damaged material

Voids from the fracture line up to 0.8 mm distance, in the necking zone, were not computed. In fact, it was not possible to obtain a cropped area from its tomographic slices that was consistent with the cropped area from the rest of the specimen. In addition, the most interesting part was outside that zone.

By using the image processing method introduced in Section 3.3.2, it was found that void volume fraction was in the range 1.8% - 1.2% at a distance of 0.8 mm to 2.5 mm below the fracture surface.

At a distance of 5 mm from the fracture surface, as for scanning electron microscope images, there appeared to be almost no voids. This is shown in Fig. 5.32.

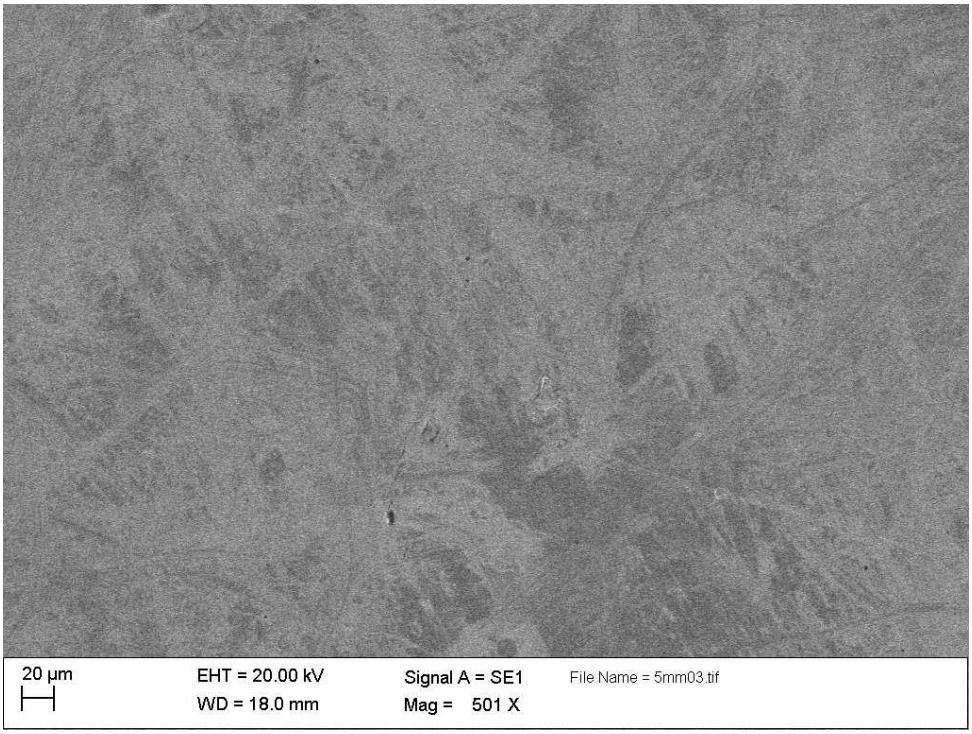

Fig. 5.32. Slice at 5 mm distance from fracture surface, 1000 °C creep.

Quantification of damage was not repeated on larger specimens subjected to the same 1000 °C creep testing. Metallographic evidence of voids was deemed to be satisfactory.

5.4 Fracture toughness testing

5.4.1 Sharp-notched round bar specimen

The experiment was conducted on the sharp-notched tensile specimen depicted in Fig. 3.16 for all the relevant "damaged" states obtained experimentally, together with the "undamaged" state for comparison.

The following Fig. 5.33 reports the output in the form of load vs. displacement plots:

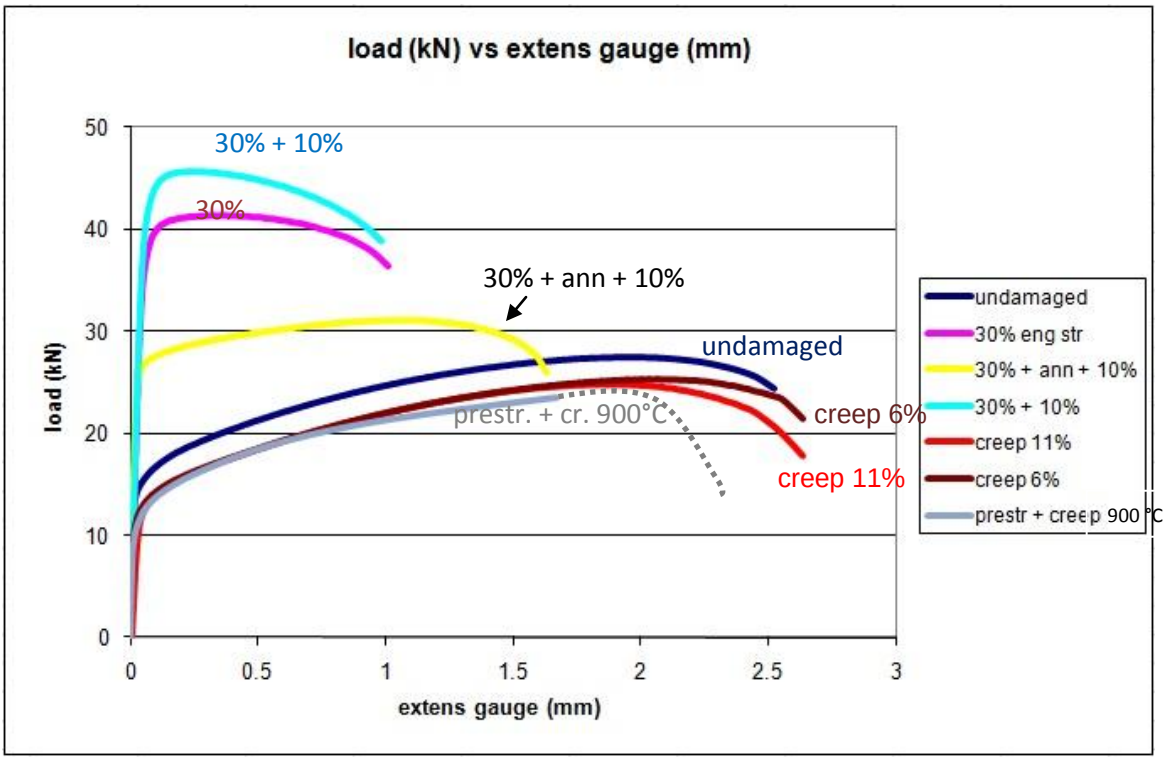

Fig. 5.33. Fracture toughness test by sharp-notched round bar specimens.

Fractographic evidence from the most brittle specimen (that is the 30% + 10% strain hardened) is still of ductile fracture, as shown in Figs. 5.34 - 5.35:

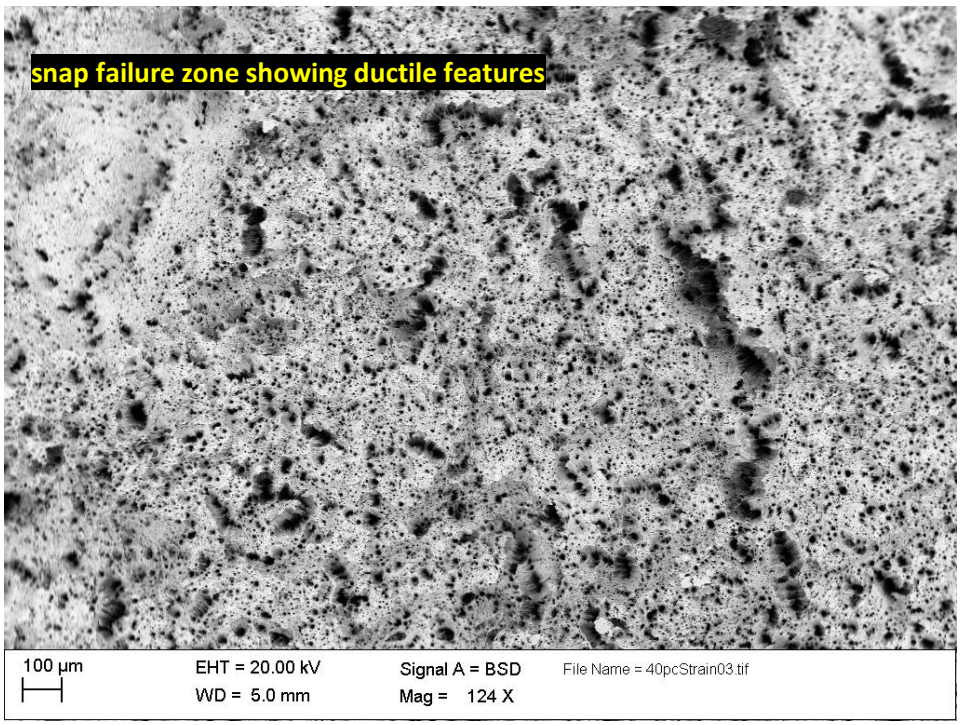

Fig. 5.34. Fractography from the 30% + 10% specimen, central zone.

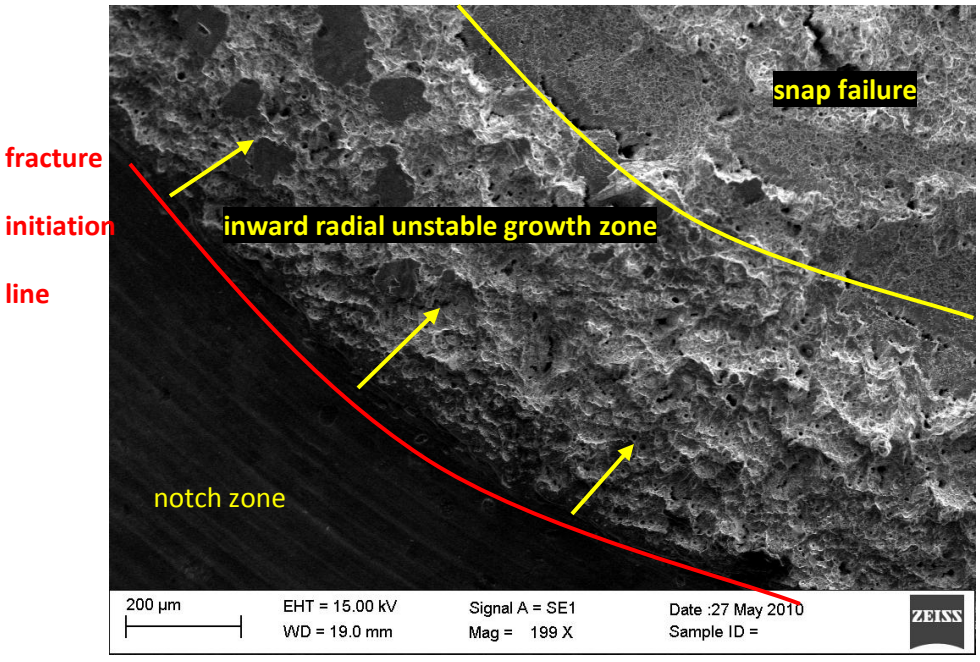

Fig. 5.35. Fractography from the 30% + 10% specimen, edge zone.

Fig. 5.35 shows the progression of unstable crack growth followed by snap failure.

According to Scibetta [171], the sharp-notched tensile specimen is comparable with the Compact Tension specimen for ductile fracture initiation, without a correction being required for loss of constraint. He also states that it is not good for measuring the tearing resistance because unstable crack growth very soon becomes the dominant process. In fact, because of the high compliance of the grip compared with the low compliance of the specimen, a large amount of energy is stored into the grips. Due to the crack growth, the specimen section is reduced and the energy stored in the grips is released leading to unstable crack growth. No parametric study aimed at minimizing that stored energy in relation to the testing parameters (crosshead displacement rate, machine stiffness, specimen height, notch depth) was carried out.

5.4.2 Small Disk Compact specimen

One similar test was conducted on DCT specimens. As shown in Fig. 5.36, it gave the following plots for some of the "damaged" materials and for the "undamaged":

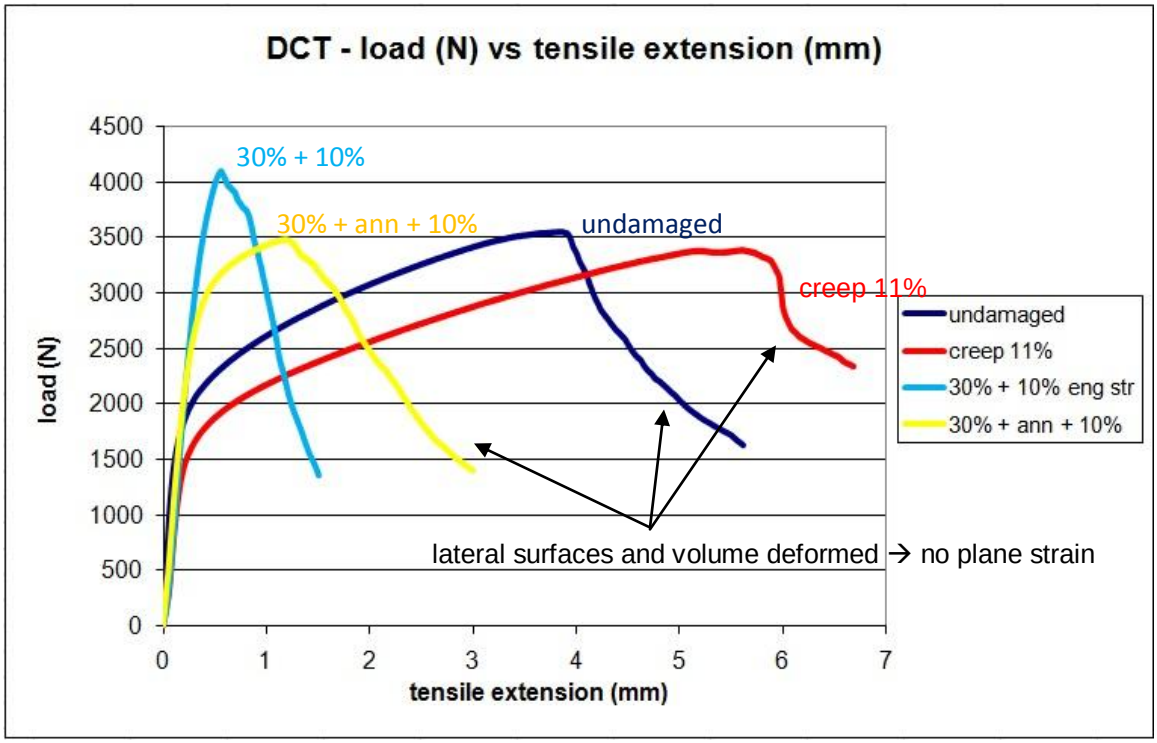

Fig. 5.36. Fracture toughness test by disk compact specimens.

The test was followed by fractography in order to investigate the crack front and the adherence to the plane strain condition (which was not verified for any specimen apart of the brittle 40% eng. strain "damaged" material). The "undamaged" and the 40% strained fracture surfaces are presented in the following Fig. 5.37:

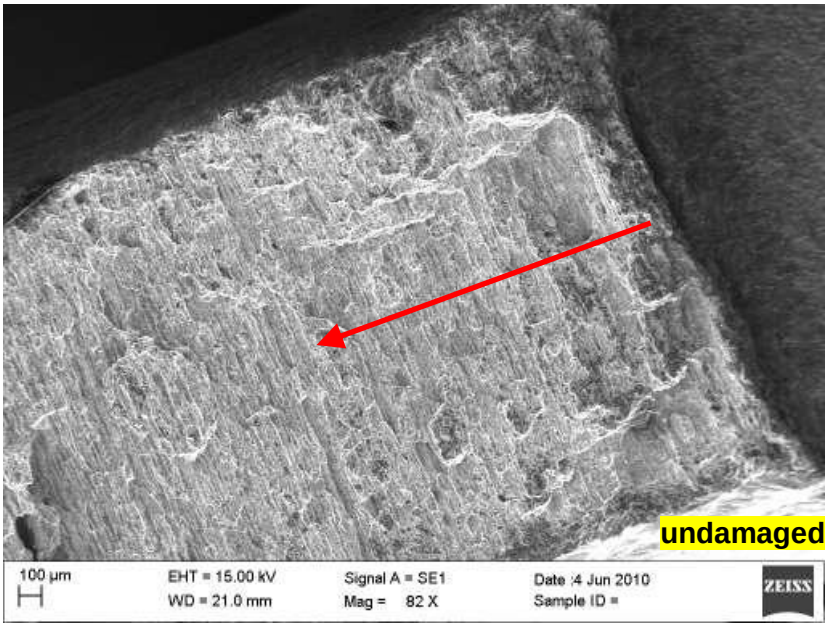

Fig. 5.37. Fracture surface from "undamaged" (a) and 40% strained (b) disk specimen.

5.4.3 Fracture criteria employed

Opportune fracture criteria for the onset of crack growth were used, based on the experimental findings. In particular:

- vvf = 0.09 for "undamaged", creep at 1000 °C, creep at 900 °C, 30% + sol. ann. + 10% engineering strain (representing dominant ductile failure mechanism with relevant blunting, as inferred from Fig. 5.33).

Notched tensile tests and void measurements, as reported in Section 5.1.3 and 5.3.1, suggested that value for the "undamaged" material. It was not possible to perform the same procedure for any other "damaged" material obtained in this project.

- $S_{max,\ principal}$ = 1583 N/mm² as the maximum principal stress for the 30% + 10% strain hardened case and $S_{max,\ principal}$ = 1454 N/mm² for the 30% strain hardened case (both representing semi-brittle failure mechanism with very little blunting, short and unstable crack growth followed by fast failure). The choice of these particular values comes from guessing –in accordance with the literature- the zone in which the crack probably started, that is slightly before the peak stress.

Several researchers [243-248] suggest that as pre-strain value increases, the fracture toughness and critical fracture strain decrease. The fracture properties gradually change from ductile into brittle. The brittle criterion then obeys to one stress-controlled model: the local tensile stress normal to the crack plane, ahead of a crack tip, must exceed a local fracture stress over some microstructurally significant characteristic distance. Different initial void volume values were tested numerically in order to estimate trends for fracture toughness initiation. It was found that, beyond some threshold value of initial void volume fraction (different for each "damaged" material considered), the brittle-like behaviour reverted to a ductile mechanism. Details are given in Section 6.4.4.

6. Numerical results

6.1 Gurson model calibration on the "undamaged" state

Results from tensile test of "undamaged" specimens were used to estimate statistically the Young's Modulus of 316L for the ABAQUS model. Minimum mechanical properties required by ASTM A240 [249] for 316L are E = 170 GPa, generally rating at E = 200-210 GPa. One set of four counts was obtained from interrupted tensile tests shown in Fig. 5.12. It was considered the linear (purely elastic) part of every stress vs. strain plot. Results are shown in Table 6.1.

	#1	#2	#3	#4	E mean	st. dev.
E (MPa)	211400	200700	202400	201700	**204050**	**4286**

Table 6.1. Young's Modulus values from "undamaged" 316L tensile tests.

Validation of the true stress vs. true strain diagram (for finite elements chosen inside the experimental gauge length zone) follows in Fig. 6.1 for "undamaged" material, as for the elastic + plastic part of the model. It does not account for damage growth, because during the early stages of deformation that growth was considered limited and not modifying the overall behaviour. This is shown in Fig. 6.2, where "small" refers to NT = 2.083, "medium" to NT = 4.583 and "large" to NT = 6.6. The Gurson-Tvergaard-Needleman model must to be introduced to obtain a better fit.

Notched tensile specimen tests were then used to calibrate the Gurson model parameters. Three different triaxialities -that is to say a multi specimen approach- were used in order to improve the consistency of results: in fact, more than one set of fitting parameters may emerge from calibration.

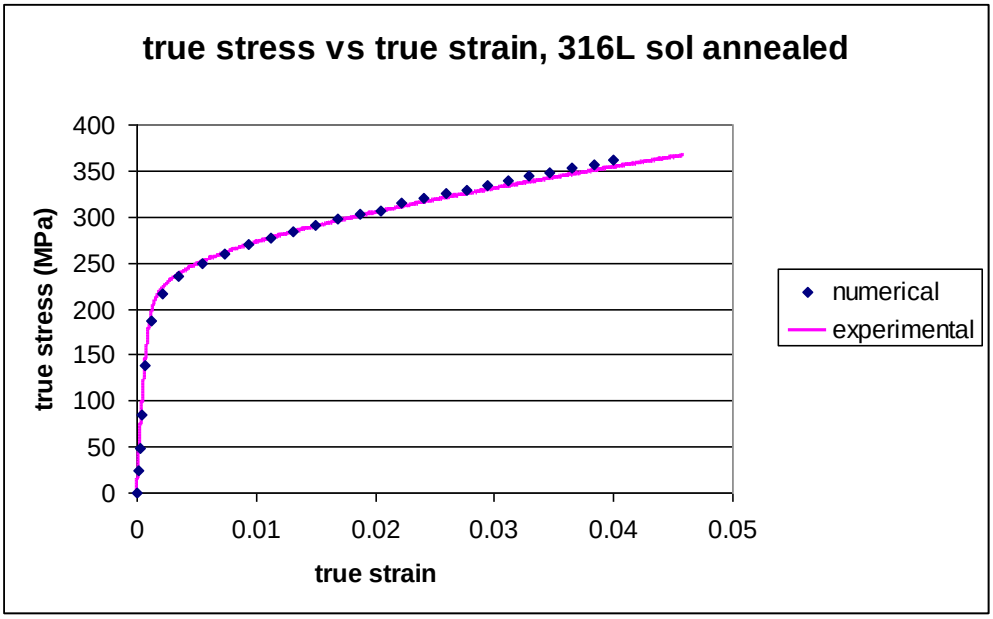

Fig. 6.1. True stress vs. true strain validation for “undamaged” 316L.

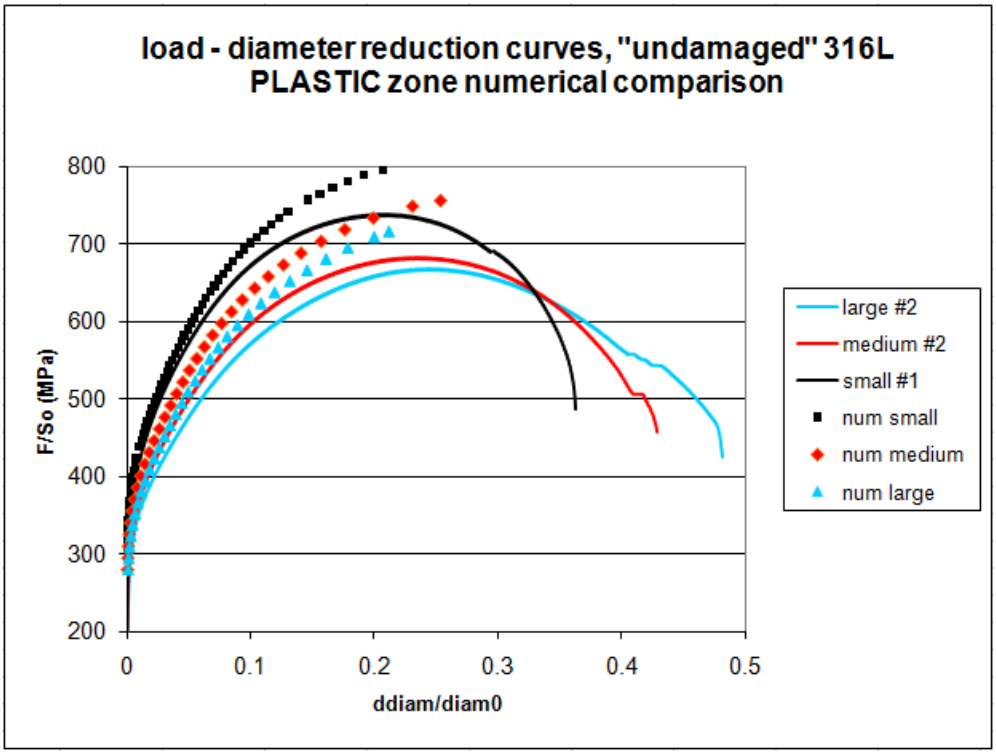

Fig. 6.2. Load vs. diameter reduction, without porosity in the model, for “undamaged” 316L.

Gurson's porous plasticity was used as implemented in the ABAQUS 6.6.1 package.

For a metal containing a dilute concentration of voids, the model proposes a yield condition as a function of the void volume fraction f and gives physically reasonable results for $f < 0.1$. Several parameters need to be specified by the modeller. In the case of 316L, literature usually reports the following values:

- relative density or initial porosity f_o. It is conventionally set equal to the volume fraction of the dominant particles involved in the ductile fracture process; for 316L Franklin's formula is normally used, which relates manganese-sulphide inclusions content to f_o:

$$f_0 = 0.054\left(S(\%) - \frac{0.001}{Mn(\%)} \right) \tag{6.1}$$

S(%) and Mn(%) are given in the vendor's certification or are inferred by chemical analysis. The initial porosity can also be directly measured using image analysis and, sometimes, it is considered an adjustable parameter to be fitted;

- the critical void volume fraction at failure f_c is typically set equal to 0.15 in the case of small scale yielding, as in Sherry [197]. It is not implemented in Abaqus Standard and was not used here;

- q_1, q_2, q_3 are transferable material parameters requiring calibration for the material of interest; as for 316L, it can be found [4, 197] that $q_1 = 1.25$, $q_2 = 1.00$ and $q_3 = q_1^{\,2} = 1.56$;

- the Chu-Needleman distribution parameters ε_N, S_N, f_N are provided to account for secondary nucleation and are defined as field variables; literature reports values for typical metals as ε_N = 0.1 to 0.3, S_N = 0.05 to 0.1 and f_N = 0.04.

The initial void volume fraction was firstly established in accordance with Franklin's formula on the 316L composition given by the vendor, so that $d_o = 0.98114$. This value was tested against $d_o = 1$, that is to say no initial damage at all. An intermediate value $d_o = 0.99$ was also used for comparison. Fig. 6.3 reports the findings:

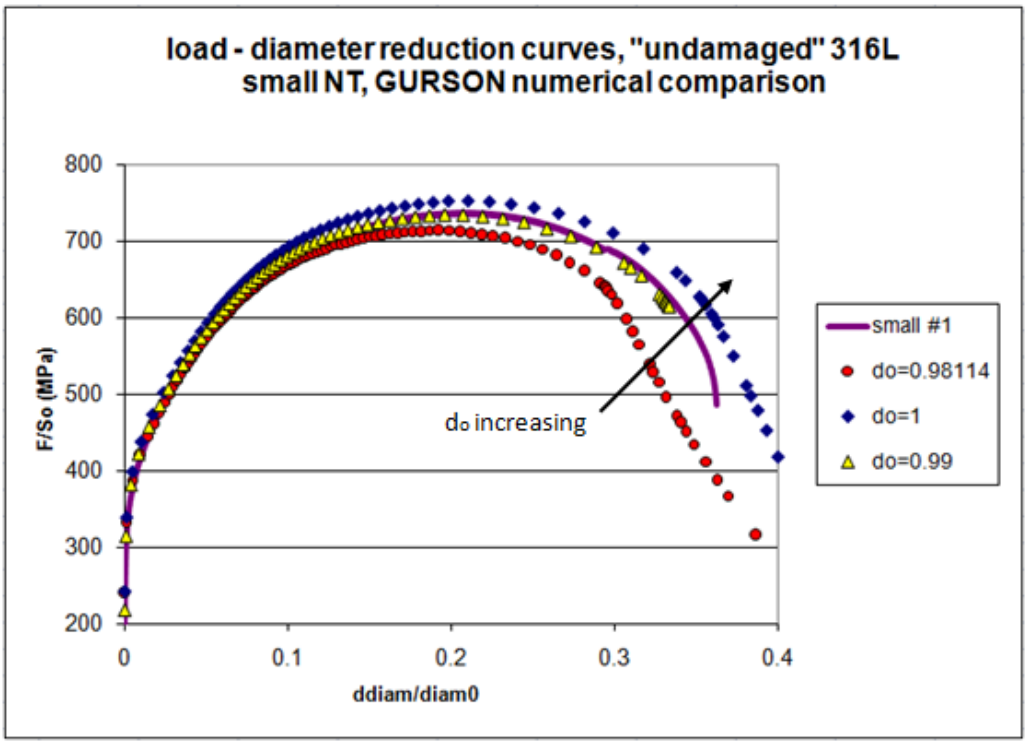

Fig. 6.3. Void volume fraction calibration for small NT specimen.

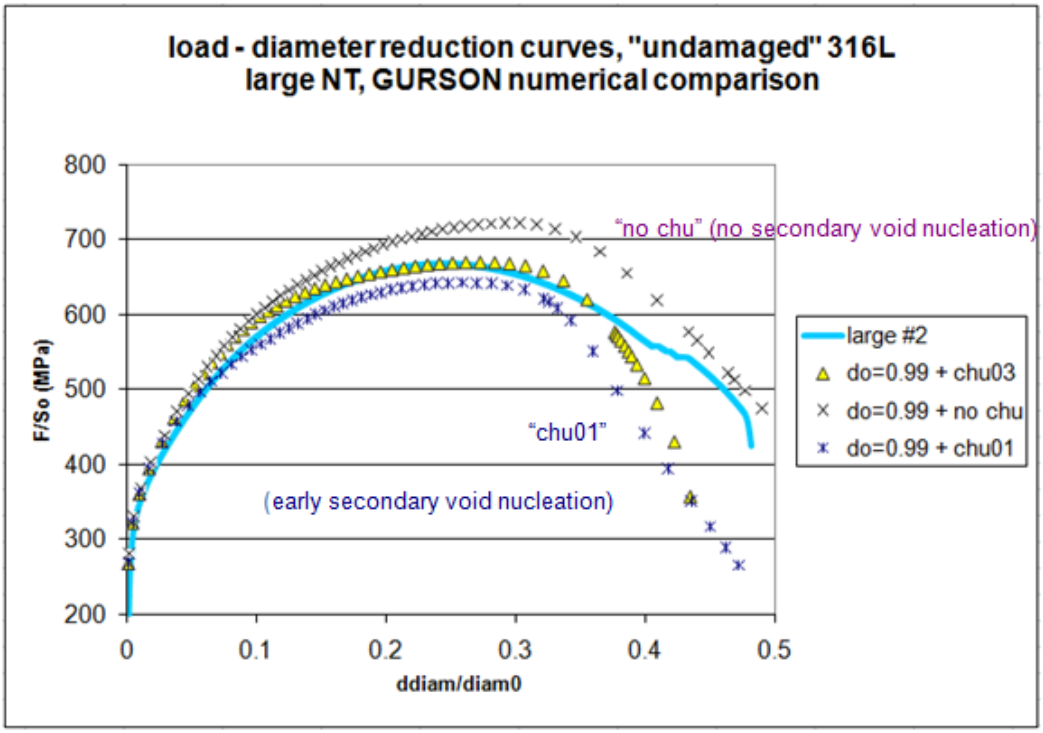

Fig. 6.4. Chu-Needleman first examination for “large” NT specimen.

Secondary void nucleation parameters were investigated as in Fig. 6.4. No secondary void nucleation (that is "no chu" in Fig. 6.4) was tried first. After that, a set of values reported in the literature as the minimum allowed for steels, that is $\varepsilon_N = 0.1$, $s_N = 0.05$ and $f = 0.05$ was tried. The physics underlying this numerical behaviour eventually needs to be validated against microstructural evidence [185]. It was not done here.

From the simulations shown in Figs. 6.3 - 6.4, a sharp drop of the load at about $d_{diam} / d_o = 0.35$ is constantly seen. From a physical point of view, it occurs when a localization band appears at the centre of the specimen. In practice, after the onset of load drop, the result was mesh size dependent. The load drop was faster with the smallest mesh size, where finite elements appeared to lose their convergent properties. Repeated tolerance warnings were registered. Progressively increasing the size of the elements in the notch zone, those tolerance warning receded, until a "no warning" simulation was performed. Fig. 6.5, in which $d_o = 0.99$, $\varepsilon_N = 0.3$, $s_N = 0.1$ and $f = 0.04$, just reports that. In retrospect, such behaviour may be attributed to the use of full specimens because the different length scale of the notch zone from the rest was significant. Successive analyses on notched tensile specimens, notably sharp-notched round bars, made use of half-bar models. It added symmetry with respect to the notch zone and made the computations smoother. A characteristic length for fracture toughness purposes was implemented.

Generally speaking, mesh sensitivity is an important issue in finite element analyses. Simulations performed with bigger mesh elements at the notch location ("BB" in Fig. 6.5, while "BE" is a smaller increase in size) led to better fitting of the experimental curves. This also happened for small and medium-notched specimens. The size of the elements at the notch location is a characteristic parameter when investigating crack propagation. On the contrary, mesh size is not critical when calibrating the elastic–plastic constitutive model. Considerable attention was paid to this aspect at a later stage of the project.

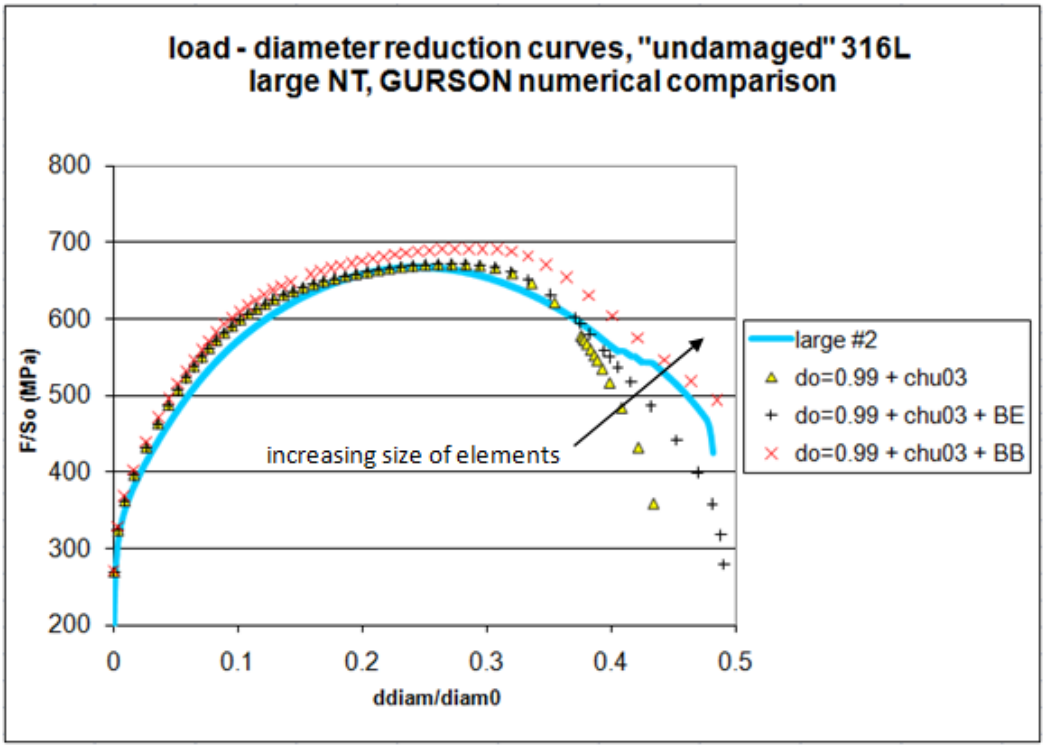

Fig. 6.5. Finite elements size trend at notch zone for “large” NT specimen.

Initial void volume fraction of about 1% was common in the steel industry some decades ago; it is widely assumed that modern steels should present initial void volume fraction in the order of 0.1% or slightly less, that is to say $d_o = 0.999$. The calibration for “undamaged” 316L was done again after reconsidering the plastic behaviour, in particular the results from interrupted tensile tests performed at a later stage and shown in Fig. 5.12. They appeared to show that the plastic law used in the first instance was slightly overestimated.

The initial density was recalculated as $d_o = 0.9986$ using the Franklin formula and the actual composition of the material, as got from external testing and shown in Table 5.1. That answered the question about the “modernity” of the steel. As a consequence of the parametric study, the plastic part of the constitutive model was established as follows:

	common part			final model
true stress (MPa)	true strain (mm/mm)		true stress (MPa)	true strain (mm/mm)
167	0		**450**	0.0853
173	6.23E-05		**500**	0.114
179	8.50E-05		**550**	0.145
185	0.000122		**600**	0.179
191	0.000181		**650**	0.216
197	0.000271		**700**	0.256
203	0.000416		**750**	0.3
209	0.000589		**800**	0.336385084
215	0.000817		**850**	0.374436834
221	0.00106		**900**	0.412488584
227	0.00137		**950**	0.450540335
233	0.00173		**1000**	0.488592085
239	0.00218		**1050**	0.526643836
245	0.00271		**1100**	0.564695586
251	0.00336		**1150**	0.602747336
257	0.00415		**1200**	0.640799087
263	0.00507		**1250**	0.678850837
269	0.00619		**1300**	0.716902588
275	0.00748		**1350**	0.754954338
281	0.00893		**1400**	0.793006088
287	0.0106		**1450**	0.831057839
300	0.0147		**1500**	0.869109589
325	0.0244			
350	0.0355			
375	0.0472			
400	0.0595			

Table 6.2. Revised plastic model for “undamaged” 316L.

In conclusion, the model for the “undamaged” 316L was the following:

E = 205000 MPa; υ = 0.3 for the elastic part;

the true stress / true plastic strain values shown in Table 6.2 for the plastic part;

d_o = 0.9986; $q_1 = 1.25,\ q_2 = 1,\ q_3 = 1.56$; $\varepsilon_N = 0.3,\ s_N = 0.1,\ f = 0.04$ for the porous part.

In retrospect, it was noted that the fit was not very good. However, it did not compromise the original part of this project. In fact, the values for “undamaged” 316L material are widely accepted in the literature and not controversial. In addition, refined finite element models were used at a later stage and a characteristic length for the notch zone was considered for fracture toughness purposes.

6.2 Irradiation hardening effect on constitutive equation

These plots are based on the statement that a correlation exists between post yield strain hardening and irradiation hardening, as argued by Byun [80] and shown in Fig. 4.3. Therefore, it was assumed here that the yield stress increase caused by irradiation may be reproduced by tensile hardening. The plot in Fig. 2.20 for 316L, showing irradiation hardening, can then be correlated with the strain hardening from this project, as obtained from interrupted tensile tests. Fig. 6.6 shows the correlation obtained:

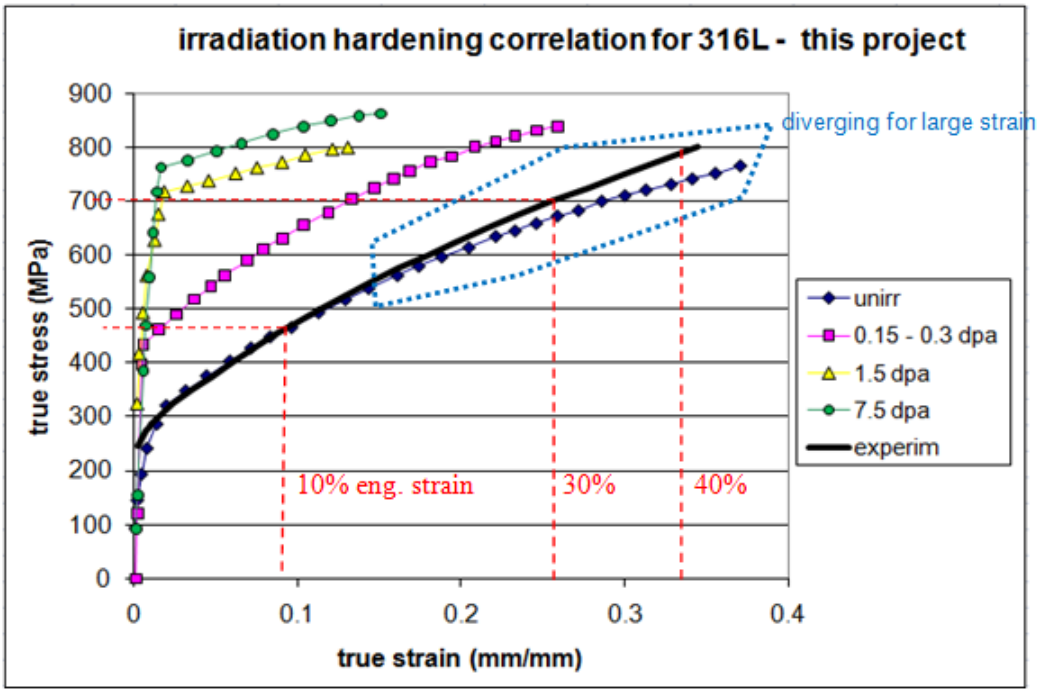

Fig. 6.6. Irradiation hardening correlation for 316L.

In particular, the 30% + sol. ann. + 10% engineering strain may be roughly correlated with the 0.15 – 0.3 dpa level from the irradiation benchmark. The 30% eng. strain level may be linked to 1.5 dpa level. Finally, the 30% + 10% eng. strain level, because of some slight divergence appearing at high levels of deformation between the material used in this project and the one taken as benchmark, may be conservatively considered to be somewhere in the range 1.5 – 4 dpa without further analysis.

6.3 Preliminary numerical analysis of candidate specimens

If $J(0)$ is the J-integral value in the midsection, then it is possible to compare the J-integral value over the thickness z. Due to symmetry, only half the thickness B was considered in these analyses, so that z was normalized to $B/2$.

The load level reference (or normalized load level) was expressed in terms of $J_{avg} / l_{rem} * \sigma_0$.

J_{avg} is a thickness average J-integral value. It was formulated as follows:

$$J_{avg} = \frac{\sum J_i b_i}{B/2} \tag{6.2}$$

b_i (in mm) is the discretized length -part of thickness- associated with each J_i value;

l_{rem} (in mm) is the remaining ligament ahead of the crack tip;

σ_0 (in N/mm^2) is the yield strength of the material.

J-integral values were calculated in contours along the crack tip [115]. Then they were extrapolated for each zone and each load level after reaching a stable value. It has to be noted that increasing the load level, the number of contours needed to reach a stable value became higher. All calculations attempted proved to have a stable value of J.

The behaviour of the J-integral value over the thickness was investigated in order to estimate the trends by varying the aspect ratio of the specimen, the elastic-plastic constitutive law of the material and the load applied. Two main trends were identified: the first and the most common, showed the maximum value of J-integral at the centre of the specimen, at its midsection. In thickness terms, it says that the crack develops from the centre towards the outside edges. The second trend showed the maximum value of the J-integral not being at a centered position in the specimen, but shifted towards the outside edges. The crack was expected to arise at that position and at its symmetric point with respect to the midsection plane. This was in agreement with the benchmark [163].

6.3.1 SENB specimen

One class of 3D Single Edge Notched Bend specimens was analyzed in order to familiarize with the fracture toughness parameters against the aspect ratio of the specimen, the constitutive laws of the material and load level applied. Some results are here presented and discussed against the benchmark [163]. Abaqus Standard uses Newton's method as a numerical technique for solving the nonlinear equilibrium equations [250]. All solutions were computed without errors or warnings concerning the numerical convergence. The crack was supposed to be sharp for all the models.

The plot in Fig. 6.7 (parameters: shallow crack or $a / W = 0.1$; plane strain case or $W / B = 1$; strongly hardening material or $n = 5$; loads increasing from the elastic range up to the plastic zone response) represents the behaviour of J integral over the thickness z, when normalized to its value in the midsection $J(0)$. It is depicted against the value of thickness z, where $z = 0$ is the midsection and $z = B / 2$ the outside edge. The solution is symmetrical with respect to the midplane over the thickness direction.

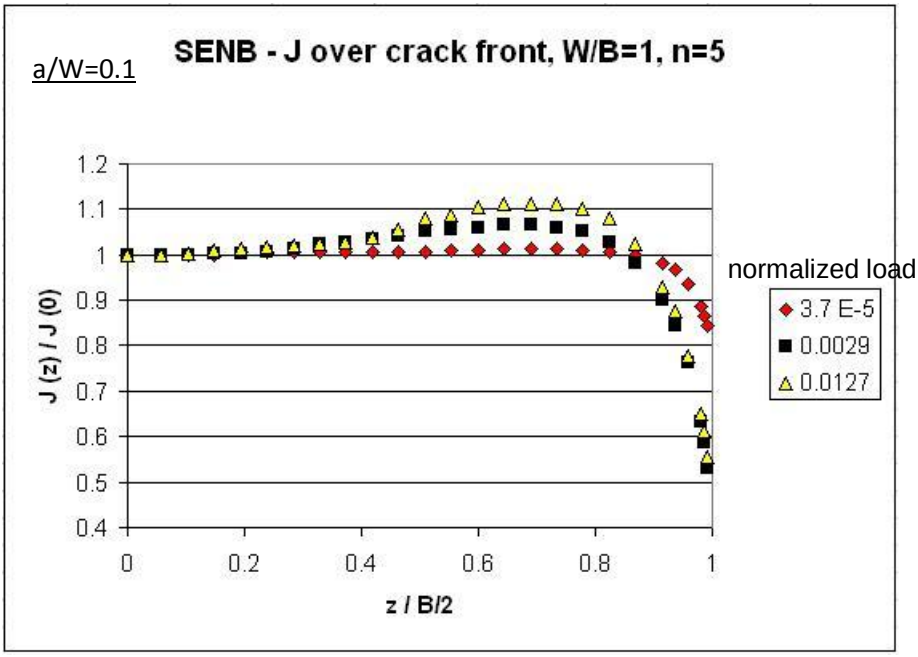

Fig. 6.7. SENB elastic-plastic response from $a / W = 0.1$.

This specimen showed the maximum value of *J*-integral at about 0.7 along the normalized thickness and there the crack was supposed to arise. That is explained in Fig. 6.8, concerning the actual geometry of the specimen.

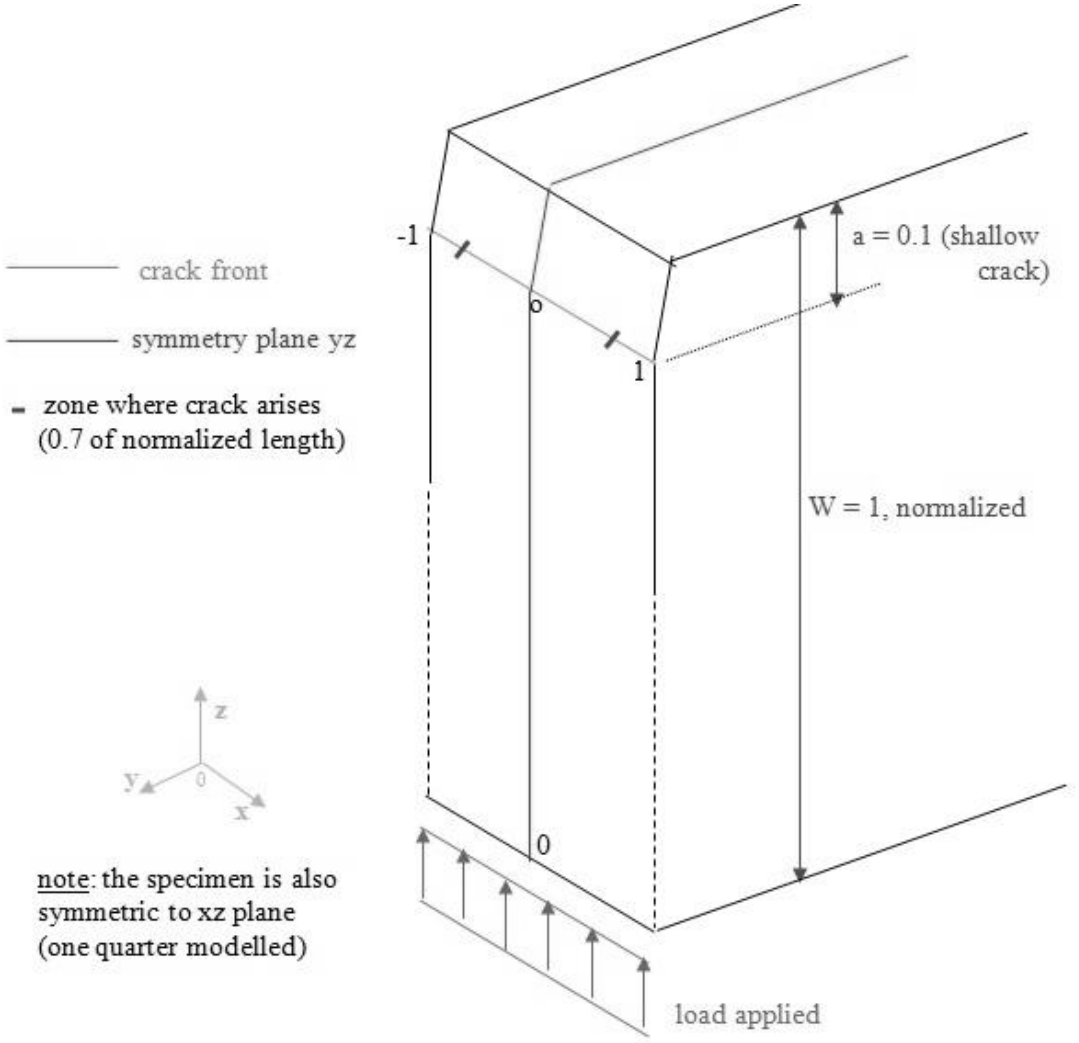

Fig. 6.8. SENB $a / W = 0.1$, zones of maximum J value.

The plot in Fig. 6.9 shows the behaviour of *J*-integral value with regards to one specimen designed with deep crack ($a / W = 0.5$), plane strain ($W / B = 1$), strongly hardening material ($n = 5$). In this case, the maximum value of J was located in the midsection of the specimen and the crack was expected to arise there.

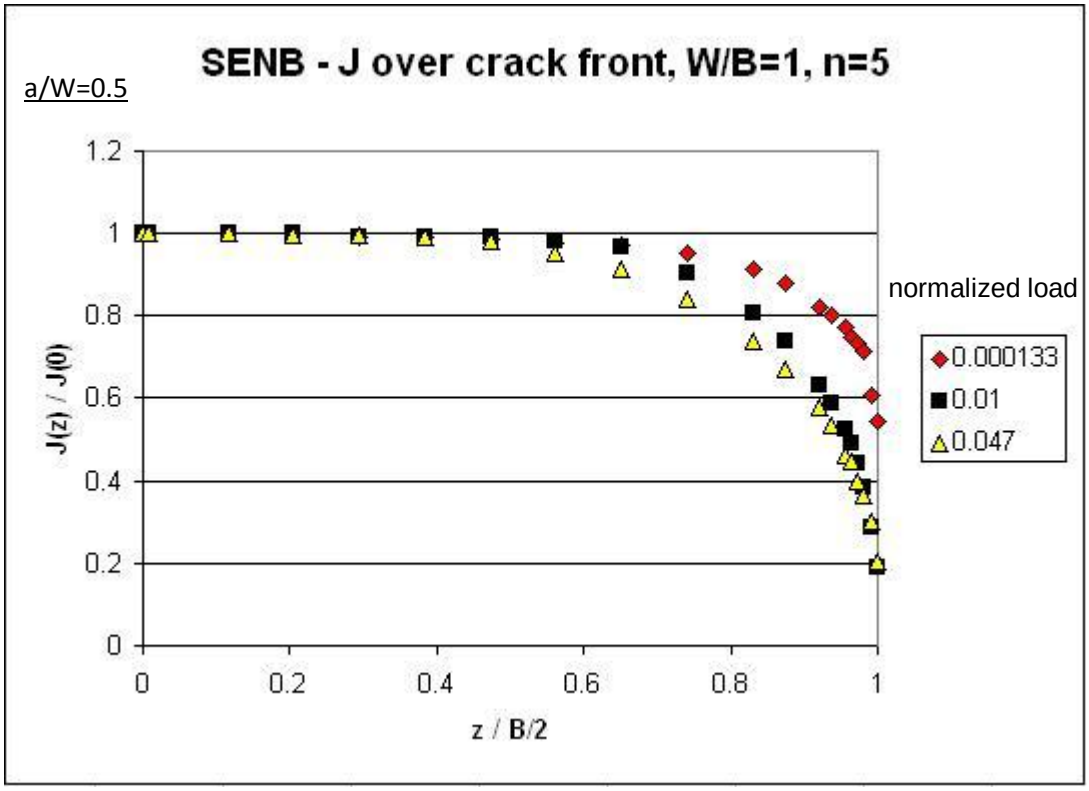

Fig. 6.9. SENB elastic-plastic response from $a / W = 0.5$.

The bias pictured in Fig. 6.9 does not fully represent the bias adopted in the simulation, in the sense that only a part of the computed values was extrapolated. More detail is provided for the outside zone of the specimen, where the gradient was bigger.

Trends proved to be in agreement with the benchmark [163].

6.3.2 CT specimen

Aiming to the simulation of DCT specimen, more attention was given to the similar CT specimen (which is directly comparable to DCT) and the experience with SENB was

concluded without going further. The load was applied as a load-line displacement, in accordance with BS 7448-1 Standard [127]. Crack depth was $a / W = 0.6$ for all the cases.

The normalized load-displacement response was first investigated. Its behaviour is shown in Fig. 6.10, where the test is performed in linear geometries, LGEOM (it means that there are not corrections for large rigid body rotations and translations when a small strain constitutive relation is used; for large strain models, strain measures are not accounted for higher order terms) conditions:

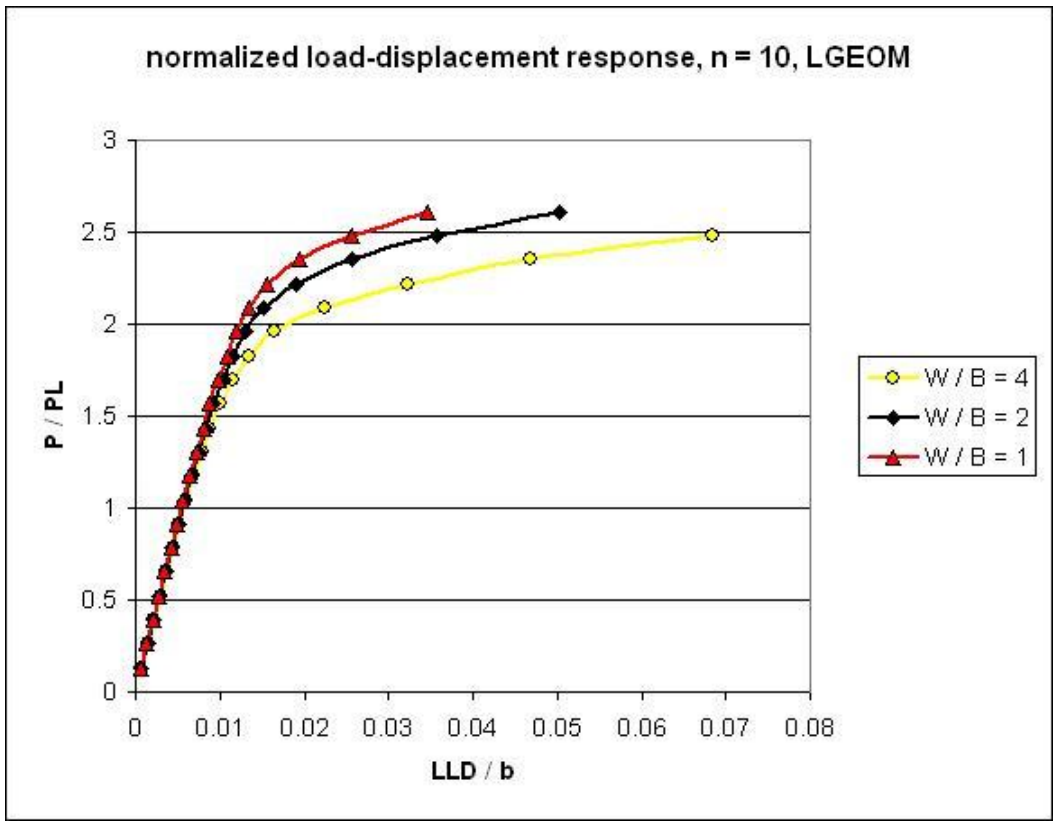

Fig. 6.10. Normalized load vs. displacement response for CT.

P is the computed load, expressed in N;

PL is the general yield load or the load at which plasticity first spreads over the ligament and for which the load-displacement record begins to deviate from linearity [251], also expressed in N; its formulation for CT specimen is given in [252];

LLD is the load-line displacement or the displacement along the load line, in mm;

b is remaining ligament length, in mm.

Fig. 6.10 shows the different response at different thicknesses obtained approaching plane stress ($W / B = 4$) or plane strain ($W / B = 1$) conditions.

Several plots of *J* behaviour over the crack front are shown for different thicknesses and elastic-plastic power law parameters. The load was calculated and normalized in respect of different load-line displacements. The small difference in load levels in the plots, for same load-line displacements, was due to the different elastic-plastic power law parameters, which led to different actual *J* and different normalized loads. In Figs. 6.11 – 6.13, plots for $W / B = 1$ and $n = 5$, 10, 20 are presented. In Fig. 6.14, a plot for $n = 10$ and $W / B = 2$ is compared against the relevant benchmark. In the end, in Fig. 6.15, one plot for $n = 10$ and $W / B = 4$ is presented.

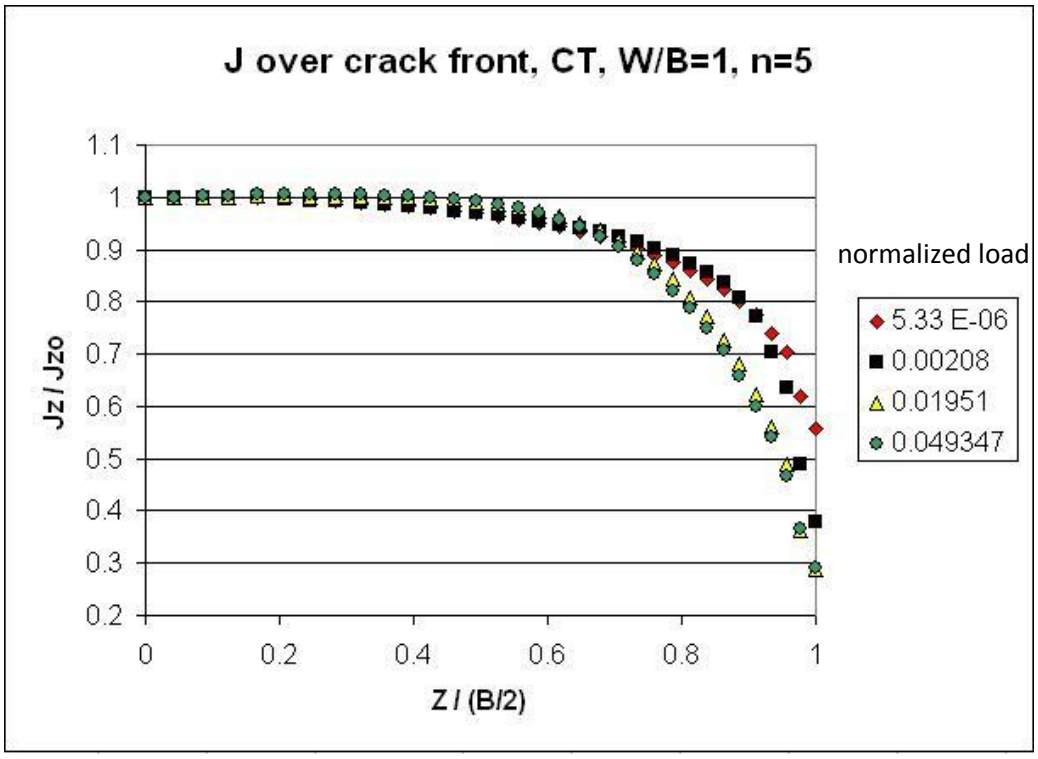

Fig. 6.11. *J* over crack front for CT specimen, $W / B = 1$ and $n = 5$.

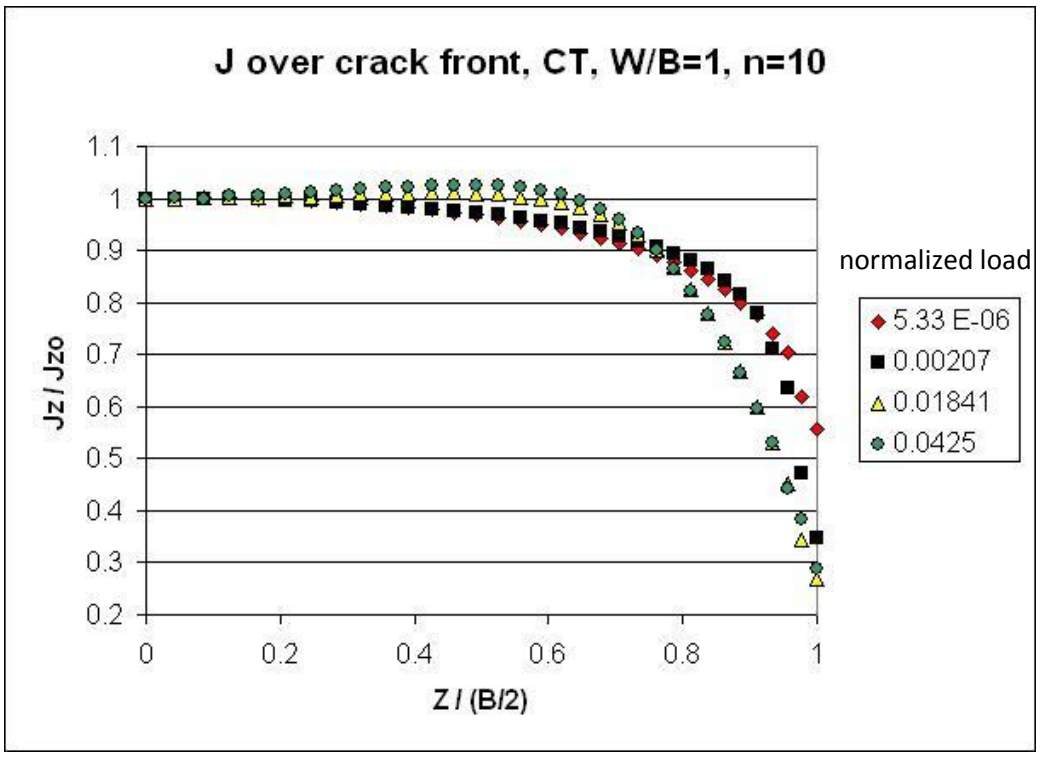

Fig. 6.12. *J* over crack front for CT specimen, $W / B = 1$ and $n = 10$.

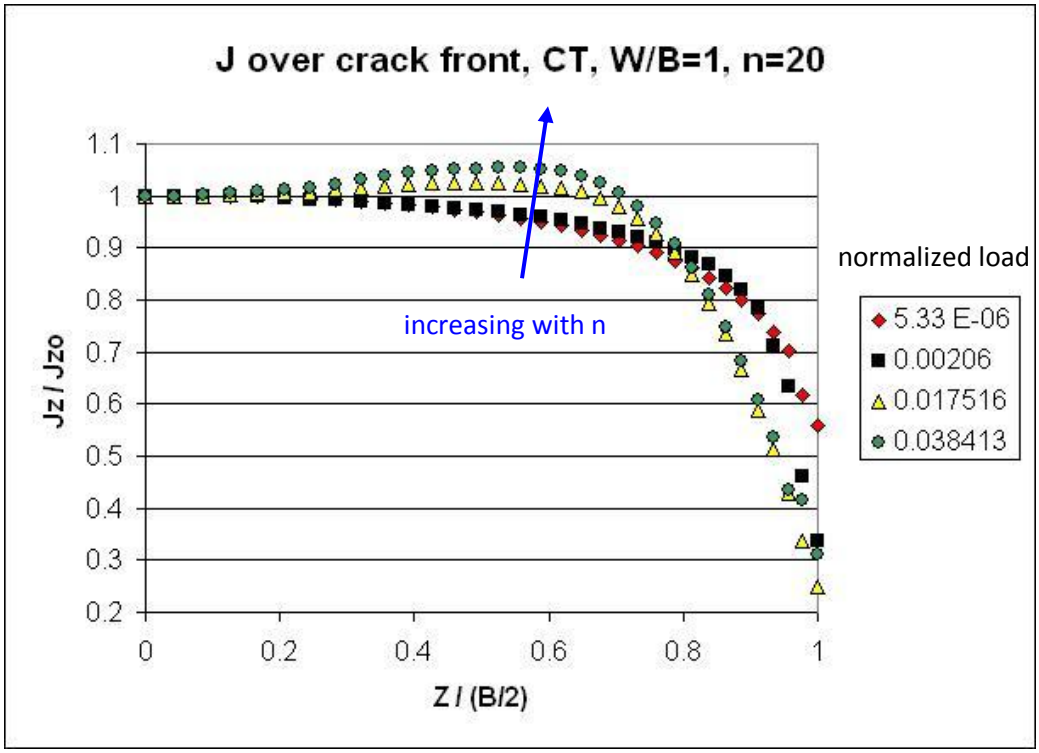

Fig. 6.13. *J* over crack front for CT specimen, $W / B = 1$ and $n = 20$.

In Figs. 6.11 – 6.13, the increasing value of $J(z) / J(0)$ in the zones $Z / (B/2)$ = 0.4–0.8 for $W / B = 1$ at increasing power law hardening parameter n can be noted. This suggests that for very low hardening materials (n = 20), the crack happens at a different location than the midsection and it is shifted towards the outside edge.

One plot for $W / B = 2$, $n = 10$ is depicted in Fig. 6.14:

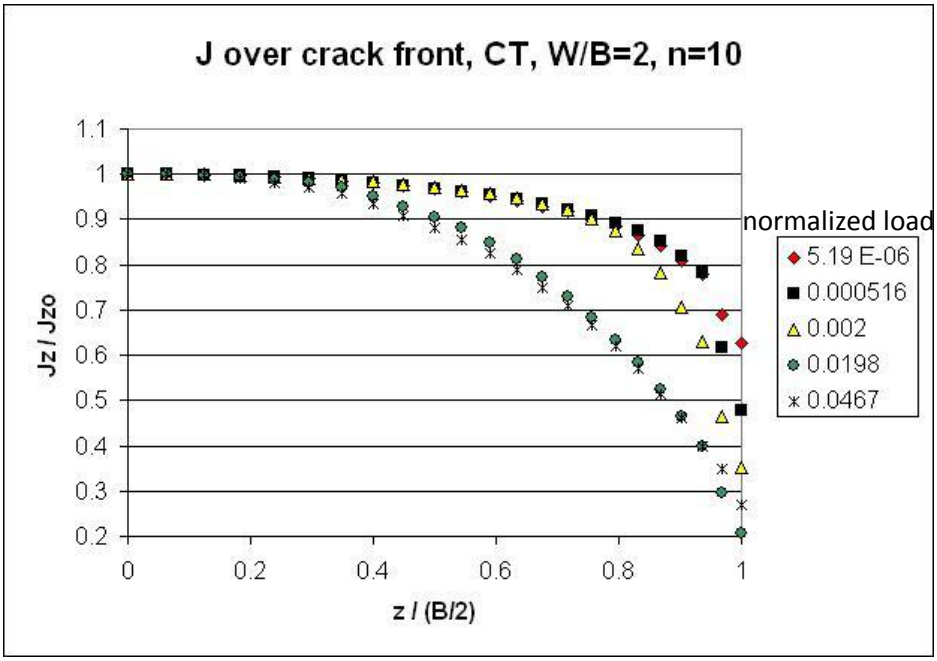

Fig. 6.14. J over crack front for CT specimen, $W / B = 2$ and $n = 10$.

As a conclusion of this set, one plot for $W / B = 4$, $n = 10$ is shown in Fig. 6.15 in order to give a full view for $n = 10$, together with Fig. 6.12 and Fig. 6.14:

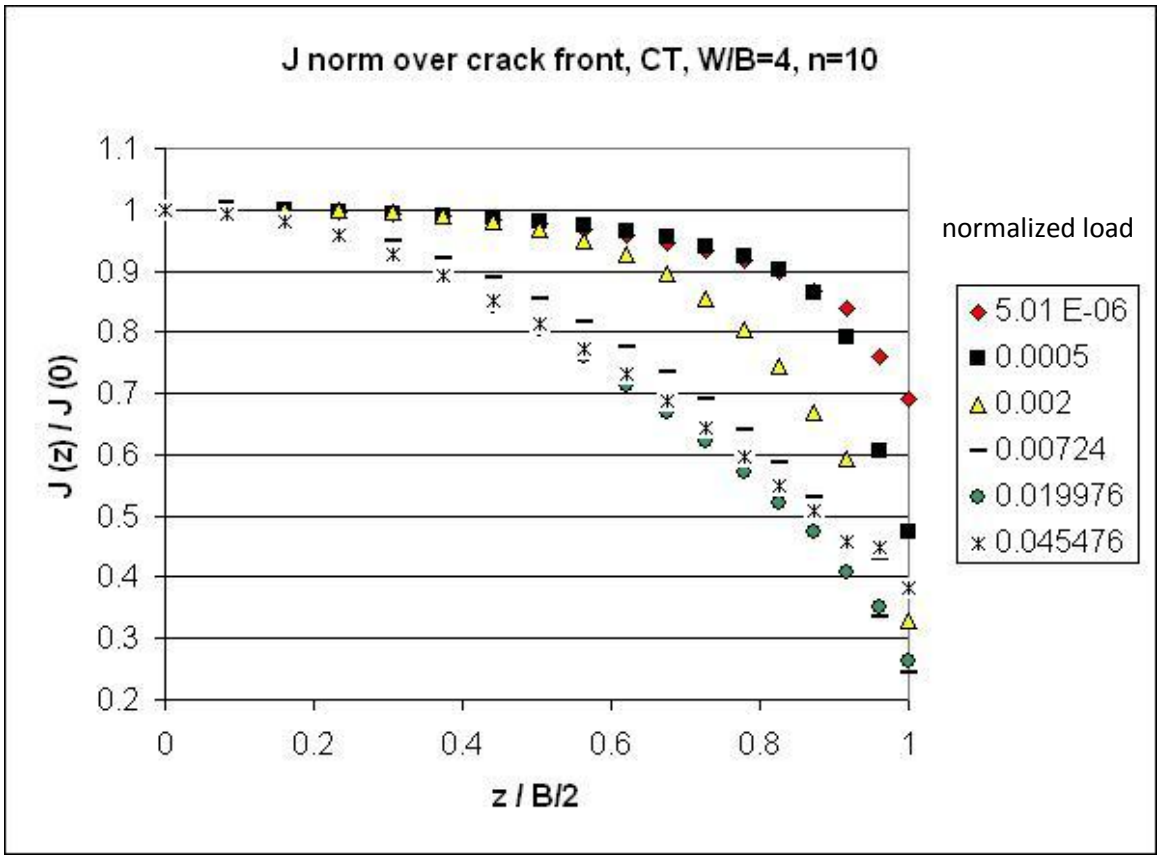

Fig. 6.15. *J* over crack front for CT specimen, $W / B = 4$ and $n = 10$.

In the end, the normalized stress for opening mode I was plotted against the normalized distance from the crack tip along the plane corresponding to the midsection, Fig. 6.16. The distance from the crack tip is the actual one, after displacement. The computed results (plotted as thin curves associated with different load levels) were consistent for large strain case and non-linear geometries. As a direct comparison, the Hutchinson–Rice-Rosengren [137-138] singular crack tip field for elastoplastic material response was calculated by the means of Shih's parameters for $n = 10$ for the approximate plane strain case $W / B = 2$. This is shown in the plot as a thick red curve going to infinity for $\frac{r * s_0}{J} = 0$:

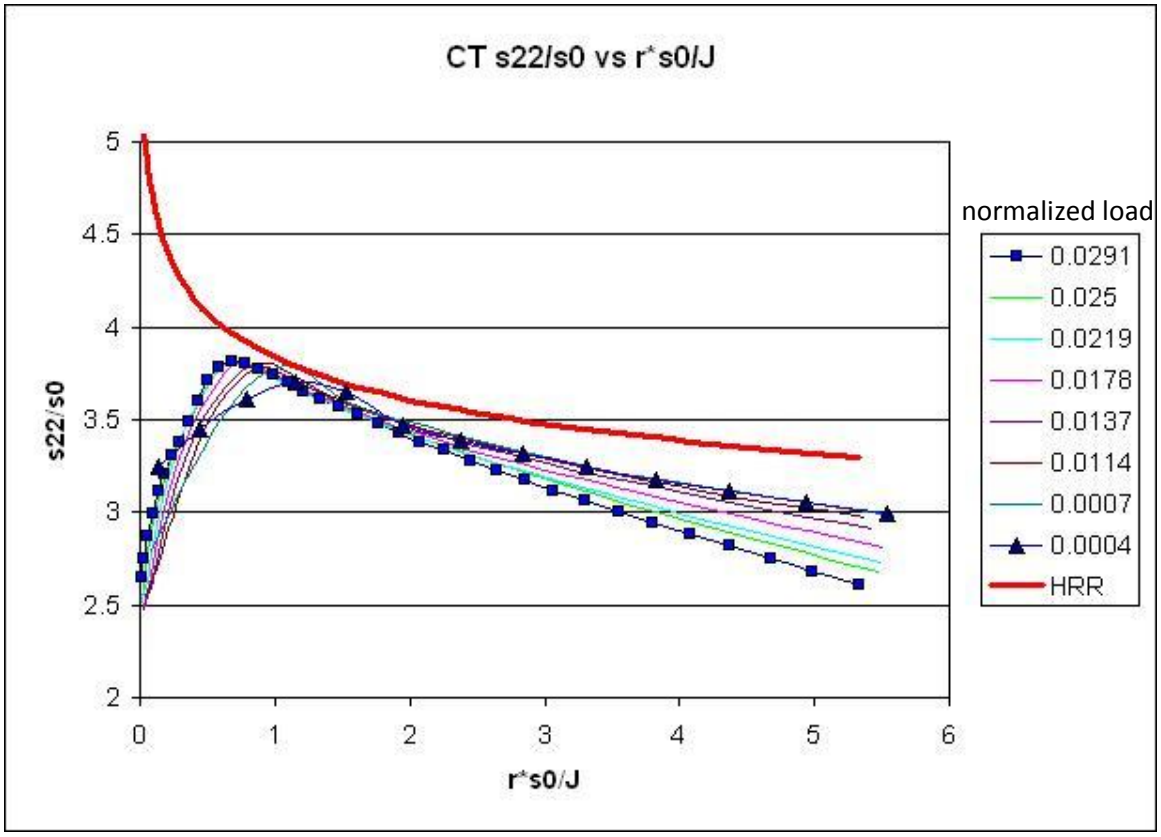

Fig. 6.16. Normalized stress against normalized distance from crack tip for CT.

In the plot, *s22* (N/mm²) is the principal stress in the direction of the applied load, *s0* (N/mm²) is the yield strength, *r* (mm) is the actual distance ahead of the crack tip, *J* (N/mm) is the computed integral value.

The theoretical stress infinity, that is the HRR field curve in Fig. 6.16, derives from the assumption that the crack tip is perfectly sharp and it remains sharp during the loading of the crack tip. When the assumption of small strains is relaxed, the crack tip blunts and the stresses in front of the crack become finite. In fact, in a finite element model with a crack, stresses near the crack tip are always finite. The opening stress reaches its maximum at a normalized distance $\frac{r * s_0}{J}$ equal to 0.5 to 2, and its value depends on material properties, specimen geometry and external loading.

6.3.3 DCT specimen

It has to be remembered that crack depth was $a / W = 0.335$ for all the cases. The line load-displacement was monitored and the load applied as a pressure on surface.

In the CT specimen case, the normalized stress for opening mode I was plotted against the normalized distance from the crack tip, along the plane corresponding to the midsection, as in Fig. 6.17. The distance from the crack tip is the actual one, after displacement. The results are still consistent for large strain case and non-linear geometries. The HRR field was been calculated by the same Shih's parameters for $n = 10$ and the approximate plane strain case $W / B = 2$.

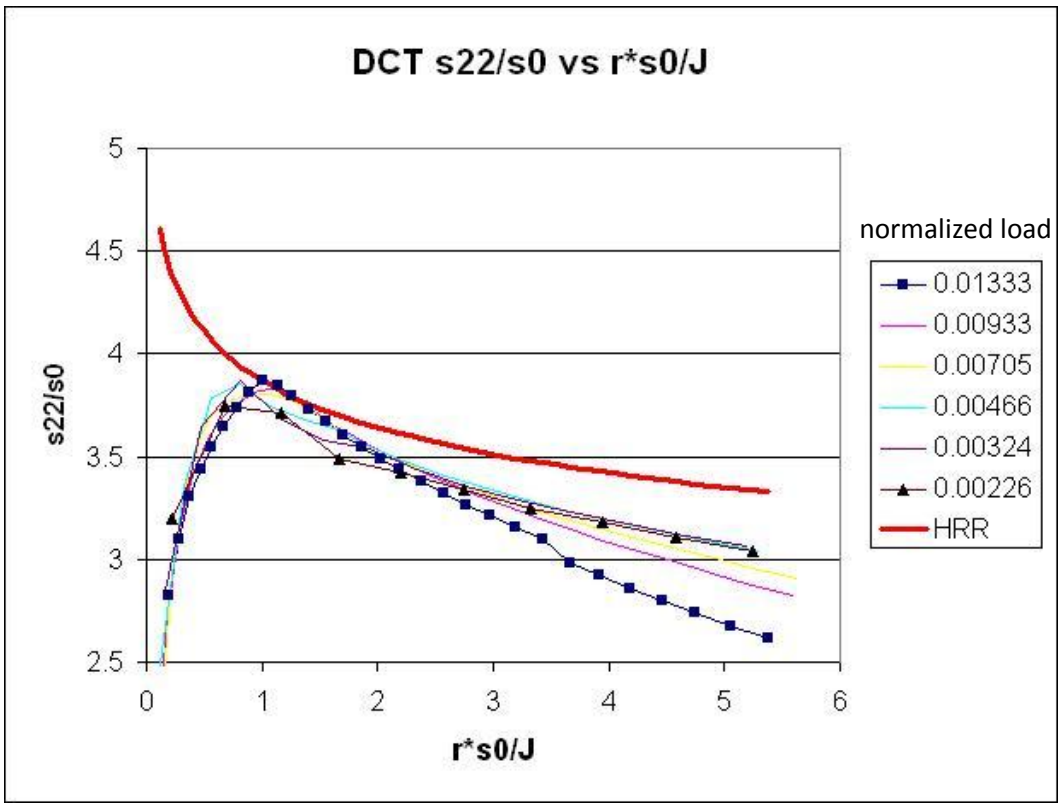

Fig. 6.17. Normalized stress against normalized distance from crack tip for DCT.

The behaviour of the large strain, finite element analysis at different load levels, compared with the small strain theoretical calculation of the HRR model, still showed the expected difference. This confirmed that CT and DCT were being analyzed starting from the same finite element analysis approach of large strain, non-linear geometries and permitted a direct comparison between the two.

For this goal, a plot of J behaviour over the crack front is shown in Figs. 6.18–6.20 for several DCT thicknesses at the elastic-plastic power parameter n = 10. The load was normalized in respect of different load-line displacements.

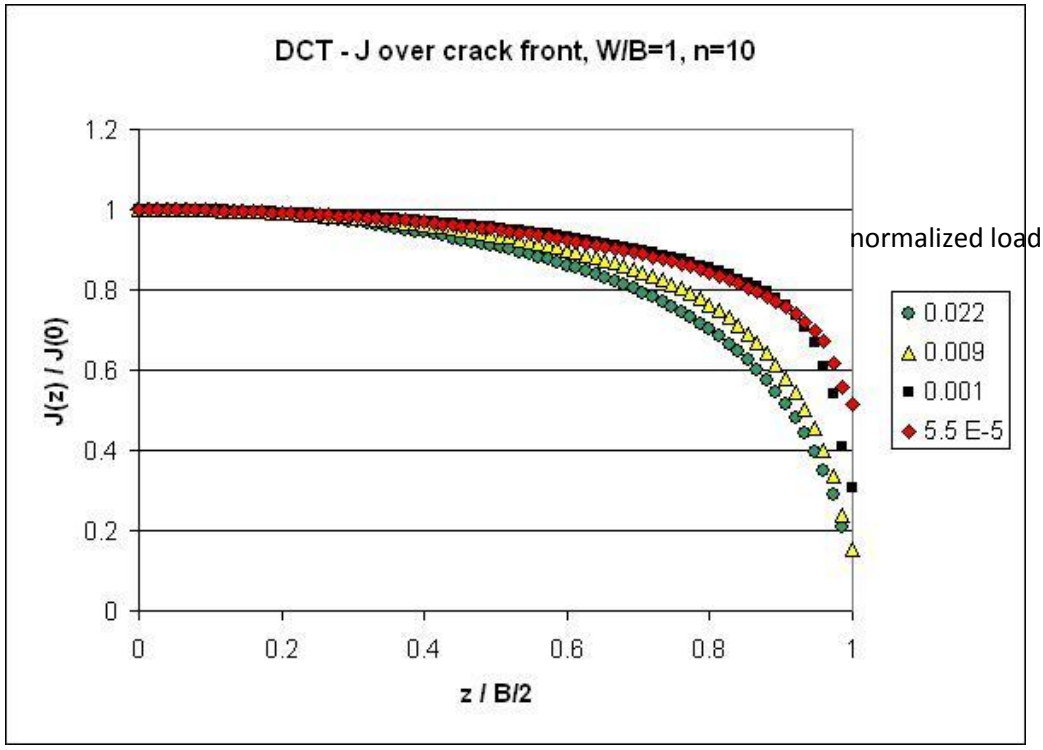

Fig. 6.18. J over crack front for DCT specimen, W / B = 1, n = 10.

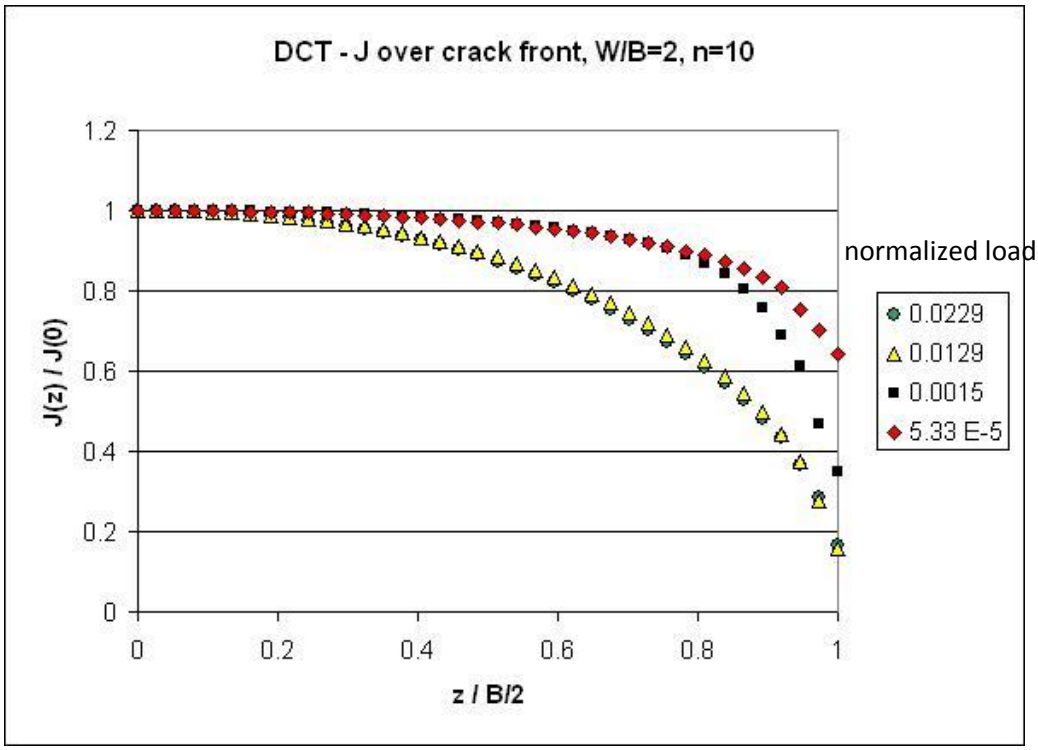

Fig. 6.19. *J* over crack front for DCT specimen, *W* / *B* = 2, *n* = 10.

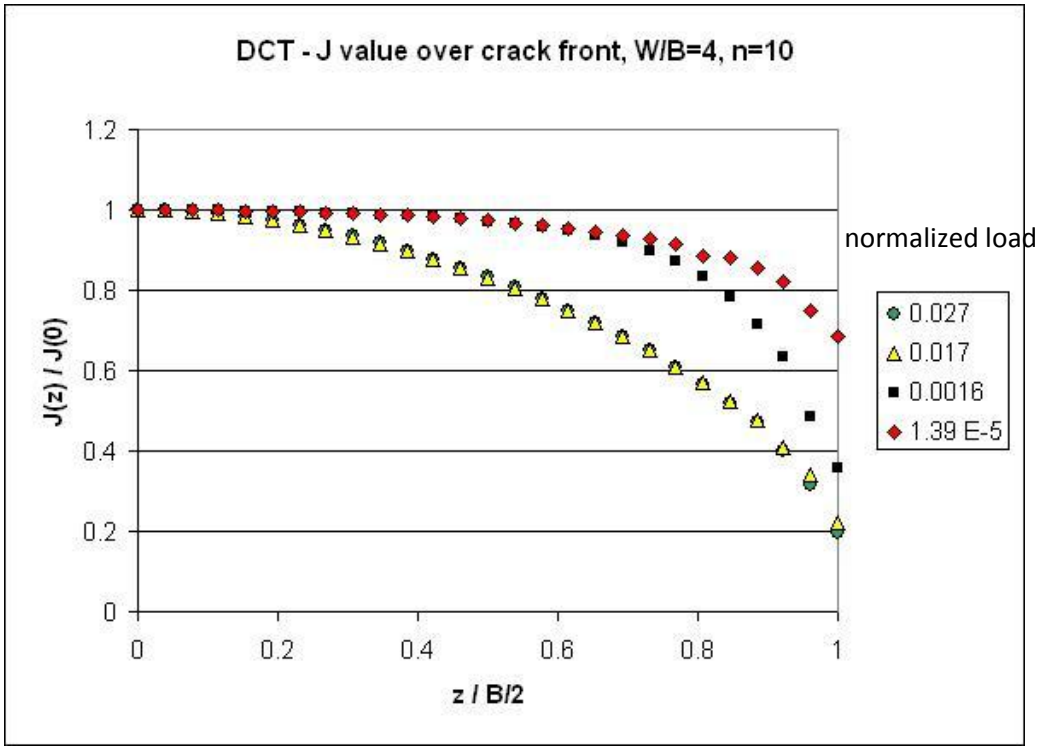

Fig. 6.20. *J* over crack front for DCT specimen, *W* / *B* = 4, *n* = 10.

The specimen initially supposed to be used for fracture toughness evaluation was the Compact Tension. A comparison with the benchmark [163] is shown in Fig. 6.21. The distribution of $J(z) / J(0)$ over the load levels of the benchmark was plotted against the same discretized values obtained by calculation.

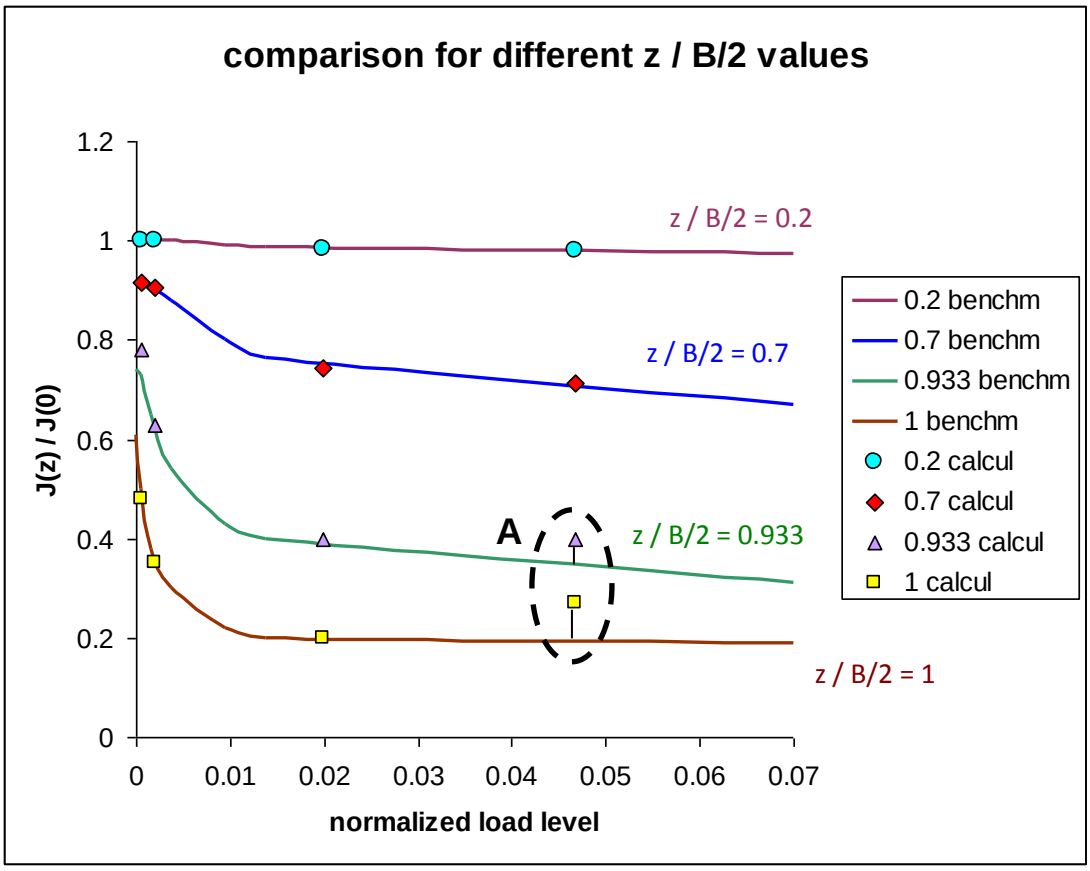

Fig. 6.21. Elastic-plastic response for CT, $W / B = 2$, $n = 10$ compared with benchmark.

Four points along the thickness line were considered, in particular: $z / B/2 = 0.2$ (near the midsection at 0.0), $z / B/2 = 0.7$ (relevantly shifted towards the outside edge), $z / B/2 = 0.933$ and $z / B/2 = 1$ (outside edge). Evidence in the dashed zone A suggests that, at higher load levels, the calculated $J(z)$ significantly differs from the benchmark when the outside part of the specimen ($z / B/2 = 0.933$ and $z / B/2 = 1$) is considered.

These edge effects were not investigated more because not directly relevant to the aim of this project. In fact, crack initiation for the given DCT was always found at midsection.

6.3.4 CT – DCT specimens comparison

It was important to investigate similarities and differences between Compact Tension and Disk Compact Tension specimens to the scope of this project. Literature is not abundant on this topic and one small Disk Compact Tension specimen was the direct reference, from [85], for fracture toughness evaluation.

The comparison was made between the parametric CT reported in [163], with $a / W = 0.6$, and the DCT specimen here taken as a benchmark [85], with $a / W = 0.335$ as used in this project. It has to be pointed out that the ASTM 1820 standard requires relatively deep cracks ($0.50 < a / W < 0.70$) because the unloading compliance technique is less sensitive for $a / W < 0.5$ [253]. Snead [85] followed ASTM 1820 for his fracture toughness experiments by fatigue pre-cracking his DCT specimen to $a / W = 0.5$.

A first comparison over the load levels applied was attempted for $n = 10$ and $W / B = 1, 2, 4$, as shown in Fig. 6.22(a)–(c):

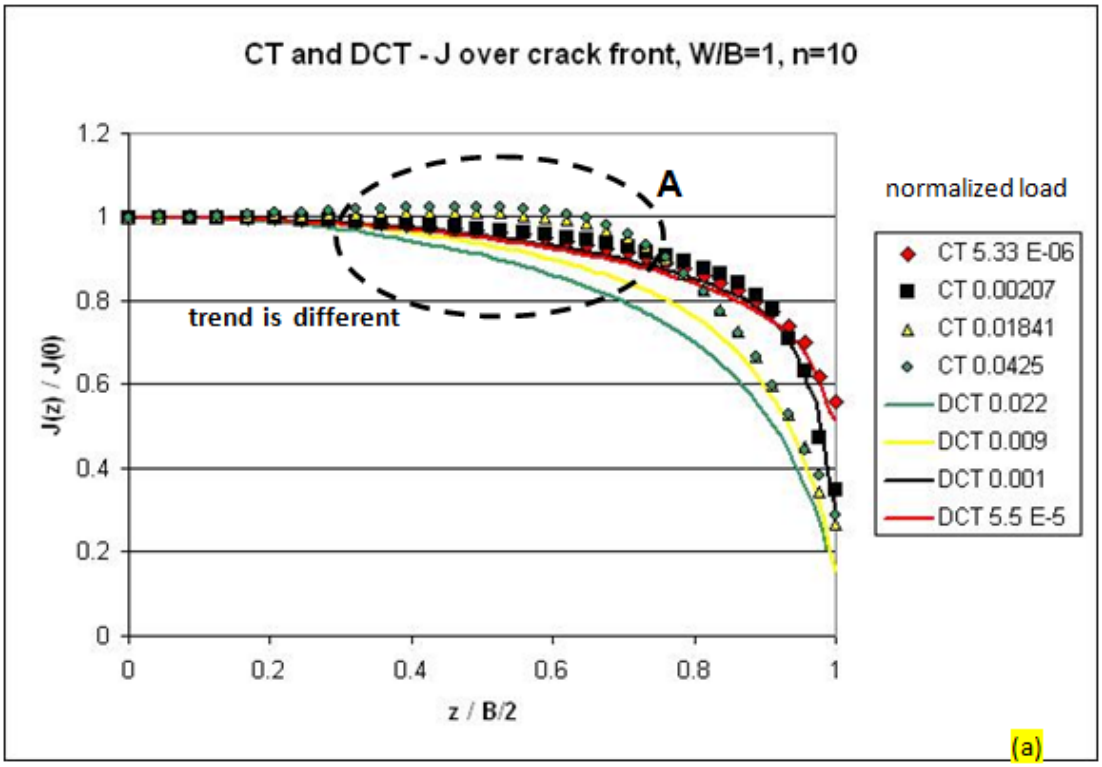

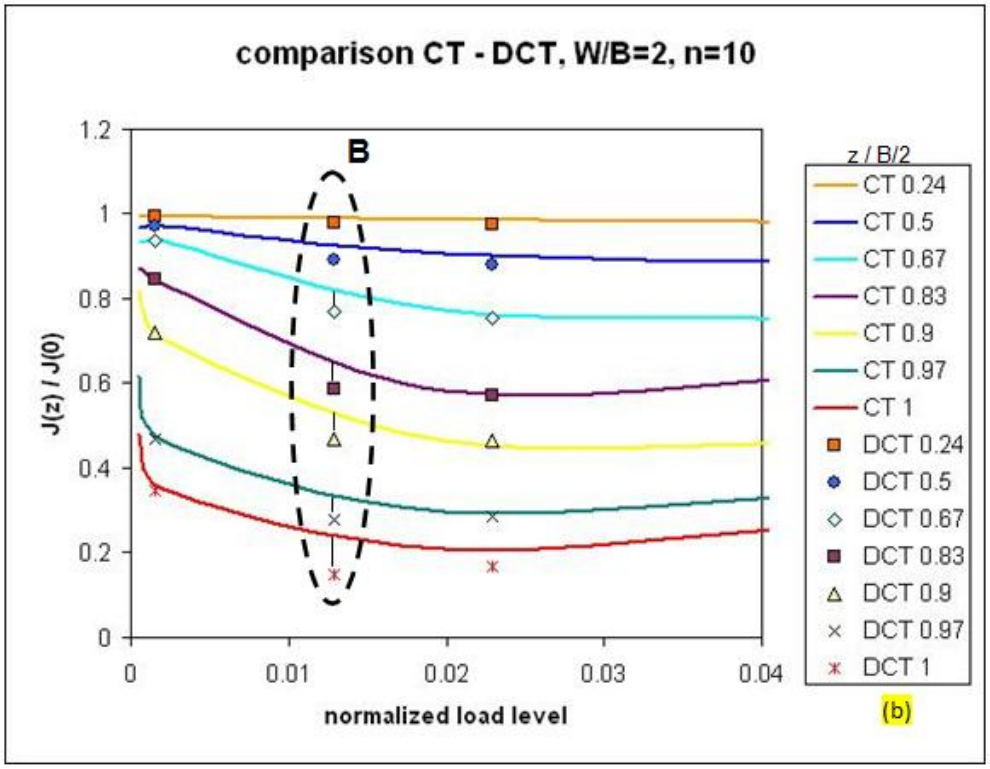

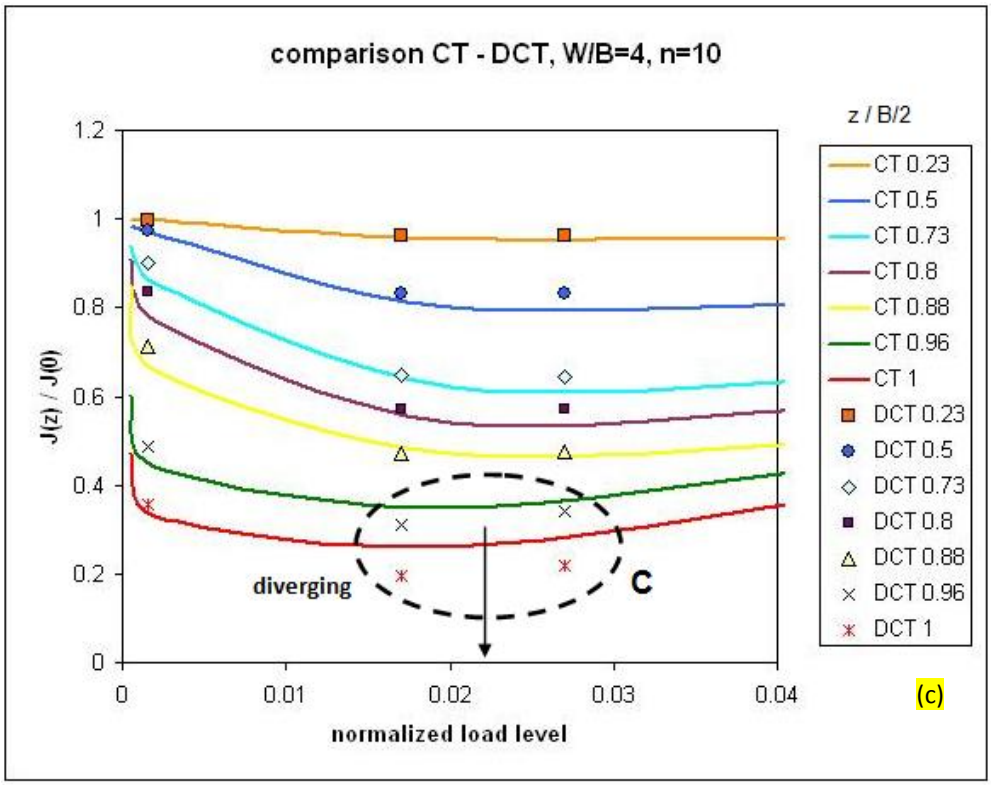

Fig. 6.22(a)-(c). *J*-integral vs. normalized load levels for CT vs. DCT.

Fig. 6.22(a) shows that the trend of *J*-integral along the crack thickness for CT and DCT, $W / B = 1$, $n = 10$, was different. In particular, CT specimen appeared to have its maximum *J*-integral value at a position z / B/2 equal to about 0.6 for increasing normalized load levels, while DCT showed its maximum J-integral value at midsection $z / B/2 = 0$, which also exhibited a progressively decreasing value while the load level became higher. It has to be noted that, to the scope of this project, $W / B = 1$ was not directly important because $W / B = 2$ and $W / B = 4$ aspect ratios were the main references reported in [85].

For $W / B = 2$ and $W / B = 4$, the continuous curves of normalized *J*-integral against normalized load levels for CT specimens were compared with the discrete points corresponding to the load levels calculated at the same positions, along the crack tip, for DCT specimens. That way, it was possible to make a direct comparison between the specimens, as shown in Figs. 6.22(b)-(c). The main difference for $W / B = 4$, $n = 10$, was spotted at the outside part of the specimens, where the discrete values encircled in A, corresponding to DCT specimen, appeared to diverge in trend from the continuous curve corresponding to CT. This was probably due to edge effects but, being the crack developed in the midsection (J is max at $z / B/2 = 0$ for every load level), it was not important, so the specimens were considered comparable and admitted to a further future stage of analysis. Fig. 6.22(b) showed a direct comparison for $W / B = 2$ and $n = 10$ and put in evidence a significant difference for DCT normalized load level 0.0129, encapsulated in zone B, that difference increasing from about 5% at $z / B/2 = 0.5$ up to about 40% at $z / B/2 = 1$ with regards to the correspondent CT values. On the other hand, lower and higher load level associated values appeared to be almost uniform. To the scope of this project, this different behaviour could be critical, because DCT specimens of aspect ratio $W / B = 2$ are widely used in the literature taken as the main experimental reference for this project [85].

That comparative work provided a first investigation about the trend of the relevant parameters and the criticalities in the modelling. From a practical point of view, however, the experiments with DCT specimen were found to play no role in determining the fracture toughness of the material.

6.4 Fracture toughness modelling

Validation for small DCT and sharp-notched round bar experiments is going to be presented in this Section. After that, fracture toughness values were estimated.

6.4.1 Small Disk Compact Tension specimen

Validation was not successful, as can be seen from Fig. 6.23. The presence of a considerable amount of compliance "shifted" the curves to the right. It means that more displacement than expected was obtained at a given load level.

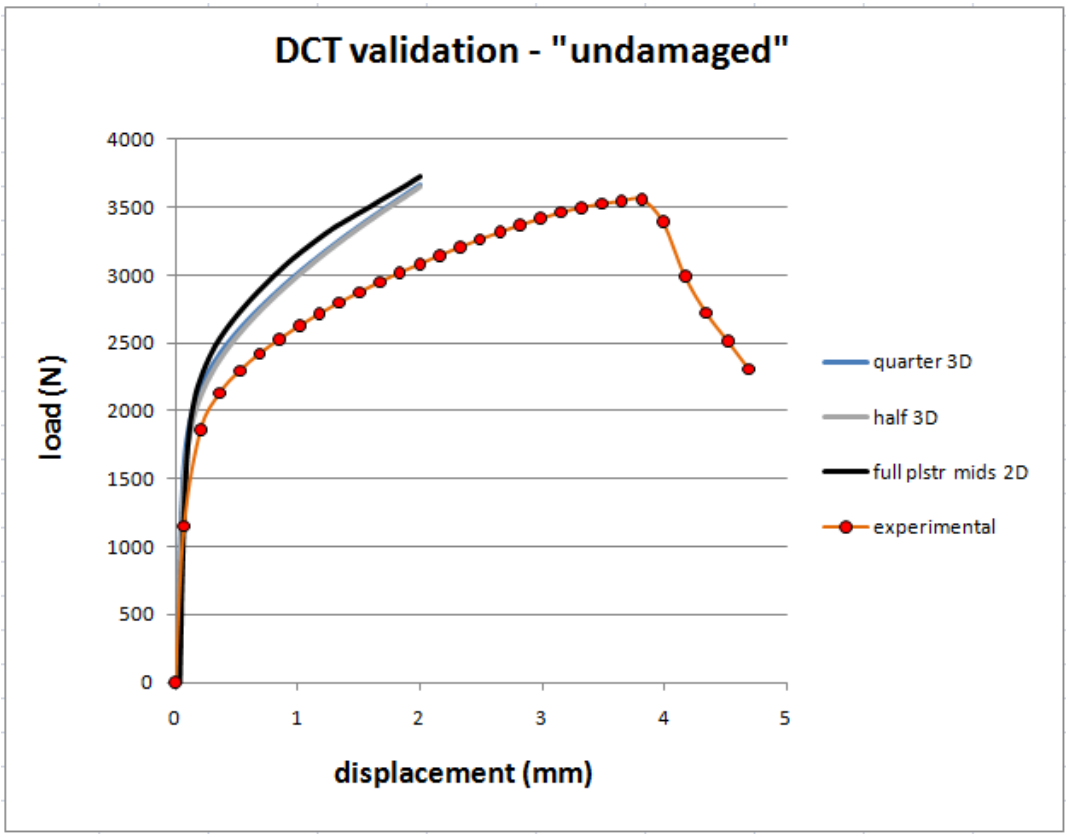

Fig. 6.23. Failed validation for disk compact specimens.

The numerical analysis was repeated using three different models, so that errors in the set up of the simulations were avoided, but this did not solve the problem.

In particular, they were used:

- one quarter 3D model with 2 planes of symmetry;
- half 3D model with symmetry at the crack front plane;
- 2D model of the midsection of the specimen, plane strain elements.

One spring model could have been tried to account for compliance numerically, but it was not attempted. In fact, fracture toughness evaluation was however compromised by not having reliable experimental load vs. load-line displacement plots.

The set-up of the experiment was then reconsidered in order to understand the origin of that compliance. One reason could be identified in the position of the extensometer on the clevis system, as in Fig. 6.24, instead of on the specimen (impossible to locate there). The clevis system in Fig. 3.21 was hardened, but compliance still affected the results.

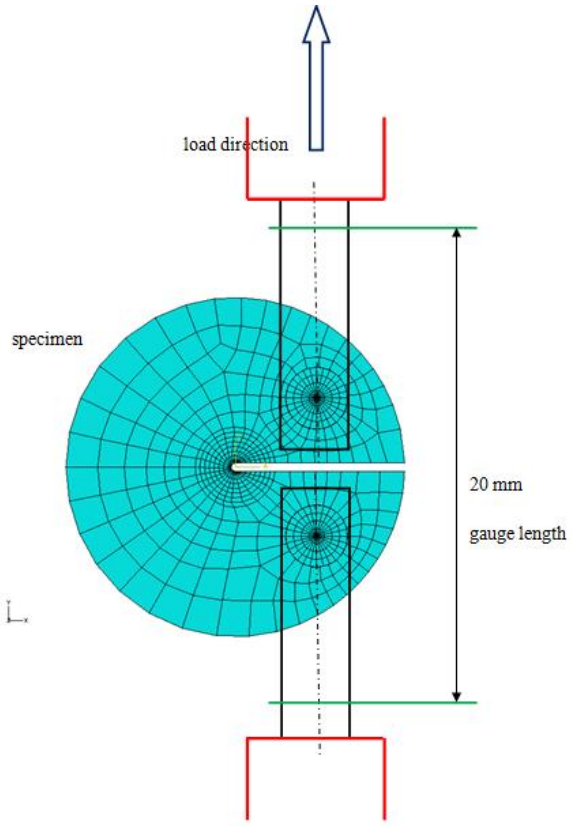

Fig. 6.24. Position of the extensometer on the disk compact specimen.

Analytical results for the 40% eng. strain "damaged" material were considered to be too conservative and lacking one clear physical explanation. One other consideration came from the 3D models. They confirmed that volume deformation happened at the outside edge of the specimen, as in Fig. 6.25 for the "undamaged" material, so invalidated the plane strain assumption from the benchmark [85].

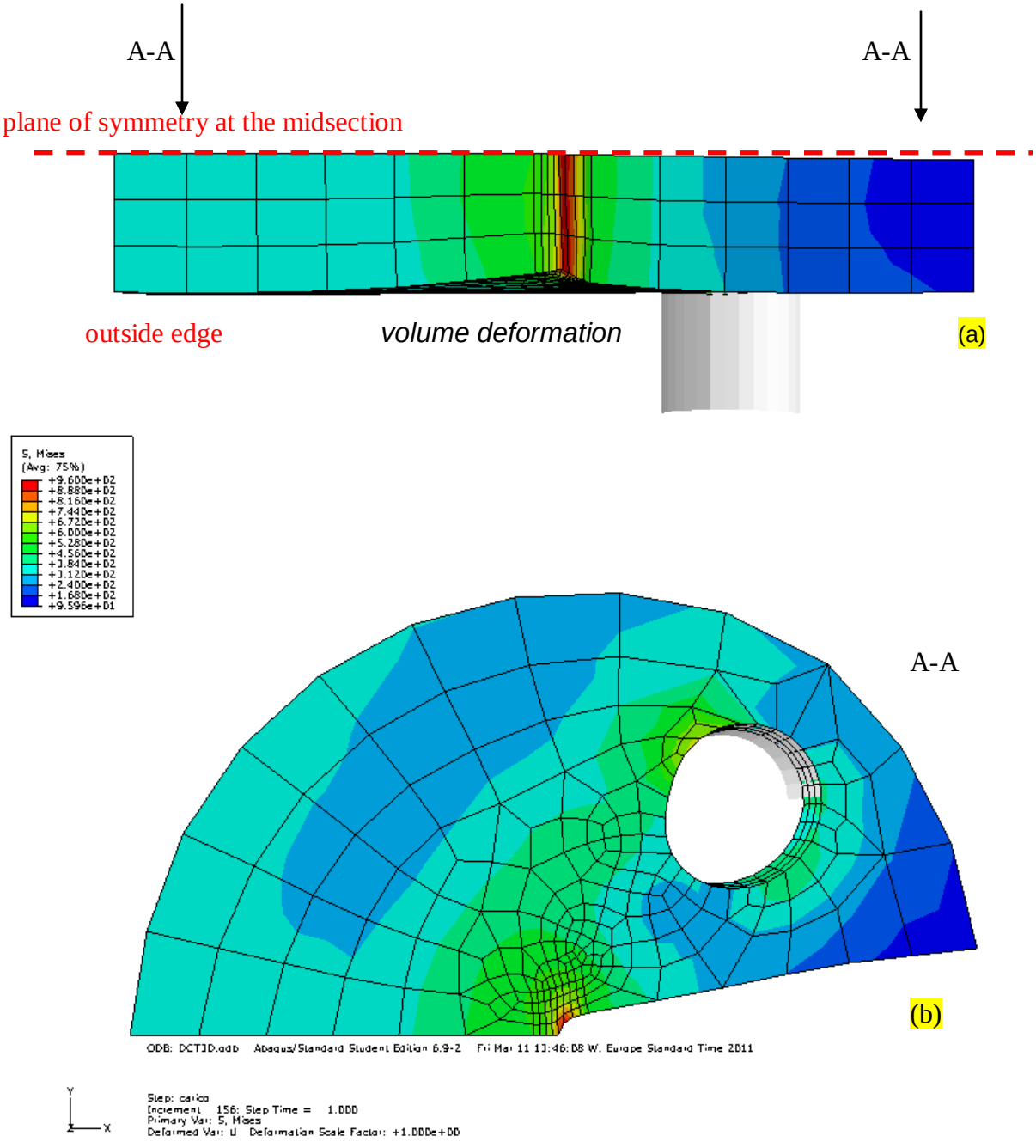

Fig. 6.25(a)-(b). Deformation of "undamaged" disk compact specimen at crack opening.

6.4.2 Sharp-notched round bar specimen

One preliminary note to the numerical results, related to the aspect ratio of the notch of the specimen in Fig. 3.16, is to the plastic zone that develops under uniaxial stress. According to Scibetta [171], the aspect ratio a / R that maximises J before widespread plasticity is in the range 0.4 – 0.6. This is shown in Fig. 6.26.

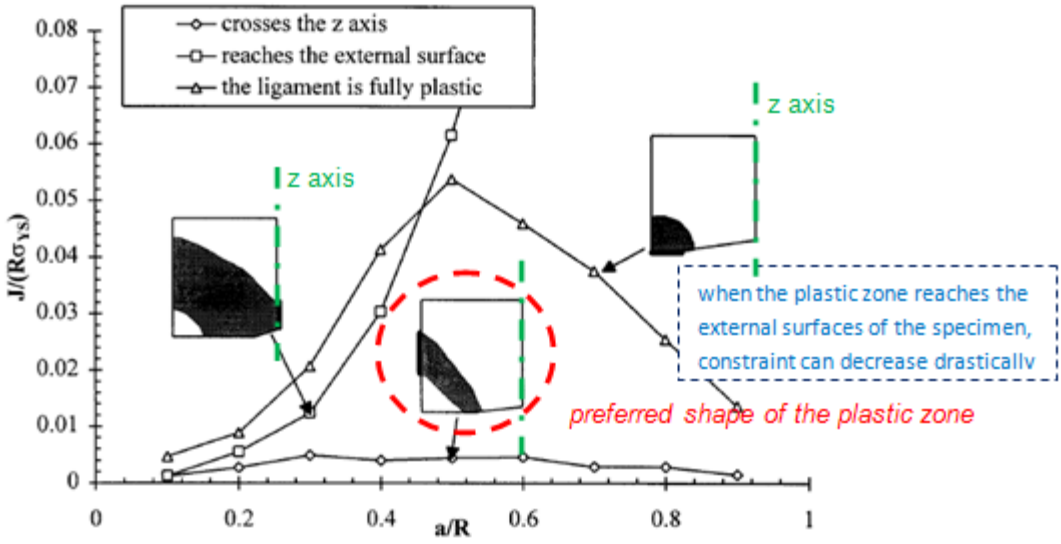

Fig. 6.26. Aspect ratio relation with plasticity for sharp-notched specimens [127].

Scibetta adds that this plot cannot state specimen size requirements in a direct manner. It was used here to compare the loss of constraint, if any, produced by testing sharp-notched bars machined from differently "damaged" material. The aspect ratio employed in this project was $a / R = 0.222$.

The experimental plots in Fig. 5.33 were validated by finite element analysis. Validation did not take into account the propagation of the crack, that is to say only displacements up to the fracture initiation zone were considered for each specimen. For each "damaged" state, the constitutive law was modified accordingly to the process undergone. The plastic law and the parameters of the Gurson model were retrofitted. Details are given in Table 6.3 and explained case by case.

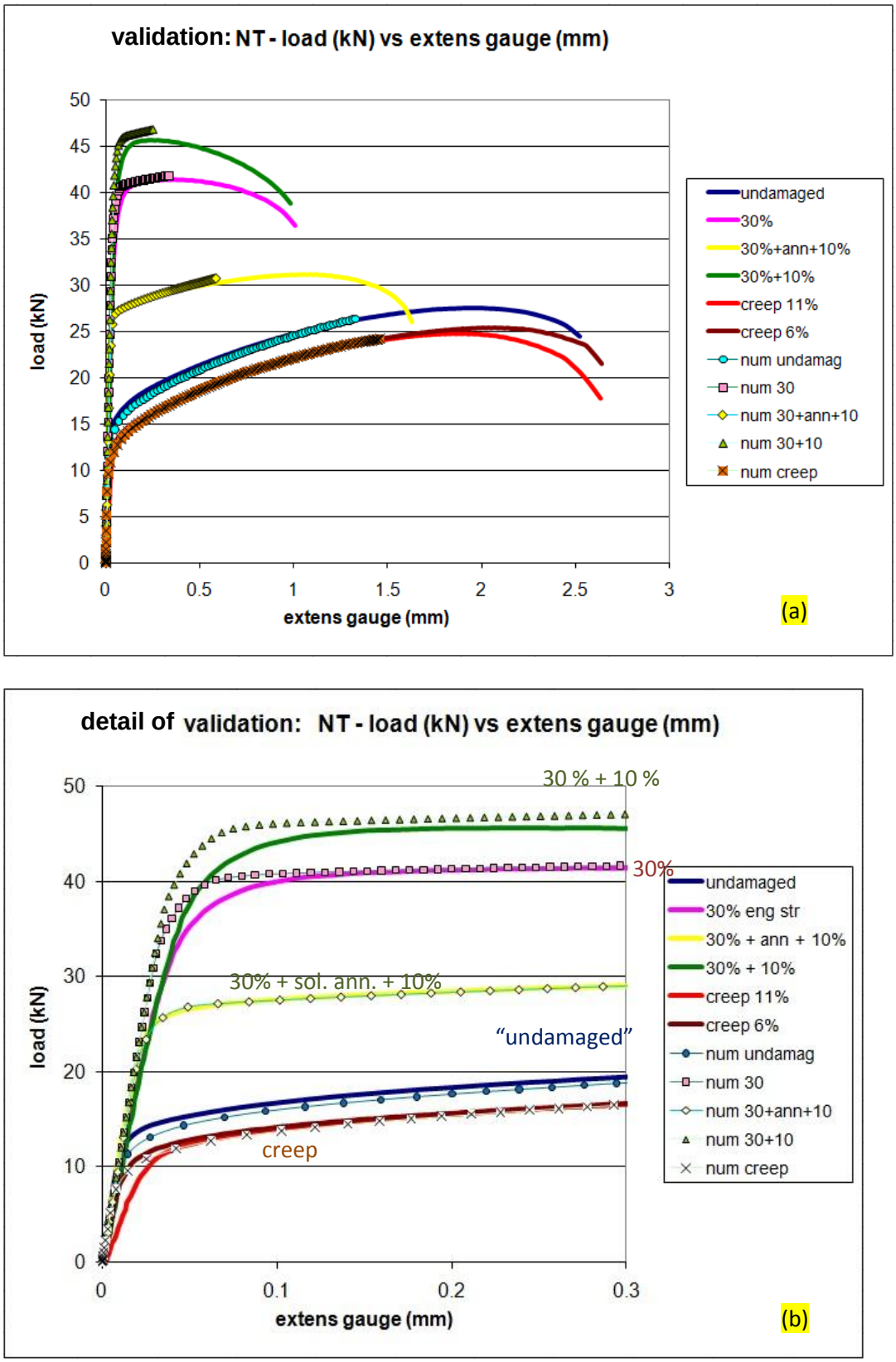

Fig. 6.27(a)-(b). Validation of notched tensile specimens results (a) and detail (b).

6.4.2.1 Retrofitting of the constitutive models for "damaged" materials

prestr + creep 900°		creep 1000 °C		"undamaged"	
127	0	127	0	167	0
133	6.23E-05	133	6.23E-05	173	6.23E-05
139	8.50E-05	139	8.50E-05	179	8.50E-05
145	0.000122	145	0.000122	185	0.000122
151	0.000181	151	0.000181	191	0.000181
157	0.000271	157	0.000271	197	0.000271
163	0.000416	163	0.000416	203	0.000416
169	0.000589	169	0.000589	209	0.000589
175	0.000817	175	0.000817	215	0.000817
181	0.00106	181	0.00106	221	0.00106
187	0.00137	187	0.00137	227	0.00137
193	0.00173	193	0.00173	233	0.00173
199	0.00218	199	0.00218	239	0.00218
205	0.00271	205	0.00271	245	0.00271
211	0.00336	211	0.00336	251	0.00336
217	0.00415	217	0.00415	257	0.00415
223	0.00507	223	0.00507	263	0.00507
229	0.00619	229	0.00619	269	0.00619
235	0.00748	235	0.00748	275	0.00748
241	0.00893	241	0.00893	281	0.00893
247	0.0106	247	0.0106	287	0.0106
260	0.0147	260	0.0147	300	0.0147
285	0.0244	285	0.0244	325	0.0244
310	0.0355	310	0.0355	350	0.0355
335	0.0472	335	0.0472	375	0.0472
360	0.0595	360	0.0595	400	0.0595
375	0.0722	385	0.0722	425	0.0722
390	0.0853	410	0.0853	450	0.0853
405	0.0991	435	0.0991	475	0.0991
425	0.114	460	0.114	500	0.114
445	0.129	485	0.129	525	0.129
465	0.145	510	0.145	550	0.145
485	0.162	535	0.162	575	0.162
505	0.179	560	0.179	600	0.179
525	0.197	585	0.197	625	0.197
545	0.216	610	0.216	650	0.216
565	0.236	635	0.236	675	0.236
585	0.256	660	0.256	700	0.256
605	0.278	685	0.278	725	0.278
625	0.3	710	0.3	750	0.3
645	0.322	735	0.322	775	0.322
665	0.345	760	0.345	800	0.345
705	0.374437	810	0.374437	850	0.374437
745	0.412489	860	0.412489	900	0.412489
785	0.45054	910	0.45054	950	0.45054
825	0.488592	960	0.488592	1000	0.488592
865	0.526644	1010	0.526644	1050	0.526644
905	0.564696	1060	0.564696	1100	0.564696
945	0.602747	1110	0.602747	1150	0.602747
985	0.640799	1160	0.640799	1200	0.640799
1025	0.678851	1210	0.678851	1250	0.678851
1065	0.716903	1260	0.716903	1300	0.716903
1105	0.754954	1310	0.754954	1350	0.754954
1145	0.793006	1360	0.793006	1400	0.793006
1185	0.831058	1410	0.831058	1450	0.831058
1225	0.86911	1460	0.86911	1500	0.86911
1265	0.907	1500	0.907		

Values in the table must be read as follows: true stress (MPa) and true plastic strain (mm/mm) for each state considered.

Starting from the "undamaged" law shown in the third column, the creep laws were retrofitted in order to validate the experiments. Initial void volume fraction was considered equal to the "undamaged" state, that is to say $d_o = 0.9986$. In fact, the sharp-notched round bars were quite large. On the other hand, the voids produced from creep damaging experiments were confined into a small volume near the fracture zone. There were no voids into the sharp-notched bars at all, apart of the "undamaged" quantity inferred by the Franklin formula.

Then, the voids produced were not taken into account in this fracture toughness experiment. On the contrary, the voids effect was superimposed numerically, at a later stage, in the form of parametric initial void volume fraction. The actual value of voids produced experimentally was among the parametric set.

30%+sol.ann.+10%			30%		30% + 10%	
463	0					
475	0.0059					
500	0.0208					
525	0.0358					
550	0.0518					
575	0.0688					
600	0.0858					
625	0.1038					
650	0.1228					
675	0.1428					
700	0.1628		703	0		
725	0.1848		725	0.0183		
750	0.2068		750	0.0403		
775	0.2288		775	0.0623	799	0
800	0.2518		800	0.0853	800	0.0113
850	0.281237		850	0.114737	850	0.040737
900	0.319289		900	0.152789	900	0.078789
950	0.35734		950	0.19084	950	0.11684
1000	0.395392		1000	0.228892	1000	0.154892
1050	0.433444		1050	0.266944	1050	0.192944
1100	0.471496		1100	0.304996	1100	0.230996
1150	0.509547		1150	0.343047	1150	0.269047
1200	0.547599		1200	0.381099	1200	0.307099
1250	0.585651		1250	0.419151	1250	0.345151
1300	0.623703		1300	0.457203	1300	0.383203
1350	0.661754		1350	0.495254	1350	0.421254
1400	0.699806		1400	0.533306	1400	0.459306
1450	0.737858		1450	0.571358	1450	0.497358
1500	0.77591		1500	0.60941	1500	0.53541

In the case of strain hardened material, plastic laws were calibrated from the interrupted tensile tests plots shown in Fig. 5.12.

It was also presumed some presence of voids from decohesion, as shown in Fig. 5.13. It was then expected an initial void volume fraction larger than the "undamaged" material. That was tentatively retrofitted numerically after the sharp-notched round bar experiments, as shown in Section 6.4.3.

Table 6.3. Constitutive laws for "damaged" materials.

The parameters of the Gurson-Tvergaard-Needleman model also needed reconsideration. In particular, the following reasoning was applied.

The initial void volume fraction, as estimated by using the Franklin formula for "undamaged" 316L as vvf = 0.0014, was no more valid for strain hardened material. In fact, this had been subjected to cold work and, for that reason, was expected to show higher void volume fraction in the volume from decohesion. The "undamaged" value was still valid for creep at 1000 °C "damaged" material (for which it was shown that the void fraction was negligible at 5 mm distance from the fracture line) and for the 7% prestrained + creep at 900 °C "damaged" material (which did not exhibit voids).

q_1 and q_2 parameters from Tvergaard – Needleman are linked to softening in the sense that their increase induces more softening in the material, enhanced by void growth. The

starting values q_1 = 1.25 and q_2 = 1 were obtained from the calibration of "undamaged" 316L. Corigliano [254], Vadillo [186] and Benseddiq [187] suggest that q_1 and q_2 decrease with pre-strained material, because lower softening is expected. They also suggest that q_1 and q_2 decrease with increasing initial porosity. In addition, the increase of q_2 raises the effect of triaxiality on the yield locus and strongly reduces the collapse stress of a voided cell: if q_2 is reduced, then, we ask for higher stress, that is we raise the yield limit.

The parameters for the Gaussian strain controlled nucleation from Chu - Needleman, established as ε_N = 0.3 (the strain for which 50% of the inclusions are broken), s_N = 0.1 (the standard deviation on the nucleation strain), f_N = 0.04 (the volume fraction of inclusions at which damage can be nucleated) for "undamaged" 316L, needed to be reconsidered for the strain hardened material. It was not possible to perform microstructural analysis of the "damaged" material. On a theoretical basis, ε_N should be lower than 0.3, which is good for "undamaged" material, in the case nucleation is accelerated. It was argued that a 30% pre-strained material should have already experienced some nucleation and that its ε_N was actually lower. Standard deviation was supposed to remain unchanged. Volume fraction of inclusions at which damage can be nucleated should have been lower too, because part of it had already nucleated.

That said, the changes for each "damaged" state are presented and discussed.

6.4.3 Fracture toughness initiation values

40% cold worked specimen: the plastic flow implemented into the numerical model for this case was presented in Table 6.3. The initial void volume fraction was negligible according to metallography shown in Fig. 5.14. Nevertheless, decohesion of inclusions at

single points and at slag locations was supposed to happen, as shown in Fig. 5.13. The number was then obtained as a continuous, average value by retrofitting the numerical model on the sharp-notched bar experimental curve, as shown in Fig. 6.28:

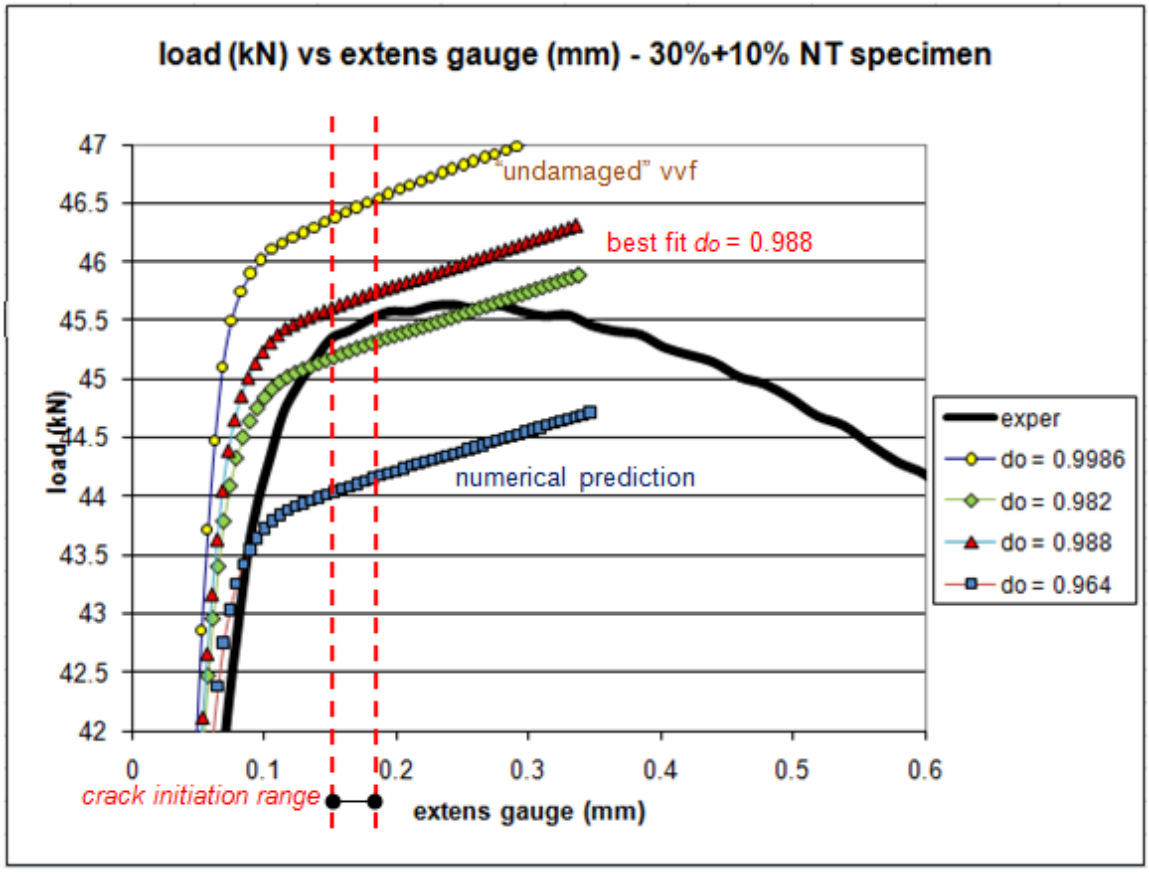

Fig. 6.28. 40% strain hardened specimen's crack initiation range.

From the plot, it can be seen that the "undamaged" void volume fraction (d_o = 0.9986 in terms of density, as if nothing happened in terms of void development) was too low to fit the curve: more voids should have been considered. It can also be seen that the void volume fraction predicted to happen at 40% engineering strain from using the "undamaged" model, that is density d_o = 0.964, was too high: too many voids were considered. The best fit was somewhere between these numbers and was found at d_o = 0.988, that is 1.12% void volume fraction. This was assumed to be the actual quantity of voids homogeneously present into the material after the sharp-notched bar test. That fit is debatable and not supported experimentally. The damage mechanism

undergone by the 40% pre-strained specimen, machined as a sharp-notched round bar and subjected to uniaxial tensile test until coalescence and failure, must be considered. It was not possible to perform metallography of this specimen after the test. Results from a very similar test performed on "as received" material (20% cold worked), shown in Fig. 5.9 and Fig. 5.29, may help give a trend. They show that some generation of voids happened before failure and that it was estimated at 2% to 4% volume fraction from the fracture line and up to 1 mm distance. It appears that the GTN model was not able to capture properly the damage progression for this case, which was not ductile and did not follow the void growth model implied by Gurson. Works from Xue [142], Zhang [255] and Pardoen [256] extended the GTN model to include Thomason's findings and might have been useful in this case. In the given circumstances, they were out of the reach of this project. They may be considered for future work in this line of research.

The other parameters of the Gurson-Tvergaard-Needleman model were not decisive for the fit in Fig. 6.28. Their value was modified relying upon different considerations.

As for q_1 and q_2, it was considered the state of the specimen greatly hardened. Their values were reduced to $q_1 = 1.15$ and $q_2 = 0.9$ respectively. Corigliano [254] reports that fitting these values is somewhat arbitrary and it does not modify the load vs. displacement plot, but only the maximum principal stress, that is to say the equivalent plastic strain at failure. In this case, the fracture happened in a brittle-like manner, so this fitting affected the value given to the fracture criterion.

The values for the nucleation parameters ε_N, s_N, f_N were modified in order to account for the actual strain present into the specimen before the sharp notch test, that is true plastic strain = 0.3337 from superimposed 40% engineering prestrain. In particular, they were put at $\varepsilon_N = 0.001$ (it was $\varepsilon_N = 0.3$ for the "undamaged" state), so that nucleation resumed as soon the new plastic regime started; $s_N = 0.1$, without modifying the original value; $f_N = 0.01$ (it was $f_N = 0.04$ for the "undamaged" case) in order to account for the missing quantity of void fraction still to nucleate at true plastic strain = 0.3328.

That said and keeping in mind that crack propagation usually starts slightly before the peak load value in the load vs. displacement plot, considering Fig. 6.28 it was estimated that fracture toughness initiation had to be estimated for displacements in the range 0.15 – 0.18 mm. That gave as a numerical result for J = 56 – 65 N/mm, a stable value occurring at the 10th contour of the numerical model in ABAQUS and the conservative case here being J_c = 65 N/mm. At that value, the numerical package gave as a fracture criterion one maximum principal stress = 1583 N/mm², as shown in Fig. 6.29.

This maximum principal stress was also assumed to be the fracture criterion while repeating the numerical calculations for different values of initial void volume fraction (namely 0.0014, 0.005, 0.01, 0.015, 0.02, 0.025, 0.03, 0.035, 0.04, 0.045, 0.05, chosen in range experimentally obtained during this project). It became evident from Table 6.4 that for initial void volume fraction values 0.035 and higher, the dominant fracture criterion became vvf = 0.09 as it was for the other, more ductile cases.

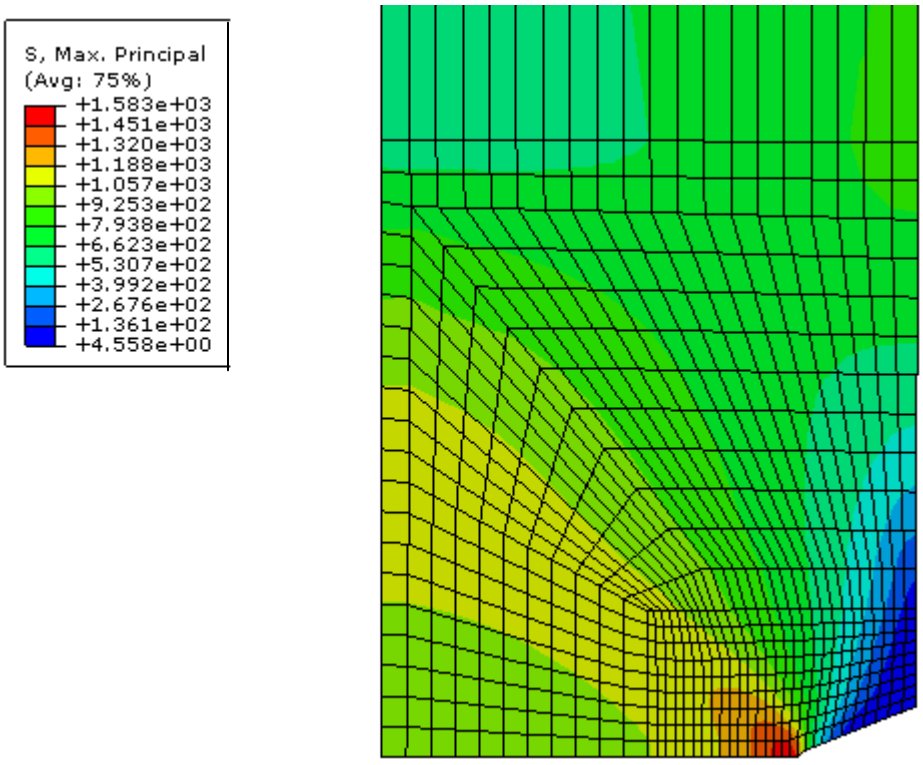

Fig. 6.29. Fracture criterion assumed for 40% strained specimen.

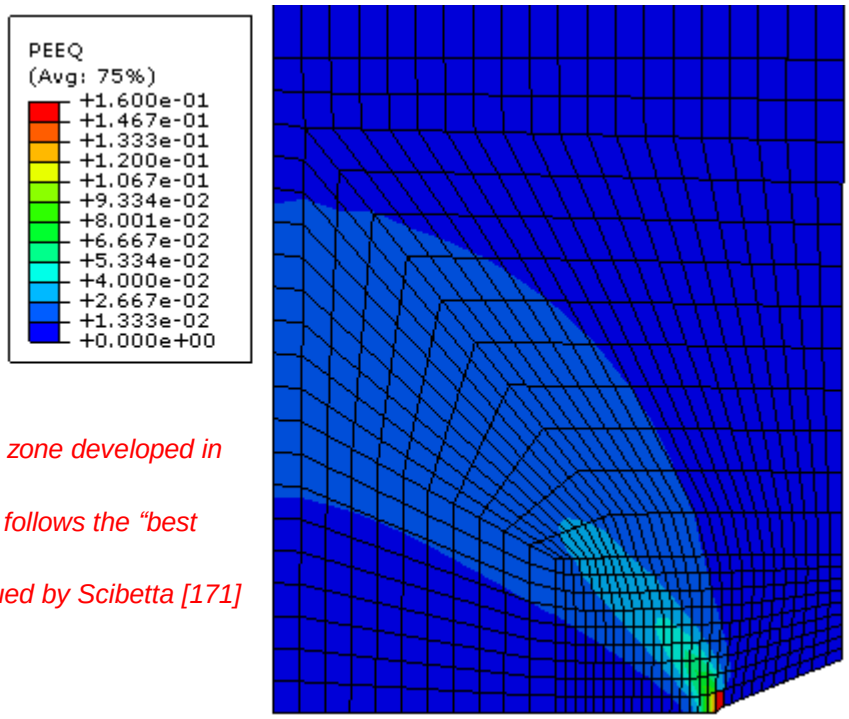

the plastic zone developed in the model follows the "best case" argued by Scibetta [171]

Fig. 6.30. Equivalent plastic strain at fracture for 40% strained case.

Fig. 6.30 addresses numerically study about plastic zone and loss of constraint from Scibetta [171], as reported in Fig. 6.26. This 40% eng. strain "damaged" material appeared to show a small loss of constraint, in the sense that the plastic zone did not reach the external surface. Creep at 1000 °C "damaged" material was also investigated.

30% cold worked specimen: as described for the previous case, the initial void volume fraction was inferred from a fit procedure and found to give a vvf = 0.4%, as can be seen in the following Fig. 6.31. The other parameters in the Gurson-Tvergaard-Needleman model were set as follows: q_1 = 1.18 and q_2 = 0.93 (suggesting lower hardening than 40% strained specimen); ε_N = 0.001 (suggesting that nucleation happens as soon as possible), s_N = 0.1, f_N = 0.02 (in order to account for the missing quantity of void fraction still to nucleate at true plastic strain = 0.2589). Crack initiation was estimated to happen at extension gauge = 0.18 – 0.22 mm from the experimental plot; the latter value was taken as a conservative case, giving J_c = 73 N/mm.

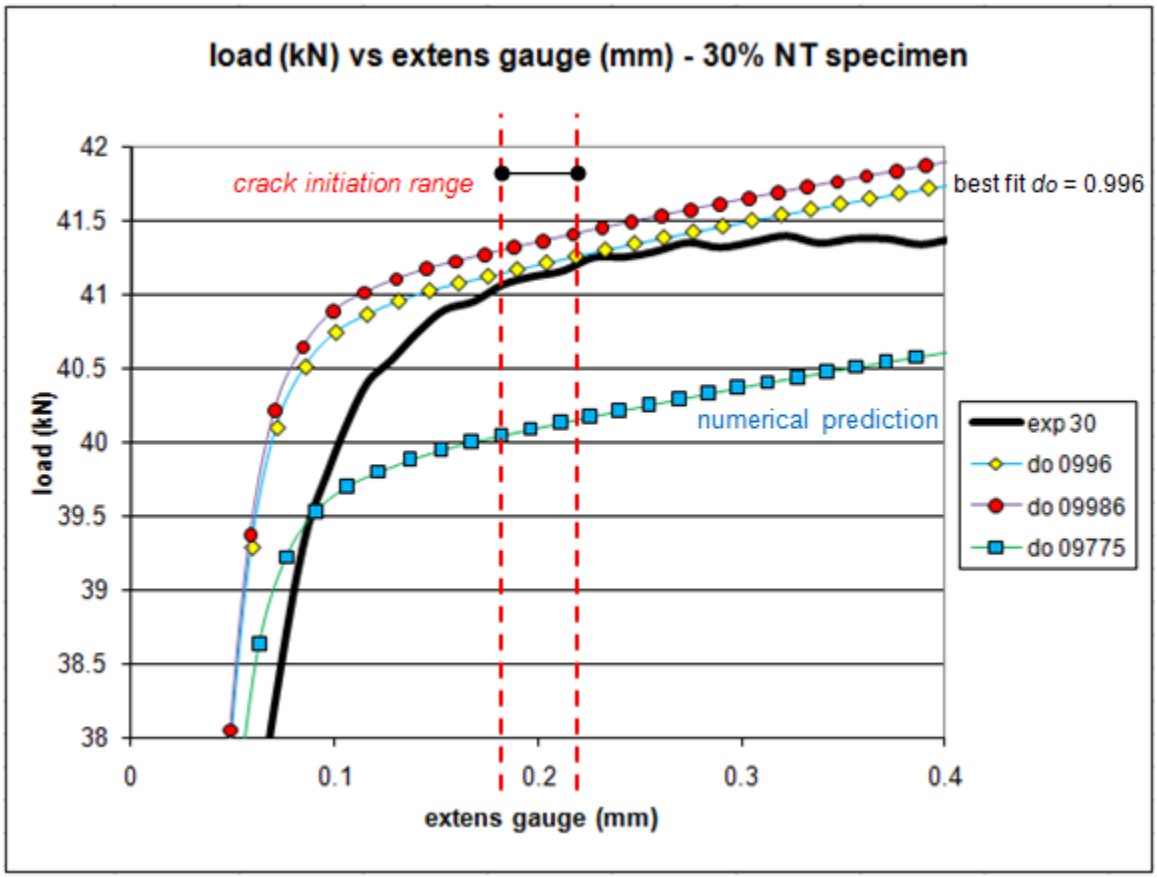

Fig. 6.31. 30% strain hardened specimen's crack initiation range.

As for the case of 40% eng. strain, the dominant fracture criterion switched from the brittle maximum principal stress to the ductile void volume fraction critical value, here for initial void volume fraction 0.025 and greater.

30% + sol. ann. + 10% strained specimen: in this case, the values were vvf = 0.0014 (the same of the "undamaged" case); q_1 = 1.2 and q_2 = 0.98 (suggesting noticeably lower hardening than 30% strained specimen); ε_N = 0.2, s_N = 0.1, f_N = 0.04 (suggesting that nucleation still had to come, but a plastic strain value lower than the one imposed for the "undamaged" case and involving the entire fraction destined to that use).

That said, the computation hits the void volume fraction criterion vvf = 0.09 at a gauge extension value compatible with the expected behaviour (a bit before the peak stress in the load vs. displacement plot) and the fracture initiation value occurred at J_c = 170 N/mm, as can be seen in Fig. 6.32.

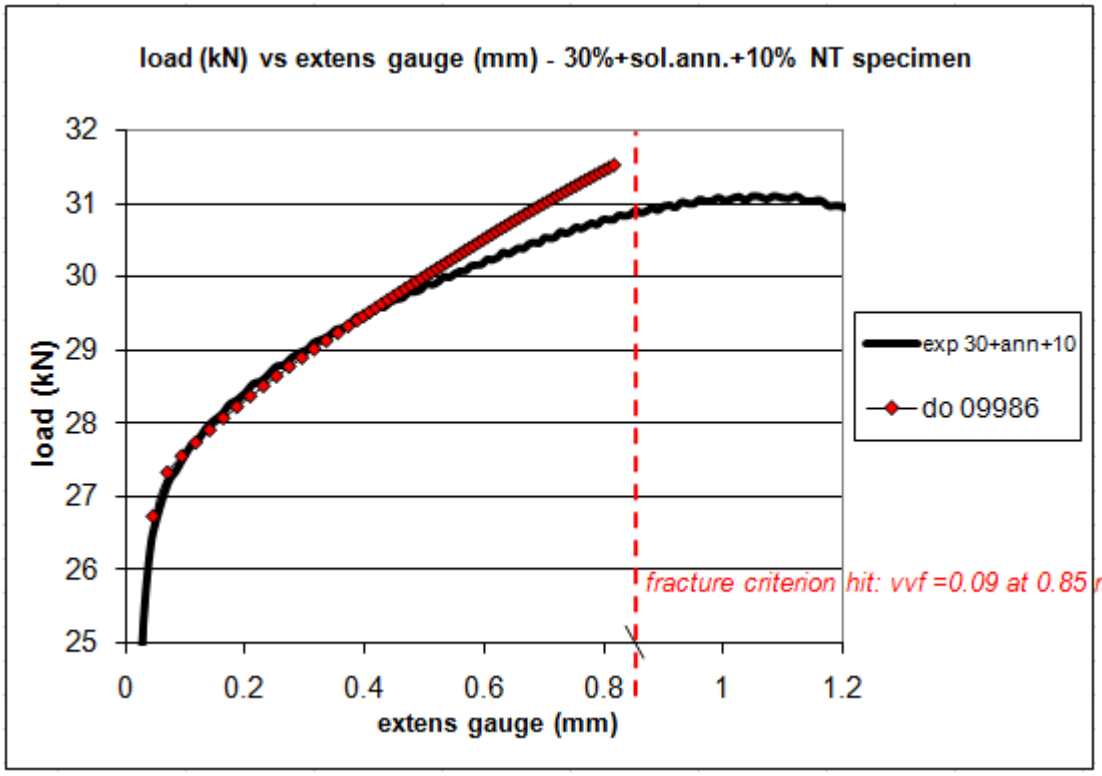

Fig. 6.32. 30% + sol. ann. + 10% strain hardened specimen's crack initiation point.

The numerical model used was the half bar in Fig. 4.14, while in the first instance, the extensometer zone only was used. The latter proved to be not good enough because some compliance was missed.

"undamaged" 316L: validation is shown in Fig. 6.33 and numerical detail is in Fig. 6.34.

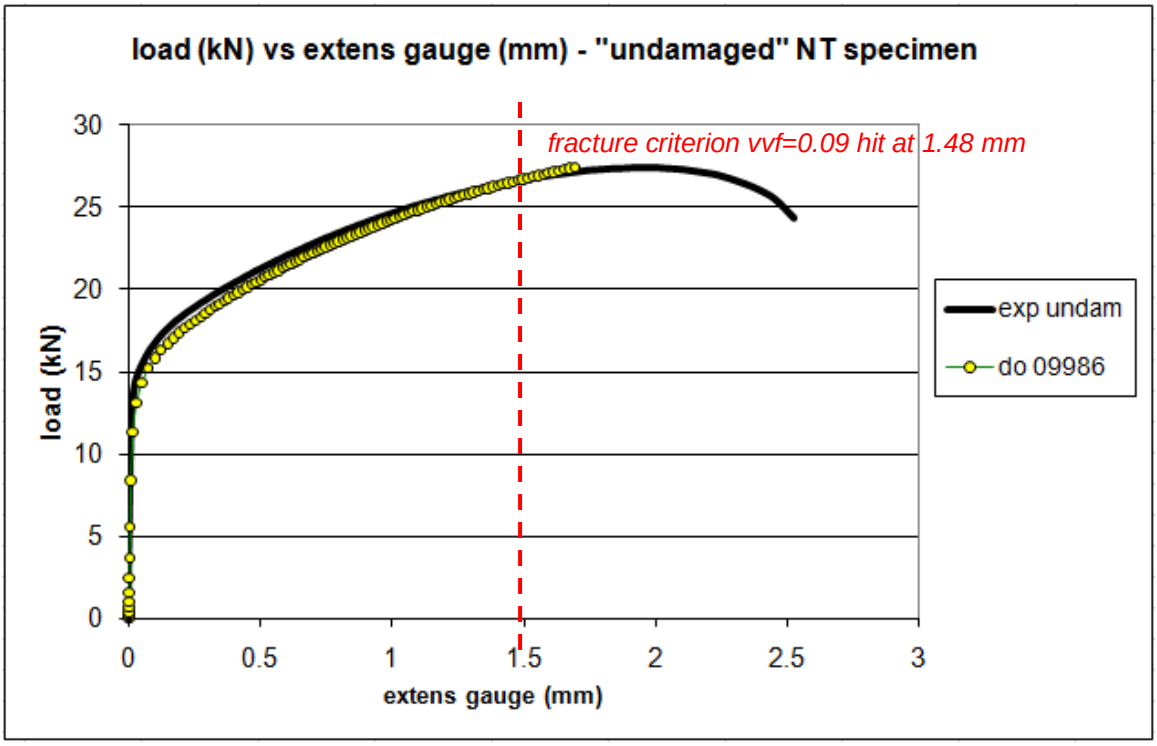

Fig. 6.33. "undamaged" specimen's crack initiation point.

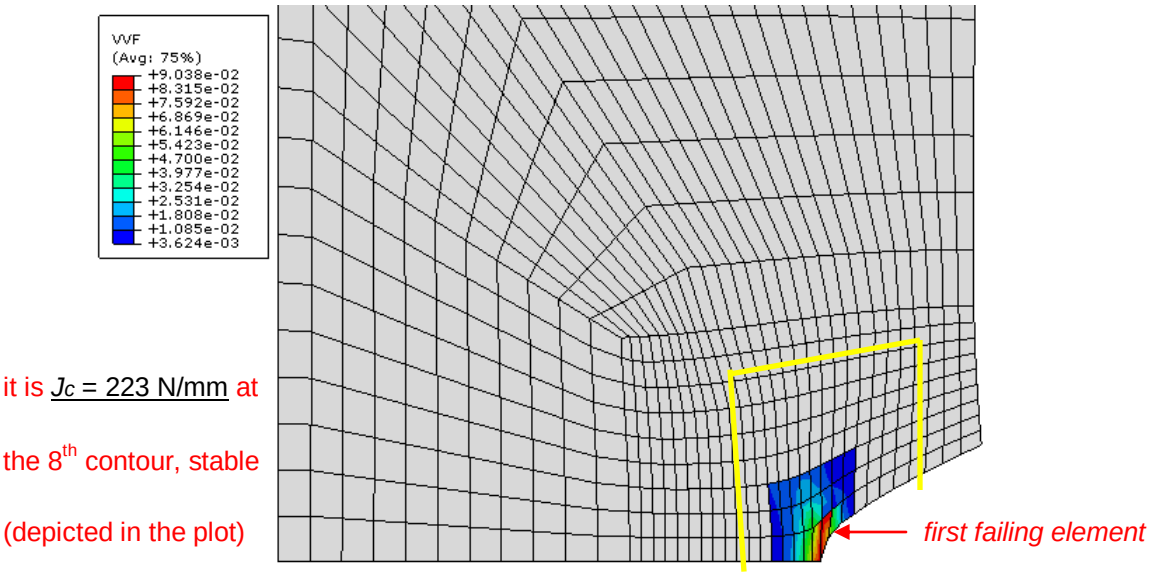

Fig. 6.34. Void volume fraction at failure for "undamaged" specimen.

Validation in Fig. 6.33 was performed by using the numerical model for the "undamaged" material that was calibrated as reported in Section 6.1. The numerical criterion hit at 9% vvf and the 8th contour, which provided a stable value for *J*, can be seen from Fig. 6.34. The fracture toughness was in agreement with the literature for this kind of material.

The Gurson-Tvergaard-Needleman model appeared to be working well in this case.

Creep at 1000 °C specimen: the numerical plastic law retrofitted from experiments was used. As for the Gurson model parameters, they were used in the same exact form that was employed for the "undamaged" material. According to the numerical computation, the fracture criterion was hit at 1.57 mm extensometer gauge –as shown in Fig. 6.35- and gave a value J_c = 214 N/mm for fracture toughness initiation.

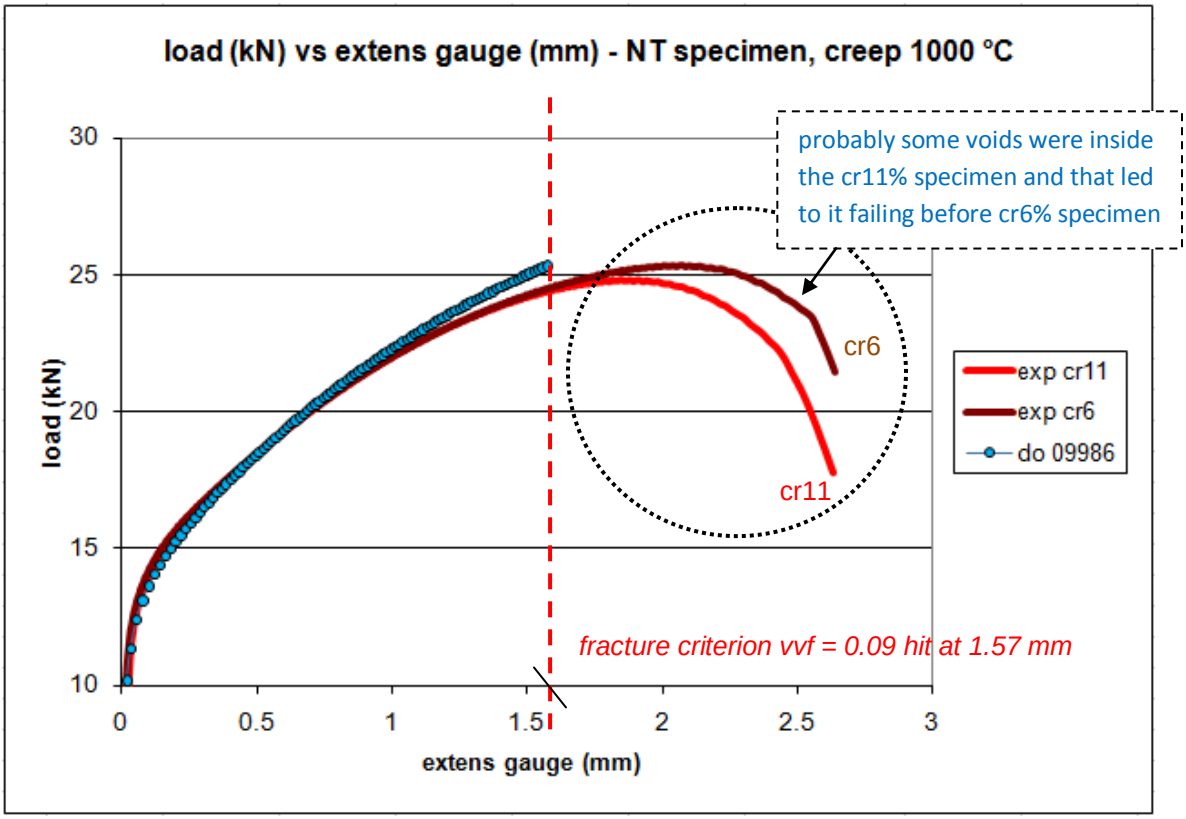

Fig. 6.35. Creep at 1000 °C specimen's crack initiation point.

For this creep at 1000 °C case, it is interesting to notice that two specimens from "damaged" materials were used, the first with strain 11% and the second with strain 6%. The numerical model was the same for both of them because calibrated up to the fracture point. Nevertheless, it appears from Fig. 6.35 that one specimen failed before the other. This effect has not been intercepted by the analysis because that was limited to the initiation stage. It was supposed that 11% creep strained specimen had some voids inside, more than its 6% creep strained counterpart did. These voids became important after crack initiation, accelerating the failure process. No further investigating step could be performed in the given circumstances.

The plastic zone developed in the most brittle specimen, the 40% eng. strain "damaged" material shown in Fig. 6.30, was adherent to the recommendation from Scibetta for getting the lowest value of fracture toughness, with small or negligible loss of constraint. On the contrary, the creep at 1000 °C "damaged" material, which appeared to be the most ductile, showed a widespread plastic zone, as in the following Fig. 6.36:

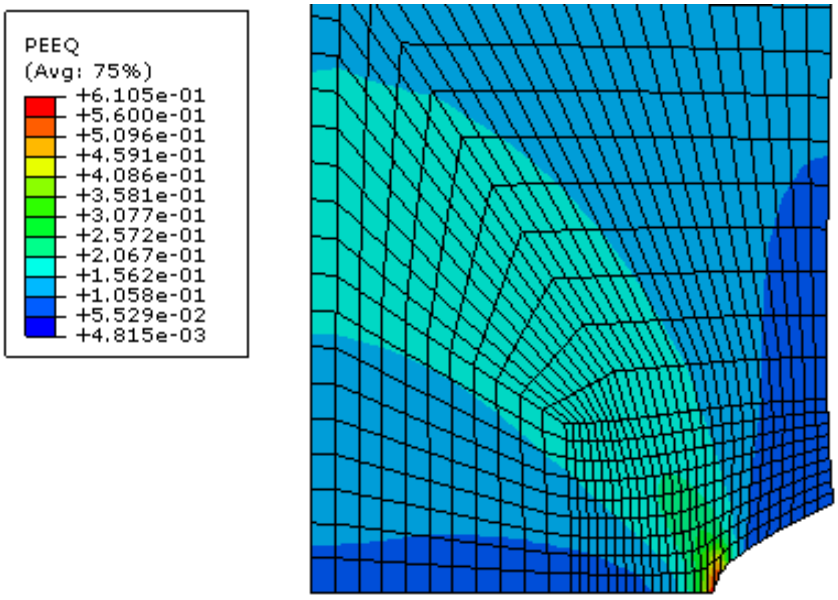

Fig. 6.36. PEEQ at crack initiation point for creep at 1000 °C "damaged" material.

In that case, a notable amount of plasticity interested all the zones, including the ligament and the external surface. Fracture toughness was expected to be slightly higher than due.

Pre-strained 7 % at room temperature + creep at 900 °C: the plastic law fitted from experiments and shown in Table 6.3 was used. As for the Gurson model parameters, they were used in the same exact form employed for the "undamaged" material. According to the numerical computation, the fracture criterion was hit at 1.4 mm extensometer gauge – as shown in Fig. 6.37- and gave a value J_c = 177.5 N/mm for fracture toughness initiation.

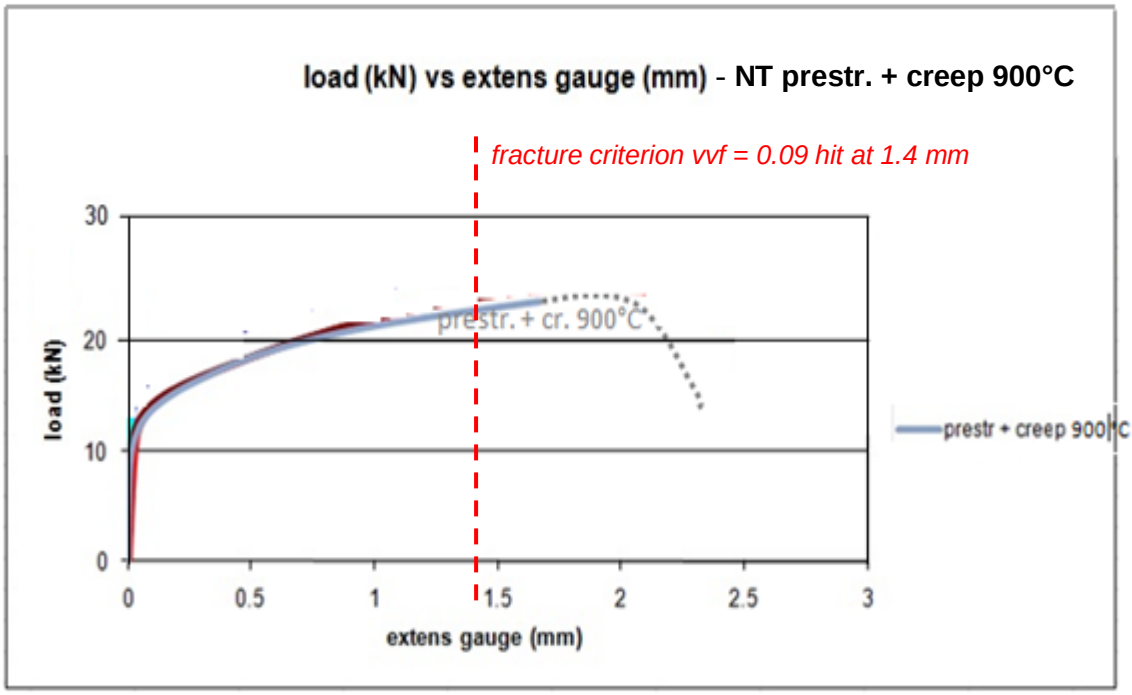

Fig. 6.37. Prestrained + creep at 900 °C specimen's crack initiation point.

6.4.4 Fracture toughness against initial void volume fraction

In conclusion, the following Table 6.4 answers in terms of J_c (and K_{Jc} by the means of a converting relation) the question at the core of this project, which was: "Describe what happens to fracture toughness initiation for different yield stress values (that is differently "damaged" material) and for different values of initial void volume fraction (the one actually induced into the specimens during this project plus some other values inducible in accordance with the findings in Section 5.3)".

NT specimen, fracture toughness initiation J_c (N/mm) - half specimen axisymmetric model, 920 CAX4R elements, 983 nodes, characteristic length at crack front = 70 µm

fr. criterion from experiment	"damaged" state	initial void volume fraction (%)												
		0.0014	0.004	0.005	0.01	0.012	0.015	0.02	0.025	0.03	0.035	0.04	0.045	0.05
vvf = 0.09	"undamaged" 316L	223		163	126		103	87	74.3	63.2	54	45.5	38	31.5
vvf = 0.09	creep at 1000 °C	214		159	121		99	83	70.6	60	51	43	35.8	29.2
vvf = 0.09	prestrain 7% + creep at 900 °C	177.5		137.4	106		88	74.6	63.5	54.5	46.2	39.3	33	27.2
vvf = 0.09	strain 30% + sol. ann. + strain 10%	170		138	112		93	80	69.5	61	53.4	46.8	40.7	35
S max, princ = 1454 N/mm^2	strain 30% *	67	73	78	94		111	142	145	118	97.5	81	68	55
S max, princ = 1583 N/mm^2	strain 30% + strain 10% **	32.5		40	57.5	65	75	93	115	149	143	118	97.5	80

* from initial vvf = 0.025 the fracture criterion vvf = 0.09 is hit before the max principal stress S = 1454 N/mm^2 and becomes dominant

** from initial vvf = 0.035 the fracture criterion vvf = 0.09 is hit before the max principal stress S = 1583 N/mm^2 and becomes dominant

The values can be passed from J_c to K_c and compared with the benchmark by using the relation: $Kc = \sqrt{\frac{E * Jc}{1 - \nu^2}}$ as follows:

NT specimen, fracture toughness initiation K_c (MPa * m^0.5) - half specimen axisymmetric model, 920 CAX4R elements, 983 nodes, characteristic length at crack front = 70 µm

fr. criterion from experiment	"damaged" state	initial void volume fraction (%)												
		0.0014	0.004	0.005	0.01	0.012	0.015	0.02	0.025	0.03	0.035	0.04	0.045	0.05
vvf = 0.09	"undamaged" 316L	224		191.6	168.5		152.3	140	129.4	119.3	110.3	101	92.5	84.2
vvf = 0.09	creep at 1000 °C	219.5		189.3	165.1		149.3	136.7	126.1	116.3	107.2	98.4	89.8	81.1
vvf = 0.09	prestrain 7% + creep at 900 °C	200		175.9	154.5		140.8	129.6	119.6	110.8	102	94.1	86.2	78.3
vvf = 0.09	strain 30% + sol. ann. + strain 10%	195.7		176.3	158.8		144.7	134.2	125.1	117.2	109.7	103	95.7	88.8
S max, princ = 1454 N/mm^2	strain 30% *	123	128.2	132.6	145.5		158.1	178.9	180.7	163	148.2	135	123.8	111
S max, princ = 1583 N/mm^2	strain 30% + strain 10% **	85.5		95	113.8	121	130	144.7	161	183.2	179.5	163	148.2	134

* from initial vvf = 0.025 the fracture criterion vvf = 0.09 is hit before the max principal stress S = 1454 N/mm^2 and becomes dominant

** from initial vvf = 0.035 the fracture criterion vvf = 0.09 is hit before the max principal stress S = 1583 N/mm^2 and becomes dominant

Table 6.4. Fracture toughness initiation values from this project.

The results from Table 6.4 are plotted in the following Fig. 6.38:

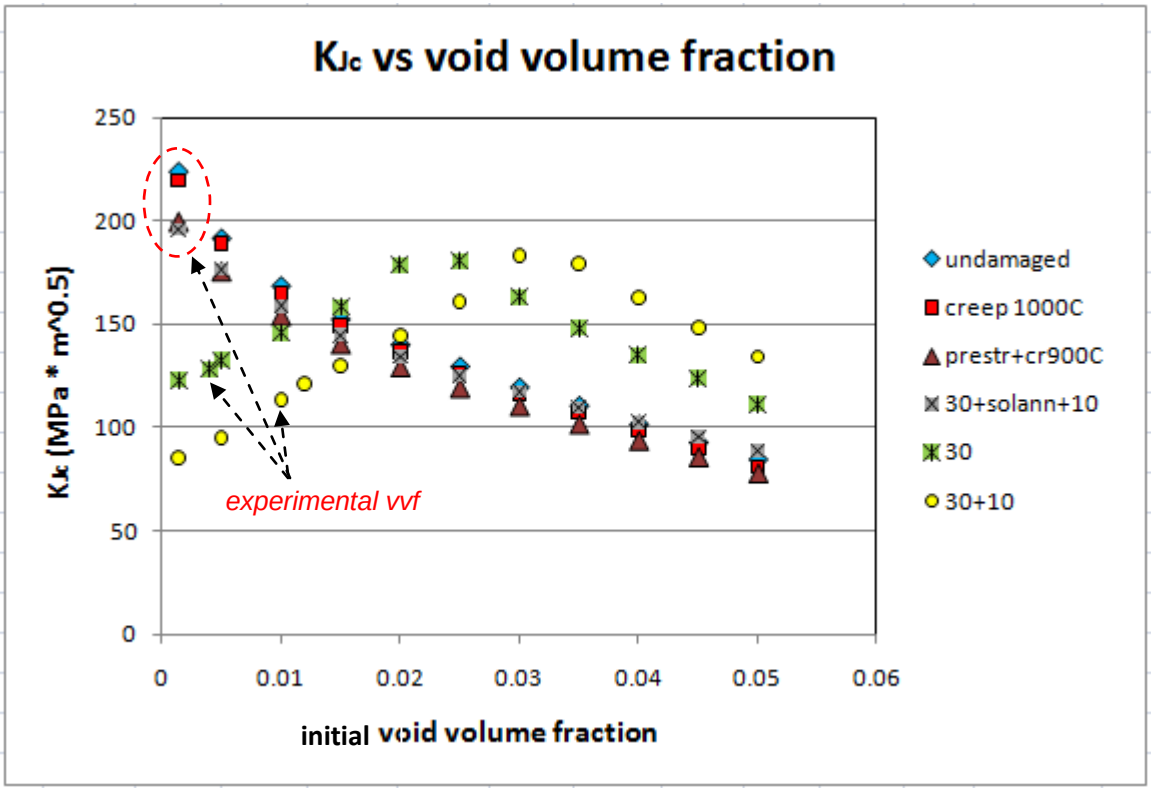

Fig. 6.38. K_{Jc} vs. initial void volume fraction, from Table 6.4.

The plot shows that for fully ductile cases (namely "undamaged"; creep 1000 °C; prestrain 7% + creep 900 °C; 30% strain + sol. ann. + 10% strain) the increase in void volume fraction leads to a decrease in the fracture initiation value. On the other hand, for brittle–like cases (namely 30% strain and 40% strain) fracture toughness initiation increases until the failure mechanism switches to ductile again, because of the higher level of initial porosity. After that, the decreasing behaviour resumes.

In Fig. 6.38, the actual values of void volume fraction present into the specimens for fracture toughness are set in evidence. Their corresponding fracture toughness initiation was compared with the effect of helium embrittlement on the same property.

Some of the void volume fractions in Table 6.4 were obtained from "damaging" experiments. Nevertheless, these quantities were not actually present into the

sharp-notched tensile specimens machined for fracture toughness purpose. For example, considering the creep at 1000 °C "damaged" material, the void volume fraction into the corresponding machined sharp notched tensile specimen was 0.14% and it showed a fracture toughness initiation K_{Jc} = 219.5 MPa * $\sqrt{m}$. If the void volume fraction into that specimen was 1.5%, as found by tomography in Section 5.3.2, the fracture toughness initiation would have been K_{Jc} = 149.5 MPa * $\sqrt{m}$. The latter makes a sensible difference entirely due to porosity. One other extension could be suggested for the "undamaged" material: the results described in Figs. 5.30–5.31 showed that a void volume fraction up to some percent could be introduced by performing notched tensile tests, as reported in Section 3.1.3. That porosity would again lead to a sensible decrement in fracture toughness entirely due to voids.

From Table 6.4, fracture toughness values obtained with different initial void volume fraction for each "damaged" state are considered. How to introduce that porosity is shortly suggested in Chapter 8, while proposing further work.

6.5 Correlation with helium effect on fracture toughness

Starting from the values summarized in Table 6.4 for K_{Jc}, it was possible to relate the conventional simulations attempted in this project with the helium embrittlement effect on fracture toughness initiation. This was done graphically in Fig. 6.39. It can be seen that the values of fracture toughness initiation K_{Jc}, as obtained from the "damaging" experiments inducing hardening and porosity executed in this project and compared with effect of irradiation doses for 316L, follow the benchmark [85] in trend up to the dpa considered. Nevertheless, the result from this procedure is debatable. It has to be made clear that the GTN model does not appear to be suitable for simulating strain hardened / irradiated hardened material because it implies a ductile damage progression, which is not the case when the mechanism is strain localization, as for two brittle-like cases here.

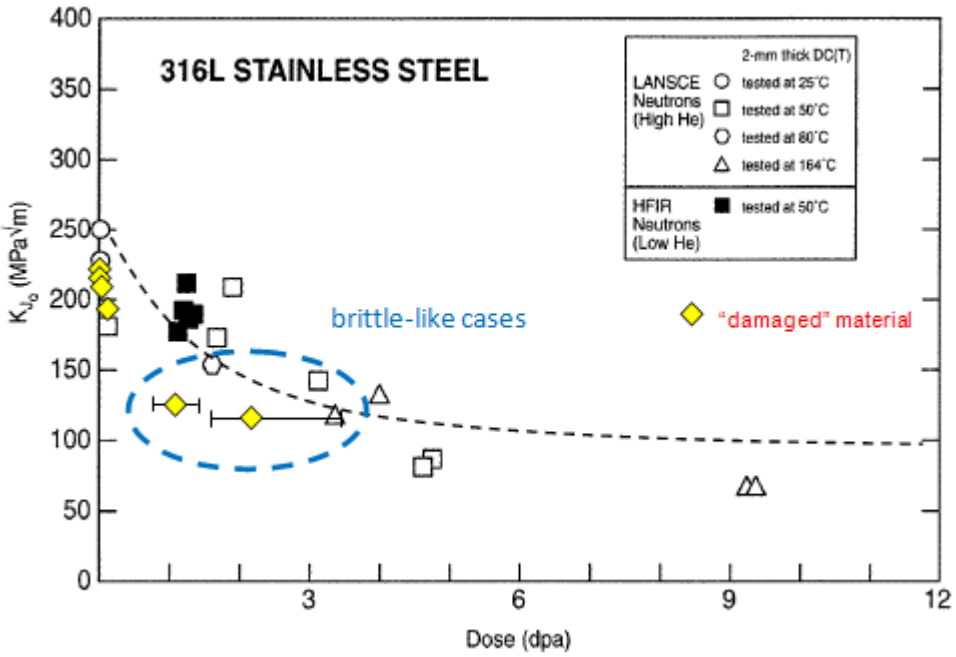

Fig. 6.39. Graphical correlation with helium embrittlement effect.

As for the relevance to the nuclear case, it has been already stated that Byun [80, 116-118] found a similarity between the post-yielding behaviour of irradiated and work hardened material when tested at room temperature, from which a correlation of yield stress in terms of dpa has been used in this project as an extension of that. On the other hand, Pokor [257] investigated quantitatively the effect of irradiation defects on the work hardening behaviour of austenitic stainless steels when tested at the more technologically relevant temperature, for PWRs, of 300 °C. Irradiation hardening has a maximum effect when irradiation and mechanical testing are conducted at about 300 °C, with the post-irradiation strength decreasing weakly with temperature below 300 °C, and relatively rapidly with increasing temperature above 300 °C [76]. This was not considered here.

The nucleation of bubbles, which is the main cause of helium embrittlement, has not been reproduced experimentally in a satisfactory manner. Sensitization from creep at 650 °C, which was deemed to be comparable to helium embrittlement by Morgan [240], has not been incorporated into the damage progression model used in this project because out of reach.

Summary of results

"Undamaged" (solution annealed at 1050 °C for 30 minutes and water quenched) and "damaged" (from interrupted uniaxial tensile testing at room temperature; from creep testing at low and high temperatures; from a combination of pre-strain and creep) 316L materials were obtained experimentally in this project. Non-standard sharp-notched round bar specimens were then machined from the "undamaged" and "damaged" materials for fracture toughness evaluation purposes.

Fracture toughness initiation was inferred numerically from the load vs. displacement plot of the sharp-notched round bar specimens subjected to tensile test at room temperature. A ductile fracture criterion was established experimentally for the "undamaged" material and then extended to the other ductile cases. For every "damaged" material, fracture toughness initiation resulted in lower toughness than for the "undamaged" material. The decrement was substantial for the 40% eng. strain and 30% eng. strain "damaged" materials, which fractured in a brittle manner. A maximum principal stress criterion was employed for both the brittle cases.

A rough correlation between irradiation hardened and strain hardened 316L was attempted in terms of yield stress, starting from recent literature findings:

- 30% + sol.ann. + 10% eng. strain corresponding to 0.15 – 0.3 dpa;
- 30% eng. strain corresponding to 1.5 dpa or slightly lower;
- 40% eng. strain corresponding to 1.5 – estimated 3-4 dpa.

Porosity was generated experimentally by grain boundary sliding from creep at 1000 °C and quantified by processing images from X-ray Microtomography.

The fracture toughness initiation values found in this project followed the same trend as the helium embrittlement effect cited by Snead [85], but a correlation cannot be stated because the mechanical processes involved are different.

Fracture toughness initiation was also calculated parametrically for different values of initial void volume fraction. It is here suggested that the 40% eng. strain and 30% eng. strain "damaged" materials experience a competition between brittle fracture and ductile fracture. In particular, they revert to ductile fracture behaviour at some threshold value of initial void volume fraction, which is different for the two materials.

The numerical Gurson-Tvergaard-Needleman model for porous plasticity was used to characterize the damage progression in the "undamaged" and "damaged materials. It proved to work for the "undamaged" material. It proved to be not suited to capture the damage progression in the brittle-like 40% eng. strain and 30% eng. strain "damaged" materials, for which a flow localization model is suggested.

7. Conclusions

At the end of this doctoral project, some considerations about the actual relevance, both theoretical and practical, of the results obtained must be given.

The mechanisms of irradiation damage, ductile damage and creep damage were described and compared in Chapter 2. A link between strain hardening and irradiation hardening was established in the recent literature in terms of post yield behaviour and used in this project. As for porosity, it was generated from grain boundary sliding in the range of μm and cannot be considered effective in simulating helium bubbles nucleation, growth and coalescence at the grain boundaries, which are in the scale of a few nm.

Experimental originality came from the use of a non-standard sharp-notched round bar specimen for estimating the fracture toughness initiation of the "undamaged" and "damaged" 316L materials obtained experimentally. One ductile fracture criterion for the "undamaged" material was established experimentally in terms of void volume fraction. Such a value is not a material constant because it depends on the composition, the internal state and the shape of the specimen used.

From a numerical perspective, the Gurson-Tvergaard-Needleman model for porous plasticity was used to characterize "undamaged" and "damaged" 316L materials. It did not appear suited to describe the progression of damage for the strain hardened "damaged" materials that fractured in a brittle manner.

7.1 Material

Preliminary investigation on the given 316L led to the definition of one "undamaged" state after a solution annealing heat treatment at 1050 °C for 30 minutes, followed by water quenching. The grain size was measured at 65-70 μm.

The elastic, plastic and porous plastic constitutive laws for "undamaged" 316L were calibrated relying upon experiments conducted on both smooth and notched tensile

specimens. Attention was given to some parameters of the Gurson-Tvergaard-Needleman model for porous plasticity. Results were in agreement with literature.

7.2 Introducing damage into the given material

A tentative correlation between irradiation hardened and tensile hardened 316L in terms of yield stress was attempted starting from recent literature findings. In particular:

- 30% + sol.ann. + 10% eng. strain corresponding to 0.15–0.3 dpa;
- 30% eng. strain corresponding to 1.0-1.5 dpa;
- 40% eng. strain corresponding to 1.5 – estimated 3-4 dpa.

The porosity generated into each "damaged" state was the following:

- 40% eng. strain had 1.12% void volume fraction (retrofitted numerically and debatable because not fully supported experimentally);
- 30% eng. strain had 0.4% void volume fraction (retrofitted numerically and debatable because not fully supported experimentally);
- 30% eng. strain + solution annealing + 10% eng. strain kept the initial 0.14% void volume fraction attributed to the "undamaged" material;
- Creep at 650 °C showed sensitization but no voids into the matrix;
- Creep at 1000 °C showed 1.8 – 1.2% void volume fraction at 0.8 - 2.5 mm distance from the fracture line. No noticeable voids were found at 5 mm distance and the initial 0.14% attributed to "undamaged" material was considered;
- Prestrain 7% + Creep at 900 °C, stopped at 5% creep strain, showed no noticeable void inside, so the initial 0.14% from "undamaged" material was considered.

Literature [240] points at sensitization as a prospective way to simulate the effect of helium bubbles on fracture toughness. Opportune numerical techniques should be used to characterize and investigate that link, but they were out of the reach of this project.

7.3 Fracture toughness of the "damaged" material

It was shown that the maximum J integral value in the 3D Disk Compact Tension specimen used in this project (a / W = 0.335) is always localized at the midsection, irrespective of its thickness and power hardening law parameter. This differs from the behaviour of Compact Tension specimen described in the Standard [163] (a / W = 0.6).

The fracture toughness initiation for all the "damaged" states, as inferred from sharp-notched tensile specimens load vs. displacement data, was lower than for the "undamaged" state. The constitutive law and the Gurson-Tvergaard-Needleman model for porous plasticity were calibrated on the "undamaged" material and then retrofitted in order to validate the experimental results from "damaged" material. Some discussion about the GTN parameters was attempted. The GTN model appeared to work for the "undamaged" state, but was not suited to describe the damage progression in brittle cases.

Fracture toughness initiation was calculated parametrically for "undamaged" and "damaged" states by employing different values of initial void volume fraction. It is here suggested that 40% eng. strain and 30% eng. strain materials experience a competition between brittle-like fracture and ductile fracture. At certain level of initial void volume fraction, which is different for each material, they revert to ductile behaviour.

7.4 Correlation with helium effect on fracture toughness

Fracture toughness initiation for all the "damaged" states followed the same trend as the helium embrittlement effect cited by Snead [85] and Little [15]. Nevertheless, a correlation cannot be said to exist because the mechanical processes involved are different. Some interest remains in the conventional fracture toughness decrement though: the fracture toughness values calculated by varying the initial void volume fraction may add depth and perspective to future work in the analysis of welding.

8. Further work

Four lines of work have been identified for upgrading this project and get results for prospective publications in peer reviewed journals.

1 - From a numerical point of view, it could be interesting to develop a detailed comparison between the Compact Tension specimen and the Disk Compact Tension specimen in relation to single and double parameter fracture toughness' properties. The two specimens are both in the standard ASTM E 1820 but, during this project, a comprehensive work like one of Nevalainen–Dodds [163] for benchmarking has not been found. In addition, that work does not consider any damage model, being limited to the elastic and the elastic-plastic cases. Taking into account damage would also open to the problem of non-uniqueness of the set of damage parameters chosen to fit the experimental results employed for calibration. Further consideration could also be given to the different behaviour existing between four-noded and eight-noded elements when imposing a fracture criterion in terms of void volume fraction in large strain cases. The proposed development would add a contribution to the line of work investigating standard and non-standard subsize specimens, for which great interest is arising in the nuclear field.

2 - From an experimental point of view, it could be interesting to investigate further the effects of high temperature creep tests on the fracture toughness variation. In fact, there is little study in the range 800–900 °C for stresses leading to the creation of porosity. It has to be noted that in the nuclear operational conditions, some other phenomena overlap and one line of work addressing them at European level, in the nuclear field, is called PERFORM 60. Nevertheless, the interest in such higher temperatures (around 0.6 T_m) may also involve conventional applications. In addition, results from creep at 650 °C could be investigated more in depth in order to evaluate the correlation between sensitization and helium embrittlement, as for example suggested by Morgan [240]. This line of work has not been exploited yet.

3 - A more sound and experimentally based correlation with fracture toughness reduction under irradiation hardening and helium embrittlement (even not being easy to distinguish the respective contributions at low temperatures in real life operations) can be tried by exploring grain refinement techniques of solution annealed 316L stainless steel. That way, yield stress is increased as if it was subject irradiation hardening up to saturation level. Notched tensile test may follow, so that porosity is inserted at the fracture line up to 1 mm distance. Finally, a fracture toughness test of such damaged material may employ a small punch specimen, for which 10 mm diameter, 0.5 to 1 mm thickness may suffice as for one recent work from Wang Z. [178] in the nuclear field. Starting from literature, it was argued in this project that some prestrain might actually reproduce the macroscopic effect of irradiation hardening on the yield stress. It was also shown that notched tensile tests introduce measurable void volume fraction into the matrix. This procedure is much faster than creep-based experiments and much simpler to plan and execute.

4 – The Gurson-Tvergaard-Needleman model proved to work for "undamaged" material. On the contrary, it was not effective for capturing the progression of damage into 30% and 40% eng. strain "damaged" materials. It could interesting to test the extended Gurson models developed by Xue [142], Zhang [255] and Pardoen [256], which incorporate the Thomason model and account for localization. It could also be interesting to explore the sensitivity of the fracture toughness initiation values presented in Table 6.4 to the parameters of the GTN model and to the fracture criteria employed here.

On a broader sense, the very recent development of X-ray tomography facilities may permit the reconstruction of material damaged in nuclear power plants – if and when available / disposable – even at the crystal level. The calibration and the introduction of a more realistic constitutive model may then be attempted beyond the limits of the Gurson model and of the continuum framework. This could also help investigate the helium embrittlement mechanisms in the range of temperatures technologically relevant, again in reference to the open problems reported by Trinkaus [108]. The time and the effort needed to operate on nuclear damaged material appear to be quite consistent and likely to be linked to existing joint programmes at European level, relying upon contributions from different institutions.

9. References

[1] Honeycombe, R. and Bhadeshia, H. K. D. H., 1995. *Steels. Microstructure and properties.* 2nd ed. London: Edward Arnold, p.2

[2] Yescas-Gonzalez, M. A. and Bhadeshia H. K. D. H, 2001. *Cast irons*. The University of Cambridge. [online] Available at http://www.msm.cam.ac.uk/phase-trans/2001/adi/cast.iron.html [Accessed 11 August 2010]

[3] Honeycombe, R. and Bhadeshia, H. K. D. H., 2006. *Steels. Microstructure and properties.* 3rd ed. London: Edward Arnold. Chapter 12, pp. 259-274

[4] Boom, R, 1999. *Iron, the hidden element - The Role of Iron and Steel in the 20th Century*. 47th Hatfield Lecture. The Univeristy of Sheffield.

[5] Lo, K. H. et al., 2009. Recent developments in stainless steels. *Materials Science and Engineering*, R65, pp 39–104

[6] Bhadeshia H. K. D. H, 2010. Personal perspective on microstructure of steels: 25th anniversary of MST and collection of papers in honour of Sir Robert Honeycombe. *Materials Science and Technology*, vol. 26, no. 4, pp. 379-385

[7] British Standard Institution, 2000. *BS EN 10020:2000 Definition and classification of grades of steel*. Milton Keynes: BSI

[8] West Yorkshire Steel Company Ltd, 2008. *AISI Steel SAE Steel grades*. [online] Available at http://www.westyorkssteel.com/AISI_steel.html [Accessed 11 August 2010]

[9] World Nuclear Association, 2009. *Nuclear Power in the World Today*. [online] Available at http://www.world-nuclear.org/info/inf01.html [Accessed 11 August 2010]

[10] World Nuclear Association, 2009. *The Nuclear Renaissance*. [online] Available at http://www.world-nuclear.org/info/inf104.html [Accessed 11 August 2010]

[11] Wang, J.L. and Hansen, C. J., 2007. Revisiting Nuclear Renaissance. *International Atomic Energy Agency Bulletin* 49/1, pp. 22-23

[12] Knott, J., 2008. Energy – Materials and Mechanisms. *FESI International Bulletin of Structural Integrity*, vol. 3, issue 3, pp. 12-18

[13] Dalton Nuclear Institute – The University of Manchester, National Nuclear Laboratory, Battelle, 2010. *A review of the UK's Nuclear R&D Capability* (Report)

[14] Research Councils UK Energy Programme. *Keeping the Nuclear Option Open*. [online] Available at http://www.knoo.org [Accessed 11 August 2010]

[15] Little, E. A., 2006. Development of radiation resistant materials for advanced nuclear power plant. *Materials Science and Technology*, vol. 22, no. 5, pp. 491-518

[16] Server, W. L., Joint ICTP/IAEA Workshop on Irradiation-induced Embrittlement of Pressure Vessel Steels, 2009. *Reactor Vessel Internals Embrittlement*. Trieste, Italy, 23 - 27 November 2009. Trieste: The Abdus Salam International Centre for Theoretical Physics

[17] Massoud, J. P., Topical day: 10 years of stress corrosion cracking research at SCK-CEN, 2007. *Keynote - Radiation damage to reactor internal materials*. Mol, Belgium, 22 January 2007. [online] Available at http://www.sckcen.be/en/content/download/2866/27617/file/TDSCC09JeanPaulMassoud abstract.pdf [Accessed 11 August 2010]

[18] EURATOM Seventh Framework programme for Nuclear Training and Research Activities (2007-2011). *Perform60 - Prediction of the Effects of Radiation For RPV and in-vessel Materials using MSM-60 years foreseen plant life time*. [online] Available at http://perform60.net/ [Accessed 11 August 2010]

[19] Zinkle, S. J., 2007. Fission Energy Workshop: Opportunities for Fundamental Research and Breaktrough in Fission – Global Climate & Energy Project, 2007. *Advanced Material for Future Nuclear Plants*. Cambridge, MA, USA, 29-30 Nov 2007.

[20] Baindur, S., 2008. Materials challenges for the Supercritical Water-Cooled Reactor (SCWR). *Bulletin of the Canadian Nuclear Society*, vol. 29, no.1, pp. 32-38.

[21] Barabash, V., et al., 2007. Materials challenges for ITER – Current status and future activities. *Journal of Nuclear Materials*, voll. 367–370, pp.21–32

[22] Sahin, S. and Ubeyli, M., 2008. A Review on the Potential Use of Austenitic Stainless Steels in Nuclear Fusion Reactors. *Journal of Fusion Energy*, vol. 27, pp. 271–277

[23] Edstrom Industries Inc., 2010. *Stainless Steels Home*. [online] Available at http://www.edstrom.com/Resources.cfm?doc_id=129 [Accessed 12 August 2010]

[24] Gross, D. and Seelig, T., 2006. *Fracture Mechanics – With an introduction to Micromechanics*. Berlin: Springer, p.53

[25] Department of Materials Science and Engineering - University of Virginia. *Introduction to materials science.* (Outline) [online] Available at www.synl.ac.cn/org/non/zu1/knowledge/Structure%20of%20Crystalline.pdf [Accessed 12 August 2010]

[26] Bui, H. D., 2006. *Fracture Mechanics – Inverse Problems and Solutions*. Berlin: Springer, p.2

[27] Dieter, G.E., 1988. *Mechanical Metallurgy*, SI Metric Edition. New York: McGraw-Hill, p. 8

[28] Zurek, A. K. et al, 2003. Damage Evolution in Ductile Metals – Developing a quantitative and predictive understading. *Los Alamos Science*, n. 28, pp. 111-113

[29] Besson, J. et al., 2004. *Local approach to fracture*. Paris: Ecole des Mines de Paris, p. 34

[30] Goods, S. and Brown, L., 1979. Overview n.1: The nucleation of cavities by plastic deformation. *Acta Metall.*, vol. 27, pp.1-15

[31] Beremin, F., 1981. Cavity formation from inclusions in ductile fracture of A508 steel. *Met. Trans.*, vol. 12A, pp.723-731.

[32] Pineau, A., 2007. Development of the local approach to fracture over the past 25 years: theory and applications. *Anales de la Mecánica de Fractura*, Vol 1, pp. 9-24.

[33] Besson, J. et al., 2004. *Local approach to fracture*. Paris: Ecole des Mines de Paris, pp. 411-416

[34] Hutchinson, J. and Tvergaard, V., 1989. Softening due to Void Nucleation in Metals. *ASTM, Standard Technical Publication 1020*.

[35] Gurson, A. L., 1977. Continuum theory of ductile rupture by void nucleation and growth. Part 1 – yield criteria and flow rates for porous ductile media. *Journal of engineering materials and media*, vol.99, pp 2-15

[36] Needleman A. and Tvergaard V., 1987. An Analysis Of Ductile Rupture Modes At A Crack Tip. *Journal of the Mechanics and Physics of Solids*., vol. 35(2), pp.151–183

[37] McClintock, F.A., 1968. A Criterion for Ductile Fracture by Growth of Holes. *Journal of Applied Mechanics*. Vol. 35, pp. 363-371

[38] Brown, L. M. and Embury, J. D., 1973. The initiation and growth of voids at second phase particles. *Proceedings 3rd International Conference on Strenght of Metals and Alloys*. Institute of Metals, London, pp. 164-169.

[39] Benzerga, A. and Leblond, J.B., 2010 – article in press. Ductile Fracture by Void Growth to Coalescence. *Advances in Applied Mechanics*, pp. 1-131.

[40] Ohno, N. and Hutchinson, J.W., 1984. Plastic flow localization due to non-uniform void distribution. *J. Mech. Phys. Solids*. Vol. 32, No. 1, pp. 63-85

[41] Tvergaard, V. et al., 1981. Flow localization in the plane strain tensile test. *J. Mech. Phys. Solids*. Vol. 29, No. 2, pp. 115-142.

[42] Thomason, P.F., 1985. A three dimensional model for ductile fracture by the growth and coalescence of microvoids. *Acta metall.*, vol. 33, No. 6, pp. 1087-1095

[43] Tonks, D.L. et al., 2001. Void coalescence model for ductile damage. *CP620, Shock Compression of Condensed Matter-2001*. American Institute of Physics. Pp. 611-614

[44] Rudd, R.E. et al., 2006. Void Coalescence Processes Quantified through Atomistic and Multiscale Simulation. *UCRL-CONF-217946. 16th European Conference on Fracture*. Alexandroupolis, Greece, July 3-7, 2006

[45] Weck, A. et al., 2008. Visualization by X-ray tomography of void growth and coalescence leading to fracture in model materials. *Acta Materialia*. Vol. 56, pp. 2919–2928

[46] McVeigh C. et al., 2007. An interactive micro-void shear localization mechanism in high strength steels. *Journal of the Mechanics and Physics of Solids*. Vol. 55, pp. 225–244

[47] Li, H. et al., 2010 – article in press. Ductile fracture: Experiments and computations. *International Journal of Plasticity*, doi:10.1016/j.ijplas.2010.04.001

[48] Department of Nuclear Engineering - University of California. *Basic Explanation of Creep Processes*. NE-161 Report

[49] Was, G., 2007. *Fundamentals of radiation materials science*. Berlin: Springer, p. 716, Fig. 14.4

[50] Schuh, C., 2009. *Physical Metallurgy lectures*. Massachusetts Institute of Technology Open Course Ware, number: IT 3.40J / 22.71J / 3.14

[51] Wilshire, B. and Burt, H. Damage evolution during creep of steels. *International Journal of Pressure Vessels and Piping*, vol. 85, pp. 47–54

[52] Kassner, M.E. and Perez-Prado, M.T., 2004. *Fundamentals of Creep in Metals and Alloys*. Amsterdam: Elsevier, pp.155-158

[53] Besson, J. et al., 2004. *Local approach to fracture*. Paris: Ecole des Mines de Paris, p.66

[54] Mills, K., Davis, J.R., 1987. *ASM Handbook, Volume 12 - Fractography*. ASM International.

[55] Ashby, M. F. et al, 1979. Fracture mechanism maps and their construction for fcc metals and alloys. *Acta Metallurgica,* vol. 27, pp.699–729

[56] Li, M. and Zinkle, S. J., 2007. Fracture mechanism maps in unirradiated and irradiated metals and alloys. *Journal of Nuclear Materials,* vol. 361, pp.192–205

[57] Michel, B., 2004. Formulation of a new intergranular creep damage model for austenitic stainless steels. *Nuclear Engineering and Design,* vol. 227, pp.161–174

[58] European Creep Collaborative Committee, *ECCC Data Sheets 2005*

[59] Giris Shastry, C. et al., 2004. Creep of 316L(N) stainless steel – mechanistic and engineering aspects. *International Symposium of Research Students on Materials Science and Engineering*. Chennai, India, 20-22 December 2004.

[60] Auzoux, Q. et al., 2005. Intergranular damage in AISI 316L(N) austenitic stainless steel at 600 °C: Pre-strain and multiaxial effects. *Nuclear Engineering and Design*, vol. 235, pp. 2227-2245

[61] Sasikala, G. et al., 2000. Creep deformation and fracture behavior of types 316 and 316L(N) stainless steels and their weld metals. *Metallurgical and Matierals Transactions*, vol. 31A, pp. 1175-1185

[62] Was, G., 2007. *Fundamentals of radiation materials science*. Berlin: Springer, p. 723

[63] Ruano, O. et al., 1985. Deformation mechanisms in an austenitic stainless steel (25Cr-20Ni) at elevated temperature. *Journal of Materials Science*, vol 20, pp. 3735-3744

[64] Schweitzer, P.A. , 2010. *Fundamentals of Corrosion*. Boca Raton: CRC Press, p. 32

[65] Schweitzer, P.A. , 2010. *Fundamentals of Corrosion*. Boca Raton: CRC Press, p. 34

[66] Padilha, A. F. et al, 2007. Precipitation in AISI 316L(N) during creep tests at 550 and 600C up to 10 years. *Journal of Nuclear Materials*, vol. 362, pp.132–138

[67] Little, E. A., 1976. Neutron irradiation hardening in irons and ferritic steels. *Int. Met. Rev.*, vol. 21, pp. 25-60

[68] Norgett, M. J. et al., 1975. A proposed method of calculating displacement dose rates. *Nuclear Engineering Design*, vol. 33, pp. 50-54

[69] ASTM E521-96, 2009. Standard Practice for Neutron Radiation Damage Simulation by Charged-Particle Irradiation

[70] Was, G., 2007. *Fundamentals of radiation materials science*. Berlin: Springer.

[71] International Atomic Energy Agency. [online] Available at http://www.iaea.org/OurWork/ST/NE/NENP/WCR/LWR/ [Accessed 12 August 2010]

[72] Bulanova, T. et al., 2004. Effect of irradiation on the steels 316L/LN type to 12 dpa at 400 °C. *Journal of Nuclear Materials*, voll. 329–333, pp. 639–642

[73] Was, G., 2007. *Fundamentals of radiation materials science*. Berlin: Springer, p. 11

[74] Rowcliffe, A.F. et al., 1998. Austenitic stainless steels and high strength copper alloys for fusion components. *Journal of Nuclear Materials*, voll. 258-263, pp. 183-192

[75] Lucas, G.E. et al., 1996. Implications of radiation-induced reductions in ductility to the design of austenitic stainless steel structures. *Journal of Nuclear Materials*, voll. 233-237, pp. 207-212

[76] Pawel, J.E. et al., 1996. Effects of low temperature neutron irradiation on deformation behavior of austenitic stainless steels. *Journal of Nuclear Materials*, voll. 233-237, pp. 202-206

[77] Wu, Xianglin et al. 2007. An EBSD investigation on flow localization and microstructure evolution of 316L stainless steel for Gen IV reactor applications. *Journal of Nuclear Materials*, vol. 371, pp. 90–97

[78] Maloy, S.A. et al., 2003. Comparison of fission neutron and proton/spallation neutron irradiation effects on the tensile behavior of type 316 and 304 stainless steel. *Journal of Nuclear Materials*, vol. 318, pp. 283–291

[79] Bailat, C. et al., 2000. Deformation modes of proton and neutron irradiated stainless steels. *Journal of Nuclear Materials*, vol. 276, pp. 283-288

[80] Byun, T.S., 2007. Dose dependence of true stress parameters in irradiated bcc, fcc, and hcp metals. *Journal of Nuclear Materials*, vol. 361, pp. 239–247

[81] Singh, B.N., 1999. Damage production, accumulation and materials performance in radiation environment. *Journal of Computer-Aided Materials Design*, vol. 6, pp**.** 195–214

[82] Louthan, M.R. et al., 1999. Helium/Hydrogen Effects on the Properties of Materials for the APT Target/Blanket Region. *Materials Characterization*, vol. 43, pp. 179–186 © Westinghouse Savannah River Company. Published by Elsevier Science

[83] Odette, G.R. and Lucas, G.E., 1992. Deformation and fracture in irradiated austenitic stainless steels. *Journal of Nuclear Materials*, voll. 191-194, pp. 50-57.

[84] Little, E.A., 1996. Proceedings *EUROMAT 96* - Conference on Materials and nuclear power, 29; London, Institute of Materials.

[85] Snead, L.L. et al., 2002. Experimental determination of the effect of helium on the fracture toughness of steel. *Journal of Nuclear Materials*, voll. 307–311, pp. 187–191

[86] Hamilton, M. L., et al., 1987. In *Influence of radiation in materials properties: 13th International Symposium*, ASTM STP 956, 245, Philadelphia, PA, ASTM.

[87] Olander, 1975. *Radiation Effects in Metals: Hardening, Embrittlement and Fracture*. Boston: MIT. Section 18.10

[88] Trinkaus, H., 1985. Modeling of helium effects in metals: high temperature embrittlement. *Journal of Nuclear Materials*, voll. 133-134, pp. 105-112

[89] Fabritsiev, S.A. and Yaroshevich, V.D., 1986. Mechanism of helium embrittlement of metals and alloys. *Problemy Prochnosti*, No. 9, pp. 48-55. Translation © 1987 Plenum Publishing Corporation

[90] Bloom, E.E. and Weir, I.R., 1966. Development of austenitic stainless steels with improved resistance to elevated temperature irradiation embrittlement. *ASTM Special Publication*, No. 457, pp. 261-289

[91] Barnes, K.S., 1965. Embrittlement of stainless steels and nickel-based alloys at high temperature induced by neutron irradiation. *Nature*, vol. 206, pp. 1307-1308

[92] Rowcliffe, A.F., 1966. The observation of helium bubbles in irradiated 20% Cr--25% Ni--Ti stainless steels. *Journal of Nuclear Materials*, vol. 18, pp. 60-65

[93] Sokurskii, Yu.N. et al., 1980. Effect of helium on the structure and properties of structural materials and its behavior in the crystal lattice. *Vopr. Atomnoi Nauki i Tekhniki*. Ser. Fizika Radiatsonnykh Povrezhdenii i Radiatsonnoe Materialovedenie, No. 2 (13), pp. 39-46.

[94] Onufriev, V.D. et al., 1978. Study of the effect of helium on the properties of materials by means of implantation experiments. *Preprint No. 3070*, Inst. of Atomic Energy, Acad. Sci. USSR, Moscow.

[95] Agapova, I.P. et al., 1976. Study of the structure and mechanical properties of steel Okh16N15M3B irradiated by helium ions. *At. Energ.*, vol. 41, pp. 314-320.

[96] Kiryukhin, N.M. and Ozhigov, L.S., 1979. The role of evolution of gas bubbles in high-temperature radiation embrittlement of materials. *Vopr. Atomnoi Nauki i Tekhniki*. Ser. Fizika Radiatsonnykh Povrezhdenii i Radiatsonnoe Materialovedenie, No. 3, pp. 3-9

[97] Nix, W.D. et al., 1977. Model for creep fracture based on the plastic growth of cavities or the tips of grain boundary wedge cracks. *Acta Met.*, vol. 25, pp. 495-503

[98] Matlock, K.D. and Nix, W.D. Effect of helium on the high-temperature creep and fracture properties of Ni-6% W. *Journal of Nuclear Materials*, vol. 56, pp. 145-152

[99] Goods, S.H. and Nix, W.D. A comparison of the embrittlement effects of H20 bubbles in Ag with those of He bubbles in Ni-6% W. *Acta Met.*, vol. 24, pp. 1041-1046

[100] Waddington, I.S, 1967. Aspects of the high-temperature irradiation embrittlement of stainless steel. *Met. Sci. J.*, vol. 1, pp. 156-160

[101] Gifkins, A.R., 1956. A mechanism for the formation of intergranular cracks when grain boundary sliding occurs. *Acta Met.*, vol. 4, pp. 98-99

[102] Ghoniem, N.M. et al., 2002. *Helium embrittlement: progress and future research*. US Fusion materials science program – Strategic Plan Meeting

[103] Trinkaus, H. and Singh, B.N., 2003. Helium accumulation in metals during irradiation – where do we stand? *Journal of Nuclear Materials*, vol. 323, pp. 229–242

[104] Lind, A. and Bergenlid, U., 2000. Mechanical properties of hot isostatic pressed type 316LN steel after irradiation. *Journal of Nuclear Materials*, voll. 283-287, pp. 451-454

[105] Dobmann, C. et al., 2008. Helium and radiation defect accumulation in metals under stress. *Vacuum*, vol. 82, pp. 856–866

[106] Wirth, B.D. et al., 2004. Multiscale modeling of radiation damage in Fe-based alloys in the fusion environment. *Journal of Nuclear Materials*, voll. 329–333, pp. 103–111

[107] Trinkaus, H., 1983. On the modelling of the high temperature embrittlement of metals containing helium**.** *Journal of Nuclear Materials*, vol. 118, pp. 39-49

[108] Was, G., 2007. *Fundamentals of radiation materials science*. Berlin: Springer, p. 268

[109] Abbaschian, R. et al., 2009. *Physical Metallurgy Principles, Fourth edition*. Stamford, Cencage Learning, p. 119

[110] Was, G., 2007. *Fundamentals of radiation materials science*. Berlin: Springer, p. 601

[111] Zinkle, S.J. and Lucas, G.E., 2003. Deformation and fracture mechanisms in irradiated fcc and bcc metals. *Fusion materials semiannual progress report for the period ending June 30, 2003*. DOE Office of Fusion Energy Sciences (AT 60 20 10 0) pp. 101-125

[112] Was, G., 2007. *Fundamentals of radiation materials science*. Berlin: Springer, p. 191

[113] Was, G., 2007. *Fundamentals of radiation materials science*. Berlin: Springer, p. 143

[114] Was, G., 2007. *Fundamentals of radiation materials science*. Berlin: Springer, p. 595

[115] Was, G., 2007. *Fundamentals of radiation materials science*. Berlin: Springer, p. 614

[116] Byun, T.S., 2006, Deformation mode map of irradiated 316 stainless steel in true stress-dose space. *Journal of Nuclear Materials.* Vol. 351, pp. 303–315

[117] Kim, J.W. and Byun, T.S., 2010. Analysis of tensile deformation and failure in austenitic stainless steels: Part II – irradiation dose dependence. *Journal of Nuclear Materials*. Vol. 396, pp. 10–19

[118] Kim, J.W. and Byun, T.S., 2010, Analysis of tensile deformation and failure in austenitic stainless steels: Part I – temperature dependence. *Journal of Nuclear Materials*. Vol. 396, pp. 1–9

[119] Was, G., 2007. *Fundamentals of radiation materials science*. Berlin: Springer, p. XI

[120] Was, G., 2007. *Fundamentals of radiation materials science*. Berlin: Springer, Chapter 14, pp. 711-763

[121] Zehnder, A., 2007. *Lecture Notes on Fracture Mechanics*. Cornell Univ., p. 1

[122] Griffith, A.A., 1921. The phenomena of rupture and flow in solids. *Philosophical Transactions* of the Royal Society of London. Series A, vol. 221, pp. 163-198

[123] Zehnder, A., 2007. *Lecture Notes on Fracture Mechanics*. Cornell Univ., p. 3

[124] Anderson, T.L., 1995. *Fracture mechanics – Fundamentals and Applications*, 2nd edition. Boca Raton: CRC Press, pag. 17

[125] Anderson, T.L., 1995. *Fracture mechanics – Fundamentals and Applications*, 2nd edition. Boca Raton: CRC Press, pag. 87

[126] Zehnder, A., 2007. *Lecture Notes on Fracture Mechanics*. Cornell Univ., p. 4

[127] British Standard Institution, 1991. *BS 7448-1:1991 Fracture mechanics toughness tests – Part 1: Method for determination of K_{IC}, critical CTOD and critical J values of metallic materials*. Milton Keynes: BSI

[128] Anderson, T.L., 2005. *Fracture mechanics – Fundamentals and Applications*, 3rd edition. London: Taylor and Francis, p. 299

[129] Irwin, 1958. Fracture. *Handbuch der Physik*. Springer Verlag, Berlin. Vol. 6, p. 551

[130] Suo, Z., 2010. *Energy release rate. Fracture Energy*. Engineering Sciences 247: Fracture Mechanics lectures. University of Harvard.

[131] Zehnder, A., 2007. *Lecture Notes on Fracture Mechanics*. Cornell Univ., p. 5

[132] Rice, J.R., 1968. A Path Independent Integral and the Approximate Analysis of Strain Concentration by Notches and Cracks. *Journal of Applied Mechanics*, vol. 35, pp. 379-386.

[133] ABAQUS 6.7 documentation: section 2.16.2 of ABAQUS Theory Manual

[134] Wang, Introduction to Fracture Mechanics, *DSTO GD 0103, Aeronautical and Maritime Research Laboratory (Australia*), 1996, pag. 41

[135] Kurtz, R.J., et al, 1995. Effect of specimen size on the fracture toughness of V-4Cr-4Ti. *Fusion Materials Semiannual Progress Report for the period ending December 31, 1995*. DOE Office of Fusion Energy Sciences (AT 15 05 01 0) pp. 44-49

[136] ABAQUS 6.7 documentation: section 2.16.1 of ABAQUS Theory Manual

[137] Hutchinson, J.W., 1968. In *Journal of the Mechanics and Physics of Solids,* vol. 16 pp. 13–31.

[138] Rice, J.R. and Rosengren, G.F., 1968. In *Journal of the Mechanics and Physics of Solids,* vol. 16, pp. 1–12.

[139] Anderson, T.L., 1995. *Fracture mechanics – Fundamentals and Applications*, 2nd edition. Boca Raton: CRC Press, pag. 130

[140] Suresh, S., 2003. *Elastic-Plastic Fracture Mechanics*. Massachusetts Institute of Technology Open Course Ware, number 3.35

[141] Shih, C.F., 1983. *Tables of Hutchinson, Rice, Rosengren singular field quantities*. MRL E-147, Materials Research Laboratory Brown University

[142] Xue, Z. et al., 2010. Calibration procedures for a computational model of ductile fracture. *Engineering Fracture Mechanics*, vol. 77, pp. 492–509

[143] Pineau, A., and Pardoen, T., 2008. Failure of Metals. *Comprehensive Structural Integrity*. Elsevier Science & Technology, chapter 2.06; pp. 686–783

[144] Las, V., et al., 2005. Identification of material parameters of the complete Gurson Model. *22nd DANUBIA-ADRIA Symposium on Experimental Methods in Solid Mechanics*, September 28 - October 1, 2005, Monticelli Terme / Parma, Italy

[145] Howard, I.C. et al.,1994. Ductile crack growth predictions for large centre cracked panels by damage modelling using 3-D finite element analysis. *Fatigue Fract. Engng Muter. Struct.* Vol. 17, pp. 958-969

[146] Pijaudier-Cabot. G. and Bazant Z.P., 1987. Nonlocal damage theory. *Journal of Engineering Mechanics*. Vol. 113(10), pp. 1512–1533

[147] Chu, C.C. and Needleman, A., 1980. Void Nucleation Effects in Biaxially Stretched Sheets. *Journal of Engineering Materials and Technology*, vol. 102, pp. 249–256

[148] ASTM International E561, 2010e1. *Standard Test Method for K-R Curve Determination*. West Conshohocken, PA, USA: ASTM

[149] Anderson, T.L., 1995. *Fracture mechanics – Fundamentals and Applications*, 2nd edition. Boca Raton: CRC Press, p. 367

[150] Anderson, T.L., 1995. *Fracture mechanics – Fundamentals and Applications*, 2nd edition. Boca Raton: CRC Press, p. 370

[151] ASTM International E399, 2009. *Standard Test Method for Linear-Elastic Plane-Strain Fracture Toughness K_{Ic} of Metallic Materials.* West Conshohocken, PA, USA: ASTM

[152] British Standard Institution, 1977. *BS 5447:1977 Methods of test for plane strain fracture toughness (KIc) of metallic materials*. Milton Keynes: BSI

[153] ASTM International E1820, 2009. *Standard Test Method for Measurement of Fracture Toughness.* West Conshohocken, PA, USA: ASTM

[154] Anderson, T.L., 2005. *Fracture mechanics – Fundamentals and Applications*, 3rd edition. London: Taylor and Francis, p. 347, Table A7.1

[155] Anderson, T.L., 2005. *Fracture mechanics – Fundamentals and Applications*, 3rd edition. London: Taylor and Francis, p. 388, Fig. 7.21

[156] Landes, J.D., 1995. The blunting line in elastic-plastic fracture. *Fatigue Fract. Engng Mater. Struct.*, Vol. 18, No. 11, pp. 1289-1297

[157] Herrera, R. and Landes, J.D., 1988. A direct J–R curve analysis of fracture toughness tests. *Journal Test Eval*., vol. 16, no. 5, pp. 427–449.

[158] Herrera, R. and Landes, J.D., 1990. Direct J–R curve analysis: a guide to the methodology. In *Fracture mechanics: 21st symposium*. ASTM STP 1074. Philadelphia: American Society for Testing and Materials, pp. 24–43.

[159] Zhou, Z. et al. 1991. Normalization: an experimental method for developing J–R curves. *Elastic–plastic fracture test methods: the user's experience (2nd volume)*. ASTM STP 1114. Philadelphia: American Society for Testing and Materials, pp. 42–56.

[160] Anderson, T.L., 2005. *Fracture mechanics – Fundamentals and Applications*, 3rd edition. London: Taylor and Francis, p. 147, Fig. 3.22

[161] Anderson, T.L., 2005. *Fracture mechanics – Fundamentals and Applications*, 3rd edition. London: Taylor and Francis, p. 395, Fig. 7.25

[162] Elliott, C. et al., 1991. Development of disc compact tension specimens and test techniques for HFIR irradiations. *Journal of Nuclear Materials*, voll. 179-181, pp. 434-437

[163] Nevalainen, M. and Dodds, R.H., 1995. Numerical investigation of 3-D constraint effects on brittle fracture in SE(B) and C(T) specimens. *International Journal of Fracture* vol. 74, pp. 131-161.

[164] Wallin, K. 2007. *Specimen Size Limitations in J-R Curve Testing – Standards versus Reality*. Journal of ASTM International, vol. 4, issue 9, DOI: 10.1520/JAI100978

[165] taken from The Committee on Rapid Inexpensive Tests for Determining Fracture Toughness, 1977. Rapid inexpensive tests for determining fracture toughness. *International Journal of Fracture*, vol. 13, pag. 277

[166] Driscoll, D.E., 1970. *Impact testing of metals*. ASTM STP 466, p. 120.

[167] Driscoll, D.E., 1970. *Impact testing of metals*. ASTM STP 466, p. 3.

[168] Ray, K.K. and Poddar, G.P., 2004. Estimation of fracture toughness of steel using chevron notched round bar specimens. *Fatigue Fract Engng Mater Struct*, vol. 27, pp. 253–261,

[169] Nath, S.K. and Das, U., June 2006. Effect of microstructure and notches on the fracture toughness of medium carbon steel. *Journal of Naval Architecture and Marine Engineering*, pp. 15 - 22.

[170] Shabara, M.A.N. et al., 1996. Estimation of plane strain fracture toughness from circunferentially bluntly notched round bar specimens. *Engineering Fracture Mechanics*, Vol. 54, No. 4, pp. 533-541

[171] Scibetta, M., 1999. *Contribution to the evaluation of the circumferentially cracked round bar for fracture toughness determination of reactor pressure vessel steels.* Dissertation for the degree of Doctor in Applied Sciences. Universite de Liege, Belgium

[172] Scibetta, M. et al., 2000. Fracture toughness analysis of circumferentially-cracked round bars. *International Journal of Fracture*, vol. 104, pp. 145–168

[173] Trattnig, G. et al., 2008. Fracture of austenitic steel subject to a wide range of stress triaxiality ratios and crack deformation modes. *Engineering Fracture Mechanics*, vol. 75, pp. 223–235

[174] Alexander, D.J., 1993. Fracture toughness measurements with subsize disk compact specimens. *ASTM International Symposium on Small Specimen Test Techniques and Their Applications To Nuclear Reactor Vessel Thermal Annealing and Plant Life Extension*. New Orleans, LA, 29-31 Jan. 1992

[175] Lucon, E., 2001. Material damage evaluation and residual life assessment of primary power plant components using specimens of non-standard dimensions. *Materials Science and Technology*, vol. 17, pp. 777- 785

[176] Lucas, G.E. et al., 2007. The role of small specimen test technology in fusion materials development. *Journal of Nuclear Materials*, voll. 367–370, pp. 1549–1556

[177] Scibetta, M. et al., 2008. On the use of the crack tip opening angle parameter to explain the ductile crack growth behavior of miniature compact specimens. *Engineering Fracture Mechanics*, vol. 75, pp. 3599–3610

[178] Wang, Z. et al., 2008. Small punch testing for assessing the fracture properties of the reactor vessel steel with different thicknesses. *Nuclear Engineering and Design*, vol. 238, pp. 3186–3193

[179] Ling, X. et al., 2007. Creep damage in small punch creep specimens of Type 304 stainless steel, *International Journal of Pressure Vessels and Piping*, vol. 84, pp. 304–309

[180] Wei, T. et al., 2006. Assessment of the fracture toughness of 6061 aluminum by the small punch test and finite element analysis. *Materials Forum,* vol. 30. Institute of Materials Engineering, Australasia Ltd

[181] Besson, J., 2010. Continuum Models of Ductile Fracture: A Review. *International Journal of Damage Mechanics*, Vol. 19, pp. 1-51. DOI: 10.1177/1056789509103482

[182] Suo, Z., 2008. *Solid Mechanics – Finite Element Method*. Note of lecture at the University of Harvard

[183] O'Dowd, N., 1994. Crack growth in an elastic-plastic material and effects on near tip constraint. *Computational Materials Science*, vol. 3, pp. 207-217

[184] Pineau, A., 2007. Development of the local approach to fracture over the past 25 years: theory and applications. *Anales de la Mecanica de Fractura*, vol. 1, pp. 9-24

[185] Chhibber, R. et al., 2008. Estimation of Gurson material parameters in bimetallic weldments for the nuclear reactor heat transport piping system. *Journal Mechanical Engineering Science*. Proceedings ImechE 2008 Vol. 222 Part C

[186] Vadillo, G. and Fernandez-Saez, J., 2009, An analysis of Gurson model with parameters dependent on triaxiality based on unitary cells. *European Journal of Mechanics A/Solids*. Vol. 28, pp. 417–427

[187] Benseddiq, N. and Imad, A., 2008. A ductile fracture analysis using a local damage model. *International Journal of Pressure Vessels and Piping*. Vol. 85, pp. 219–227

[188] Butcher, C.J. and Chen, Z., 2009. Continuum void nucleation model for Al-Mg alloy sheet based on measured particle distribution. *Acta Mechanica Solida Sinica*, Vol. 22, No. 5, pp. 391-398

[189] Horstmeyer, M.F. and Gokhale, A.M., 1999. A void-crack nucleation model for ductile metals. *International Journal of Solids and Structures*, vol. 36, pp. 5029-5055

[190] Horstmeyer, M.F. et al., 2003. Using a micromechanical finite element parametric study to motivate a phenomenological macroscale model for void/crack nucleation in aluminum with a hard second phase. *Mechanics of Materials*, vol. 35, pp. 675–687

[191] Rakin, M. et al., 2000. Micromechanism of ductile fracture initiation – void nucleation in growth. *FACTA UNIVERSITATIS*. Series: Mechanical Engineering Vol.1, No 7, pp. 825 – 833

[192] Surh, M.P. et al., 2008. Void nucleation, growth, and coalescence in irradiated metals. *Journal of Nuclear Materials*, vol. 378, pp. 86–97

[193] Was, G., 2007. *Fundamentals of radiation materials science*. Berlin: Springer, p. 343

[194] Bonora, N., 1999. Identification and measurement of ductile damage parameters. *Journal of Strain Analysis*, vol. 34, n.6, pp. 463-478

[195] Besson, J. et al., 2004. *Local approach to fracture*. Paris: Ecole des Mines de Paris, p. 303

[196] Anderson, T.L., 2005. *Fracture mechanics – Fundamentals and Applications*, 3rd edition. London: Taylor and Francis, chapter 7

[197] Sherry, A.H. and Wilkes, M.A., 2005. Numerical simulation of tearing–fatigue interactions in 316L(N) austenitic stainless steel. *International Journal of Pressure Vessels and Piping*, vol. 82, pp. 905–916

[198] Was, G., 2007. *Fundamentals of radiation materials science*. Berlin: Springer pp. 622-626

[199] British Standard Institution, 2005. *BS EN ISO 6507-1:2005 Metallic materials - Vickers hardness test – Part 1: Test method*. Milton Keynes: BSI

[200] Bhadeshia H. K. D. H. *Metallography*. The University of Cambridge. [online] Available at http://www.msm.cam.ac.uk/phase-trans/abstracts/CP1b.html [Accessed 11 August 2010]

[201] Zipperian, N. *Metallographic Specimen Preparation Basics*. Pace Technologies Educational Web page [online] Available at http://www.metallographic.com/Basics.htm [Accessed 11 August 2010]

[202] ASTM International, 2001. A 262–01, *Standard Practices for Detecting Susceptibility to Intergranular Attack in Austenitic Stainless Steels, Practice A — Oxalic Acid Etch Test for Classification of Etch Structures of Austenitic Stainless Steels*. West Conshohocken, PA, USA: ASTM

[203] Davidson, M.W. and Abramovitz, M., 1999. *Optical Microscopy*. Florida State University. [online] Available at http://micro.magnet.fsu.edu/primer/opticalmicroscopy.html [Accessed 11 August 2010]

[204] British Standard Institution, 2003. *BS EN ISO 643:2003 Steels — Micrographic determination of the apparent grain size*. Milton Keynes: BSI

[205] Alegre, J.M. and Gutierrez-Solana, F., 2005. Finite element simulation of fracture behaviour for aged duplex stainless steels. *International Journal of Fracture*, vol. 134, pp. 23–39

[206] British Standard Institution, 2001. *BS EN 10002-1:2001, Metallic materials – tensile testing - Part 1: Method of test at ambient temperature*. Milton Keynes: BSI

[207] Parrington, R.J., 2002. Fractography of Metals and Plastics. *Practical failure analysis*, vol. 2(5), pp. 16-19 and 44-46

[208] Swapp, S. *Scanning electron microscopy*. University of Wyoming. [online] Available at http://serc.carleton.edu/research_education/geochemsheets/techniques/SEM.html [Accessed 11 August 2010]

[209] Cut-off Wheels, Struers brochure. [online] http://www.struers.com/resources/elements/12/180436/Cut_offWheelsBrochureEnglish.pdf [Accessed 11 August 2010]

[210] Zipp, R.D. and Dahlberg, E.P., 1987. Preparation and Preservation of Fracture Specimens. *ASM Handbook, Volume 12: Fractography*. Pp. 72-77.

[211] Sun Jun, 1990. Strength for decohesion of spheroidal carbide particle-matrix interface. *International Journal of Fracture*, vol. 44, pp. R51-R56.

[212] Sun Jun et al., 1990. Fracture strength of spheroidal carbide particle. *International Journal of Fracture*, vol. 42, pp. R39-R42.

[213] Vignal et al., 2003. Local analysis of the mechanical behaviour of inclusions-containing stainless steels under straining conditions, *Scripta Materialia*, vol. 49, pp. 779–784

[214] Besson, J. et al., 2004. *Local approach to fracture*. Paris: Ecole des Mines de Paris, pp. 79-105

[215] Stock, S.R., 2009. *MicroComputed Tomography: Methodology and Applications.* Boca Raton: CRC Press.

[216] [online] Available at http://www.mxif.manchester.ac.uk/index.php/xradia-microxct

[217] Bridgman, P.W., 1952. *Studies in large plastic flow and fracture*. New York: McGraw-Hill.

[218] Hilders, O.A. and Santana, M.G., 1988. Toughness and Fractography of Austenitic Type 304 Stainless Steel with Sensitization Treatments at 973 °K. *Metallography*, vol. 21, pp. 151-164

[219] Anderson, T.L., 1995. *Fracture mechanics – Fundamentals and Applications*, 2nd edition. Boca Raton: CRC Press, p. 368

[220] Chopra, O.K. and Rao, A.S., 2011. A review of irradiation effects on LWR core internal materials – Neutron embrittlement. *Journal of Nuclear Materials*. Vol. 412, pp. 195–208

[221] West Yorkshire Steel Co Ltd. *D2 Tool Steel*. [online] Available at http://www.westyorkssteel.com/d2.html [Accessed 11 August 2010]

[222] Tanner, G.M. and Bradley, W.L., 1988. Evaluation of the Fracture Toughness of the Ductile Iron using fatigue precracked Charpy, Dynamic Tear, and Compact Tension

Specimens. *Fracture mechanics: Eighteenth Symposium, ASTM STP 945*. D.T. Read and R.P. Read, Eds., American Society for Testing Materials, Philadelphia, pp. 405-418

[223] Besson, J. et al., 2004. *Local approach to fracture*. Paris: Ecole des Mines de Paris, p. 298

[224] Ramberg, W. and Osgood, W.R., 1941. Determination of Stress-strain Curves by Three Parameters. *Technical Note No. 503*. National Advisory Committee on Aeronautics

[225] Besson, J. et al., 2004. *Local approach to fracture*. Paris: Ecole des Mines de Paris, p. 297

[226] Besson, J. et al., 2004. *Local approach to fracture*. Paris: Ecole des Mines de Paris, p. 336

[227] Besson, J. et al., 2004. *Local approach to fracture*. Paris: Ecole des Mines de Paris, p. 299

[228] Borvik, T. et al., 2003. On the influence of stress triaxiality and strain rate on the behaviour of a structural steel. Part II. Numerical study. *European Journal of Mechanics A/Solids.* Vol. 22, pp. 15–32

[229] Li, Y.N. et al., 2007. Mesh Size Effects in Simulating Ductile Fracture of Metals. *10th International Symposium on Practical Design of Ships and Other Floating Structures*. American Bureau of Shipping, Houston, Texas, United States of America.

[230] Wu, X., et al., 2007. Analysis of notch strengthening of 316L stainless steel with and without irradiation-induced hardening using EBSD and FEM. *Journal of Nuclear Materials.* Vol. 361, pp. 228–238

[231] Samal, M.K. et al., 2009. A mesh-independent Gurson–Tvergaard–Needleman damage model and its application in simulating ductile fracture behaviour, *Proceedings of the Institution of Mechanical Engineers, Part C: Journal of Mechanical Engineering Science,* pp. 223- 283

[232] Tsubota, M. et al., 2005. Stress corrosion crack growth behavior of cold worked austenitic stainless steel in high temperature water. *Proceedings of the 12th International Conference on Environmental Degradation of Materials in Nuclear Power System – Water Reactors.* The Minerals, Metals & Materials Society

[233] Datsko, 1997. *Materials selection of design and manufacturing*, 2nd edition. Boca Raton: CRC Press, pp. 219-220

[234] Celikin, M. et al., 2009. Compressive creep behaviour of cast magnesium under stresses above the yield strength and the resultant texture evolution. *Canadian Metallurgical Quarterly*, Vol. 48, No. 4, pp. 419-432

[235] Ghosh, S. et al., 2009. Deterioration in Fracture Toughness of 304LN Austenitic Stainless Steel Due to Sensitization. *Metallurgical and Materials Transaction A*, vol. 40A, pp. 2938 – 2949.

[236] Tavares, S. S. M. et al., 2003. Influence of the starting condition on the kinetics of sensitization and loss of toughness in an AISI 304 steel. *Journal of Materials Science*, vol. 38, pp. 3527 – 3533.

[237] Senior, B. A., et al., 1989. Effects of aging at 700°C on ductile fracture of AIS1 316 stainless steel. *Materials Science and Technology*, vol. 5, pp. 1090 - 1094

[238] Simonovski, I. et al., 2008. Modelling of Intergranular Damage in Polycrystalline Metals. *Nuclear Energy for New Europev- International Conference*. Portoroz, Slovenia

[239] Kamaya, M. and Itakura, M., 2009. Simulation for intergranular stress corrosion cracking based on a three-dimensional polycrystalline model. *Engineering Fracture Mechanics*, vol. 76, pp. 386–401

[240] Morgan, M. J., 2008. Tritium aging effects on the fracture toughness properties of forged stainless steel. *Materials Innovations in an Emerging Hydrogen Economy: Ceramic Transactions volume 202*, The American Ceramic Society, Wiley & Sons pub.

[241] Guillamet, R., et al., 1993. Oxidation of stainless steels (AISI 304 and 316) at high temperature. Influence on the metallic substratum. *Journal de Physique IV*, Colloque C9, supplement au Journal de Physique 111, vol. 3, pp. 349-356

[242] Di Schino, A. et al., 2002. Analysis of the recrystallization and grain growth processes in AISI 316 stainless steel. *Journal of Materials Science*, vol. 37, pp. 5291-5298

[243] Zhang, Z.L. and Skallerud, B., 2010. Void Coalescence With and Without Prestrain History. *International Journal of Damage Mechanics*. Vol. 19, pp. 153-174

[244] Kamaya, M., 2010. Effect of Plastic Strain on Fracture Strength of Cracked Components. *Paper n. 09-0743*. The Japan Society of Mechanical Engineers.

[245] Hanxing, Z. et al., 1992. Effects of prestrain on the fracture properties of pressure vessel steel, *International Journal of Fracture*. Vol. 53, pp. 291-299

[246] Amouzouvi, K.F., 1986. A Comparative Fracture Study of a Slightly Prestrained Low Alloy Steel and a Slightly Prestrained Austenitic Stainless Steel. *Materials Science and Engineering*. Vol. 78, pp. 65-70

[247] Cosham, A., 2001. A model of pre-strain effects of Fracture Toughness. *Transactions of the ASME*. Vol. 123, pp. 182-190

[248] Eikrem, P.A. et al., 2008. Numerical study on the effect of prestrain history on ductile fracture resistance by using the complete Gurson model. *Engineering Fracture Mechanics.* Vol. 75, pp. 4568–4582

[249] ASTM International, 2009. A240 – 11, *Standard Specification for Chromium and Chromium-Nickel Stainless Steel Plate, Sheet, and Strip for Pressure Vessels and for General Applications*. West Conshohocken, PA, USA: ASTM

[250] Abaqus 6.7 documentation, "Abaqus theory manual": 2.2.1 Nonlinear solution methods in Abaqus/Standard

[251] Miannay, D.P., 1997. *Fracture Mechanics*. Berlin: Springer, p. 113

[252] Evans, J.T., et al., 1995. A method for fracture toughness testing cylinder material. *Engineering Fracture Mechanics,* vol. 50, no. 2, pp. 295-310

[253] Zhu, X., 2009. *J*-integral resistance curve testing and evaluation. *Journal of Zhejiang University SCIENCE A.* Vol. 10(11), pp. 1541-1560

[254] Corigliano, A., et al., 2000. Identification of Gurson–Tvergaard material model parameters via Kalman filtering technique. I. Theory. *International Journal of Fracture*, vol. 104, pp. 349–373

[255] Zhang, Z.L., 2001. A complete Gurson Model, in *Nonlinear Fracture and Damage Mechanics*, edited by M. H. Alibadi, WIT Press Southampton, UK, pp. 223-248.

[256] Pardoen, T., 2006. Numerical simulation of low stress triaxiality ductile fracture. *Computers and Structures*. Vol. 84, pp. 1641–1650

[257] Pokor, C., et al, 2004. Irradiation damage in 304 and 316 stainless steels: experimental investigation and modeling. Part II: Irradiation induced hardening. *Journal of Nuclear Materials*, vol. 326, pp. 30–37

Appendices

This Section contains more literature review and minor results. They did not add to the original research but were interesting enough to deserve a mention.

A. Helium embrittlement theories

The nature of helium embrittlement is still under discussion and many theories have been postulated. They are here reported as taken from one comprehensive work of Fabritsiev [89]. Bloom and Weir [90] suggested that helium strengthening of the boundary region makes the relaxation of stresses concentrated at ternary junctions difficult during intergranular sliding, thus stimulating the initiation of wedge-shaped intergranular cracks. Barnes [91] suggested that embrittlement is connected with an increase of pressure at the grain boundary helium pores, coalescence of which leads to failure. Both of the above theories are not completely satisfactory: during experimental tests, the helium bubbles that Barnes postulated were not observed, yet embrittlement occurs and, under the Bloom-Wier conditions, embrittlement at high temperatures (T ≥ 850 °C) cannot be explained, as the stress concentration required for crack initiation should not be achievable. Rowcliffe [92] improved the Barnes model arguing that materials contained minute helium bubbles that were carried away during deformations by dislocations at the grain boundaries. These bubbles were suggested to be of the size $d \leq 400$ nm and, when they coalesce, bubbles are formed of a supercritical size:

$$r_{\sup} > \frac{0.76\gamma}{\sigma_{act}} \tag{A.1}$$

where r_{sup} is the radius of the supercritical bubble. When the bubble reaches this value, it is suggested that it has the capacity for spontaneous growth; γ is the material surface tension energy and σ_{act} is the actual tensile stress normal to the boundary in which a

bubble is created. Even with this suggestion though, on occasion, resolvable bubbles were not present when embrittlement occurs.

Sokurskii and others [93-95] put forward the idea that "embrittlement was connected to the suppression of polygonization processes (formation of misoriented subgrains via dynamic recovery) in materials containing helium. This would lead to the strengthening of the bodies of grains, and the weakening of grain boundaries with precipitation of helium in them." The resulting imbalance of grain-to-grain boundary strengths would lead to stimulation to a change over to inter-granular failure of materials containing helium.

Ozhigov and Kiryukhin [96] showed that the helium embrittlement of materials might be connected with the evolution of helium porosity during high temperature deformation. They showed this via means of a computer simulation of the strengthening of a solid solution with fine helium bubbles. However, a study of the failure mechanisms such as initiation and growth of grain boundaries microdiscontinuities, was beyond their scope. The main point of this work was that, via this model, grain boundary strengthening is done by fine helium bubbles.

Nix and Matlock [97-99] tried two approaches towards helium embrittlement. They suggested that the failure is due to the growth of fine pores in the stress field of a grain-boundary wedge shaped crack. Their studies did manage to show, as had the earlier work of Waddington [100], that this synthetic nature of failure does occur sometimes.

General modelling of the growth of helium bubbles is not a problem by means of the widely accepted rate theory, described in [87]. It is difficult to model the supercritical micro-discontinuity formation. The analysis of the nature of failure of specimens containing helium shows that the failure is caused by the growth and coalescence of the grain boundary micro-discontinuities. However, in the actual specimens, this micro-discontinuity nucleus is either not detected at all, or its size is much less than the r_{sup} value defined in equation (A.1). None of the existing theories describing helium embrittlement provides an answer to this. The most likely reason for this failure of

models to describe accurately the process is that they do not take account of the dynamic processes occurring in the material during in high temperature deformation [89].

Gifkins [101] tried to consider the dynamic mechanism for grain boundary pore nuclei by the means of the well-known microstructures of austenitic steels and alloys, at high test temperatures, letting them fail with some proportion of intergranular fracture. He argued that the high stresses that would be necessary for these pores to grow, only occur with considerable deformation.

$$\sigma_{act} > \frac{2\gamma}{r} \tag{A.2}$$

According to this model, a step forming at intergranular slip at a grain boundary leads, with subsequent sliding along this boundary, to breakage and pore formation. If the applied stress is large enough to fulfil the equation (A.2), then the pore remains stable or it will grow. If the stress is too low, then the pore is unstable and will be reabsorbed. Therefore, according to Gifkins model, pores in materials containing helium forming at grain boundaries, stabilise at much lower stresses than in materials without helium because of precipitation of helium at pore nuclei [89].

If the subsequently arising pore has a radius of r_0, with operating tensile stress σ_{act}, then the equation (A.2) can be restated as:

$$\sigma_{act} < \frac{2\gamma}{r_0} \tag{A.3}$$

From which it can be taken that the pore will be unstable and simply reabsorbed. However, if helium is precipitated into the pore, from the solid solution around it, then the equation (A.3), can be reworked as:

$$\sigma_{act} + \rho_{He} < \frac{2\gamma}{r_0} \tag{A.4}$$

where ρ_{He} is the pressure of helium; with further helium precipitation, there can be an instant reached where:

$$\sigma_{act} + \rho_{He} = \frac{2\gamma}{r_0} \tag{A.5}$$

Experiments have shown that the stabilisation of pores filled with helium may occur for a value of σ_{act} that is a factor of 2.36 smaller than for a vacant pore. From an energy viewpoint, this precipitation of helium in a pore will always be favourable (in the sense of Gibbs free energy change, that is to say products have less free energy than the reactants), since the energy of helium in a solid-solution pore is greater than a system with solid-solution helium in the pore. Via tensile tests, it can be seen that the growth of pores, and inter-granular failure in specimens containing helium start at much lower stresses and strains than in specimens that don't contain helium [89].

To realise this embrittlement mechanism, several factors are required [89]:

(1) Intergranular slip (plastic deformation produced by a dislocation motion),
(2) Intergranular (grain-boundary) sliding,
(3) Effective diffusion mobility for helium,
(4) Effective self-diffusion, and
(5) A certain stress level.

Conditions (2), (3), and (4) can be realised at high test temperatures, (where $T_{test} \geq 0.4 \ldots 0.5\ T_m$). An increase in helium concentration can speed up the process of pore stabilisation, since the effective volume from which it is necessary for helium to diffuse into pore nuclei will decrease. The consequence of this is that embrittlement will also intensify.

Helium has to travel to the grain boundaries and this leads into the mechanism of helium embrittlement. Helium transport is depicted by flows. Due to the general insolubility in metals, the extrinsic interstitial energy is very low. Transport to grain boundaries is dependent on the microstructure of the material. There is a strong dependence between the bubble nucleation growth and the flow of helium to the grain boundaries [102].

There are three main mechanisms of transportation, He-diffusion, He-bubble migration, and He-atom and He-bubble dragging by dislocation moving [107] and there are multiple complex possibilities that also contribute to the transportation [102], these being:

(1) Thermal trapping/de-trapping in vacancies and vacancy clusters.
(2) Replacement of substitutional helium by Self-Interstitial atoms (SIAs).
(3) Extrinsic interstitial diffusion.
(4) Dynamic displacement by cascades.
(5) Pipe diffusion along dislocation cores.
(6) Stress-induced transport by dislocation motion, and
(7) Bubble thermal, and stress gradient transport.

The helium diffusion is strongly influenced by microstructure defects such as vacancies and impurities, or extended microstructure defects like dislocations, solid precipitates or helium bubbles formed on them. These defects are known as "traps", and when under creep conditions, the already formed helium bubbles make the most effective traps.

It is the nucleation of these bubbles that is the main cause of helium embrittlement. How this nucleation occurs, and its particular effects depends on whether it occurs under low temperatures or high temperatures [103].

At low temperatures, the thermal dissociation from helium atom traps is negligible, so there will be need for determining factors to solve whether the nucleation will be homogeneous (without preferential sites) or heterogeneous (happening at so called nucleation sites). If the sink strength of the bubble nuclei and their size is larger than the sink strength of pre-existing traps, then the nucleation will be homogeneous. With high temperatures though, the thermal dissociation of helium atom traps must be taken into consideration. In this situation the relationship between sink strength does not provide a sufficient criterion for determining whether homogeneous or heterogeneous nucleation of the embrittlement causing bubbles occurs. Effects of dislocation cores, the thermal dynamics of critical bubble nuclei, i.e. the state of helium atoms within them and the corresponding thermal equilibrium of helium atoms around them, are much more crucial, as formally described in [103].

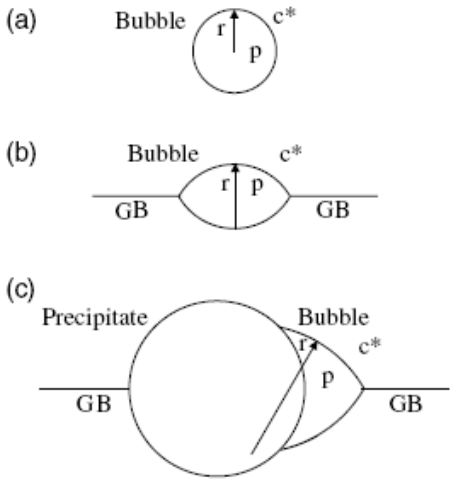

Fig. A.1. Interfacial effects on cavity nucleation at high temperatures [87].

Fig. A.1 shows the "classic" understanding of these effects on the thermodynamic state of a nucleus of a given volume, (on the radius of curvature of the surface, *r*). The corresponding equilibrium gas pressure inside it is:

$$p = \frac{2\gamma}{r} \tag{A.6}$$

where γ is the specific surface free energy. Part (b) of Fig. A.1 shows the interfacial equilibrium of the triple junction between surface segments of a bubble and a grain boundary. Part (c) of Fig. A.1 shows an increase in r, which in turn creates a corresponding decrease in both *p(r)*, and *c(r)*, the gas pressure inside the bubble, and the concentration of helium around the bubble respectively. These relationships suggest that heterogeneous nucleation occurs at a lower concentration of helium than homogeneous nucleation, and therefore would be reached earlier. Therefore, a significant reduction of helium concentration from premature heterogeneous nucleation would prevent additional homogeneous nucleation [104].

The usual size distribution of helium bubbles is in the order of very few nanometres. Their behaviour under stress at different temperatures is described in [105].

B. Preliminary qualitative results for fracture toughness

A qualitative estimation of fracture toughness can be inferred from the size of the dimples of the specimens used for introducing damage into the material. The reference study is from Hilders and Santana [218]. The following cases are shown in Fig. B.1:

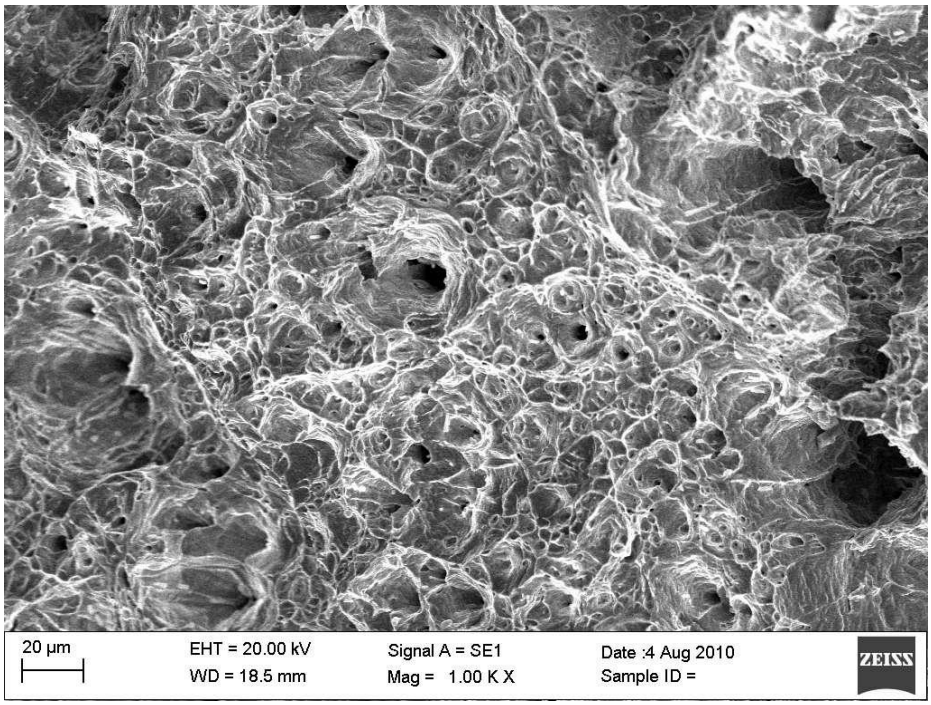

(a) "undamaged"

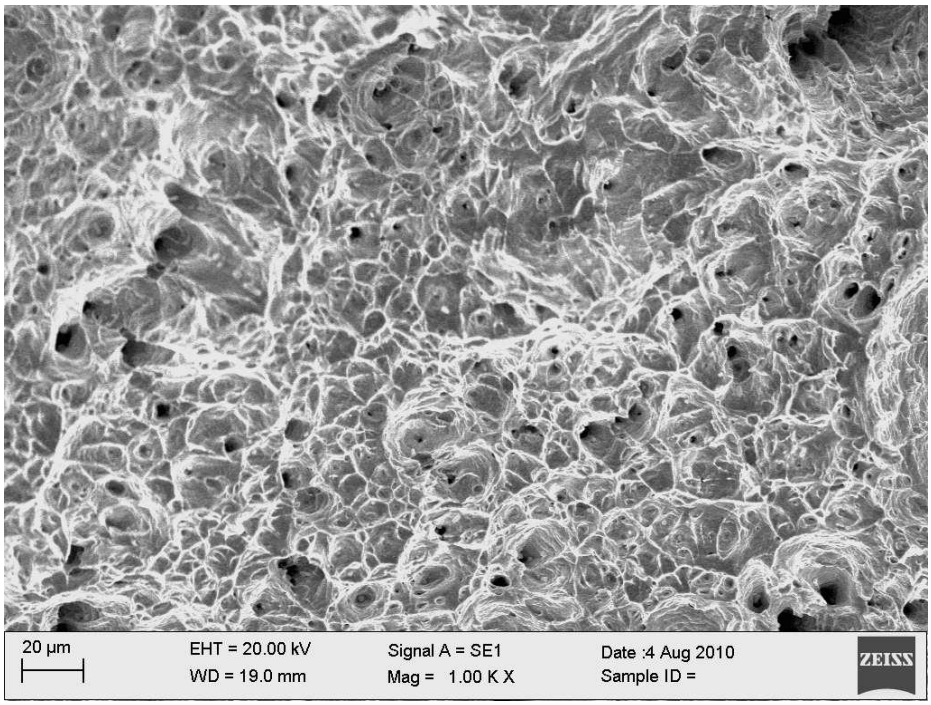

(b) 30% + sol. ann. + 10%

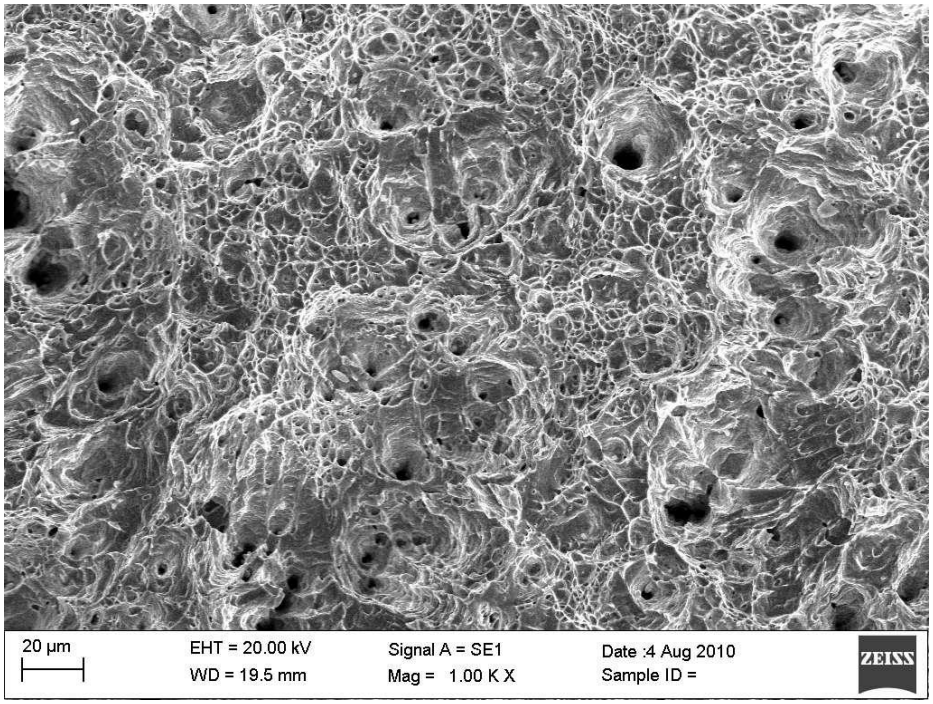
20 µm
EHT = 20.00 kV
WD = 19.5 mm
Signal A = SE1
Mag = 1.00 K X
Date :4 Aug 2010
Sample ID =
ZEISS

(c) 30%

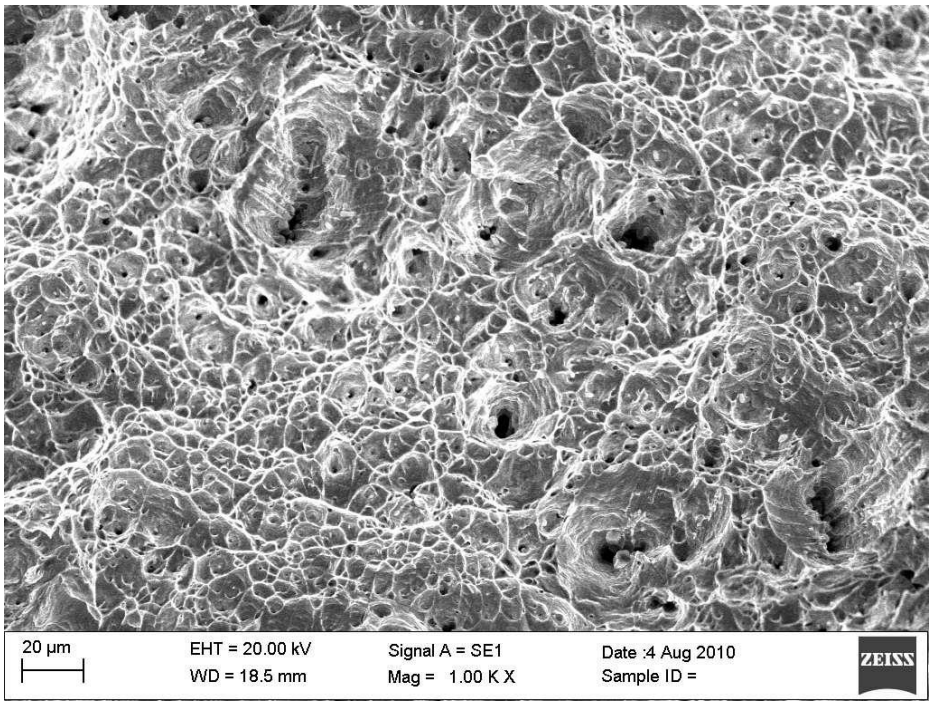
20 µm
EHT = 20.00 kV
WD = 18.5 mm
Signal A = SE1
Mag = 1.00 K X
Date :4 Aug 2010
Sample ID =
ZEISS

(d) 30% + 10%

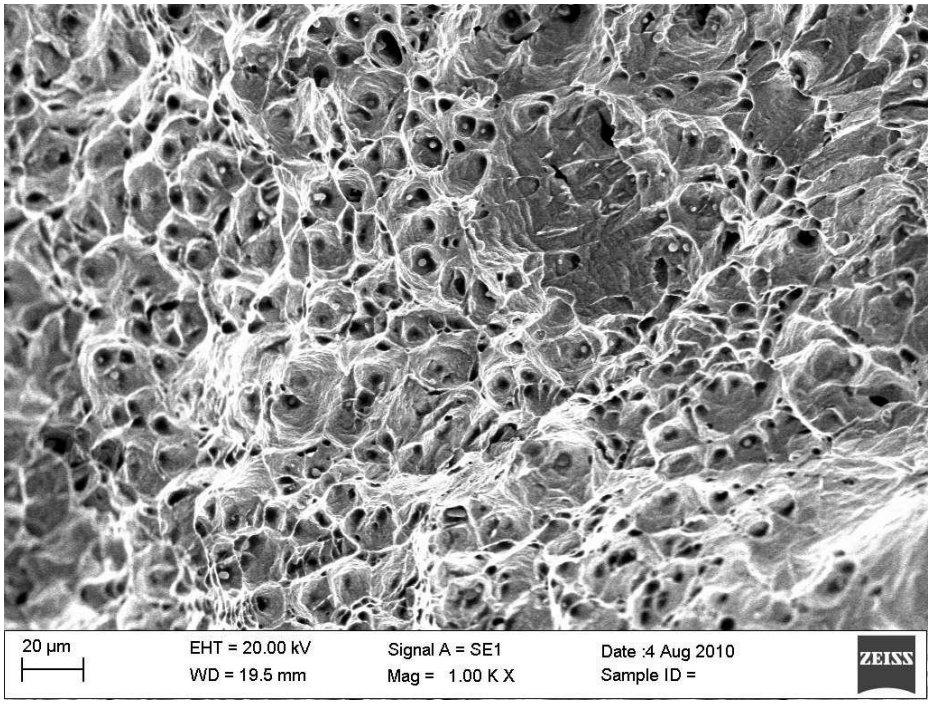

(e) creep 1000°C, 6% elongation

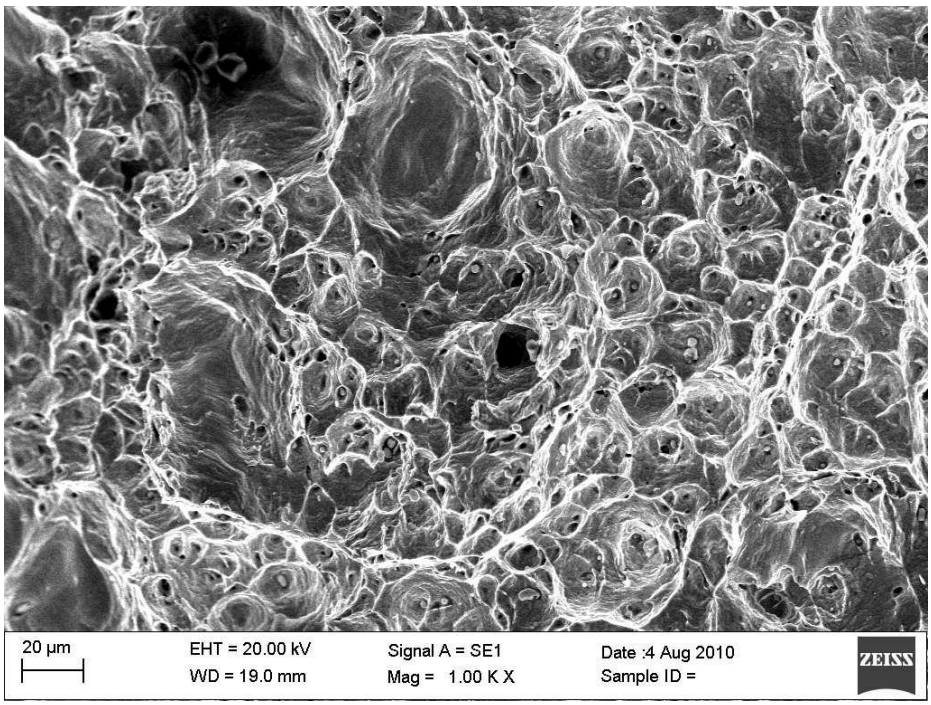

(f) creep 1000°C, 11% elongation

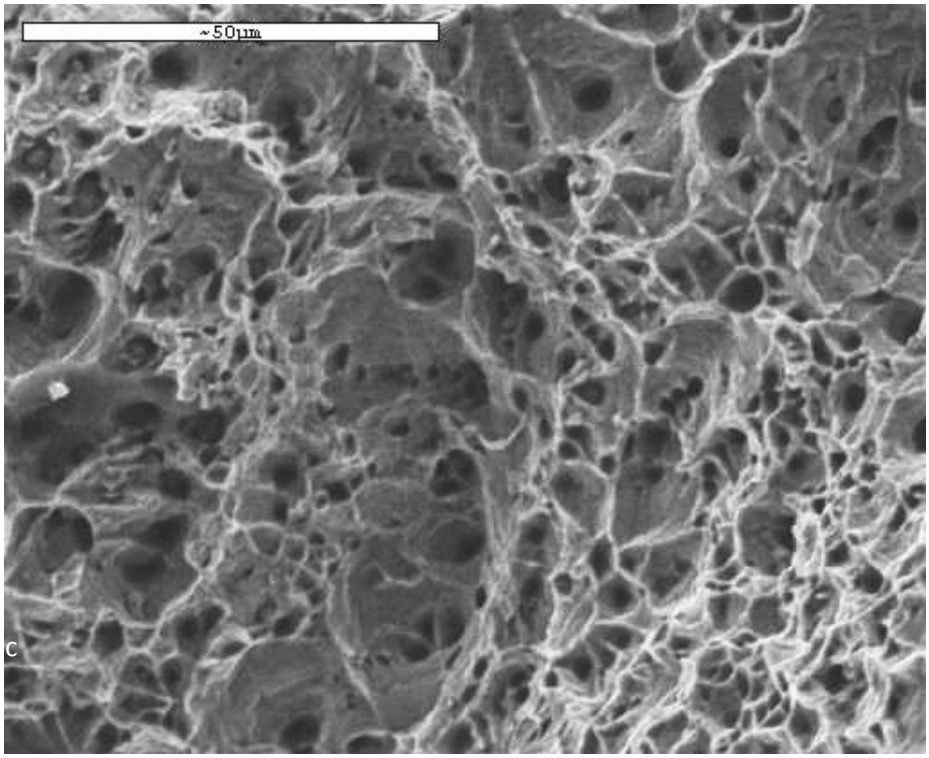

(g) creep 650°C, 70 hours

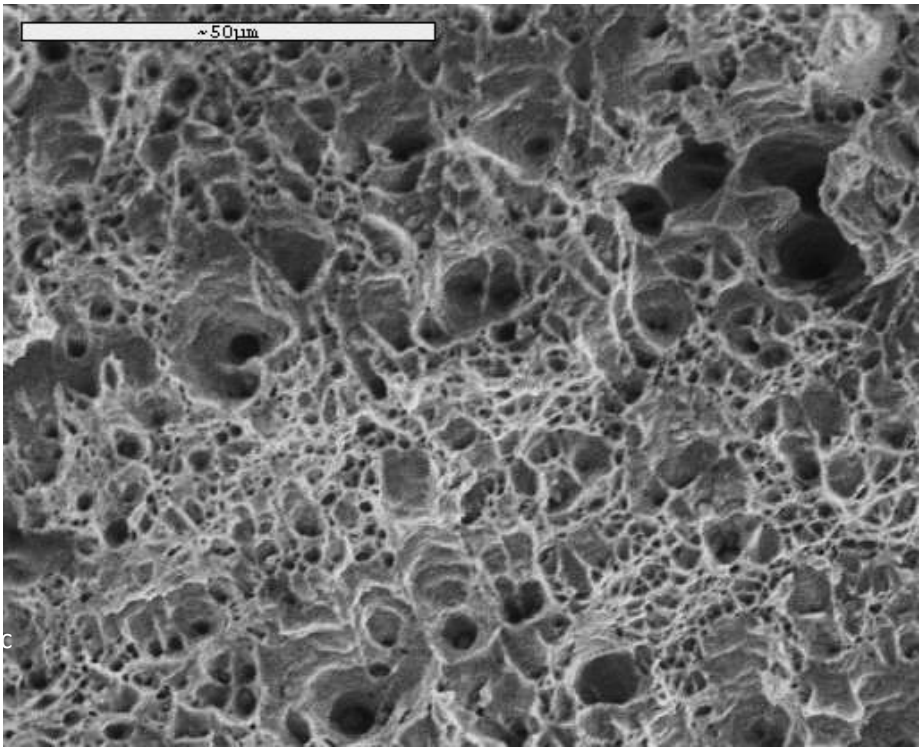

(h) creep 650°C, 1500 hours

Fig. B.1(a)-(h). Dimples from sharp-notched specimens.

In this model, the crack growth increment is considered equal to the dimple size, which can be measured by means of the mean intercept length of 3D bodies or mean chord in space L_3. Eccentricity and dimple size might then be estimated and a relation with K_{IC} established in axial stress conditions as

$$K_{IC} = En(2\pi\bar{L}_3)^{1/2} \quad \text{(B.1)}$$

where E is the Young Modulus and $n = \mathrm{d}\log\sigma / \mathrm{d}\log\varepsilon$. Instability then happens when a critical strain takes place over the process zone size, that is one dimple [218].

The model is valid at the centre of the fracture surface, where the stresses are predominantly tensile and the dimples roughly equiaxed, with the major axis of the ellipsoids is oriented in the tensile direction. Fig. B.1(a)-(h) were all taken at the centre of the respective specimens.

For the aim of this project, however, this way presented too much a variance in the mean size of the dimples from each specimen (in particular for the "undamaged" and the strain hardened ones) for being deemed acceptable. It could not be established univocally the predominant dimension among them. However, qualitatively speaking it appeared that dimples from strain hardened material were smaller than for "undamaged" material. Dimples also appeared to be slightly bigger for creep-damaged material than for the "undamaged" material. Smaller dimples correspond to lower fracture toughness initiation, so strain hardened material appeared to show lower fracture toughness initiation than "undamaged" material. The latter appeared to show comparable or slightly lower fracture toughness than creep damaged material.

This qualitative conclusion could be improved by considering blunting. Blunting is sometimes defined as "apparent crack growth" and it is one indicator of the plastic component of the fracture toughness initiation. If the elastic component is the same for all the specimens, higher the blunting higher the total fracture toughness value. Blunting was investigated for broken strain hardened specimens. The profiles obtained by optical microscopy are shown in Fig. B.2:

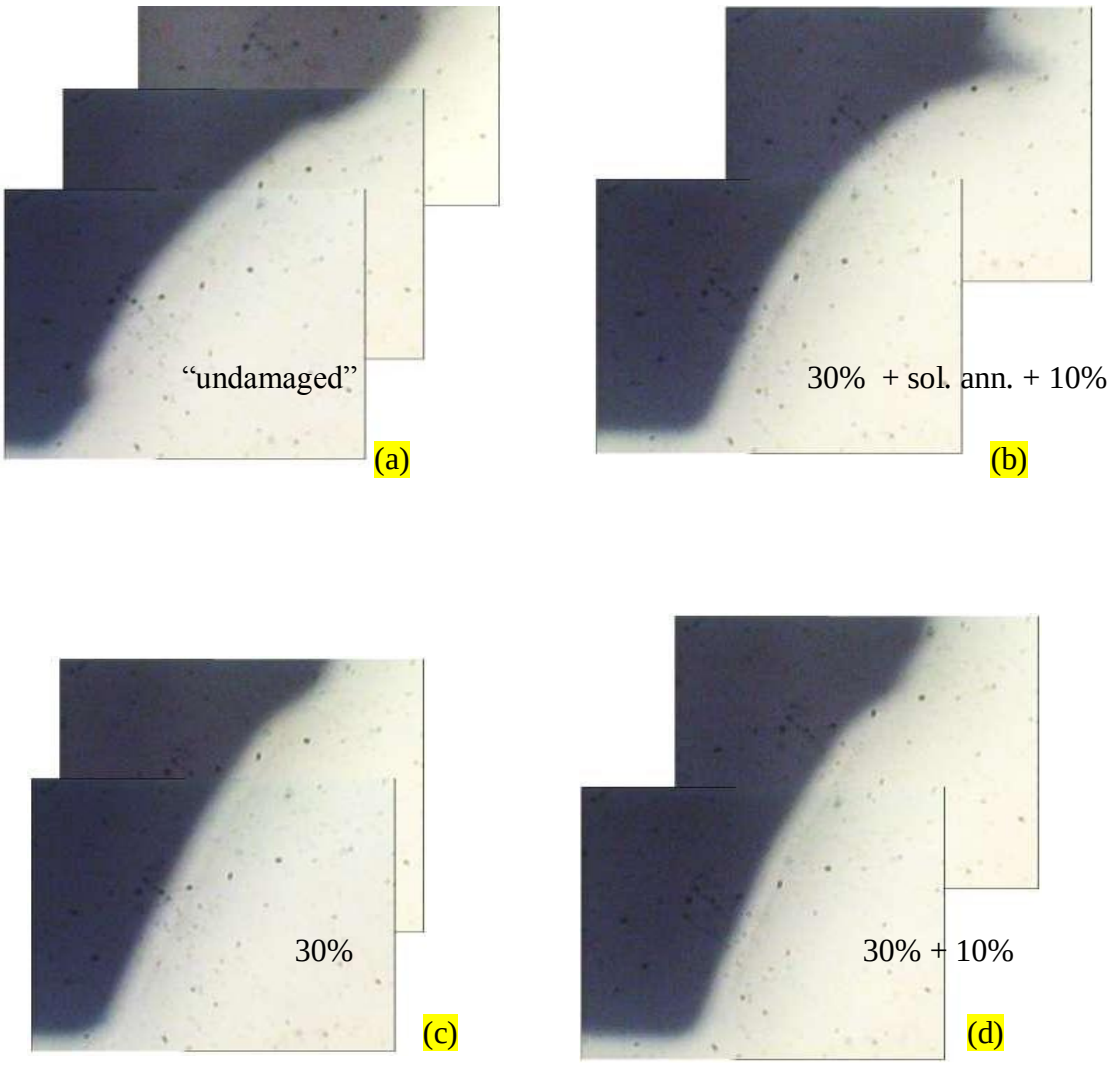

Fig. B.2. Blunting from sharp-notched round bar specimens.

These images again did not provide quantitative evidence but they still permit to narrow the scale of comparison. In particular, it appears that blunting was the highest for the "undamaged" material, followed by the 30% + sol. ann. + 10% strain hardened specimen, the 30% strain hardened specimen and the 40% strain hardened specimen.

C. Tentative fracture toughness resistance curves

The normalization method, as used by Landes [156-159], was attempted. It was done by computing the load vs. displacement data for the sharp-notched tensile specimens. One crack front element was removed each time, as it was a stationary crack. It was then evaluated the area under every curve and its intercept starting from the experimental one, as in Fig. 2.44:

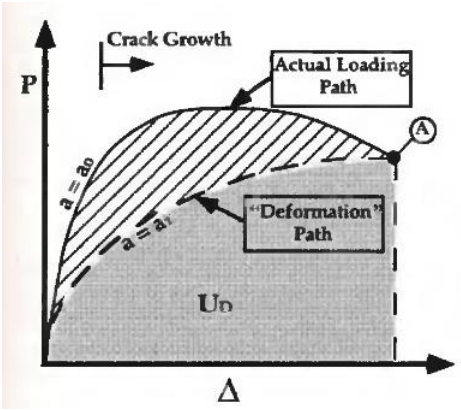

Fig. 2.44. Schematic load-displacement curve with a crack that grows from a_0 to a_1.

The actual loading path in the figure was the actual experimental path, as obtained from specimens, while the deformation paths corresponding to different crack openings a1, a2, a3 ... aN was computed numerically by removing the elements at crack front, one at time, and repeating the calculation.

The smooth tensile specimen used for interrupted tensile tests, reproduced in Fig. C.1, were modelled as follows:

MODEL	NODES	ELEMENTS	TECHNIQUES
smooth bar	356	306 CAX4R	free meshing + minimize transition

Table C.1. Finite element model specification for hardening simulation.

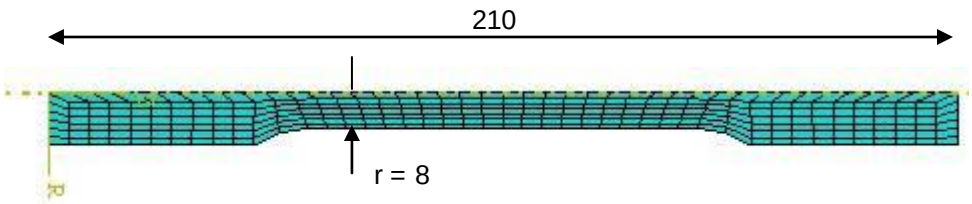

Fig. C.1. Model from interrupted tensile test specimen.

In accordance with the Section 2.3.3 and considering the limitations of sharp-notched specimens for *J*-resistance curves, pointed out by Scibetta [171], the normalization method from Landes [156], as modified by Byun and based on the energy release rate definition of Rice, was here applied. Blunting was accounted for and superimposed as apparent crack growth.

The method employed for *J* calculation made use of the load vs. displacement plot, as in Fig. C.2 for one of the "damaged" states:

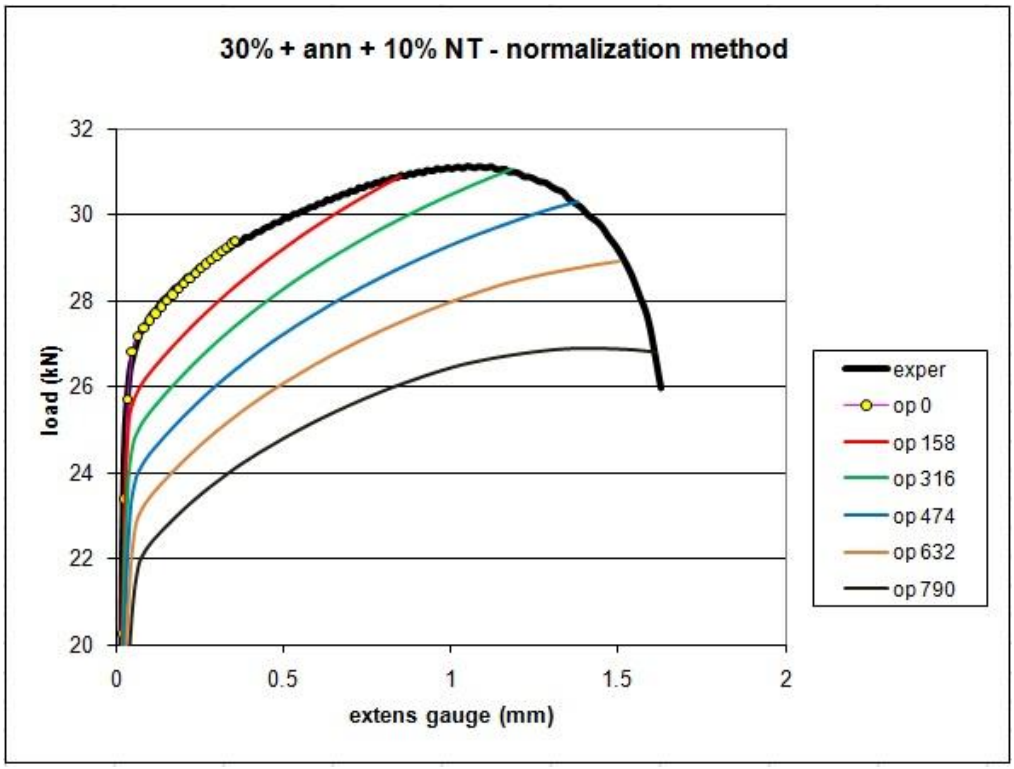

Fig. C.2. Normalization method on one notched specimen.

The normalization method was the only feasible, considering that a single specimen had been tested for each "damaged" case and that the numerical models used to validate the experimental results were only good up to the crack initiation point.

The elements at the crack front were removed once at time from the model already used for validation. The computation was repeated as if the initial crack length was the updated one. The strain hardening curves relative to each crack growth step (0 - 0.158 mm - 0.316 mm - 0.474 mm - 0.632 mm in Fig. C.3, reporting the finite element model partitioned at the crack front, with the removal progression) were computed in ABAQUS by using the calibrated and validated constitutive models relative to each case here considered: "undamaged" – 40% strained – creep at 1000 °C, both 11% and 6% strain.

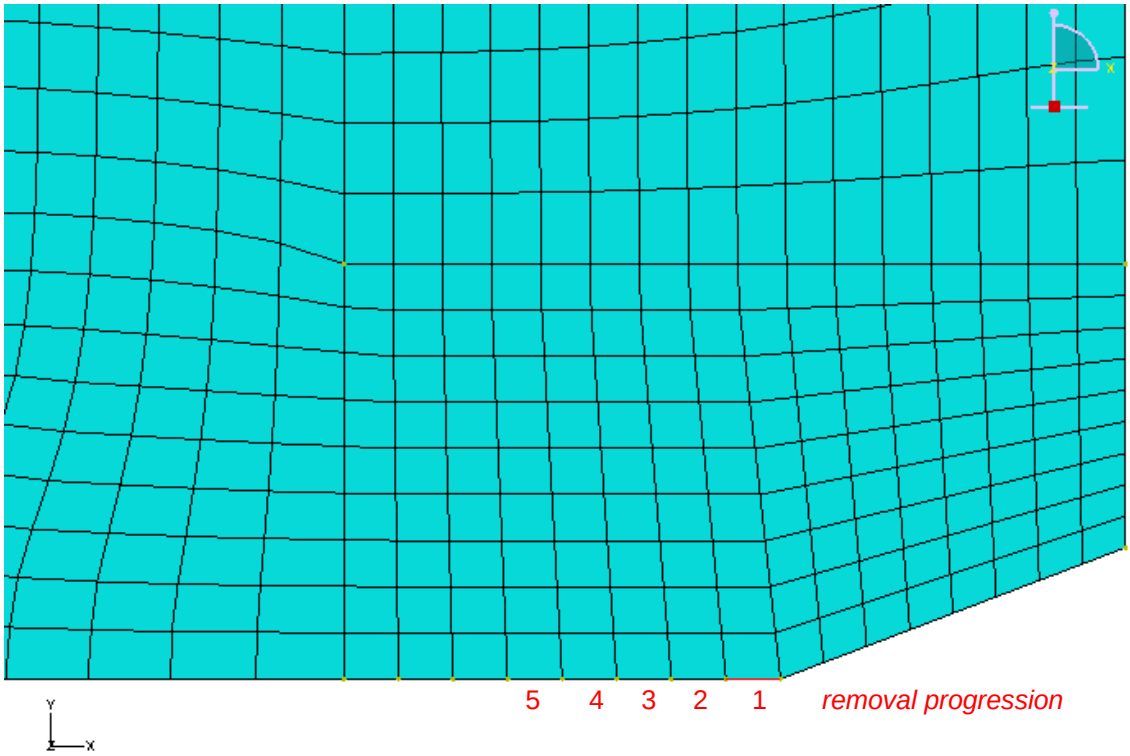

Fig. C.3. Detail of elements removal progression at the crack front.

The curves were then used to compute *J* for the crack rounded bar specimen as follows:

$$J_i = \frac{(2-n_i)}{2\pi r_i^2} U_i \qquad \text{(C.1)}$$

n_i : exponent of the actual hardening curve at step i, r_i : actual ligament at step i, U_i : elastic plastic energy measured as the area under the hardening curve.

The area under the curves was computed numerically partitioning the integrals. In particular, the area OAB represents the J value for a crack opening 0.158 mm, the area OCF is for a crack opening 0.316 mm and so on, as in Fig. C.4 (which extends Fig. C.2):

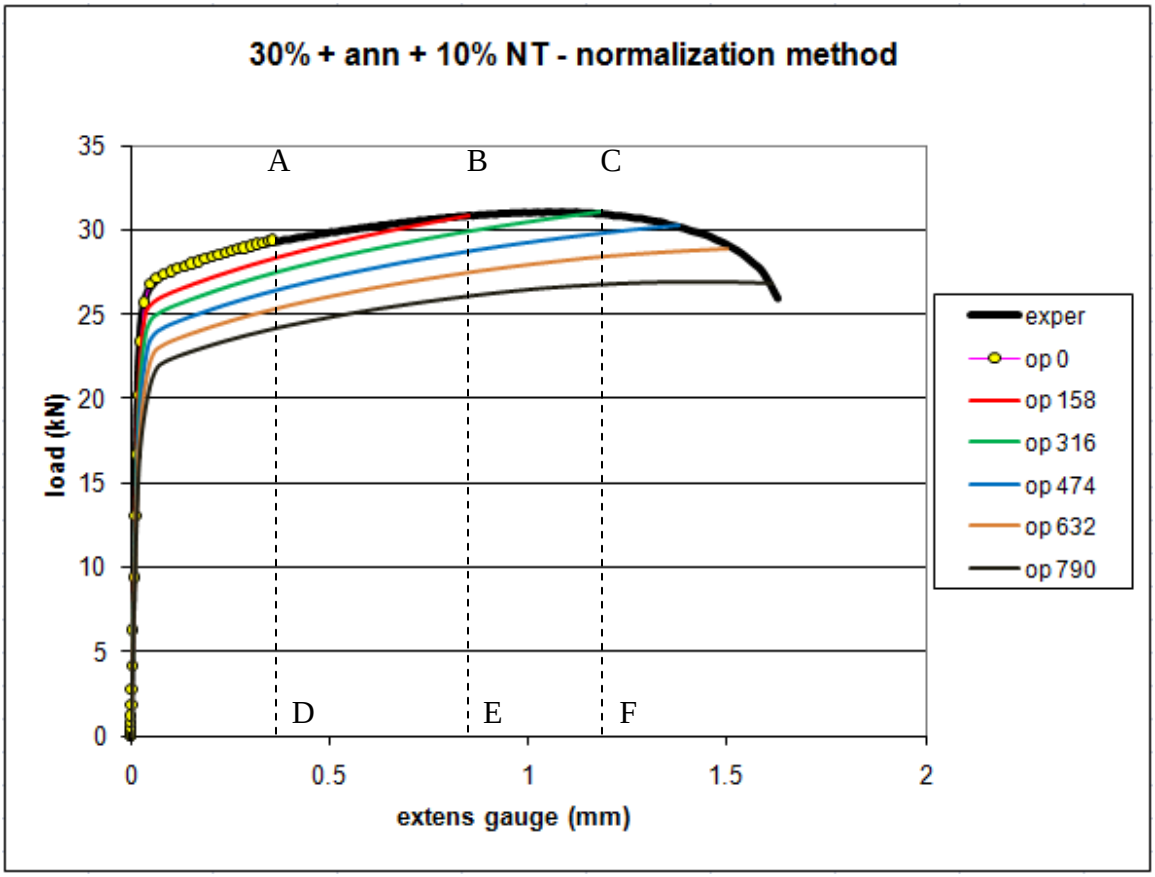

Fig. C.4. Area under curves computed for *J* calculation in normalization method.

Scibetta [171] suggested the following limits for the ductile crack growth Δa to be acceptable in the case of semi-brittle or brittle specimens (as they can be considered the 40% eng. strained and the 30% eng. strained ones in this project):

$$\Delta a / b < 0.1 \quad , \qquad a, b > \frac{J_C}{0.2\sigma_{YS}} \tag{C.2}$$

where 2*b* is the ligament diameter, *a* is the crack length, J_c the fracture toughness leading to unstable growth (brittle case), σ_{YS} the yield stress for the state considered.

Therefore, the results for 40% cold worked specimen are mostly invalid in the Fig. C.5, where the curves are presented. It is important to note that these curves are not related to the load line displacement, as it should have been, but to the gauge extension (gauge length being 10 mm around the notch), the only measured -and then uncontestable- value obtained from experiments. For that reason, the *J* values appeared to be much higher than expected. A conversion to load line displacement was not executed.

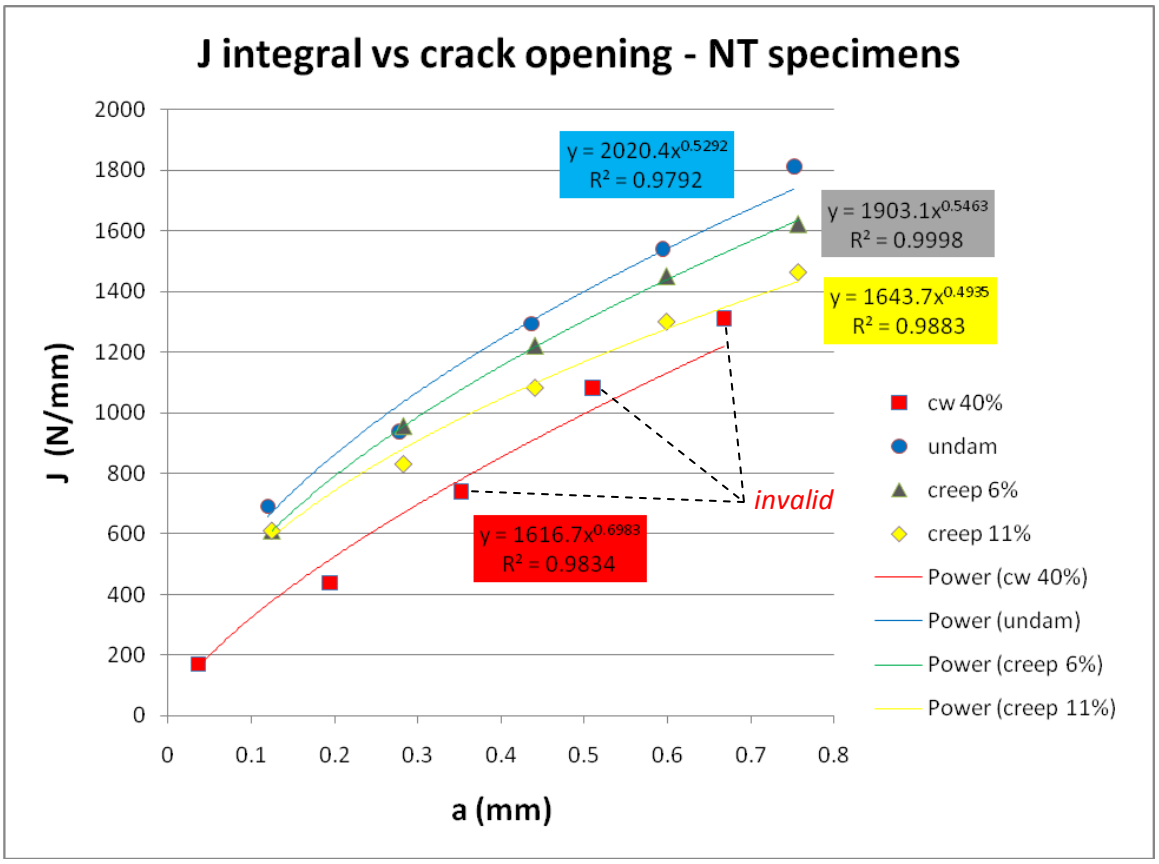

Fig. C.5. *J* curves from normalization method on sharp-notched round bar specimens.

Taking into account the limitations said before, results in Fig. C.5 did not add much to the investigation.